

# SOUND TRANSMISSION LOSS THROUGH A LIGHTWEIGHT DOUBLE-LEAF PANEL

A THESIS SUBMITTED TO AUCKLAND UNIVERSITY OF TECHNOLOGY  
IN PARTIAL FULFILMENT OF THE REQUIREMENTS FOR THE DEGREE OF  
DOCTOR OF PHILOSOPHY

Supervisors

Dr. Hyuck Chung

Dr. Kate Lee

Prof. Jiling Cao

June 2018

By

Mohammad Sazzad Mosharrof

School of Engineering, Computer and Mathematical Sciences



# Acknowledgements

I would like to begin by showing my gratefulness to Allah the Almighty, Who in the course of time has guided me and bestowed upon me His mercy. Without His will it would never have been possible for me to achieve anything. I am also grateful to AUT for giving me an opportunity to do PhD and also for supporting me financially by awarding me the full scholarship. I am thankful to all my supervisors Dr Hyuck Chung, Dr. Kate Lee and Prof. Jiling Cao for their support. A special thank to my primary supervisor Dr. Hyuck Chung, whom I interacted most of the times. I could not have finished my PhD without their support. I wish them all more success in life. I am thankful to Dr. Quan Bai, who along with my supervisors strengthened me mentally at a very crucial moment of my study. I thank all of my friends and fellow PhD students of AUT. Their friendly company made me feel like at home. I am grateful to the New Zealand government and people for letting me come to this lovely country for study. I pray for the well-being of all my Muslim brothers. I show deep appreciation to my family members back home, who took care of my responsibilities in my absence. Especially, my mother, I pray and wish for her well-being and long life. I am grateful to my wife for her unselfish generosity, my two sons and others. A special thank to my brother, who in absence of me took care of my family and treated my children as his own. I do not know how can I compensate other than praying for the sacrifice these people made for me. It is for their patience, good heart and sense of responsibility that I was able to stay away and continue studying PhD for more than 3 years. I believe this PhD is not my own effort only, but a continuous struggle of a number of people.

# Abstract

The topic of my PhD research is the sound transmission loss ( $\mathcal{T}_L$ ) of lightweight double-leaf panels based on an analytical model. Computed values of  $\mathcal{T}_L$  are used to analyze the effects of various dimensions, parameters and boundary conditions of the panel. A double-leaf panel is usually made of two plates attached by a number of beams. Analyses are carried out on finite sized panels, where multiple separate cavities between the plates and the beams are taken into account. These panels are widely used in building, aerospace and shipbuilding industries. Although the construction and transportation of these lightweight panels are convenient, a drawback of such a panel is that it is easy to make the panel vibrate and the vibration propagates through the structure and radiates sound. There are many factors that influence the transmission of sound, which are the boundary conditions, material properties, dimensions of the plates and the beams. The effects of the variations of the panel parameters on  $\mathcal{T}_L$  through these panels is another topic of this thesis. The small scale (variation in apparently identical panel components) and the large scale variations in the panel parameters are taken into account.  $\mathcal{T}_L$  is computed for an airborne excitation. The Kirchhoff thin elastic plate equation, the Euler beam equation and the continuity conditions at each plate and cavity connection are used. Spring type connection is used for plate-beam-plate connections. The coupling operator  $K$  is found to be very crucial, which needs to be selected accurately through trial and error. The panel is subjected to simply supported, clamped or mixed boundary conditions. The Fourier series and the Galerkin methods

are implemented. The boundary conditions mainly affect the lower frequency range and the effects are prominent for smaller panels. The first resonance frequency ( $f_1$ ) is the most significant parameter in the low frequency region. Splitting the cavities does not affect the  $f_1$  dominated low frequency region. Multiple partial cavity resonances occur when multiple cavities are considered.  $\mathcal{T}_L$  shows higher values above  $f_0$  till a certain frequency  $f_t$ .  $f_t$  is found to be related to the cavity width. Materials with comparatively less Young's moduli for the plates are recommended, and thicker and denser beams are also recommended. The cavities are recommended not to be too deep when no absorbing materials are used. A method of studying the effect of small scale variation in parameter values on  $\mathcal{T}_L$  variation is described, where  $\mathcal{T}_L$  is calculated for a range of values of parameters.  $\pm 5\%$  variation in three parameters e.g. thickness of the radiating plate and beams, and the cavity depth, are used as an example. The joint effects of two parameters are also studied. The difference in the maximum and the minimum  $\mathcal{T}_L$  is used to quantify the effects. The analysis is done in 125 Hz, 250 Hz, 400 Hz and 800 Hz bands. The effectiveness of different parameters varies with the frequency bands. A regression model based on the Response Surface Method (RSM) is proposed to study the trend in  $\mathcal{T}_L$  variation for small scale ( $\pm 5\%$ ) parameter variations. Effect of variations in seven parameters on  $\mathcal{T}_L$  variation is demonstrated as an example. The seven parameters are thickness of the two plates and the beams, the mass density of the plates and the beams, and the cavity depth. A method of optimizing  $\mathcal{T}_L$  is also described.

# Contents

<b>Acknowledgements</b>	<b>iii</b>
<b>Abstract</b>	<b>iv</b>
<b>1 Introduction</b>	<b>1</b>
1.1 Motivation . . . . .	1
1.2 Lightweight double-leaf panels . . . . .	3
1.3 Vibration of the panel . . . . .	6
1.4 Variation in the panel parameters . . . . .	7
1.5 Research questions . . . . .	8
1.6 Modelling method . . . . .	11
1.7 Literature Survey . . . . .	14
1.7.1 Infinite panels . . . . .	15
1.7.2 Finite panels . . . . .	19
1.7.3 Connection between the plates and the beams . . . . .	21
1.7.4 Periodicity . . . . .	22
1.7.5 Cavities . . . . .	23
1.7.6 Boundary conditions . . . . .	24
1.7.7 Variations in panel parameter . . . . .	26
1.8 Research contribution . . . . .	29
1.9 Summary of each chapter . . . . .	32
<b>2 Mathematical preliminaries</b>	<b>35</b>
2.1 Structural components of the double-leaf panel . . . . .	36
2.1.1 Euler beam . . . . .	37
2.1.2 Kirchhoff plate . . . . .	38
2.2 Plate-beam-plate Connection . . . . .	39
2.3 Boundary conditions . . . . .	42
2.3.1 Simply supported plates and beams . . . . .	43
2.3.2 Clamped plates and beams . . . . .	44
2.4 Fourier series expansion method . . . . .	45
2.5 Galerkin method . . . . .	46
2.6 Helmholtz's equation for sound wave . . . . .	48
2.6.1 Propagation of sound . . . . .	49

2.6.2	Solution to the Helmholtz's equation for a rectangular cavity . . . . .	50
2.7	Sound radiation from vibrating object . . . . .	52
2.8	Sound transmission loss . . . . .	54
2.9	Characteristics of $\mathcal{T}_L$ through lightweight panels . . . . .	56
2.9.1	$\mathcal{T}_L$ through a single panel . . . . .	57
2.9.2	Effect of finite size . . . . .	60
2.9.3	$\mathcal{T}_L$ through a double panel with air cavity . . . . .	61
<b>3</b>	<b>The lightweight double-leaf panel model</b>	<b>63</b>
3.1	Design of the double-leaf panel . . . . .	65
3.2	Scope of the model . . . . .	66
3.3	Derivation of the system of equations . . . . .	69
3.3.1	Solving the system of equations . . . . .	74
3.3.2	$\mathcal{T}_L$ calculation . . . . .	77
3.4	Parameter values . . . . .	78
3.5	Convergence check . . . . .	79
3.5.1	Convergence through repeated calculation of $\mathcal{T}_L$ . . . . .	79
3.5.2	Alternate method of convergence check . . . . .	81
3.6	$\mathcal{T}_L$ verification . . . . .	83
3.6.1	Comparison with infinite panel model . . . . .	84
3.6.2	Comparison with the measurement data . . . . .	86
3.6.3	Comparison with $\mathcal{T}_L$ generated by Insul . . . . .	88
3.6.4	Model consistency check . . . . .	90
3.6.5	Effect of the incident angles . . . . .	93
<b>4</b>	<b>Effects of boundary conditions</b>	<b>95</b>
4.1	Solving the system of equations . . . . .	98
4.1.1	Selecting the appropriate modal function . . . . .	98
4.1.2	Selecting the appropriate weighting function and generating the system of equations . . . . .	99
4.2	Convergence . . . . .	106
4.3	Model verification . . . . .	107
4.3.1	Model consistency check . . . . .	111
4.4	Effects of boundary conditions on different sized panels . . . . .	112
4.4.1	Comparison between the simply supported and clamped bound- ary conditions . . . . .	113
4.4.2	Comparison between the identical and mixed boundary condi- tions between the edges . . . . .	118
4.4.3	Effects of structural resonances . . . . .	119
<b>5</b>	<b>Effects of varying parameters</b>	<b>124</b>
5.1	Effects of the plate-beam-plate coupling . . . . .	127
5.2	Effects of the dimension of the panel . . . . .	129
5.2.1	Effect of varying panel length $A$ . . . . .	130

5.2.2	Effect of varying panel width $B$ . . . . .	132
5.3	Effect of multiple cavities . . . . .	134
5.3.1	Low frequency characteristics . . . . .	139
5.3.2	$\mathcal{T}_L$ characteristics above $f_0$ . . . . .	141
5.3.3	Relationship of $f_t$ with the cavity parameter $l$ . . . . .	145
5.4	Parametric analysis . . . . .	146
5.4.1	Effect of the plate parameters . . . . .	147
5.4.2	Effects of the beam parameters . . . . .	155
5.4.3	Effects of the cavity parameters . . . . .	161
<b>6</b>	<b>Effects of minor variations in panel parameters</b>	<b>165</b>
6.1	Methods . . . . .	167
6.2	Sensitivity analysis for three parameters . . . . .	168
6.2.1	Varying one parameter . . . . .	169
6.2.2	Varying two parameters . . . . .	169
<b>7</b>	<b>Variation in <math>\mathcal{T}_L</math> using the Response Surface Method</b>	<b>175</b>
7.1	Model based on RSM . . . . .	177
7.2	Simulation design . . . . .	179
7.2.1	Full Factorial Design . . . . .	179
7.2.2	Box-Behnken Design . . . . .	180
7.2.3	Central Composite Design . . . . .	181
7.2.4	Model verification . . . . .	182
7.3	Results . . . . .	183
7.3.1	Discussion . . . . .	184
7.3.2	Optimization . . . . .	191
<b>8</b>	<b>Concluding remarks</b>	<b>201</b>
8.1	Conclusion . . . . .	201
8.2	Future works . . . . .	207
	<b>Appendices</b>	<b>215</b>

# List of Tables

3.1	$M_{ct}$ in each frequency band for the simply supported 3 m × 3 m panel. .	81
3.2	$M_{ct}$ in each frequency band for the simply supported 3 m × 3 m panel.	82
4.1	Modal functions for different boundary conditions. . . . .	99
4.2	Material and cavity properties of the double-leaf panel used by Xin & Lu (2009). . . . .	108
4.3	$M_{ct}$ and number of terms in the displacements series per cavity width for four clamped panels . . . . .	109
4.4	$M_{ct}$ in each band for clamped (CCCC) and simply supported (SSSS) boundary conditions. . . . .	117
5.1	Parameter data from the manufacturers' catalog . . . . .	127
5.2	Ratio of $l/\lambda_t$ at $f_t$ for various cavity width of 3 m × 3 m panels . . . . .	146
7.1	Values of 7 selected parameters. . . . .	178
7.2	Corner points of the design with 3 parameters and 3 levels. . . . .	180
7.3	Axial points of the design with 3 parameters and 3 levels. . . . .	180
7.4	Edge points of the design with 3 parameters and 3 levels. . . . .	181
7.5	Design of simulation using CCD for 7 parameters. . . . .	194
7.6	Input $\mathcal{T}_L$ inserted to $\mathbf{R}$ corresponding to all simulation run at 4 frequency bands, calculated using the analytical model. . . . .	196
7.7	Estimation for 125 Hz. . . . .	198
7.8	Estimation for 250 Hz. . . . .	198
7.9	Estimation for 400 Hz. . . . .	198
7.10	Estimation for 800 Hz. . . . .	199
7.11	Optimum level values of the parameters derived from $\mathbf{R}$ . Level values more than 1 and less than -1 are rounded as 1 and -1, respectively to keep the parameter variations within the limit. . . . .	199
7.12	Optimum $\mathcal{T}_L$ and the parameter values at the stationary point with the extreme values of $\mathcal{T}_L$ . . . . .	200

# List of Figures

1.1	Typical lightweight double-leaf panel with beams placed along $x$ direction.	4
2.1	Schematic diagram of an Euler beam.	37
2.2	Schematic of the spring type connection at the plate-beam connections i.e. incident plate-beams-radiating plate.	40
2.3	Schematics of a closed cavity between two beams.	50
2.4	Coordinate system for the radiation of the sound wave.	52
2.5	Sound transmission through a plate.	55
2.6	Sound transmission through an infinite plate Fahy (2007).	59
3.1	Typical lightweight double-leaf panel with beams placed along $x$ direction.	66
3.2	$\mathcal{T}_L$ calculated for different values of $N_c$ for the 3 m $\times$ 3 m panel.	80
3.3	Comparison of $\mathcal{T}_L$ between different finite sized panels and the infinite panel	85
3.4	Comparison of $\mathcal{T}_L$ calculated for 3 m $\times$ 4.2 m panel with the measured data.	87
3.5	$\mathcal{T}_L$ corresponding to the panels used in this model (1.2 m wide and 4.2 m wide) and in Insul (1.2 m wide and 4 m wide). The blue lines and the red lines correspond to the Insul model and the model used here, respectively, where the lines with markers correspond to the Insul model.	88
3.6	$\mathcal{T}_L$ through four different sized simply supported panels when $\theta_i, \phi_i = \pi/4$ . The dashed lines (- - -) and the solid lines (—) corresponding to panels without stiffeners and panels with stiffeners, respectively.	91
3.7	1 <sup>st</sup> mode of 1.2 m $\times$ 1.2 m panels, a) without the stiffeners (15 Hz), and b) with the stiffeners (50 Hz).	92
3.8	$\mathcal{T}_L$ at different $\theta_i$ . Red dotted line ( $\cdots$ ), blue dash-dotted line ( $-\cdot-$ ), solid line (—) and brown dashed line ( $- - -$ ) corresponding to $\theta_i = \pi/18, \pi/6, \pi/4$ and $\pi/3$ , respectively.	94
4.1	Mixed boundary conditions. a) Type 1 boundary conditions, b) Type 2 boundary conditions.	96
4.2	Floor panel, a) Schematic diagram of the panel, and b) clamped boundary conditions.	97
4.3	The schematic diagram of the panel used by Xin & Lu (2009).	107

4.4	Comparison of $\mathcal{T}_L$ with the measured data corresponding to a 1 m $\times$ 1 m double panel without any beam stiffener. . . . .	110
4.5	Predicated $\mathcal{T}_L$ corresponding four sized square double-leaf panels without any beam stiffener. Material data given in Section 3.4 are used. . . . .	112
4.6	Mode shape corresponding to the 1 <sup>st</sup> resonance frequency of the 2.4 m $\times$ 2.4 m clamped double-leaf panel without any beam stiffener. Material data given in Section 3.4 are used. Top and bottom graphs correspond to the mode shape of the incident and radiating plates, respectively. . . . .	113
4.7	$\mathcal{T}_L$ for different boundary conditions. Red dotted line ( $\cdots$ ) and blue solid line ( $\text{---}$ ) correspond to the simply supported and the clamped boundary conditions, respectively. . . . .	114
4.8	$\mathcal{T}_L$ for different boundary conditions. Red dotted line ( $\cdots$ ), blue solid line ( $\text{---}$ ), dashed line ( $\text{- - -}$ ) and green dash-dotted line ( $\text{-}\cdot\text{-}$ ), correspond to the simply supported, clamped, type 1 and type 2 boundary conditions, respectively. . . . .	116
4.9	$\mathcal{T}_L$ 2.4 m $\times$ 2.4 m panel under different boundary conditions for four different $\theta_i$ . Solid line ( $\text{---}$ ), blue dashed line ( $\text{- - -}$ ), blue dash-dotted line ( $\text{-}\cdot\text{-}$ ) and red solid line ( $\cdots$ ) correspond to the clamped, Type 1, Type 2 and simply supported boundary conditions, respectively. . . . .	119
4.10	Comparison of the mode shape of the incident plate corresponding to the clamped, Type 1, Type 2 and simply supported boundary conditions. . . . .	121
5.1	Double-leaf panel. . . . .	125
5.2	$\mathcal{T}_L$ calculated for three different $K = [7, 70, 1000] \times 10^7 \text{ Nm}^{-2}$ for double-leaf panels with various $B = [12, 1.8, 2.4, 3] \text{ m}$ and fixed $A = 3 \text{ m}$ . Dotted line ( $\cdots$ ), solid line ( $\text{---}$ ) and dash-dotted lines ( $\text{-}\cdot\text{-}$ ) correspond to $K = [7, 70, 1000] \times 10^7 \text{ Nm}^{-2}$ , respectively. . . . .	129
5.3	$\mathcal{T}_L$ calculated for different panel length $A$ , when panel width is fixed at $B = 3 \text{ m}$ . . . . .	131
5.4	$\mathcal{T}_L$ calculated for different panel width $B$ , when panel length is fixed at $A = 3 \text{ m}$ and $K = 10^{10} \text{ Nm}^{-2}$ . . . . .	132
5.5	$\mathcal{T}_L$ calculated for different panel width $B$ , when panel length is fixed at $A = 3 \text{ m}$ and $K = 70 \times 10^7 \text{ Nm}^{-2}$ . . . . .	134
5.6	$\mathcal{T}_L$ calculated for different panel width $B$ , when panel length is fixed at $A = 3 \text{ m}$ and $K = 7 \times 10^7 \text{ Nm}^{-2}$ . . . . .	135
5.7	$\mathcal{T}_L$ calculated for different finite panels and different cavity conditions. Red ( $\text{---}$ ) and blue ( $\text{- - -}$ ) lines correspond to single cavity and multiple cavities, respectively. $\mathcal{T}_L$ is averaged in 1/3 octave bands over all incident angles. . . . .	136
5.8	$\mathcal{T}_L$ calculated for different finite panels and different cavity conditions. Red ( $\text{---}$ ) and blue ( $\text{- - -}$ ) lines correspond to single cavity and multiple cavities, respectively. $\mathcal{T}_L$ is averaged in 1/3 octave bands over all incident angles. . . . .	138

5.9	Transmission loss calculated for a 3 m × 3 m panel at $\theta_i, \phi_i = \pi/4$ with (—) and without (- - -) considering multiple cavities, respectively. . . .	139
5.10	Comparison of $\mathcal{T}_L$ for two cavity conditions at $\theta_i, \phi_i = \pi/4$ and at $f = 88$ Hz. Top and bottom figures correspond to the single cavity and the multiple cavity conditions, respectively. . . . .	140
5.11	Comparison of $p_c(x, y, 0)$ for two cavity conditions at $\theta_i, \phi_i = \pi/4$ for 180 Hz. Top and bottom figures correspond to the single cavity and the multiple cavity conditions, respectively. . . . .	142
5.12	Comparison of $p_c(x, y, 0)$ for two cavity conditions at $\theta_i, \phi_i = \pi/4$ for 395 Hz. Top and bottom figures correspond to the single cavity and the multiple cavity conditions, respectively. . . . .	143
5.13	Comparison of $p_c(x, y, 0)$ for two cavity conditions at $\theta_i, \phi_i = \pi/4$ for 3 kHz. Top and bottom figures correspond to the single cavity and the multiple cavity conditions, respectively. . . . .	144
5.14	Comparison of $\mathcal{T}_L$ for 3 m × 3 m panels at various $l$ with (—) and without (- - -) considering multiple cavities, respectively. . . . .	146
5.15	Transmission loss calculated for different $\rho_1$ , where the nominal value $\rho_1^N = 838.46$ kg/m <sup>3</sup> . . . . .	148
5.16	Transmission loss calculated for different $E_1$ , where the nominal value $E_1^N = 2.840$ GPa. . . . .	150
5.17	Transmission loss calculated for different $h_1$ , where the nominal value $h_1^N = 0.013$ m. . . . .	152
5.18	Transmission loss calculated for different $\rho_2$ , where the nominal value $\rho_2^N = 838.46$ kg/m <sup>3</sup> . . . . .	153
5.19	Transmission loss calculated for different $E_2$ , where the nominal value $E_2^N = 2.8457$ GPa. . . . .	155
5.20	Transmission loss calculated for different $h_2$ , where the nominal value $h_2^N = 0.013$ m. . . . .	156
5.21	Transmission loss calculated for different $\rho_b$ , where the nominal value $\rho_b^N = 550$ kg/m <sup>3</sup> . . . . .	158
5.22	Transmission loss calculated for different $E_b$ , where the nominal value $E_b^N = 9.8$ GPa. . . . .	159
5.23	Transmission loss calculated for different $h_b$ , where the nominal value $h_b^N = 0.045$ m. . . . .	160
5.24	Transmission loss calculated for different $d$ , where the nominal value $d^N = 0.095$ m. . . . .	162
5.25	Transmission loss calculated for different $d$ at 151 frequency points below 200 Hz, where the nominal value $d^N = 0.095$ m. . . . .	163
6.1	$\Delta\mathcal{T}_L$ is plotted against the percentage change of three parameters. Blue dashed line (- - -), red solid line (—) and green dotted line (⋯) represent the $\Delta\mathcal{T}_L$ , corresponding to the variations in $h_1, d$ and $h_b$ , respectively. . . . .	170
6.2	Variation of $\Delta\mathcal{T}_L$ due to the variations in $\bar{h}_b$ and $\bar{h}_1$ , when $\bar{d} = 1$ . . . . .	171
6.3	Variation of $\Delta\mathcal{T}_L$ due to the variations in $\bar{d}$ and $\bar{h}_1$ , when $\bar{h}_b = 1$ . . . . .	172

6.4	Variation of $\Delta\mathcal{T}_L$ due to the variations in $\bar{h}_b$ and $\bar{d}$ , when $\bar{h}_1 = 1$ . . . . .	173
7.1	Comparison between $\Delta\mathcal{T}_L$ calculated by RSM (lines with no marker) and the analytical model (lines with marker). $\Delta\mathcal{T}_L$ values are plotted against the percentage change of each parameter. Dashed line (- - -), solid line (—) and dotted line (⋯) represent the $\Delta\mathcal{T}_L$ , corresponding to the variations in $h_1$ , $d$ and $h_b$ , respectively. . . . .	183
7.2	Variation in $\Delta\mathcal{T}_L$ due to the variation in significant parameters at 125 Hz, predicted using RSM. When a single parameter values are varied, the remaining parameters take their respective nominal values. . . . .	185
7.3	Variation in $\Delta\mathcal{T}_L$ due to the variations in significant parameter pairs at 125 Hz, predicted using RSM. When the values of a parameter pair are varied, the remaining parameters take their respective nominal values. . . . .	186
7.4	Variation in $\Delta\mathcal{T}_L$ due to the variation in significant parameters at 250 Hz, predicted using RSM. When the a single parameter values are varied, the remaining parameters take their respective nominal values. . . . .	187
7.5	Variation in $\Delta\mathcal{T}_L$ due to the variations in significant parameter pairs at 250 Hz, predicted using RSM. When the values of a parameter pair are varied, the remaining parameters take their respective nominal values. . . . .	188
7.6	Variation in $\Delta\mathcal{T}_L$ due to the variation in significant parameters at 400 Hz, predicted using RSM. When the a single parameter values are varied, the remaining parameters take their respective nominal values. . . . .	189
7.7	Variation in $\Delta\mathcal{T}_L$ due to the variation in significant parameters at 800 Hz, predicted using RSM. When single parameter values are varied, the remaining parameters take their respective nominal values. . . . .	190
7.8	Variation in $\Delta\mathcal{T}_L$ due to the variations in significant parameter pairs at 800 Hz, predicted using RSM. When the values of a parameter pair are varied, the remaining parameters take their respective nominal values. . . . .	192

## List of Symbols

$A$	dimension of the plates along $x$ direction
$A_b$	cross-sectional area of the beams
$B$	dimension of the plates along $y$ direction
$C_{mn}^i$	series' coefficients for $w_i$ corresponding to the simply supported panels
$C_{mn}^{b,i}$	series' coefficients of $w_i$ for the clamped and mixed boundary conditions, where $b = c, t, q$ represent clamped, Type 1 and Type 2 boundary conditions, respectively
$c_0, \rho_0$	speed of sound in air and mass density of air, respectively
$D_i$	Bending stiffness of the plates
$d$	depth of the cavity
$E_i, E_b$	Young's moduli of the plates and the beams, respectively
$f_b$	frequency, where boundary effects (simply supported and clamped) are similar
$f_{cr}$	critical frequency
$f_t, \lambda_t$	frequency and wavelength, respectively (where cavity condition is insignificant)
$f_0$	mass-air-mass resonance frequency
$f_{cav}$	cavity resonance frequency (due to the standing waves inside the cavity)
$f_{bm}, f_p$	resonance frequencies of beams and plates, respectively
$h_i, h_b$	thicknesses of the plates and the beams, respectively
$I_b$	moment of inertia of the beams
$i = 1, 2$	corresponds to the incident and radiating plates, respectively.
$J$	Number of beams (except the beams at the edges, i.e $y = 0, B$ )
$K$	Spring constant for the assumed springs between the beams and the radiating plate
$k_m, q_n$	$m, n = 1, 2, 3 \dots$ spatial wavenumber along the $x$ and $y$ axes, respectively
$k$	wavenumber of sound in air
$l$	width of each cavity
$M_c, N_c$	upper limits for $m$ and $n$ , respectively, in the $p_c^j$ series
$M, N$	upper limits for $m$ and $n$ , respectively in the plate displacement series
$m_i$	mass per unit area of the plates
$p_c^j$	pressure in the $j^{\text{th}}$ cavity
$S_{mn}^j, T_{mn}^j$	series coefficients for $p_c^j$ corresponding to the simply supported panels
$S_{mn}^{b,j}, T_{mn}^{b,j}$	series coefficients of $p_c^j$ for clamped and mixed boundary conditions, where $b = c, t, q$ represent clamped, Type 1 and Type 2 boundary conditions, respectively
$w_i$	displacements of the plates
$\Phi$	function representing the plates' vibration along $x$ axis
$\Psi$	function representing the plates' vibration along $y$ axis
$\alpha$	function representing the cavity pressure along $x$ axis
$\beta^j$	function representing the pressure of the $j^{\text{th}}$ cavity along $y$ axis
$\rho_i, \rho_b$	mass densities of the plates and the beams, respectively
$\eta$	loss factor for the timber materials
$\kappa_n$	$n = 1, 2, 3 \dots$ spatial wavenumber of cavity pressure along the $y$ axis.
$\gamma_{mn}$	$m = 1, 2, 3 \dots$ propagation constant for $p_c^j$
$\omega, f$	angular frequency and frequency in Hz, respectively
$\theta_i, \theta_t$	elevation angles of the incident and the radiating waves
$\phi_i, \phi_t$	azimuth angles of the incident and the radiating waves
$\tau, \mathcal{T}_L$	transmission coefficient and transmission loss, respectively
$\mathcal{T}_L^{\min}, \mathcal{T}_L^{\max}$	minimum and maximum transmission losses, respectively
$\Delta \mathcal{T}_L$	variation in transmission loss
$\Delta \mathcal{T}_L^{\max}$	maximum variation in transmission loss

# Chapter 1

## Introduction

### 1.1 Motivation

Lightweight double-leaf panels are widely used in various industries, such as building, automobile and marine industries. This thesis focuses on timber based double-leaf panels, which are commonly used in building industries. The description of the double-leaf panel considered in this thesis is given in Section 1.2. These panels are used to separate two volumes, either as a floor-ceiling structure or as a partition wall between two rooms. The primary source of panel vibration is the direct impact on the panel (structure-borne excitation) or a sound wave on the panel (airborne excitation). For the floor-ceiling structure, both these forms of excitation are important. For walls, airborne excitation is the most common source of excitation. In this thesis, only the airborne excitation is considered. Speech and music are good examples of this.

The low weight of the double-leaf panels is one of the main reasons why they are in demand. Despite the low weight, the component strength should be high. The combined effects of the component strength and weight are often understood in terms of the strength to weight ratio, which is the ratio of the maximum load a component can bear without breaking and the weight of the material. Components with a higher strength to

weight ratio are desirable for lightweight panels. One advantage of using these panels is their easy handling. The low mass of these panels makes the construction much simpler and quicker. Double-leaf panels are often made in factories and then transported to the site. The double-leaf panels can also be installed on-site. Both the options are convenient, and the abundance of the timber material makes it even more convenient.

Despite the advantages of lightweight double-leaf panels, a major drawback is their poor sound reduction or sound transmission loss ( $\mathcal{T}_L$ ) in the low frequencies compared to a heavy panel. The panel vibrates easily because of its low weight and low stiffness.  $\mathcal{T}_L$  through the panel depends on the panel parameters. The thesis is about the variation in  $\mathcal{T}_L$  due to the variations in the panel parameters. The effects of the variations in the panel parameters are further explained in Section 1.4. The real double-leaf panels are subjected to some boundary conditions, where the variations in  $\mathcal{T}_L$  due to the variations in the boundary conditions are analysed in Chapter 4.

To increase the usefulness of these double-leaf panels, it is important to have a good understanding of how sound propagates through them. Research on lightweight double-leaf panels has been carried out for many years. Literature reviews of these panels are shown in Section 1.7. Starting from the study of the acoustic properties of a single panel, gradually more complex panels were studied. Many of them use theoretical approaches based on theoretical models. Among these theoretical models, many of them are derived using an analytical approach, where governing differential equations and boundary conditions for the plates and the beams are used to compute  $\mathcal{T}_L$ . Some of the recent studies include works by Brunskog (2005); Chung & Emms (2008); Mosharrof et al. (2011). Elaboration on these works and many others are given in Section 1.7. The study carried out in this thesis can be considered as the continuation of these existing studies. The main contribution in terms of modelling in this thesis is that a finite panel is considered, where all the cavities between the beams and the plates are considered as separated cavities. The air inside one cavity does not interact with

the air in the neighbouring cavities. The implication of the modification is discussed in Chapter 5. A significant improvement in  $\mathcal{T}_L$  can be achieved between 100 Hz to 630 Hz frequency bands for a 3 m  $\times$  3 m panel with this modification.

## 1.2 Lightweight double-leaf panels

A lightweight double-leaf panel consists of two plates placed at a distance and a core, where the core is the portion between the plates. One of the main functions of the core is to make the whole structure stiffer. The core of a typical lightweight double-leaf panel is made up of a number of parallel beams. Often only one set of parallel beams is placed, sometimes two perpendicular sets of beams are also used, forming a cross beam connection. Panels having one set of parallel beams are considered in this thesis. A number of cavities are formed between the plates and the beams and air fills the inside of the cavities. The drawing (not to scale) of the double-leaf panel is presented in Fig 1.1. The excitation is given on one plate, termed as the incident plate and the other one is termed as the radiating plate. The vibration of incident plate propagates through the core and reaches the radiating plate.

For the lightweight double-leaf panel considered in this thesis, sound can propagate from the incident plate to the radiating plate through two paths, 1. through the air inside the cavities, which is termed as the airborne path, and 2. through the beams, which is termed as the structure-borne path. Sound propagating through the airborne path experiences some attenuation because the air inside each cavity acts as a spring and the system behaves as a mass-spring-mass system. As a result, a resonance called mass-air-mass resonance arises at low frequency region where  $\mathcal{T}_L$  reduces considerably. Another type of resonance takes place at comparatively higher frequencies. Air inside the cavities gets reflected at the two plates. As a result, resonance takes place at some frequencies ( $f_{cav}$ ) because of the formation of standing waves. The structure-borne path

provides a direct connection between the plates, and the vibration of the incident plates can directly propagate through the beams to the radiating plates. Beams act as a sound bridge between the plates and transmit sound efficiently.

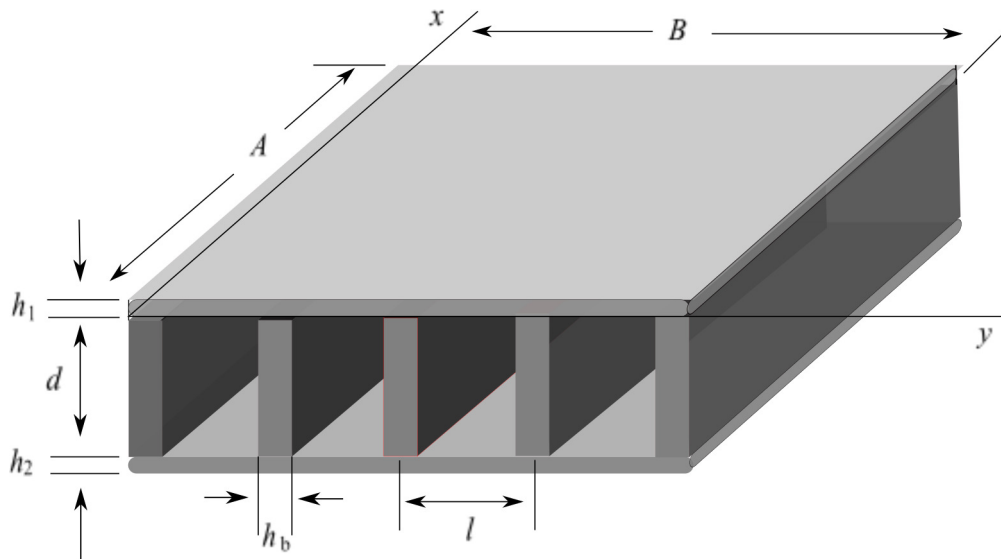


Figure 1.1: Typical lightweight double-leaf panel with beams placed along  $x$  direction.

$\mathcal{T}_L$  can be increased considerably by blocking or reducing the transmission through airborne and structure-borne paths. Often the air cavity is filled partially or fully with absorbing materials, which provide some damping to the system and increase the sound reduction over all frequencies including at the resonance. Another possible way of reducing the effect of the mass-air-mass resonance is to use Helmholtz resonator, which works in a narrow frequency band (Mao & Pietrzko, 2005). There are some other types of panel designs, where the direct connection between the plates is broken completely. Sometimes, two separate sets of beams are used for two plates, where beams attached to one plate do not directly connect to the other plate, which can be termed as decoupled panels (Mosharrof et al., 2011). Thus, the sound bridge between the plates is fully broken and this causes an increase in  $\mathcal{T}_L$ . Mosharrof et al. (2011) studied the effect of decoupling on impact sound level of an infinite decoupled double-leaf panel, where

the panel parameters, except the beam heights, are the same as considered in this thesis. One consequence of the decoupling is that the whole structure vibrates as a mass-spring-mass system which gives rise to a resonance. Below this resonance frequency, both plates vibrate more or less in phase and cause an increase in sound level compared to the coupled conditions (Mosharrof et al., 2009). Mosharrof et al. (2009) found approximately 10 dB increase in sound level below 150 Hz band having a peak at 100 Hz band. Above the resonance frequency, the coupling between the plates gradually weakens and the radiating plate vibration gradually gets isolated, which causes a reduction in sound level. Mosharrof et al. (2009) found that the sound level reduces above 150 Hz band with more than 20 dB reduction above 2 kHz band.

The panel considered in this thesis is the simplest form of double-leaf panels, where beams are attached to both panels without any resilient mount as shown in Fig. 1.1. Two identical plates are attached to a set of identical beams, where the distance between any two adjacent beams remains the same, which is denoted by  $l$ . The plates are placed parallel to the  $xy$  plane with a corner of the incident plate placed at the origin. The  $z$  axis is directed vertically downward. The beams are placed parallel to the  $x$  axis. Both plates are of the same size with dimensions  $A \times B$  in  $x$  and  $y$  directions, respectively. Thicknesses, Young's moduli, mass densities and loss factors of the plates are denoted by  $h_i, E_i, \rho_i, \eta_i$ , respectively, where  $i = 1, 2$  corresponds to the incident and the radiating plates, respectively. Thickness, Young's modulus, mass density and loss factor of the beams are denoted by  $h_b, E_b, \rho_b, \eta_b$ , respectively. The displacement at  $y = 0, B$  is zero, where two extreme beams are placed. Therefore, excluding two extreme beams, the number of the attached beams is  $J$ , which makes the number of the cavities to be  $J + 1$ . The depth of these cavities ( $d$ ) is the same as the height of the beams. Therefore, ignoring the plate thicknesses, the incident and the radiating plates are placed at  $z = 0$  and  $z = d$ , respectively.

Timber-based double-leaf panels considered in this thesis have a comparatively poor

sound reduction. Therefore, these panels are not appropriate for the applications where higher  $\mathcal{T}_L$  are required. There are other types of double-leaf panels having a corrugated core or honeycomb core, which are stiffer than the ones considered in this thesis (Ford et al., 1967; Moore & Lyon, 1991; Shen et al., 2012). Double-leaf panels with corrugated cores are widely used in constructing the hulls of bullet trains (Shen et al., 2012). The corrugated double-leaf panel can be simplified by modelling it as a typical double-leaf panel having periodically connected springs with both the translational and the rotational stiffness (Shen et al., 2012).

Propagation of sound through both airborne and the structure-borne paths contribute to the direct sound transmission. Sound can also propagate through the edges and through the supports; this is known as the flanking transmission. The flanking transmission is not considered in this thesis. The edges are assumed to have infinite baffle to prevent any transmission through the flanks.

### 1.3 Vibration of the panel

A sound wave makes a lightweight panel vibrate and radiate sound on the other side. It is often desirable in the building industry to have a better sound reduction or  $\mathcal{T}_L$  but, in reality, the lightweight panels have poor  $\mathcal{T}_L$ . Mass reduction of the panel, i.e. making the panel light, is a major cause of poor sound reduction at low frequencies. According to the mass law, doubling the plate mass increases the  $\mathcal{T}_L$  through the plate by 6 dB and vice versa (Vigran, 2008; Fahy, 2007).  $\mathcal{T}_L$  increases with frequency as well. Therefore, the sound reduction is worst in the low frequency regions. The attached beams offer some resistance to the propagation of the vibration by increasing the stiffness. Attaching the beams works well in the mid and high frequency regions (Legault & Atalla, 2009). The cavities between the plates and the beams also transmit the vibration from the incident plate to the radiating plate.

The characteristics of the air and the cavities between the plates affect the vibration of the plate and the sound transmission. The attached beams split the cavity between the plates into multiple small cavities. Often the presence of the beams is ignored, and a single large cavity is considered between the plates during modelling. According to the author, this is not an accurate representation of the real double-leaf panels considered in this thesis as shown in Fig. 1.1. The multiple small cavities are considered in this thesis, and effects of this modification are studied in detail in Chapter 5. The mechanisms of sound transmission through the beams and the cavities are discussed in the next chapter.

The transmission of sound through the panels depends also on the boundary conditions and the boundary effects are size and frequency dependent. A smaller panel is expected to be influenced more by the boundary conditions. As the panel becomes larger, the effects of boundary conditions gradually decrease. The boundary effects are predominant in the low frequency regions.

## 1.4 Variation in the panel parameters

The key parameters of the panel are the material properties, the dimensions of the plates and beams and the boundary conditions. These parameters directly influence the sound propagation through the panel. For example, increasing the plate thickness is expected to increase  $\mathcal{T}_L$  according to the 'Mass law'. Sometimes various parameters or constraints are interdependent. For example, the boundary conditions are expected to have a dominant effect on the smaller panels, which gradually weaken with the increase in panel size. The effects of boundary conditions are more prominent in the low frequency region. These panels are used in various applications to serve various purposes. Sometimes the purpose is to maximise sound transmission, while at other times it is the opposite. Therefore, an adequate understanding of how these parameters and the constraints influence  $\mathcal{T}_L$  is important for making a suitable design. With this

knowledge, the panel parameters can be selected efficiently to ensure the desirable range for  $\mathcal{T}_L$  value.

One issue associated with lightweight panels is the variation in  $\mathcal{T}_L$  between the double-leaf panels that have apparently the same material properties and dimensions. Studies have shown that there is a variation between the measurement data of nominally identical structures (Onkar & Yadav, 2005; Craik & Steel, 1989; Öqvist, 2010; Johansson, 2000). Some of the possible sources of these differences are the variations in the material properties, the surroundings or boundaries and workmanship (Trevathan & Pearse, 2008; Craik & Steel, 1989). There are often hidden flaws inside the materials (Memmolò et al., 2016). Timber is a natural material which is widely used to make lightweight panels. The mechanical properties of timber vary because of many environmental factors (Machado et al., 2014; Gerhards, 2007; Smith, 2012). The material properties of the panel components may also change in the course of time. For example, the moisture content of the material may vary depending on the outside temperature or humidity. Structural movement may also cause mechanical properties to vary over time.

All these minor variations in the parameters add to the variations in  $\mathcal{T}_L$ .  $\mathcal{T}_L$  variation due to a single parameter may not be significant, but the combined effects of the variations of many parameters may accumulate to cause significant variations in  $\mathcal{T}_L$ . This issue is addressed in this thesis by generating a regression model, which is given in Chapter 7.

## 1.5 Research questions

### Question 1

How do different constraints, e.g. multiple cavities and boundary conditions, affect  $\mathcal{T}_L$  through lightweight panels? A double-leaf panel is always placed under some

constraints, and sound transmission through the panel from one side to the other is influenced by these constraints. The effects of two of such constraints are studied in this thesis, where the constraints are the multiple cavities between the plates and the beams, and the boundary conditions. The author likes to treat the multiple cavities as a constraint because it is not treated as an intrinsic property of the panel; rather it is considered as a level of complexity during modelling. Many authors did not consider this important and ignored the effects of multiple cavities. The effects of considering multiple cavities are discussed in Chapter 5 by comparing the calculated  $\mathcal{T}_L$  for two cavity conditions, 1. considering a single cavity and 2. considering multiple cavities. Another obvious constraint of a finite panel is the boundary conditions. The effects of the boundary conditions vary with the panel size and the frequency. Larger panels are less affected by the boundary conditions compared to smaller panels. The variations in the sound transmission through different sized panels at different boundary conditions and frequency bands are analysed in Chapter 4.  $\mathcal{T}_L$  is calculated at 104 frequencies between 20 Hz and 5 kHz bands, which are compared in 1/3 octave frequency bands. In this case,  $\mathcal{T}_L$  is calculated from the average transmission coefficient, which is an average of transmission coefficients calculated at all possible angles. Comparison is also made of  $\mathcal{T}_L$  calculated at a single incident angle ( $\theta_i = \pi/4$ ).

## Question 2

How do different parameters of the panel contribute to the overall sound transmission? The goal here is to understand the effects of varying the values of these individual parameters on the overall sound transmission, given a fixed set of constraints. This analysis is made considering multiple cavities for the simply supported boundary conditions only and is given in Chapter 5. The lightweight panel is composed of many parameters, each of which varies depending on the design of the panel. Ten parameters are taken into consideration in this thesis. These are, thicknesses, mass densities,

Young's moduli of the two plates and the beams, and the cavity depth. The parameter values are varied at a comparatively large scale, where the largest value is four times the smallest one. The varying effects of the dimensions of the panel are also analysed.

### Question 3

How sensitive is the sound transmission to the variations in the panel parameters? The research questions 2 and 3 seem similar because both of them are about studying the variation on  $\mathcal{T}_L$  due to the variations in the panel parameters. The difference is that a small-scale variation in the panel parameters is of interest here, which is presented in Chapter 6 and Chapter 7. These small-scale variations are observed in the material and geometric parameters of apparently identical components. One goal of this research is to study the effect of the small variations in the panel parameters on the overall sound transmission. The varying effects of the incident plate thickness, the beam thickness and the cavity depth on  $\mathcal{T}_L$  are estimated; these are discussed in Chapter 6. The author could not find any reference in the literature about the expected variation in each parameter. Therefore, the author had to apply imaginary variation limits. Each parameter is assigned its own nominal value. In Chapter 6, a  $\pm 5\%$  variation around these nominal values is considered for each parameter. This limit may be unrealistic for some parameters. For example, the nominal value of the cavity depth is set as 95 mm and  $\pm 5\%$  of which is approximately 10 mm. The cavity depth is not expected to vary by that large a margin. The idea is that the true variation in  $\mathcal{T}_L$  caused by the variation of different parameters can be extrapolated from the methods and results given in this thesis. Similarly, in Chapter 7, the varying effects of 7 parameters are studied using a method known as Response Surface Method (RSM), which uses a regression model. The varying parameters are mass densities and Young's moduli of the two plates, of the beams, and the radiating plate thickness. These are in addition to the three parameters considered in Chapter 6. Here also, an imaginary range of  $\pm 5\%$  variation is considered

for all parameters.

## 1.6 Modelling method

There are some well-known modelling methods, such as the Statistical Energy Analysis (SEA), the Finite Element Method (FEM) and the analytical method. Models based on analytical methods provide exact solutions to the set of equations. Any discrepancy in the result means that the detail of the model needs to be improved. The modelling is usually carried out for a simplified version of the actual scenario. It is not always possible to attribute a single set of parameter values for all cases in reality. As discussed in Section 1.4, the panels that are nominally identical may have variations between themselves or may develop some deviations from the initial parameter values over time. The panels will also experience variations in some external parameters, such as humidity, temperature or acoustic characteristics of the incident and the radiating rooms. Therefore, it is common to see some discrepancies in the predicted results. Another source of error is the truncation of the higher terms in the series once an acceptable accuracy is attained. Adding more terms may increase the accuracy a little but requires an unrealistic amount of memory and computation time. Therefore, a balance between the accuracy and the computational cost has to be maintained.

One issue with the analytical method is that sometimes the system of equations becomes unsolvable. The trial and error method is sometimes used to generate a solution. Despite these issues, the analytical method is a useful tool for modelling the acoustic problems of lightweight panels. The method is applicable for a broader frequency range; although, in case of higher frequencies and for large panels, it may require long computation times even for a computer with a reasonable CPU speed.

Another widely used method is the finite element method (FEM), which is often categorised as an example of the numerical method. The analytical equations are

considered in this method and the solution is found by solving them. Therefore, from this perspective, FEM is a form of analytical approach. The main difference between the analytical method and FEM is that the analytical method considers different panel components separately and uses the governing equation of the whole component. For example, plates and beams are different components of the whole structure, and separate equations for each plate and beam may be used in the model. For FEM, the whole structure and thus, each component of the structure, is subdivided into a number of small elements. The number of elements for different components may vary. The appropriate governing equations are set for each element. Since two adjacent elements are connected via some nodes, the elements satisfy some inter-element boundary conditions at the nodes. Combining all the elemental equations and the boundary conditions, a system of governing equations is derived which is then solved for the desired variables. The elements can be linear, quadratic or of a higher order. The size of these elements is crucial for estimating the solution (Łodygowski & Sumelka, 2006). It is desirable to have the element size as small as possible. The number of elements will increase with the reduction of the element size, which will result in an increase in governing equations and computation time. Therefore, the rule of thumb is that the element size must be twelve times smaller than the smallest wavelength for linear elements; for quadratic elements, it is six times. Therefore, a large number of elements are required at high frequencies when the wavelengths are small (Łodygowski & Sumelka, 2006). Thus, FEM breaks down in the high frequency region because of unrealistic calculation time and memory consumption.

To reduce the computation time and memory consumption FEM is sometimes used in combination with other methods, which is known as wave FEM (Zhou et al., 2015; Yang et al., 2018). The whole structure is divided into multiple small segments, and FEM is applied only to a small segment (named as the basic segment). Naturally, this drastically decreases the number of elements. Solutions for the remaining segments are

found by translating the derived solution of the basic segment using any inter-segment boundary conditions between the adjacent segments or some other physical conditions. For example, the Floquet principle can be used to make the translation for a periodic lightweight double-leaf panel.

SEA works in the high frequency range but fails in the low frequency range. SEA is an energy-based method and considers the energy flow through different components. The system is analysed in terms of energy transmission between the components. It is not required to describe each and every detail of the components when using this method. SEA assumes that the coupling between the subsystems is weak, which is not the case here. The plates and the beams are so strongly connected that the connections between them can be considered as almost rigid. A prerequisite for SEA is the diffuse energy field in the subsystems. The diffuse energy field is approximated at the high frequency region, where mode counts, i.e. the number of modes in a frequency band, are high. The system acts independently without being much influenced by the boundary conditions. It fails in the low frequency region, where modes are few and the natural frequencies are widely spread. This means that only a few modes are dominant in low frequency region, leaving the rest of the modes insignificant.

The vibration of a complex structure is often determined by using the SEA method when it is too complicated to construct an analytical model. The SEA model is based on the energy loss factor in each component and the coupling loss factors between these components. The known values of loss factors are often used; sometimes these values are measured experimentally. Sun & Richards (1985); Sun et al. (1986), in the series of their papers, described procedures for calculating the total loss factor for various structures using the SEA. Crocker & Price (1969) derived models for sound transmission through a single wall and Craik & Smith (2000) worked on the  $\mathcal{T}_L$  of a double-leaf panel attached with beams. In these cases, the loss factors of the individual components were measured separately. After determining the values of the loss factors,

the energy balance equations for the adjacent subsystems were established. All these energy balance equations together formed the system of governing equations.

The analytical modelling method is used in this thesis. The Fourier series expansion method is considered in particular, which has been one of the most common methods for modelling  $\mathcal{T}_L$  through lightweight finite panels. The exact solution of the problem dealt in this thesis can be derived analytically without any trial and error. Therefore, the result is reliable, with reasonable accuracy. It is convenient to vary the parametric detail of the panel in the analytical model, which is crucial for this thesis. The parameter values can be varied individually at a large scale or at a small scale so that the effects of these variations to  $\mathcal{T}_L$  can be analysed. The reason for choosing the method is not because it is the best modelling method. The same analyses can be made using the FEM based models. The analytical method is one of the methods that can serve the purpose of the thesis. Another alternate modelling option is FEM, which is known to be computationally costly in the higher frequency region. Indeed, there are some computational techniques, e.g. wave FEM, to reduce the computation time of FEM. Once the  $\mathcal{T}_L$  form the model is verified, This analytical model can be used for verification of any other models, e.g. FEM based models.

There are some other types of models, where the detail of the panel is not considered with great accuracy, rather the equations are simplified by some reasonable assumptions. Sharp (1978) proposed a simplified form of  $\mathcal{T}_L$  equations for various types of panel. Bradley & Birta (2001) constructed an empirical formula of  $\mathcal{T}_L$  for studying the effect of resilient supports of a double-leaf panel with attached beams.

## 1.7 Literature Survey

In this section, an overview of the existing research on lightweight panels based on the theoretical modelling of lightweight panels is given. SEA and FEM based modelling

are discussed in the previous section. In this section, only the research works based on the analytical models are reviewed. The research area of the lightweight panels is broad, and the analytical approach has been one of the primary methods for developing models. The intention here is to provide a brief overview of different aspects of lightweight panel modeling. For example, the effect of the multiple cavities, the attached beams and the connections between the plates and the beams. A step-by-step improvement of the modelling of lightweight panels over the course of time is highlighted. Depending on the panel extent, the available models can be categorised into two groups, infinite panel models and finite panel models. Models are developed by applying various approaches within each category. Literature reviews based on different types of panels and different aspects of panels are presented below in separate subsections.

### 1.7.1 Infinite panels

Some early works on infinite panels were done by Beranek & Work (1949); London (1949, 1950), where sound transmission through a single plate was studied by London (1949). London (1950) extended it for a double wall without any attached beam and with the air around the panel and between the plates. London (1950) did not calculate the plate displacements. Instead, the pressure balance equations were constructed for the sound pressures on both sides of the plates.  $\mathcal{T}_L$  was calculated by solving for these pressures. Beranek & Work (1949) modelled a double-leaf panel with a flexible blanket and air gap. Beranek & Work (1949) derived the impedance of the blanket and the fluid medium separated by the panels.  $\mathcal{T}_L$  was then derived from these impedance expressions.

Mulholland et al. (1967) used a different approach to determine  $\mathcal{T}_L$  of an infinite double panel without any beams in between. He considered multiple reflections of the sound wave. The principle used is that a fraction of the incident wave gets transmitted

through the incident plate and the remainder is reflected back. This transmitted wave after reaching the radiating plate gets retransmitted and reflected in the same manner. Therefore, continuous reflection and transmission of the sound waves take place at both the plates. The plates were considered infinite and reflections at the boundaries were ignored by Mulholland et al. (1967). Summing up for all pressure waves at the incident and radiating sides,  $\mathcal{T}_L$  was calculated. The method was further modified by introducing an additional term with the reflection fraction corresponding to the absorption of the sound energy. It was assumed that a fraction of sound intensity was absorbed in the inner surfaces of the double panel. With this additional term, the agreement between the theoretical and experimental results was much better compared to the agreement found by London (1950). The inclusion of the absorption term can be treated as an ad-hoc correction to match the experimental data, rather than an exact representation of the physical phenomenon.

Cummings & Mulholland (1968) implemented this multiple reflection method for a finite double panel. Cummings & Mulholland (1968) assumed rigid boundaries or infinite baffle so that only the reflections were considered at the boundaries and no sound transmission. Unlike Mulholland et al. (1967), Cummings & Mulholland (1968) did not consider any absorption for the inner surfaces of the double panel. Instead, Cummings & Mulholland (1968) introduced a similar term as Mulholland et al. (1967) had and multiplied it with the reflected wave amplitude at the boundaries to account for the sound absorption. Cummings & Mulholland (1968) commented that the sound absorption at the cavity boundaries is more realistic than the absorption at the inner surfaces of the panel. The level of sound absorption was controlled by varying the term.

The studded double panel was modelled by Lin & Garrelick (1977). The inclusion of the studs complicates the modelling method because interactions between the beams and the plates need to be modelled accurately. Lin & Garrelick (1977) used a different approach, where the displacements of the two plates are calculated. The Kirchhoff thin

plate equations were considered, where the forces acting on the plates were put at the right-hand side of the equations. Selecting the forces acting on the plates is crucial. It is often the case that simplification is made about this aspect. The forces considered by Lin & Garrelick (1977) were a plane wave excitation along with the reactions from beams and the cavity pressure. Lin & Garrelick (1977) ignored the moment reaction and any shear forces. The connections between the plates and the beams were assumed to be rigid allowing no relative movements between the contact surfaces of the plates and the beams. Another simplification was that the effects of the beams on the cavities were ignored. A single big cavity was considered between the plates, where beams put no constraint on the cavity pressure. The Fourier transform method was used for solving the plate equations. One of the key features of this modelling method was the use of Poisson's summation formula, which converts the infinite summation of exponential series into infinite summation of Dirac functions. With this conversion, the property of Dirac function can be implemented.  $\mathcal{T}_L$  is then calculated from the plate displacements. The vibration can propagate from the incident plate to the radiating plate through the cavity and the beams. Lin & Garrelick (1977) found that the propagation through the beams was stronger than that for the cavity.

The Fourier transform method was also implemented by Brunskog & Hammer (2003); Takahashi (1983); Mosharrof et al. (2011), although the conditions were not exactly the same as considered by Lin & Garrelick (1977). Mace (1980b) used the same method but implemented it on a plate with two sets of beams attached. Brunskog & Hammer (2003); Takahashi (1983) considered the double-leaf panels attached by beams, which is of interest here. Brunskog & Hammer (2003) considered a point excitation and did not consider the moment in each plate beam connection. Mosharrof et al. (2009) studied a decoupled panel where the rigid connection between the plates via beams is broken. Sets of beams attached to any plate do not connect with the other plate. Mosharrof et al. (2009) also considered the moment at each plate-beam connection and

considered the point excitation similar to Brunskog & Hammer (2003). Mosharrof et al. (2009) compared the result with the result calculated by Brunskog & Hammer (2003) and found that the improvements of decoupling and moment inclusion were mainly in the high frequency region. Brunskog (2005) introduced the multiple cavities into the model but the panel remained infinite. He considered a plane wave excitation and calculated  $\mathcal{T}_L$ . The pressure inside each cavity was expressed in terms of cosine series to satisfy the hard boundary conditions at the beam locations.

Wang et al. (2005) studied an infinite double panel with beams and applied two methods. The model based on the first method was named as smeared model, where the studs were replaced by translational and rotational springs. The model based on the second method was named as the periodic model where a lumped mass was attached at each beam location along with the springs. The smeared model could predict the cavity resonances and the coincidences but it ignored the periodic effects. The plate displacements were expressed in terms of space harmonic series and the solution was derived in the spatial domain. The periodic model used the principle of virtual work to generate the governing equation. A set of linear equations were derived from this governing equation to solve for the unknown coefficients of the displacement series. Some additional peaks and troughs were observed for the periodic model, which corresponded to the stop and pass-bands respectively. A literature review on the periodicity of the panel will be presented later in Section 1.7.4.

There are other types of double-leaf panels having stiffer cores. Ford et al. (1967) studied a sandwich panel made of isotropic plates with a rigid polyurethane foam in the core, and Moore & Lyon (1991) considered honeycomb core. The vibration of the plates and the core was expressed in terms of symmetric and anti-symmetric modes. The symmetric modes were related to the axial stiffness of the core and the anti-symmetric modes were dependent on the bending of the panel. Coincidence can happen when any of these modes coincide with the bending modes of the plates. These modes are related

to the panel parameters and variation in the parameters causes the coincidence to take place at different frequencies. By selecting appropriate parameter values, the coincident frequency can be moved out from the preferred frequency range (Moore & Lyon, 1991).

### 1.7.2 Finite panels

The acoustic characteristics of the finite panels depend on the boundary conditions. The vibration gets reflected at the boundaries and gives rise to the structural resonances which appear as dips in  $\mathcal{T}_L$  graph. The frequency and the mode shape of the resonant vibration depend on the boundary conditions. Therefore the total vibration field of the finite panels is the superposition of the resonance and non-resonance vibrations which contribute to the overall sound radiation. The simply supported and the clamped boundary conditions are the two most common boundary conditions considered. Sewell (1970) considered simply supported single leaf panel with no beams. Only the non-resonance transmission was considered. The transmission coefficient is usually expressed in terms of incident angle and is written as  $\tau(x, y)$ . Therefore, in a diffuse field, where sound waves are incident from any direction,  $\mathcal{T}_L$  must be averaged over all incident angles and appropriate limits for the incident angles need to be set. Sewell (1970) derived an expression for transmission coefficient for the single panel as a function of frequency, size and shape of the panel. The result shows that the size and shape were important below the critical frequency denoted by  $f_{cr}$ . Above  $f_{cr}$ , these factors were insignificant.

Leppington et al. (1987) considered a simply supported rectangular panel and derived expressions for the transmission coefficients. The approach used by Leppington et al. (1987) differed from Mulholland et al. (1967) and London (1949) so that the plate motion was considered instead of the pressure balance around the plate. Leppington et al. (1987) considered both resonant and non-resonant terms and derived the expressions of  $\mathcal{T}_L$  for three cases, namely, below, at and above the  $f_{cr}$ . Below  $f_{cr}$ , both resonant and

non-resonant terms were found to be important. Leppington et al. (1987) applied the coincidence conditions at  $f_{cr}$  and ignored the non-resonant terms above  $f_{cr}$ . Later, Davy (2009) considered a finite single panel and modified the expression for the transmission coefficient derived by Cremer (1942). According to Davy (2009), the equation used by Cremer (1942) is oversimplified and thus is restricted for frequencies well above  $f_{cr}$ . Later Brunskog (2012) applied the same approach as Davy (2009) and included the fluid loading that was missing in (Davy, 2009). It was assumed that, above  $f_{cr}$ , sound radiation was dominated by the characteristics corresponding to those at the critical incident angle. Thus, to simplify the expression, the incident angle was replaced by the critical angle in most instances, whereas, for the low frequency region, it was assumed that the most dominating region was near the grazing incident. Thus, the incident angle was replaced by  $\pi/2$  in most places. Brunskog (2012) dealt with a finite single wall in an infinite baffle and calculated the radiation impedance for below and above  $f_{cr}$  to calculate  $\mathcal{T}_L$ . He restricted the calculation for the forced vibration case. The effect of azimuth angle was ignored in the radiation impedance calculation. The results were the same above  $f_{cr}$  but differed for the various methods below the critical frequencies.

White & Powell (1966) considered a double panel without beams. He derived an expression for the transmission coefficient for random incident waves. The complexity of random incidence was simplified and parameters were expressed in terms of averaged or equivalent values. This method is applicable for reverberant vibrating panels having multi-modal characteristics, a case that is better understood in terms of average over space, time and frequency bands.

Roussos (1984) modelled the vibration and  $\mathcal{T}_L$  of a single plate under plane wave incidence. The plate was simply supported on four sides with an infinite baffle. Roussos (1984) used a different method, where the Kirchhoff plate equation was used and the plate displacement was expressed as a Fourier sine series so that the simply supported boundary conditions were satisfied. Roussos (1984) calculated the radiating pressure

from the plate displacement using the Rayleigh integral (Cremer & Heckl, 2013; Fahy, 2007). With this method,  $\mathcal{T}_L$  contribution from each mode can be calculated and compared. Thus, the most influential mode of vibration can be identified. Similarly, the angle of maximum sound transmission can also be identified. Chung & Emms (2008) studied double-leaf panel attached via periodically connected beams. The Fourier series method was used here as well. The governing equations are similar to Lin & Garrelick (1977). For example, same Kirchhoff plate equation and Euler beam equations were considered. Chung & Emms (2008) modified the plate-beam-plate connections by including the slippage between the plates and the beams and also used a point excitation. Later, Chung et al. (2014) added an additional upper layer, and the two upper plates were treated as a single plate having equivalent mass and stiffness. The pressure inside the cavity for a double plate structure was expressed as a Fourier cosine series. The cosine terms satisfy the condition of the hard cavity walls. The numbers of terms in the sine and cosine series are crucial. They were carefully truncated after a finite number for computational purposes ensuring an acceptable accuracy. Using the orthogonality of the Fourier sine and cosine terms, an independent equation was derived corresponding to each Fourier term. The same modeling method is implemented in this thesis.

### 1.7.3 Connection between the plates and the beams

The connection type between the plates and the beams is an important factor for modeling and there are several options for modelling these. For example, similar to Brunskog & Hammer (2003); Lin & Garrelick (1977); Takahashi (1983), the connection type can be considered as rigid, where the plates and the beam have the same displacements at the connection. In that case, beam exerts the same force on both the plates. The connection can also be considered as spring type, where a spring is considered in between the plate and the beam (Brunskog & Hammer, 2003). For the double plate panel, the spring type

connection is considered by assuming one plate to be connected rigidly with the beams and having the same displacement as the beams at the connections. A spring is assumed to exist between each beam and the other plate. In this case, the forces acting on the plates are different and so are the displacements. A connection can also be categorised as point connection and a line connection. Connections considered by Brunskog & Hammer (2003); Lin & Garrelick (1977) correspond to a line connection, where the plate and the beams are considered to be connected along a line. This resembles the case where plates and beams are connected with glue or nails/screws that are very close to each other. The point type connections consider the plates and the beams to be connected at some specific points at considerable distances and a nail on one side does not affect the nails on the other side. Craik & Smith (2000) developed a SEA model where both types of connections were studied. According to Craik & Smith (2000), if the spacing between nails is large, the connection should be considered as point connection. Whereas, if the spacing is small the connection corresponds to the line connection. The transition from point to line connection takes place when the bending wavelength equals the spacing of the nails.

#### **1.7.4 Periodicity**

Regardless of the connection type, these periodically connected beams have a real impact on how the vibration propagates through the structure. Beams usually act as a barrier to the vibration propagation at some frequencies, known as the stop-band. While vibrations with some other frequencies can propagate; these are known as pass-bands. These pass and stop-bands are observable in the frequency graphs as alternate peaks and dips (Wang et al., 2005). A considerable number of studies have been carried out on the wave propagation through these periodic panels (Mead, 1975; Gupta, 1970; Mead & Pujara, 1971). The main assumption here was that the motions at corresponding points

in two consecutive periodic sections, i.e. bays, are related by the factor  $e^g$ . The term  $g$  is the propagation constant, which is generally complex. The propagation constant is a unique property of the structure and is dependent on the spatial periodicity, frequency, boundary condition, but not the excitation pressure.

### 1.7.5 Cavities

Several cavities are formed between the plates and beams. In many studies, these cavities were often ignored and only one cavity was considered instead of all (Lin & Garrelick, 1977; Takahashi, 1983; Brunskog & Hammer, 2003; Chung & Emms, 2008). The attached beams were not considered to disturb the pressure field inside the cavities at all. The pressure field inside the cavity is a strong transmitter of vibration and has a significant role in vibration transmission from upper plate to the lower plate. Even if there is no beam attached between the plates, the cavity air transmits the vibration significantly. The cavity is often filled with absorbing materials to dampen the transmission through the cavity. The absorbing material dampens the mass-air-mass resonances. The propagation of the sound wave inside the cavity in the presence of the absorbing material is disturbed. The absorbing material is modelled by modifying the wave-number in the medium and the density of the medium inside the cavity. Delaney & Bazley (1969) modelled the mineral wool by treating it as an equivalent fluid, and derived an empirical formula for the wavenumber of sound in the equivalent fluid and the impedance of the equivalent fluid.

There are some active control techniques for reducing sound transmission through the cavities using actuators or loudspeakers inside the cavities (Li & Cheng, 2008; Gardonio & Elliott, 1999). Actuators apply forces to the plates to counteract the plate vibration due to the excitation. Actuators can be used to reduce the transmission due to structural resonances whereas the loudspeaker attempts to neutralise the sound pressure

inside the cavities, and thereby the effects of cavity resonances are reduced. Another option for reducing the sound transmission through the cavities is to use a Helmholtz resonator inside the cavity, which is considered as a passive control technique (Mao & Pietrzko, 2005; Li et al., 2010). The resonator has a cavity and a neck, where the air inside the neck acts as an air spring. It behaves as a single degree of freedom system having a single natural frequency. It is effective only at a narrow frequency band around its natural frequency, and ignores the neighbouring modes. A more broadband reduction in sound transmission can be achieved by selecting appropriate damping of the resonator. Li et al. (2010) used six resonators to achieve considerable enhancement in  $\mathcal{T}_L$  in a much broader frequency band. The resonators were placed at theoretically identified optimum locations, e.g. at the location of maximum pressure.  $\mathcal{T}_L$

Brunskog (2005) considered the effect of the finite cavities and expressed the total fields of the cavity pressure in terms of the pressure field in a single cavity by relating the pressure field in two neighbouring cavities by a phase difference. The decoupled model considered by Mosharrof et al. (2011) had only one cavity, both the plates had separate sets of beams. This is an example where the assumption of having a single cavity is appropriate.

### 1.7.6 Boundary conditions

A finite panel is subjected to boundary conditions. The boundary conditions are expected to have a large effect on a smaller panel and at lower frequencies. One of the key consequences of the finite panels is that they will show additional dips due to structural resonances. The resonance frequencies vary with the boundary conditions. Leissa (1973) studied the free vibration of the plates, where 21 different possible combinations of the boundary conditions were discussed. Only a few of the boundary conditions are relevant for the panels used for buildings. Leissa (1973) calculated the

natural frequencies of the plate at different boundary conditions. Haçiegan et al. (2018) calculated the natural frequencies of clamped plates using FEM. Sung & Jan (1997) calculated the natural frequencies of a clamped rectangular panel and also calculated the transmitted sound power.

Most of the works on lightweight finite double-leaf panels are based on the simply supported boundary conditions. There are not many works on the double-leaf panel with attached beams under other boundary conditions. According to the research made by the author, Xin et al. (2008); Xin & Lu (2009, 2011a,b) showed lots of interest in the clamped double-leaf panels, where clamped double-leaf panels with various designs are considered. For example, double-leaf panels with only an air cavity, with porous material inside the cavity and double panels with studs. The series expansion method was used in these articles for finite clamped panels. Although these series functions are not orthogonal, they satisfy the clamped boundary conditions. In these papers, the coefficients of the functions were derived by using the Galerkin method (Fletcher, 2012).

Xin et al. (2008) studied the effect of the cavity depth and the panel thickness for both infinite and finite panels. The mass-air-mass resonance frequency ( $f_0$ ) was found to decrease with the increase in cavity depth for both finite and infinite panels. Additional dips, which correspond to the modal behaviour of the plates, were observed for the finite panels. The effects of incident angles were also studied where the increase in the elevation angle increases  $\mathcal{T}_L$  in the whole frequency region apart from the dips in the higher frequency region. The dips are shifted in frequency with the variation in the incident angle. The author concluded that the dips are due to the structural phenomenon rather than the cavity characteristics. Xing & Liu (2009) also studied the free vibration of an orthotropic plate and derived the exact eigenfunctions for each condition. Liu & Daudin (2017) considered a panel where only two plates were considered with a porous-elastic material between the plates. No beams were considered between the

beams by Liu & Daudin (2017). Liu & Catalan (2017) further modified the model to include the effect of an external mean flow.

In this thesis, the comparative analysis is made on  $\mathcal{T}_L$  having various boundary conditions. It is interesting to find out which edges are most effective in terms of their boundary conditions. The edges can be categorised as two types, 1. the edges parallel to the beams and 2. the edges perpendicular to the beams. The effectiveness of different edge conditions is identified by calculating  $\mathcal{T}_L$  by varying the boundary conditions at the edges.

### 1.7.7 Variations in panel parameter

Variations in different parameters have their own contributions to the overall variation of sound transmission through a lightweight panel. Panel parameters directly affect the coincidence and structural resonances. Kropp & Rebillard (1999) considered three different cases, when fundamental structural resonance frequency is 1. way below, 2. close to, and 3. far above  $f_{cr}$ . They showed that  $\mathcal{T}_L$  can be optimised by proper selection of different parameter values. Some studies on varying the parameters in panel-like structures focus on the effects of variation in the properties of individual components. For example, Vaicaitis (1974) calculated the variations in the natural frequencies, and in the normal modes, for beams with random characteristics. Vaicaitis (1974) considered the variation in cross-sectional area, density, Young's modulus and moment of inertia of the beam.

Vaicaitis (1974) considered the variations in the placement of the beam and observed that the natural frequencies and the normal modes deviate significantly from those of a uniform beam. Manohar & Adhikari (1998) considered mass density and flexural rigidity as random variables for a beam and studied the variability in shear forces at two ends of a panel. The responses are presented in terms of the mean and the standard

deviation of the forces. A significant variation in shear forces was observed for 5% variation in the input parameters around their respective means. The variation was higher near the resonance frequencies. Onkar & Yadav (2005) studied the variation in the natural frequencies caused by the variations in material properties for a composite plate. Onkar & Yadav (2005) used Hamilton's principle for generating the governing equations after which the Taylor series expansion is implemented. The Young's modulus of the plate is the most effective parameter for variation in mean values of the frequencies. A similar technique is adopted by Chung (2012) to analyse the randomness of a double-leaf panel. Chung (2012) considered the whole panel, where the stiffness of the plate, the shape of the beam and the slippage between the plate and the beam were taken as random variables. Chung (2012) found that each random parameter has an impact on the plates' displacement. Each function has different effects on the vibration, over different ranges of frequencies. In these studies by Vaicaitis (1974); Manohar & Adhikari (1998); Chung (2012), the excitation was considered a deterministic one and the same is considered in this thesis. There have also been some studies on variations in the excitation (Mazur-Śniady et al., 2013).

The variation in each parameter is introduced by adding a random term with a mean value. There are different methods for modelling the random component. Chen & Soares (2008) used a series of orthogonal random variables known as the Karhunen-Loève expansion to express the random term and implemented it in a FEM model. Onkar & Yadav (2005) and Gao et al. (2010) used the Taylor series expansion and ignored the higher order terms to represent the random part. The random parameters, expressed as random processes, are then introduced in the governing equations. After solving the equations it is possible to derive a direct correlation between the input and the output variables. For a composite panel, deriving such direct mathematical expressions and solving the system of different component equations is difficult.

Loucks et al. (2005) used a statistical method to analyse the uncertainty for an

engineering application. In this method, a set of outputs is calculated for a set of varying inputs and the relationships between any input and the output data are established. The output is calculated for several simulation runs, where a specific parametric combination corresponds to a single run. The Response Surface Method known as RSM is an alternate method of analysing the variation of input parameters to the outputs. In RSM, a regression model is derived based on a set of outputs corresponding to different combinations of some selected input parameters. Often the output of the selected parametric combinations is determined experimentally. Usually, the regression model is a quadratic model. In this method the degree of linear and nonlinear effects can be distinguished. In addition, the combined effects of any two parameters can also be determined.

Liang et al. (2007) considered two plates attached together without any beams. Three types of materials were considered. The input parameters were the thickness of the two plates and ratio of the Young's modulus and the mass density of the plate. The effects of variation in the input parameters on three outputs were analysed, where the outputs were the mean quadratic velocity of the panel, the radiated sound power from the panel and the loss factor of the panel. The analysis was done by limiting the total mass of the whole panel to 1 kg. Li & Liang (2007) considered similar panels and the same input parameters and studied the effects on the radiated sound power, the modal frequency and the loss factor. The selected parametric combination and the corresponding outputs are experimentally determined as well, but the parametric combinations differed between (Liang et al., 2007) and (Li & Liang, 2007). One advantage of this simple quadratic model is that the optimum points can be extracted from the model, as was done by Li & Liang (2007). Similar studies are carried out on optimising the vibratory loads at the rotor hub of a helicopter (Ganguli, 2002). The input parameters are considered as the blade flap stiffness, lag stiffness and the torsion stiffness. Cheng & Xiao (2007), using RSM, studied the variation of three geometric

and three material parameters on the variation in the natural frequency. Two cases were considered, first, only the geometric parameters were varied, and second, only the material parameters were varied. Three RSM models were derived for each case using three different experimental designs. The three RSM models were also compared with the results calculated from a deterministic FEM model. The free vibration and the flutter analysis of a suspension bridge is analyzed using RSM by Cheng & Xiao (2005).

## **1.8 Research contribution**

The main objective of this thesis is to achieve a better understanding of the acoustical characteristics of lightweight double-leaf panels stiffened by attached beams. The analysis is carried out on a theoretical basis using a modified mathematical model. The modifications are made in modelling the multiple cavities formed between the plates and the beams for a finite sized double-leaf panel. Often, the presence of the beams is ignored and a single cavity is considered during modelling (Lin & Garrelick, 1977; Brunskog & Hammer, 2003; Chung & Emms, 2008). The cavities may not be perfectly sealed in the real panels. There is always a possibility of having leaks between the plate-beam connections through which air can flow. Despite some possible air passages between the cavities, the beams are supposed to provide some disturbance of the cavity pressure. Ignoring the beams completely is not an accurate representation of the panel, it is one way of simplifying the cavities of the real structure. Another possible way to simplify the cavity modelling is to treat the multiple cavities between the plates and the beams as completely isolated from each other; hitherto this has not been explored much. The author was motivated to study the effects of the other simplification, where multiple cavities are considered.

According to the research by the author, only one paper considered multiple cavities formed between the plates and the beams, the panel being of infinite extent (Brunskog,

2005). This gave the opportunity to include this feature, i.e. multiple cavity consideration, in a finite panel model, which is done in this thesis. The author considers this to be one of the main contributions of the thesis. A talk on this modified model was given by the author in a conference "New Zealand Mathematics Colloquium, 2015" held in Christchurch, in December 2015. The Fourier series expansion method is used in this model, where the finiteness of the cavities is considered, which was not the case for (Chung & Emms, 2008). Similar to works done by Brunskog (2005); Chung & Emms (2008), two plates are expressed by the Kirchhoff thin plate equation and the beams are expressed by the Euler beam equation in this thesis.

Although Brunskog (2005) included the finite cavity in his model, he did not provide a detail discussion about the effects of the multiple cavities. The relative effects of the multiple cavities to the overall  $\mathcal{T}_L$  are discussed in detail in this thesis. It was found that consideration of the multiple cavities is effective up to a certain frequency band  $f_t$ . The relationship between the  $f_t$  and the cavity width  $l$  is discussed. It is observed that multiple resonance dips occur around the mass-air-mass resonance frequency ( $f_0$ ). The pressure profile inside the cavities reveals that separate resonances occur in different cavities, which is the cause for the observed additional dips around  $f_0$ . As a whole, the discussion in this thesis is more comprehensive than the discussion made by Brunskog (2005). This is also one of the research contributions of this thesis. Enhancement in  $\mathcal{T}_L$  with the present setup may lead to modifying the design for having completely enclosed multiple cavities.

The edges of the real timber based panels are fixed to the support to some degree (Craig & Smith, 2000). The timber based materials are not hard enough to consider the edges fully clamped. Therefore, it is not realistic to consider the boundary conditions of the real panels fully simply supported or fully clamped; these can be considered as two extremes of the real scenario. The real boundary conditions can be considered as something in between these two extremes, and this may also depend on the frequency.

It is more mathematically convenient to consider the boundary conditions of any edge to be either fully simply supported or fully clamped. For that reason, it is often the case that a single type of boundary condition is considered for any given side. According to the research made by the author, there are not many works studying double-leaf clamped panels attached with beams. The author is motivated to consider both these extremes and to make a comparative analysis of their effects on  $\mathcal{T}_L$ . Two mixed boundary conditions were also considered to make a variation in the boundary conditions so that the model may resemble the exact panel better. In the author's opinion, studying the effects of these two boundary conditions and the mixed boundary conditions are helpful for understanding the real scenario better. A comparative analysis between  $\mathcal{T}_L$  calculated using the modified model corresponding to these boundary conditions is given in Chapter 4. I consider this as one of my research contributions.

The modified model is used for analysing the effects of varying the panel parameter to  $\mathcal{T}_L$ . Use of the modified model is expected to provide more accurate conclusions.  $\mathcal{T}_L$  is calculated for various values of a parameter where others are kept fixed. Both large scale and small scale variations in parameters are considered. The varying effects of mass per unit area of the plates, the bending stiffness of the plates and the cavity depth on  $\mathcal{T}_L$  were studied in one of my conference papers (Mosharrof & Chung, 2016). The analysis is carried out for a broad frequency range between 20 Hz and 5 kHz 1/3 octave bands in this thesis.

As mentioned in Section 1.4, minor variations in the parameter values of identical panels are observed. Parameter values of a particular panel may also vary over time due to environmental factors. The relative effects of minor variations in three individual parameters are studied. The expected variation in  $\mathcal{T}_L$  because of the variations in seven panel parameter values are addressed using a regression model. More emphasis is given around the model and the method used for the analysis. The relative influence of any other parameters can also be studied following the method used here. This knowledge

will be helpful for selecting appropriate parametric values for achieving the desired outcome. To the author's knowledge, the use of this type of model for studying the effect of variations in the panel parameters is a novel approach for lightweight panels.

## 1.9 Summary of each chapter

### Chapter 2

Chapter 2 gives a mathematical background for the model and  $\mathcal{T}_L$  computation. The equations and other mathematical tools used for modelling are explained. The Kirchhoff thin plate equation and the Euler beam equation are presented. The spring type coupling between the plates and the beams are described. The Fourier series expansion and Galerkin methods for solving the system of equations are explained. The chapter introduces the Helmholtz equation for the sound pressure of the air in and out of the panel. The boundary conditions in a closed rectangular air cavity are given. The solution to the Helmholtz equation in the closed rectangular cavity is represented by the Fourier cosine series. A general overview of sound transmission through the lightweight double-leaf panels is presented, where the mass-air-mass resonance, the coincidence, periodicity of the panels and effects of the finiteness of the panels are discussed.

### Chapter 3

This chapter deals with the derivation of the system of equations of the model and the solution methods. The simply supported boundary conditions are used here. The Fourier sine and cosine series are truncated by checking the convergence of the model. The model corresponding to the simply supported boundary conditions is validated using the measurement data available in the literature. The model is verified by comparing its predicted  $\mathcal{T}_L$  with the  $\mathcal{T}_L$  predicted by Brunskog (2005) using the infinite panel model.

## Chapter 4

The effects of different boundary conditions on  $\mathcal{T}_L$  are analysed. The boundary conditions are simply supported, clamped and mixed. Two scenarios for the mixed boundary conditions are analysed. First, two opposite sides are simply supported and the remaining sides are clamped. Second, the simply supported and clamped edges are swapped.  $\mathcal{T}_L$  is calculated for these four sets of boundary conditions. Four sets of parameter values are used, which correspond to four different sized square panels ranging from 1.2 m  $\times$  1.2 m to 3 m  $\times$  3 m.

## Chapter 5

Chapter 5 gives the relative effects of each parameter of the panel on  $\mathcal{T}_L$ . The parameters of interest are mass densities, thicknesses, Young's moduli of the plates and the beams, the cavity depth, and the panel dimensions. Simply supported boundary conditions are used in this analysis. In most cases,  $\mathcal{T}_L$  is calculated for 104 frequencies between 20 Hz to 5 kHz, which are then averaged to one-third octave bands.

## Chapter 6

The variation in  $\mathcal{T}_L$  due to small variations in the panel parameters is addressed in Chapter 6. A  $\pm 5\%$  variation in the values of the panel parameters is used and the corresponding variations in  $\mathcal{T}_L$  are calculated. 11 evenly spaced values within the range are set for each parameter. The analysis is done at four one-third octave bands, 125 Hz, 250 Hz, 400 Hz and 800 Hz bands. The analysis is restricted to the variations in three parameters, which are the incident plate thickness, the beam thickness and the cavity depth. The combined effects of any two-parameter pairs are also studied by calculating  $\mathcal{T}_L$  for all possible combinations of any two parameter values.

**Chapter 7**

A regression model based on Response Surface Method (RSM) is applied to estimate  $\mathcal{T}_L$  for a higher number of parameter variations. The variations in  $\mathcal{T}_L$  with the variations in seven input parameters are discussed in this chapter. The seven varying parameters are thicknesses of the two plates and the beams, mass densities of the two plates and the beams and the cavity depth. A  $\pm 5\%$  variation in the input parameters is used. The analysis is carried out for the same four one-third octave frequency bands. More emphasis is given on the model so that the maximum expected variations in  $\mathcal{T}_L$  or minimum  $\mathcal{T}_L$  due to any known parameter variations can be achieved using this model.

**Chapter 8**

In this chapter, the conclusions of the thesis are enumerated and possible future works are proposed.

## Chapter 2

### Mathematical preliminaries

The main purpose of the model is to calculate  $\mathcal{T}_L$  through lightweight double-leaf panels. The sound transmission process involves various physical stages, such as structural vibration of the plates, propagation of sound through air (acoustics), and the coupling of structural vibration and the propagation of sound through air (vibro-acoustics). Therefore, all three mechanisms need to be included in the model to calculate  $\mathcal{T}_L$ . A brief explanation of these three physical backgrounds is given in this chapter.

The first five sections deal with structural vibrations. The lightweight double-leaf panel structure is made up of plates and beams. Therefore, the first section explains the equations of the beams and the plates. These equations govern their respective vibration patterns. The next section explains the modelling of the connection between the plates and the beams. The double-leaf panels considered in this thesis are of finite extent. Therefore, the finite plates and beams are subjected to some boundary conditions, which are explained in the section after. The Fourier series expansion method and the Galerkin method are both used for solving a system of equations depending on the boundary conditions. Brief explanations of these solution methods are given in Sections 2.4 and 2.5.

Section 2.6 discusses acoustics, where sound propagation through the air is explained. This section also considers a special case dealing with the sound pressure confined in a rectangular air cavity. This special case is applied in the thesis for estimating the sound pressure inside each cavity. Section 2.7 and Section 2.8 deals with the vibro-acoustics, which is about the interaction between the structural vibration and the acoustic sound waves. The calculation procedure of the sound radiated from a vibrating plate and the estimation of  $\mathcal{T}_L$  are presented in Section 2.7 and Section 2.8, respectively.

The chapter ends with Section 2.9, where a brief explanation of the different aspects of the lightweight double-leaf panel is given. The explanation discusses the separate related topics. Starting from a single plate, the complexity of the whole double-leaf panel structure is added gradually and is explained.

## 2.1 Structural components of the double-leaf panel

Plates and beams are the two types of components of a double-leaf panel. When plates and beams vibrate, they can experience axial stresses and shear stresses in all directions. The magnitudes of these stresses depend on the deflections and bending of these components. In this thesis, a very special case of plate and beam vibrations is considered, where the excitation from the air is so small that the panels hardly deflect or bend. It is convenient to consider only the axial stresses and the corresponding bending effects. The ratio of the bending stiffness to the shear stiffness is so large that any shearing effects on the beams can also be ignored. Euler's equation for beams and Kirchhoff's equation for isotropic thin plates are applicable in this case, which are well recognised for modelling the plates' and beams' vibrations, and are widely used in many papers dealing with similar problems, for instance (Lin & Garrelick, 1977; Mace, 1980a; Brunskog & Hammer, 2003; Chung & Emms, 2008; Mosharrof et al., 2009). For different types of double-leaf panels with stiffer cores, the shearing effect

may become significant (Ford et al., 1967; Moore & Lyon, 1991). Timber-based panels are orthotropic in nature, and it can be useful to include the orthotropic behaviour of the panel materials, particularly in case of denser fluid loading. In this thesis, the Euler beam equation and Kirchhoff plate equations are used because they suits the condition considered in thesis well.

### 2.1.1 Euler beam

Euler beams are subjected to the loads acting perpendicular to the longitudinal direction (direction along the length of the beam) of the beam as shown in Fig. 2.1. Beams do not stretch in the longitudinal direction. A beam is thus treated as a one-dimensional object, where deflections and bending of the beam are restricted to the transverse direction, i.e. in the direction of the applied loads. The deflections of the beams are assumed to be small and no shear stresses are considered. Bending causes the beam to rotate at an angle  $\theta$ , and one of the main assumptions of the Euler beam equation is that  $\theta$  is very small. All these assumptions perfectly match the case considered in this thesis.

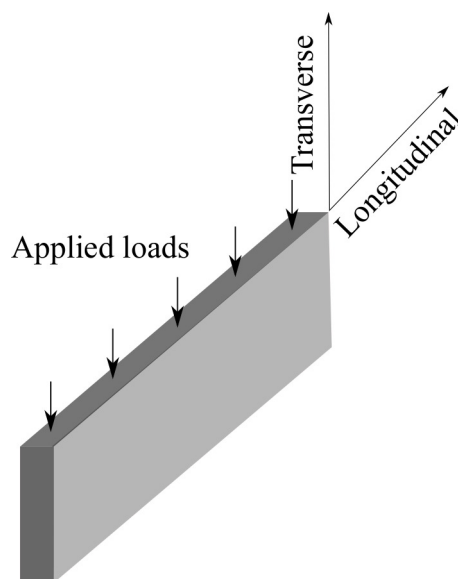


Figure 2.1: Schematic diagram of an Euler beam.

Under static axial loadings, the neutral axis of the beam will make a curve with the radius of curvature  $\psi$  on plane comprising of the longitudinal and transverse axis. When the upper half of the beam undergoes compression, the other half is in tension. The line dividing the compression half and the tension half is known as the neutral axis of the beam. The stress and the strain at the neutral axis of the beam are both zero, and they increase linearly with the distance from the neutral axis. One of the primary assumptions about Euler beams is that any cross section of the beam perpendicular to the neutral axis will remain perpendicular before and after the beam deflects. This means that beam deflection and bending can only take place on the plane comprising the longitudinal and the transverse axes.

Under dynamic axial loadings, a beam vibrates and thus, bends up and down, which is taken care of by introducing a time dependence to the governing equation. The system here is linear, the excitation and the responses have the same time dependence  $e^{i\omega t}$  where  $\omega$  is the angular frequency of vibration. Therefore, the deflection term with the time dependence is written as, where  $w_b(x, t) = w_b(x)e^{i\omega t}$ . The equation for a vibrating beam is written as (Cremer & Heckl, 2013; Dym & Shames, 2013)

$$\left[ E_b I_b \frac{d^4}{dx^4} - \rho_b A_b \omega^2 \right] w_b(x, t) = \mathcal{F}(x, t), \quad (2.1)$$

where  $A_b$  and  $\rho_b$  are the cross-sectional area and the mass density of the beam, respectively,  $\mathcal{F}(x, t)$  is the applied axial load. The term  $E_b I_b$  is a constant and known as the flexural rigidity of the beam.

### 2.1.2 Kirchhoff plate

The same assumptions considered for the Euler beams are also valid for the Kirchhoff plate equation, namely that the plate deflections are small, loads act perpendicular to the plate (transverse direction) only and no stress is considered along the transverse

direction. A plate is considered as a 2D object, where deflection and bending are restricted along the transverse direction only. Detailed descriptions of the derivation of the plate equation are available in textbooks (Dym & Shames, 2013; Timoshenko & Woinowsky-Krieger, 1940; Ventsel & Krauthammer, 2001). Here, the terms and parameters of the plate equation are described.

The thickness ( $h$ ) of a plate is assumed to be much smaller than its length and width. The ratio of  $h$  and the smallest dimension between length ( $A$ ) and width ( $B$ ), is smaller than  $1/10$ . The plate is homogeneous, meaning that the the material properties and the composition are same everywhere. The ratio of the strains along two directions is known as the Poisson's ratio ( $\nu$ ). The plate is isotropic, which assumes a constant  $\nu$  in any direction. There is a 2D neutral surface, where the stresses and deformations are zero. The cross-section perpendicular to the neutral surface is undeformed, as was the case for the Euler beams. There are vertical shear forces and bending moments for a plate. The in-plane shear stresses cancel each other and any out-of-plane shear stress is neglected. The plate equation is given as (Timoshenko & Woinowsky-Krieger, 1940; Dym & Shames, 2013)

$$D \left( \frac{\partial^2}{\partial x^2} + \frac{\partial^2}{\partial y^2} \right)^2 w(x, y) - \sigma \omega^2 w(x, y) = \mathcal{F}(x, y), \quad (2.2)$$

where  $\mathcal{F}(x, y)$  is the applied farces,  $D = Eh^3/12(1 - \nu^2)$  is the flexural rigidity of the plate,  $E$  is the Young's modulus of the plate, and  $\sigma = \rho h$  is the mass per unit area of the plate, where  $\rho$  is the mass density of the plate.

## 2.2 Plate-beam-plate Connection

The plate and beam connections form the structure borne path and act as sound bridges between the plates. Therefore, they are important with regard to modelling and accuracy.

Often simplifications are made while modelling these connections. Only the normal forces are considered. Any shear forces are ignored; this is justified because of the very small deflections of the plates. The moment exerted by each beam is also ignored at the expense of accuracy mainly in the high frequency region (Mosharrof et al., 2011). The plates and beams are assumed to be connected along lines. The line connection is appropriate when plates and the beams are connected along via glue or by nails separated by a distance less than half the bending wavelength (Craig & Smith, 2000).

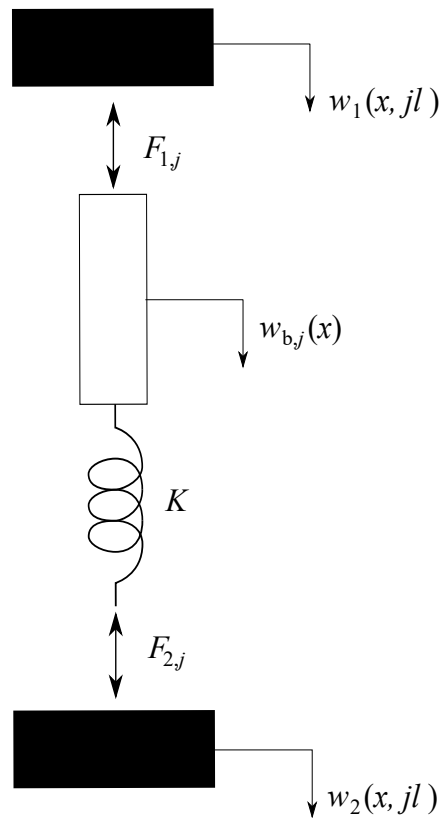


Figure 2.2: Schematic of the spring type connection at the plate-beam connections i.e. incident plate-beams-radiating plate.

The connection is sometimes considered rigid, allowing no relative motion between the plates at the connections. An alternate option is to consider the spring type connection, where a spring with spring constant  $K$  is assumed between each beam and the radiating plate. This allows some flexibility between the plates. The spring constant

corresponds to the coupling condition between the plates and the beams. A higher value of  $K$  corresponds to a stiff rigid connection, and the low value corresponds to loose coupling. Therefore, it is difficult to select the right value for the spring constant. Each connection is different and so is the coupling condition. The value of  $K$  varies with panels, and thus the exact coupling conditions are unknown.

In this thesis, the spring type connection is considered and the value of  $K$  is selected to match the measurement data given by Brunskog (2005), and same value was used by Brunskog (2005). The spacing between two adjacent beams is  $l$ . Therefore,  $j^{\text{th}}$  beam is situated at  $y = jl$ . The connection the plates and the  $j^{\text{th}}$  beam is illustrated in Fig. 2.2. The same connection is assumed for all plate-beam-plate connections. At each beam-plate connection, the incident plate is assumed to have same displacement as the attached beam, i.e.  $w_1(x, jl) = w_{b,j}(x)$ , where  $w_{b,j}(x)$  is the displacement of the  $j^{\text{th}}$  beam. Because of the springs at the connections, the displacement of the plates can be different from each other.

Each beam exerts reaction line forces on the plates. Therefore, the total reaction force acting on the plates will be the sum of all these reactions from the individual beams. As mentioned earlier, the moment reaction at each connection is ignored in this thesis. The reaction forces from the  $j^{\text{th}}$  beam to the incident and radiating plates are (Brunskog, 2005)

$$F_i(x, y) = \sum_{j=1}^J F_{i,j}(x) \delta(y - jl), \quad (2.3)$$

where  $F_{i,j}(x)$  are the forces acting on the  $i^{\text{th}}$  plates by the  $j^{\text{th}}$  beam. For the  $j^{\text{th}}$  beam,

one can write (Brunskog, 2005)

$$F_{1,j}(x) - F_{2,j}(x) = \left[ E_b I_b \frac{d^4}{dx^4} - \rho_b A_b \omega^2 \right] w_1(x, jl), \quad (2.4)$$

$$F_{2,j}(x) = K [w_1(x, jl) - w_2(x, jl)]. \quad (2.5)$$

Combining the above two equations, it can be written as

$$F_{1,j}(x) = (K + \mathcal{G})w_1(x, jl) - K w_2(x, jl), \quad (2.6)$$

$$F_{2,j}(x) = K [w_1(x, jl) - w_2(x, jl)], \quad (2.7)$$

where  $\mathcal{G} = E_b I_b \frac{d^4}{dx^4} - \rho_b A_b \omega^2$ .

## 2.3 Boundary conditions

The displacement, slope, moment and stress condition of a plate at the edges all vary depending on the boundary conditions. The simply supported and the clamped boundary conditions are the two commonly used for panel modelling. The test double-leaf panels are often simply supported at the edges in the laboratories. In many theoretical studies, lightweight double-leaf panels are modelled for simply supported boundary conditions and the model is validated using the laboratory measurements done on simply supported test double-leaf panels. Whereas, in many cases, the real double-leaf panels are fixed to supports to some extent (Craik & Smith, 2000). As mentioned in Section 1.8, it is difficult to have a fully clamped support for timber-based building materials. Simply supported and clamped boundary conditions are the two extremes for the real double-leaf panels. Therefore, in the author's opinion, studying the effect of clamped boundary conditions is as important as studying the effect of the simply supported boundary conditions. These two boundary conditions are discussed in the following sections.

### 2.3.1 Simply supported plates and beams

A simply supported beam rests on its two ends. There is no deflection and bending moment at the simply supported ends. Considering a beam of length  $A$  is placed along the  $x$  axis with one of the ends at the origin, the boundary conditions at the ends are written as

$$w_b(0) = 0, \quad w_b(A) = 0, \quad (2.8)$$

$$\left. \frac{d^2 w_b(x)}{dx^2} \right|_{x=0} = 0, \quad \left. \frac{d^2 w_b(x)}{dx^2} \right|_{x=A} = 0. \quad (2.9)$$

Considering the condition for no external load, i.e. the homogeneous condition, the natural frequency and mode shapes of the plate vibration can be evaluated. The natural frequency and mode shape vary with the boundary conditions. The expression for the natural frequency of a simply supported beam is given as (Dym & Shames, 2013)

$$\omega_n = \left( \frac{n\pi}{A} \right)^2 \left( \frac{E_b I_b}{\rho_b A_b} \right)^{1/2}, \quad n = 1, 2, 3, \dots \quad (2.10)$$

where  $\omega_n$  is called the natural frequency.

These boundary conditions are also applicable for rectangular plates of dimension  $A \times B$  having a corner placed at the origin. The boundary conditions for a simply supported plate are

$$w(0, y) = 0, \quad w(A, y) = 0, \quad w(x, 0) = 0, \quad w(x, B) = 0, \quad (2.11)$$

$$\left. \frac{\partial^2 w(x, y)}{\partial x^2} \right|_{x=0, A} = 0, \quad \left. \frac{\partial^2 w(x, y)}{\partial y^2} \right|_{y=0, B} = 0. \quad (2.12)$$

The natural frequencies  $\omega_{mn}$ , of a simply supported plate with dimension  $A \times B$  can be

derived as (Kinsler et al., 1999; Dym & Shames, 2013)

$$\omega_{mn} = \left[ \frac{D\pi^2}{\sigma} \right]^{1/2} \left[ \left( \frac{m}{A} \right)^2 + \left( \frac{n}{B} \right)^2 \right], \quad m, n = 1, 2, \dots \quad (2.13)$$

### 2.3.2 Clamped plates and beams

The two ends of a clamped plates are fixed with the supports, and no displacement takes place at these clamped ends. The slope of the beam always remains zero at the ends.

The boundary conditions for a clamped beam are

$$w_b(0) = 0, \quad w_b(A) = 0, \quad (2.14)$$

$$\left. \frac{dw_b(x)}{dx} \right|_{x=0} = 0, \quad \left. \frac{dw_b(x)}{dx} \right|_{x=A} = 0. \quad (2.15)$$

The natural frequency for a clamped beam is given as (Dym & Shames, 2013)

$$\omega_n = k_n^2 \left( \frac{E_b I_b}{\rho_b A_b} \right)^{1/2}, \quad n = 1, 2, 3, \dots \quad (2.16)$$

The value of  $k_n$  is chosen by satisfying the frequency equation (Dym & Shames, 2013)

$$\cos k_n \cosh k_n = 1. \quad (2.17)$$

For plates clamped at all edges the above conditions are satisfied for edges at  $x = 0, A$  and at  $y = 0, B$ . Therefore, the boundary conditions for a clamped plate are written as

$$w(0, y) = 0, \quad w(A, y) = 0, \quad w(x, 0) = 0, \quad w(x, B) = 0, \quad (2.18)$$

$$\left. \frac{\partial w(x, y)}{\partial x} \right|_{x=0, A} = 0, \quad \left. \frac{\partial w(x, y)}{\partial y} \right|_{y=0, B} = 0. \quad (2.19)$$

The corresponding natural angular frequencies of a clamped plate can be approximated as (Haçiegan et al., 2018)

$$\omega_{mn} = \pi^2 \left[ \left( \frac{m + \frac{1}{2}}{A} \right)^2 + \left( \frac{n + \frac{1}{2}}{B} \right)^2 \right] \sqrt{\frac{D}{\sigma}}, \quad m, n = 1, 2, \dots \quad (2.20)$$

## 2.4 Fourier series expansion method

In this method, the plate deflection is expressed as a linear superposition of a sine series and a cosine series using the Fourier series and is applicable for plates with simply supported edges. The displacements of the simply supported plates  $w(x, y)$  is expressed using the Fourier sine series as

$$w(x, y) = \sum_{m,n=1}^{\infty} C_{mn} \Phi_m(x) \Psi_n(y), \quad (2.21)$$

where  $\Phi_m(x) = \sqrt{2/A} \sin k_m x$  and  $\Psi_n(y) = \sqrt{2/B} \sin q_n y$ ,  $k_m = m\pi/A$ ,  $q_n = n\pi/B$  and  $C_{mn}$  is the set of coefficients that need to be determined. The Fourier sine series is limited to finite values  $M$  and  $N$  corresponding to  $x$  and  $y$  directions, respectively, for computation. The relation between  $M$ ,  $N$  is given as  $M/N = A/B$ , and it is shown in Section 3.5 that the convergence can be achieved maintaining this relation. Therefore,  $M = N = M$  for a square plate. The sine terms in the series are orthogonal, and the following can be written

$$\int_0^A \Phi_m(x) \Phi_n(x) dx = \begin{cases} 1 & m = n, \\ 0 & m \neq n, \end{cases} \quad (2.22)$$

$$\int_0^B \Psi_m(y) \Psi_n(y) dy = \begin{cases} 1 & m = n, \\ 0 & m \neq n. \end{cases} \quad (2.23)$$

Using the orthogonality of the series terms, the plate Equation (2.2) can be solved. Inserting Equation (2.21) into Equation (2.2), it can be written as

$$\sum_{m=1}^M \sum_{n=1}^N C_{mn} \mathcal{G}_{mn} \Phi_m(x) \Psi_n(y) = \mathcal{F}(x, y), \quad (2.24)$$

where  $\mathcal{G}_{mn} = D(k_m^2 + q_n^2)^2 - \sigma\omega^2$ . Multiplying  $\Phi_m(x)\Psi_n(y)$  to both sides of Equation (2.24) and integrating over the plate dimensions, a single independent equation is achieved. A system of  $MN$  independent equations can be derived, which is written as

$$Z\mathbf{c} = \mathbf{f}, \quad (2.25)$$

$$Z = \begin{bmatrix} \mathcal{G}_{11} & 0 & \dots & 0 \\ 0 & \mathcal{G}_{12} & \dots & 0 \\ \vdots & \vdots & \ddots & \vdots \\ 0 & 0 & \dots & \mathcal{G}_{MN} \end{bmatrix}, \mathbf{c} = \begin{bmatrix} C_{11} \\ C_{12} \\ \vdots \\ C_{MN} \end{bmatrix}, \mathbf{f} = \begin{bmatrix} f_{11} \\ f_{12} \\ \vdots \\ f_{MN} \end{bmatrix},$$

where

$$f_{mn} = \int_0^A \int_0^B \mathcal{F}(x, y) \Phi_m(x) \Psi_n(y) dy dx.$$

Solving the above system of equations, the unknown coefficients  $C_{mn}$  are determined once  $\mathcal{F}(x, y)$  is given.

## 2.5 Galerkin method

The Galerkin method is a useful and widely used method to solve differential equations (Fletcher, 2012). An approximate solution of a differential equation is expressed in

terms of a series expansion as

$$w(x, y) = \sum_{m,n=0}^{\infty} a_{mn} \mathcal{X}_m(x) \mathcal{Y}_n(y), \quad (2.26)$$

where the coefficients  $a_{mn}$  need to be determined. The 1<sup>st</sup> term  $a_{00} \mathcal{X}_0(x) \mathcal{Y}_0(y)$  is often used to satisfy the boundary conditions. This approximate solution is inserted into the differential equation. At this point, a set of suitable weighting functions is selected, which are multiplied to the differential equation. The whole differential equation is then integrated over the plate dimension. The number of multiplied weighting functions equals the number of the unknown coefficients to be determined. A linear system of equations is generated and solved for the unknown coefficients  $a_{mn}$ .

The displacement function of a plate clamped at all edges must satisfy the boundary conditions in Equation (2.14) and Equation (2.15). The approximate solution for the displacement function is expressed as

$$w(x, y) = \sum_{m=1}^M \sum_{n=1}^N a_{mn} \mathcal{X}_m(x) \mathcal{Y}_n(y), \quad (2.27)$$

where  $\mathcal{X}_m(x) = \sqrt{2/(3A)}(1 - \cos(2k_m x))$ ,  $\mathcal{Y}_n(y) = \sqrt{2/(3B)}(1 - \cos(2q_n y))$ . The series begins with  $m, n = 1$ , because both  $\mathcal{X}_0(x)$  and  $\mathcal{Y}_0(y)$  are zero. This satisfies the clamped boundary conditions in Equation (2.14) and Equation (2.15). The values of  $m, n$  are truncated at  $M, N$ , respectively, ensuring the convergence of the series. Inserting Equation (2.27) in Equation (2.2) gives

$$\begin{aligned} & \sum_{m,n=1}^M \left[ D \left( \sqrt{\frac{2}{3A}} (2k_m)^4 \cos(2k_m x) \mathcal{Y}_n(y) + \sqrt{\frac{2}{3B}} (2q_n)^4 \cos(2q_n y) \mathcal{X}_m(x) \right. \right. \\ & \left. \left. + \frac{4}{3\sqrt{AB}} (2k_m)^2 (2q_n)^2 \cos(2k_m x) \cos(2q_n y) \right) + \rho \omega^2 \mathcal{X}_m(x) \mathcal{Y}_n(y) \right] - \mathcal{F}(x, y) = 0. \end{aligned} \quad (2.28)$$

The suitable weighting functions are  $\mathcal{X}_m(x)$  and  $\mathcal{Y}_n(y)$ . Multiplying Equation (2.28) by  $\mathcal{X}_m(x)\mathcal{Y}_n(y)$  and integrating over the plate dimensions the following system of equations is derived

$$\mathbf{Z}\mathbf{a} = \mathbf{g}, \quad (2.29)$$

$$\mathbf{Z} = \begin{bmatrix} \mathcal{Z}_{11}^{11} & \mathcal{Z}_{12}^{11} & \dots & \mathcal{Z}_{MN}^{11} \\ \mathcal{Z}_{11}^{12} & \mathcal{Z}_{12}^{12} & \dots & \mathcal{Z}_{MN}^{12} \\ \vdots & \vdots & \dots & \vdots \\ \mathcal{Z}_{11}^{MN} & \mathcal{Z}_{12}^{MN} & \dots & \mathcal{Z}_{MN}^{MN} \end{bmatrix}, \mathbf{a} = \begin{bmatrix} a_{11} \\ a_{12} \\ \vdots \\ a_{MN} \end{bmatrix}, \mathbf{g} = \begin{bmatrix} g_{11} \\ g_{12} \\ \vdots \\ g_{MN} \end{bmatrix},$$

where

$$\mathcal{Z}_{mn}^{m'n'} = \int_0^A \int_0^B \mathcal{X}_{m'}(x)\mathcal{Y}_{n'}(y)(D\nabla^4 - \sigma_1\omega^2)\mathcal{X}_m(x)\mathcal{Y}_n(y)dydx,$$

and

$$g_{mn} = \int_0^A \int_0^B \mathcal{F}(x, y)\mathcal{X}_m(x)\mathcal{Y}_n(y)dydx.$$

Solving the system of equations, the unknown coefficients  $a_{mn}$  are calculated.

## 2.6 Helmholtz's equation for sound wave

The equation of a propagating sound wave is the relationship between the variation in the particle velocity and the resulting variation in the fluid pressure. A sound wave is a small fluctuation in pressure. If the air pressure in the atmosphere is  $P_0$ , and a small disturbance makes the pressure become  $(P_0 + p)$ , then the fluctuating part  $p$  will be perceived as sound. The sound propagation is fast so that the compression and expansion processes of the fluid can be assumed as adiabatic and linear. With these approximations, the equation of the sound wave is derived as (Fahy, 2007; Vigran,

2008)

$$\left( \frac{\partial^2}{\partial x^2} + \frac{\partial^2}{\partial y^2} + \frac{\partial^2}{\partial z^2} \right) p + \frac{\omega^2}{c_0^2} p = 0, \quad (2.30)$$

where  $c_0$  is the speed of sound in air.

### 2.6.1 Propagation of sound

Sound propagates through alternating compression and expansion of the fluid. The distance between any two consecutive compression or expansion areas is called the wavelength  $\lambda$ , and the number of wavelengths at a distance  $2\pi$  is called the wavenumber  $k = 2\pi/\lambda$ . The wavenumber is a vector quantity and it represents the direction of the wave as well.  $k$  can be split into its spatial coordinates  $k_x$ ,  $k_y$  and  $k_z$ , where  $k_x$ ,  $k_y$  and  $k_z$  represent the wavenumber in the  $x$ ,  $y$  and  $z$  direction, respectively. The relationship between  $k$ ,  $k_x$ ,  $k_y$  and  $k_z$  is

$$k^2 = k_x^2 + k_y^2 + k_z^2. \quad (2.31)$$

The sound wave at some distance from the source can be considered as a plane wave, which varies only in the direction it propagates. Sections normal to the direction of propagation are known as the wavefronts. There is no variation in wave amplitude anywhere in a wavefront. Any sound wave travelling from a distance can be a plane wave. The equation of a plane wave traveling along any direction is written as (Vigran, 2008)

$$p = \hat{p} e^{-i(k_x x + k_y y + k_z z - \omega t)}, \quad (2.32)$$

where  $\hat{p}$  is the amplitude of the wave and 'i' is the imaginary unit.

### 2.6.2 Solution to the Helmholtz's equation for a rectangular cavity

The cavities formed between the plates and the beams are considered as a separate rectangular compartment in this thesis. Each cavity is completely isolated from each other and the pressure field in one cavity does not interfere with the pressure field in the other cavities. The  $j^{\text{th}}$  cavity is bounded by the two plates at  $z = 0, d$  and two adjacent beams at  $y = jl, (j+1)l$ , where  $l$  is the width of the cavity. The length of the cavities ( $A$ ) and the width ( $l$ ) run parallel to  $x$  and  $y$  axes, respectively, and the positive  $z$  direction is vertically downward. The drawing (not to scale) of a single cavity is shown in Fig. 2.3.

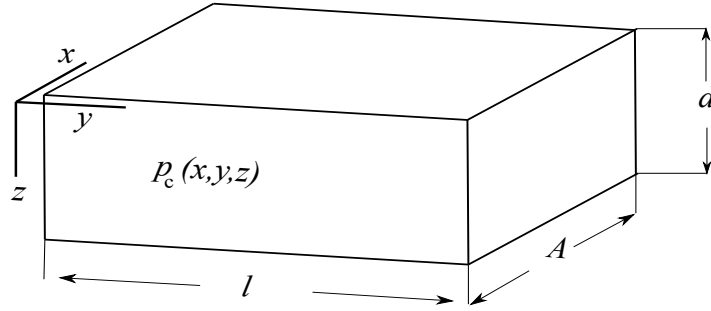


Figure 2.3: Schematics of a closed cavity between two beams.

A sound wave generated due to the incident plate vibration at  $z = 0$  propagates along the  $z$  direction and gets reflected at the lower plate at  $z = d$ . The pressure fields inside the cavities follow the Helmholtz equation and by solving the Helmholtz's equation the sound pressure in the rectangular cavity is found as

$$p_c(x, y, z) = \sum_{m,n=0}^{\infty} (S_{mn}e^{\gamma_{mn}z} + T_{mn}e^{-\gamma_{mn}z})\alpha_m(x)\beta_n(y), \quad (2.33)$$

where,  $\alpha_m(x) = \sqrt{2/A} \cos(k_m x)$  and  $\beta_n(y) = \sqrt{2/l} \cos(\kappa_n y)$ , where  $\kappa_n = n\pi/l$ .  $S_{mn}$  and  $T_{mn}$  are the sets unknown coefficients to be determined and  $\gamma_{mn} = \sqrt{k_m^2 + \kappa_n^2 - k^2}$

is the propagation constant. The cavity is bounded by the two plates at  $z = 0, d$ . Air inside the cavity interacts with the plates and  $p_c(x, y, z)$  must satisfy the continuity condition at  $z = 0, d$  as (Lin & Garrelick, 1977; Brunskog, 2005; Chung & Emms, 2008; Mosharrof et al., 2009)

$$\frac{\partial p_c(x, y, 0)}{\partial z} = \omega^2 \rho_0 w_1(x, y), \quad (2.34)$$

$$\frac{\partial p_c(x, y, d)}{\partial z} = \omega^2 \rho_0 w_2(x, y), \quad (2.35)$$

where  $w_1(x, y)$  and  $w_2(x, y)$  are the displacements of the upper and the lower plates, respectively, and  $\rho_0$  is the mass density of air. The cavity is also bounded by the hard walls at four sides,  $x = 0, A$  and  $y = 0, l$ , and  $p_c(x, y, z)$  satisfies the hard wall conditions at these four sides, which are

$$\left. \frac{\partial p_c(x, y, z)}{\partial x} \right|_{x=0, A} = 0, \quad (2.36)$$

$$\left. \frac{\partial p_c(x, y, z)}{\partial y} \right|_{y=0, l} = 0. \quad (2.37)$$

These two boundary conditions are also considered by Brunskog (2005), which corresponds to the zero displacements of these walls along  $x$  and  $y$  axis. This agrees with the assumption corresponding to Euler beams that beams' deflection and moment only take place in the plane comprised of the longitudinal axis and the transverse axis, i.e. parallel to the  $xz$  plane in Fig. 2.3.

## 2.7 Sound radiation from vibrating object

The radiated sound pressure  $p_t$ , at a distance  $r$  from a vibrating point source in a large baffle is calculated as (Cremer & Heckl, 2013; Fahy, 2007)

$$p_t = i\omega\rho_0 Q_0 \frac{e^{-ikr}}{2\pi r}, \quad (2.38)$$

where  $Q_0 = vS_0$  is the volume velocity,  $v$  and  $S_0$  are the velocity and the surface area of the radiating point source. Vibration in any large object is the summation of many small point sources. Therefore, the radiation from the large object can be determined by summing or integrating Equation (2.38) over the surface. The pressure at a distance  $r$  is

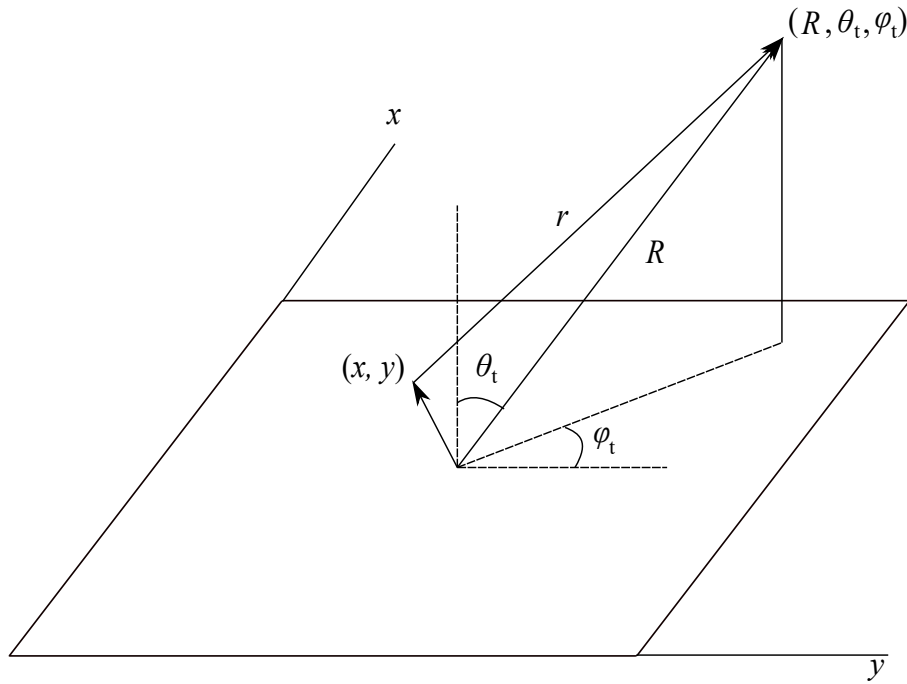


Figure 2.4: Coordinate system for the radiation of the sound wave.

$$p_t(r) = i\omega\rho_0 \int_0^A \int_0^B \frac{v(x, y)}{2\pi r} e^{-ikr} dx dy. \quad (2.39)$$

The distance  $r$  is calculated from each point  $(x, y)$  on the vibrating surface. Thus, it varies and remains inside the integration. In the far field, it is more convenient to measure the distance from the midpoint of the plate (Cremer & Heckl, 2013), or to consider the perpendicular distance from the plate (Fahy, 2007). In both cases, pressure can be reduced to the same form as Equation (2.41). Considering the case of Cremer & Heckl (2013), it can be written as

$$R(r, \theta_t, \phi_t) = r - x \sin \theta_t \cos \phi_t - y \sin \theta_t \sin \phi_t, \quad (2.40)$$

where  $R$  is the distance of the observation point from the midpoint of the plate and  $\theta_t$  is the angle made by the line connecting the mid-point and the observation point with the vertical line, and  $\phi_t$  is the angle between the  $y$  axis and the projection to the  $xy$  plane, as shown in Fig. 2.4. At the far field, it can also be assumed that  $1/R = 1/r$ . The sound pressure at a particular time  $t$ , at a distance  $R$ , and at particular set of angles  $(\theta_t, \phi_t)$  is then reduced to (Cremer & Heckl, 2013; Fahy, 2007)

$$p_t(R, \theta_t, \phi_t) = \frac{-\rho\omega^2}{2\pi R} e^{-ikR} \int_0^A \int_0^B w(x, y) e^{-ik \sin \theta_t (x \cos \phi_t + y \sin \phi_t)} dx dy. \quad (2.41)$$

This equation is known as the Rayleigh integral, where  $v(x, y) = i\omega w(x, y)$  is the vibrating velocity of the surface element at any point  $(x, y)$  on the plate. Considering that  $w$  is expressed in terms of Fourier series as in Section 2.4, the above equation can be simplified as

$$p_t(R, \theta_t, \phi_t) = \frac{-\rho\omega^2}{2\pi R} e^{-ikR} \sum_{m=1}^M \sum_{n=1}^n C_{mn} \mathcal{R}_m^{\text{sx}} \mathcal{R}_n^{\text{sy}}, \quad (2.42)$$

where

$$\mathcal{R}_m^{sx} = \int_0^A \Phi_m(x) e^{-ik \sin \theta_i \cos \phi_i x} dx, \quad \mathcal{R}_n^{sy} = \int_0^B \Psi_n(y) e^{-ik \sin \theta_i \sin \phi_i y} dy.$$

The choice of  $\Phi_m(x)$  and  $\Psi_n(y)$  depend on the boundary conditions, and thus, the values of  $\mathcal{R}_m^{sx}$  and  $\mathcal{R}_n^{sy}$  differ with the boundary conditions.

## 2.8 Sound transmission loss

A plane wave  $p_i = p_e e^{-i(k_x x + k_y y + k_z z - \omega t)}$  with wavenumber  $k$  falls on the incident plate at a set of incident angles  $(\theta_i, \phi_i)$ , where  $\theta_i$  is the angle with the vertical axis and termed as the elevation angle, and  $\phi_i$  is the azimuth angle, as shown in Fig. 2.5.  $p_e$  is the amplitude and the reflected wave is  $p_r$ . Therefore,  $k_x$ ,  $k_y$  and  $k_z$  are expressed as

$$k_x = k \cos \theta_i \cos \phi_i, \quad k_y = k \cos \theta_i \sin \phi_i, \quad k_z = k \sin \theta_i.$$

The radiating sound pressure to the other side is termed as the transmitted pressure  $p_t$ . The remaining portion of the incident wave is lost due to the reflection and damping effect. The amount of the sound energy transmitted through the partition is measured in terms of the transmission coefficient  $\tau(\theta_i)$  as

$$\tau(\theta_i) = \frac{W_t(\theta_i)}{W_i(\theta_i)}, \quad (2.43)$$

where  $W_t(\theta_i)$  and  $W_i(\theta_i)$  are powers of the transmitted and the incident sound waves corresponding to  $\theta_i$ , respectively.

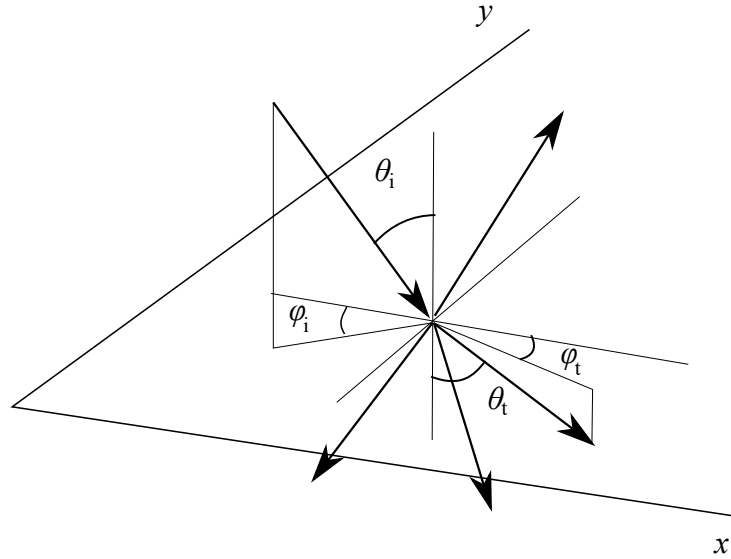


Figure 2.5: Sound transmission through a plate.

$W_i(\theta_i)$  is calculated by taking the portion of the energy incident normal to the plate surface, which is calculated as (Cremer & Heckl, 2013; Fahy, 2007)

$$W_i(\theta_i) = \frac{p_e^2 AB \cos \theta_i}{2\rho_0 c_0}. \quad (2.44)$$

$W_t(\theta_i)$  is calculated from  $p_t$  and the transmitted sound intensity, denoted by  $I_t$ .  $I_t$  at a particular direction  $(\theta_t, \phi_t)$  and at a distance  $r$  is calculated as (Fahy, 2007)

$$I_t(r, \theta_t, \phi_t) = \frac{|p_t|^2}{2\rho_0 c_0}. \quad (2.45)$$

The transmitted power is calculated by integrating  $I_t(r, \theta_t, \phi_t)$  over all possible angles. Therefore, the total transmitted power corresponding to the sound wave incident at an angle  $(\theta_i, \phi_i)$  is given by

$$W_t(r, \theta_i, \phi_i) = \int_0^{2\pi} \int_0^{\pi/2} I_t(r, \theta_t, \phi_t) r^2 \sin \theta_t d\theta_t d\phi_t. \quad (2.46)$$

The transmitted power calculated in Equation (2.46) corresponds to a single incident

wave with a set of incident angles  $(\theta_i, \phi_i)$ . Inserting Equations (2.44) and (2.46) in Equation (2.43), the transmission coefficient corresponding to the incident angles  $(\theta_i, \phi_i)$  becomes

$$\tau(\theta_i, \phi_i) = \frac{\frac{p_e^2 AB \cos \theta_i}{2\rho_0 c_0}}{\int_0^{2\pi} \int_0^{\pi/2} I_t(r, \theta_t, \phi_t) r^2 \sin \theta_t d\theta_t d\phi_t}. \quad (2.47)$$

The transmission coefficient is dependent on the incident angle, and it needs to be averaged over all possible incident angles to get an estimate of the average transmission coefficient  $\tau_{\text{ave}}$  (Fahy, 2007; Legault et al., 2011)

$$\tau_{\text{ave}} = \frac{\int_0^{2\pi} \int_0^{0.433\pi} \tau(r, \theta_i, \phi_i) \sin \theta_i \cos \phi_i d\theta_i d\phi_i}{\int_0^{2\pi} \int_0^{\pi/2} \sin \theta_i \cos \phi_i d\theta_i d\phi_i}. \quad (2.48)$$

The upper limit of  $\theta_i$  is usually set at an angle below  $\pi/2$  for the wall partitions in building acoustics (Fahy, 2007). The upper limit is chosen as  $78^\circ$  (Fahy, 2007; Legault et al., 2011) or equivalently  $0.433\pi$  in radians to best fit with the measurement data. Finally,  $\mathcal{T}_L$  is calculated as (Cremer & Heckl, 2013; Fahy, 2007)

$$\mathcal{T}_L = 10 \log_{10} \frac{1}{\tau_{\text{ave}}}. \quad (2.49)$$

## 2.9 Characteristics of $\mathcal{T}_L$ through lightweight panels

In this section, some of the key concepts of sound transmission through lightweight panels are explained. This will allow readers to become familiar with the key concepts relevant to this thesis. There is a brief discussion on  $\mathcal{T}_L$  through the lightweight double-leaf panel; this is based mainly on published books (Cremer & Heckl, 2013; Fahy, 2007;

Vigran, 2008). The discussion follows a step by step procedure, starting from a single infinite panel and gradually building to the case of the double-leaf panel attached by beams. The discussion progresses by gradually adding the complexity to the lightweight panel and explaining the effect of each complexity on  $\mathcal{T}_L$ . The discussion covers the effect of the cavity between the double-leaf panel, the effect of the boundary conditions and the effect of the periodically placed beams.

### 2.9.1 $\mathcal{T}_L$ through a single panel

The incident wave with wavenumber  $k$  and wavelength  $\lambda$  is incident upon a plate at an angle  $\theta_i$ , termed as the elevation angle. A portion of the wave is reflected back to the incident side and the remainder is transmitted to the other side. The incident plate experiences a forced wave with the wavenumber  $k_t = k \sin \theta_i$  and wavelength  $\lambda_t = \lambda / \sin \theta_i$  imposed by the incident wave. The sound is radiated to the other side of the plate due to this forced vibration. Resonance takes place when this forced wave coincides with the free bending wave of the plate, i.e.  $\lambda_t = \lambda_b$ . This is known as the coincidence effect and sound transmission reaches a peak at the corresponding frequency. This coincidence effect results in a dip, which is clearly visible in the  $\mathcal{T}_L$  curve. The necessary condition for coincidence in terms of the bending wavenumbers of plate  $k_b = \sqrt{\omega \sqrt{m/D}}$  is (Fahy, 2007)

$$k \sin \theta_i = k_b, \quad (2.50)$$

which shows that the coincidence is dependent on  $k_b$  and  $\theta_i$ . In a diffuse field, the incident wave can reach the incident plate from numerous directions. Therefore, there are numerous possible combinations of  $k_b$  and  $\theta_i$  that satisfy the coincidence condition. Since the value of  $\sin \theta_i$  cannot exceed unity, the maximum possible value of  $k_b$  at coincidence is  $k = k_b$ . Therefore, the range of  $k_t$  for coincidence is  $k \geq k_b$ . The physical

interpretation is that for  $k \leq k_b$ , there is no real angle where  $k \sin \theta_i$  can be equal to  $k_b$ , whereas, for  $k \geq k_b$ , there is always an angle where the coincidence condition (Equation (2.50)) satisfy. The expression for the angular frequency at coincidence ( $\omega_{co}$ ) is (Fahy, 2007)

$$\omega_{co} = \sqrt{\frac{mc_0^4}{D \sin^4 \theta_i}}. \quad (2.51)$$

It is important to note here that coincidence condition is only satisfied for a particular angle and a narrow range of adjacent angles. For the remaining set of  $\theta_i$ , the behaviour is non-coincident. Equation (2.51) shows that  $\omega_{co}$  varies with  $\theta_i$ .  $f_{cr}$  is the smallest frequency where coincidence takes place, which is known as the critical frequency. From Equation (2.51), the expression for  $f_{cr}$  can be derived as

$$f_{cr} = \frac{c_0^2}{2\pi} \sqrt{\frac{m}{D}}. \quad (2.52)$$

The characteristics of  $\mathcal{T}_L$  is often understood at different frequency regions relative to  $f_{cr}$ .

The physical parameters of the plate that govern  $\mathcal{T}_L$  are  $m, h, D$  and  $\eta$  of the plate.  $\mathcal{T}_L$  for an infinite single panel is (Fahy, 2007)

$$\tau = \frac{(2\rho_0 c / \omega m)^2 \sec^2 \theta}{\left[ (2\rho_0 c / \omega m) \sec \theta + (k/k_b)^4 \eta \sin^4 \theta \right]^2 + \left[ 1 - (k/k_b) \sin^4 \theta \right]^2}. \quad (2.53)$$

Below the critical frequency ( $f \ll f_{cr}$ ), the ratio  $(k/k_b)$  is much less than unity, and the associated terms can be neglected. In this case, the terms related to  $m$  become significant and  $\mathcal{T}_L$  becomes mostly influenced by panel mass. The expression for the

transmission loss reduces to (Vigran, 2008; Fahy, 2007)

$$\mathcal{T}_L \equiv 20 \log_{10}(mf) - 47. \quad (2.54)$$

The above equation is known as the mass law, which shows that  $\mathcal{T}_L$  increases by 6 dB for doubling of the mass or an octave increase of  $f$ . For frequencies above  $f_{cr}$ , the behaviour is highly dependent on  $\theta_i$ . For some angles corresponding to  $k \sin \theta / k_b < 1$ , the mass related terms become most significant. In this case, the coincidence does not take place.  $\mathcal{T}_L$  is mainly influenced by panel mass. for the remaining angles the stiffness related terms become most significant and Equation (2.53) reduces to (Fahy, 2007)

$$\tau = \frac{1}{\left[1 + (Dk^4 \sin^4 \theta \cos \theta / 2\rho_0 c \omega)^2\right]}. \quad (2.55)$$

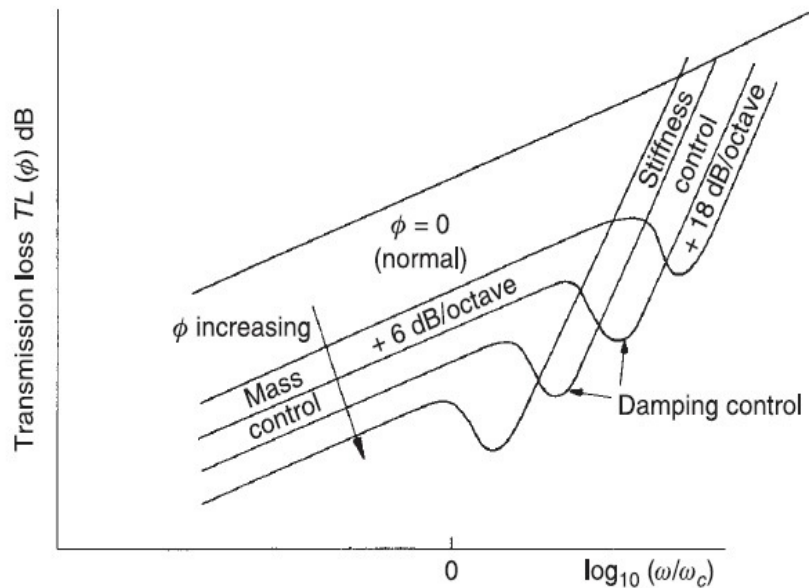


Figure 2.6: Sound transmission through an infinite plate Fahy (2007).

At  $f_{cr}$ , damping plays an important role, and the coincidence dip can be minimised by having a higher value for  $\eta$ . As shown in Equation (2.51) that the coincidence

frequency is dependent on  $\theta_i$ , and there is always a possibility at some angles that the coincidence condition does not satisfy. In that case,  $\mathcal{T}_L$  is dominated by the panel mass. Figure 2.6 summarizes the  $\mathcal{T}_L$  characteristics of an infinite panel, which is copied from Fahy (2007). The symbol  $\phi$  in the figure denotes the elevation angle, which is denoted by  $\theta_i$  in this thesis.  $f_{cr}$  is seen as a dip, which can be controlled by the damping. Below  $f_{cr}$ ,  $\mathcal{T}_L$  follows the mass law and maintains a slope of 6 dB / octave band. Above  $f_{cr}$ , the slope is about 18 dB/octave. It is also noted that  $\mathcal{T}_L$  decreases with the increase in incident angle.

### 2.9.2 Effect of finite size

So far the infinite panels have been discussed, where the incident wave is the only forcing wave that governs the vibration field of the plate. As explained earlier, the trace of the incident wave sometimes experiences resonance because of the coincidence effect and results in the decrease in  $\mathcal{T}_L$ . It is also explained in Section 2.9.1 that the behavior of  $\mathcal{T}_L$  through a single panel can be categorised in terms of coincidence, and  $\mathcal{T}_L$  during the coincidence is related to the structural damping. Increasing the material damping can increase the level of the coincidence dip. In case of a double-leaf panel, the coincidence effects of both the panels influence  $\mathcal{T}_L$ .

When waves reach any boundary, they get reflected. These reflected waves are free from the incident wave and travel freely with a speed equal to the speed of the free bending wave of the plate. The free waves get reflected at the boundaries multiple times and a vibration field is created. The phase of these reflected waves differs from the others resulting in superposition and cancellation of the waves. Resonance occurs when the phase of the reflected wave coincides with the phase of the incident wave; this is known as phase coincidence (Fahy, 2007). This phase coincidence can occur at certain frequencies, known as the natural frequencies and the patterns of the vibrations at these

frequencies are known as the vibration modes. The structural modes are dependent on the boundary conditions. Therefore, resonance occurs at different frequencies depending on the boundary conditions. Hence, the difference in  $\mathcal{T}_L$  is observed for finite panels with various boundary conditions.

There are two types of wave fields in a finite plate, which can be categorized as, non-resonant (forced by the incident waves) and resonant (free waves due to reflections at the boundaries) waves (Brunskog, 2012; Davy, 2009). The total transmission through the panel is the sum of contributions from both these waves. The non-resonant wave field is present in both finite and infinite panels, whereas the resonant wave field is present only in the finite panels. Therefore, a panel can be considered as infinite when the resonant wave field in the panel is negligible.

### 2.9.3 $\mathcal{T}_L$ through a double panel with air cavity

Double-leaf panels have two plates with a cavity in between.  $\mathcal{T}_L$  increases for the double-leaf panel compared to the single panel because of the additional plate and the air cavity. The vibration of the incident plate does not radiate sound to the receiving side directly. First, the vibration propagates through the air cavity to the radiating plate. The sound is then radiated to the receiving side from the radiating plate. Therefore,  $\mathcal{T}_L$  is calculated by the ratio of the radiated sound power by the radiating plate, and the power of the wave incident on the incident plate.

Ideally, the combined  $\mathcal{T}_L$  is supposed to be equal to the sum of  $\mathcal{T}_L$  through the two individual panels. In reality,  $\mathcal{T}_L$  is less than the supposed value due to the coupling via the air inside the cavity. The only way the sound can propagate from the incident plate to the radiating plate is through the airborne path, i.e. through the cavity. Therefore, the air inside the cavity plays an important role in the sound transmission. The air inside the cavity act as a spring and the system behaves as a mass-spring-mass system. The

mass-air-mass resonance frequency ( $f_0$ ) appears in the low frequency region as a result of this mass-spring-mass behavior of the system, provided that the mechanical and acoustic damping is negligible. The expression of  $f_0$  is written in accordance with some literature as (Fahy, 2007; Xin & Lu, 2009)

$$f_0 = \frac{c_0}{2\pi \cos \theta_i} \sqrt{\frac{\rho_0}{d} \left( \frac{\sigma_1 + \sigma_2}{\sigma_1 \sigma_2} \right)}. \quad (2.56)$$

$f_0$  is not a fixed value, it is dependent on  $\theta_i$ . In reality, the damping is there, which suppresses the resonance effects for most of the incident angles. Therefore, this resonance effect is seen over a narrow frequency range in the lower frequency region.  $\mathcal{T}_L$  around this resonance frequency is dependent on the plate masses.

$f_{cr}$  of the plates and  $f_0$  reduce  $\mathcal{T}_L$  considerably for a double-leaf panel. It is desirable to keep these frequencies outside the frequency range of interest. In the low frequency region, external factors, such as room dimensions play a significant role. The wavelengths at lower frequencies get much larger and become comparable with the room dimensions. Therefore, the radiated waves interfere with the modes of the radiating room. As mentioned in Chapter 1 that sound wave inside the cavity reflects at the plates. As a result, standing wave forms, usually in the higher frequencies given by (Fahy, 2007)

$$f_{cav} = \frac{nc_0}{2d}, \quad (2.57)$$

where  $n$  is an integer and  $d$  is distance between the two panels.

## Chapter 3

# The lightweight double-leaf panel model

In this chapter, derivation of the model of the double-leaf panel considered in this thesis is explained. The basic type of lightweight double-leaf panels are made of two plates directly connected via a set of parallel identical beams. As mentioned in Section 1.2, there are various types of other lightweight double-leaf panels with some modifications or added features that increase  $\mathcal{T}_L$ . For example, panels having resilient mounts between the beams and the radiating plate weakens the vibration propagation through the sound bridges and increases  $\mathcal{T}_L$ . The use of absorbing materials also dampens the sound inside the cavities and improves  $\mathcal{T}_L$ . Sometimes, active control actuators are used to minimise structural vibrations (Gardonio & Elliott, 1999; Li & Cheng, 2008). Helmholtz resonators are used to increase the loss of sound propagation through the cavities (Li et al., 2010; Mao & Pietrzko, 2005).

The double-leaf panel considered in this thesis does not have resilient mounts between the beams and the plates. A spring is assumed between each beam and the radiating plate to account for the coupling between the plates and the beams. By varying the value of  $K$ , the coupling between the plates and the beams can be varied. It is also

possible to include the resilient mounts to the model by selecting appropriate values for  $K$ , which may depend on frequency. In that case, a frequency dependent expression of  $K$  needs to be derived theoretically. Alternatively, the exact values of  $K$  can be determined through a number of experiments. Another simplification made in the model is that the cavities are filled only with air without any absorbing materials. By modifying the properties of the cavity air, it is possible to include absorbing materials inside the cavities (Delaney & Bazley, 1969). The above-mentioned control mechanisms are also not considered in this thesis. The double-leaf panels considered here can be treated as a simplified form of the available lightweight double-leaf panels.

As mentioned in Section 1.8, the presence of the beams were often ignored and a single cavity was considered (Lin & Garrelick, 1977; Brunskog & Hammer, 2003; Chung & Emms, 2008). According to the research by the author, only Brunskog (2005) considered the effect of the multiple cavities for an infinite panel. One of the main contributions of this thesis is to include the multiple cavities between the plates and the beams for a finite double-leaf panel. Discussion of the effects of the multiple cavities is presented in Chapter 5 and compared to the discussion by Brunskog (2005). An overview of the double-leaf panel with a schematic diagram (Fig. 3.1) is presented in Section 3.1. This simplified double-leaf panel reduces the complexity of modelling and involves a comparatively fewer number of parameters. These types of double-leaf panels are commonly used as partition walls in residential buildings, where the expected  $\mathcal{T}_L$  can be achieved using these panels.

The design of the panel is described in the following section followed by the derivation of the governing equations of the model and the solution of the equations. The simply supported boundary conditions are considered in this chapter, and  $\mathcal{T}_L$  is verified using the measurement data and the theoretical results given in an available literature (Brunskog, 2005). The model derivation and the verification of  $\mathcal{T}_L$  corresponding to the clamped boundary conditions will be discussed in the next chapter.

### 3.1 Design of the double-leaf panel

The description of the panel (Fig. 1.1) and the notations used for the parameters have already been given in Section 1.2. In this section, the panel orientation, the boundary conditions and the parameter notations used in this model are outlined. The schematic diagram of the double-leaf panel is shown in Fig.3.1, in the same orientation as Fig. 1.1. The plates are placed parallel to the  $xy$  plane with a corner of the incident plate placed at the origin. The  $z$  axis is directed vertically downward. The beams are placed parallel to the  $x$  axis. Both plates are of the same size with dimensions  $A \times B$  in  $x$  and  $y$  directions, respectively. Both the plates are assumed to be simply supported at their four edges at  $x = 0, A$ , and  $y = 0, B$  as shown in Fig. 3.1 b). This setup is more appropriate for a floor-ceiling structure, where plates are placed horizontally (Chung & Emms, 2008). For wall structures, the plates are placed vertically and the  $x$  axis in Fig. 3.1 b) corresponds to the vertical axis. In that case, it is more realistic to consider the edge conditions of the plates at  $y = 0, B$  as being free. It will be seen in Chapter 4 that the boundary conditions of the edges containing the beam ends, i.e. the edges at  $x = 0, A$ , are the most significant boundary conditions. Therefore, the results and findings of this model are equally applicable for the walls.

The beams split the cavity into several cavities. The displacement at  $y = 0, B$  is zero, where two extreme beams are placed. The same value for  $K$  considered by Brunskog (2005) is considered here as well, which is  $10^{10} \text{ Nm}^{-2}$ . With this high value of  $K$ , the connection can be considered as rigid. The slippage between the plates and the beams is ignored. The air inside each cavity is assumed to be isolated from the air inside the other cavities and the outside air.

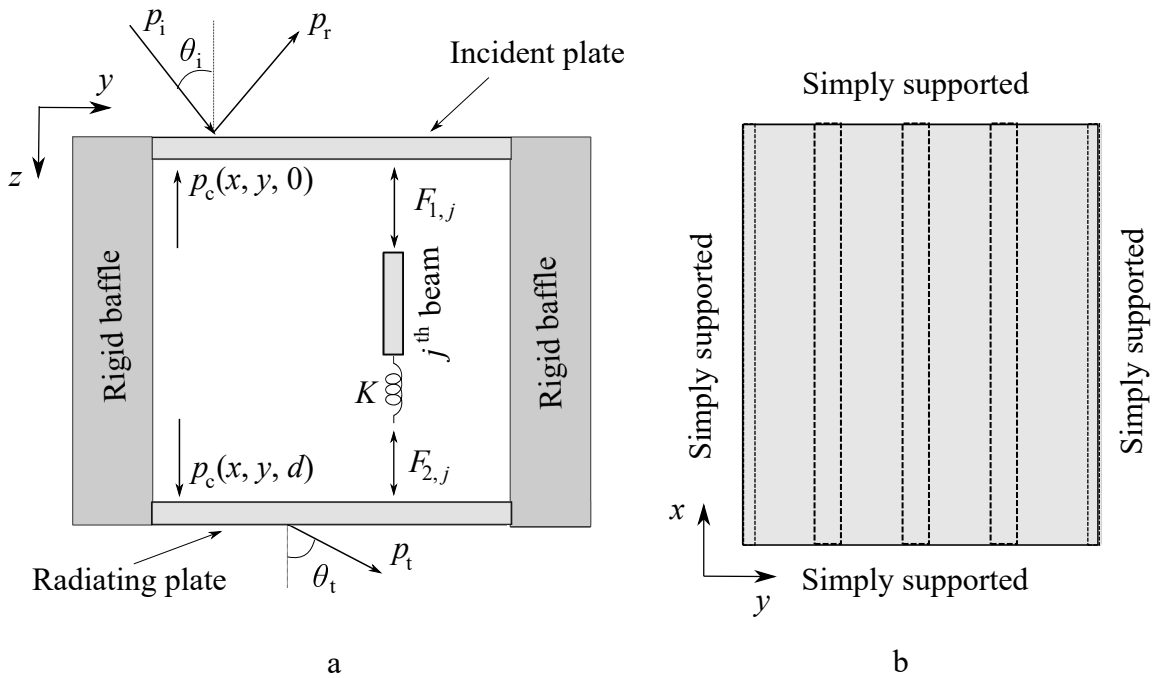


Figure 3.1: Typical lightweight double-leaf panel with beams placed along  $x$  direction.

### 3.2 Scope of the model

The model is built for predicting  $\mathcal{T}_L$  through finite panels. One of the key factor regarding the finite panels is the effects of the boundary conditions, which is ignored in the infinite panel model. As discussed in Section 2.9.2, the finite panels have two types of vibration fields, which are resonant and non-resonant. The resonant vibration are caused because of reflections at the boundaries. The amount of reflections increases with the decrease in panel dimension. Therefore, the finite panel model is more appropriate over the infinite panel model for accurate prediction of  $\mathcal{T}_L$  for smaller panels. As the panel size increases, the boundaries gradually get far apart, and so is the rate of reflection at the boundaries. The boundary effects become negligible at certain dimensions of the panel, and panels larger than this can be treated as infinite. From this aspect, double-leaf panels can be categorized as small and large, where small panels correspond to the case where the resonant field is dominant and the panel is large when the resonant

field becomes negligible. Small and large panels can not be separated by dimensions only, it depends on the material properties and the dimensions. Therefore, the terms 'small panel' and 'large panel' used in this thesis should not be taken in absolute sense, rather it is only applicable to the panels considered in this thesis with the corresponding parameter values.

The model is built for predicting  $\mathcal{T}_L$  through finite panels. One of the key factors regarding the finite panels is the effect of the boundary conditions, which is ignored in the infinite panel model. As discussed in Section 2.9.2, finite panels have two types of vibration fields, which are resonant and non-resonant. The resonant vibrations are caused because of reflections at the boundaries. The amount of reflection increases with the decrease in panel dimension. Therefore, the finite panel model is more appropriate than the infinite panel model for accurate prediction of  $\mathcal{T}_L$  for smaller panels. As the panel size increases, the boundaries gradually get farther apart, and so does the rate of reflection at the boundaries. The boundary effects become negligible above certain dimensions of the panel and panels larger than these can be treated as infinite. From this aspect, double-leaf panels can be categorised as small and large, where small panels correspond to the case where the resonant field is dominant and the panel is considered large when the resonant field becomes negligible. Small and large panels can not be separated by dimensions only, it also depends on the material properties. Therefore, the terms 'small panel' and 'large panel' used in this thesis should not be taken in an absolute sense, rather it is only applicable to the panels considered here with the corresponding parameter values.

The finite panel can still be used for predicting  $\mathcal{T}_L$  for large panels but calculations may take a much longer time compared to the infinite panel model by Brunskog (2005). From this point of view, the infinite panel model is preferable over the finite panel model for large panels. The finite panel model is also suitable for predicting  $\mathcal{T}_L$  in the low frequency region of larger panels. The low frequency region refers to the frequency

region where the propagation wavelengths are large enough to be comparable with the panel dimension. Therefore, the terms as 'low frequency' and 'high frequency' are also relative to the type of panels considered. It is possible that the boundary effects become negligible in the high frequency region of a large panel, whereas the wavelengths are still large enough in the low frequency region to exhibit boundary effects. Indeed, many external factors such as the acoustic modes of the incident and radiating room are also significant in the low frequency region. Yet, the finite panel model is expected to give a better  $\mathcal{T}_L$  prediction at the lower frequencies compared to the infinite panel model.

The model is not suitable for calculating  $\mathcal{T}_L$  at higher frequencies for a very large panel. Based on the discussion and findings in Section 3.6.1, 4.8 m  $\times$  4.8 m can be considered as a large panel corresponding to the type of panel considered in this thesis having the parameter values selected. The number of terms needed for  $\mathcal{T}_L$  convergence increases with the frequency bands. Thus, it may take an impractical amount of computation time to calculate  $\mathcal{T}_L$  for such a large panel in the higher frequencies unless supercomputers are used.

One of the key features of the model is the connection between the plates and the beams. The lightweight panel are not hard enough to form a rigid connection between them. It is expected that there is some degree of flexibility between the plates and the beams. It is not an easy job to model the connection with 100 percent accuracy. The spring type connection is a simplified model for the plate beam plate connection available in the literature and this is used here. Only the axial forces are considered at the contact lines (between plates and beams) via a spring with spring constant  $K$ . Many other features are ignored, for example, the moments are ignored, the incident plate and the beams are assumed to be fully rigid, which may not be the case.

With the increase in  $K$ , the spring become stiffer and thus, the connection become close to rigid. A high value of  $K$  is required to represent almost rigid connections. A relevant question in this regard is 'what value of  $K$  can be considered as high and

what happens to the model if the value of  $K$  exceeds this limit e.g  $K$  is impractically high'. In other words, is there a limit for the value of  $K$  ? This question is not resolved here, which I consider as a limitation of the model. Nevertheless, the consequence of this issue is addressed in Section 5.1 in Chapter 5. The value of  $K$  needs to be selected carefully, either by trial and error to best fit the measurement data or based on an accurate prior knowledge about the coupling.

### 3.3 Derivation of the system of equations

$\mathcal{T}_L$  is calculated for airborne excitation in the form of a plane wave. The incident wave  $p_i = p_e e^{-i(k_x x + k_y y + k_z z - \omega t)}$  arrives at the incident plate and gets reflected as  $p_r$ , which is shown in Fig. 2.5. Note that at the incident plate, at  $z = 0$ ,  $|p_i| = |p_r|$  (Brunskog, 2005; Roussos, 1984). Therefore the total sound pressure acting on the incident plate is  $2p_i(x, y, 0)$ . The pressure field in the incident side is also affected by the radiation caused by the incident plate vibration, which is ignored here. This simplification does not add much error to the results corresponding to the panels used here (Roussos, 1984). The plate equations are written as (Brunskog & Hammer, 2003; Brunskog, 2005; Lin & Garrelick, 1977)

$$(D_1 \nabla^4 - \sigma_1 \omega^2) w_1 = 2p_e e^{-i(k_x x + k_y y)} - p_c(x, y, 0) - F_1(x, y), \quad (3.1)$$

$$(D_2 \nabla^4 - \sigma_2 \omega^2) w_2 = p_c(x, y, d) + F_2(x, y), \quad (3.2)$$

where  $D_i = E_i h_i^3 / 12(1 - \nu^2)$  is the flexural rigidity of the plate, and  $i = 1, 2$  corresponds to the incident and the radiating plates, respectively. The differential operator  $\nabla^4$  is defined as

$$\nabla^4 = \left( \frac{\partial^2}{\partial x^2} + \frac{\partial^2}{\partial y^2} \right)^2.$$

For convenience, a new operator is defined as

$$\mathcal{D}_i = D_i \nabla^4 - \sigma_i \omega^2,$$

where  $i = 1, 2$  corresponds to the plates. The time dependence term  $e^{i\omega t}$  is suppressed. The forces acting on the plates are the reactions from the beams and the pressure from the cavities.  $F_1(x, y)$  and  $F_2(x, y)$  are the combined line forces from all the beams acting on the incident and the radiating plates (at contact lines), respectively.

The air inside each cavity interacts with the two plates and satisfies the continuity conditions given in Equation (2.34) and Equation (2.35). Lin & Garrelick (1977); Brunskog & Hammer (2003); Chung & Emms (2008) considered a single cavity and used two equations to satisfy the continuity conditions at the two interfaces between the cavity air and the two plates. In this thesis and also in the paper of Brunskog (2005), the air in each cavity interacts only with the portion of the plates attached to it. Therefore, corresponding equations satisfying the continuity conditions at the inferences between air and the plates are different in each cavity. Brunskog (2005) introduced a function called Hat function in the pressure equation. The Hat function is defined equal to ‘1’ when it lies within a particular cavity and ‘0’ elsewhere. This way, the pressure fields in different cavities are defined. Brunskog (2005) expressed the pressures in all cavities in terms of a single cavity (naming ‘0<sup>th</sup>’ cavity) using the periodic property of the structure. In this thesis, separate pairs of equations are set for each cavity. The continuity conditions for the  $j^{\text{th}}$  cavity are

$$\frac{\partial p_c^j(x, y, 0)}{\partial z} = \omega^2 \rho_0 w_1(x, y), \quad (3.3)$$

$$\frac{\partial p_c^j(x, y, d)}{\partial z} = \omega^2 \rho_0 w_2(x, y), \quad (3.4)$$

where  $p_c^j$  is the pressure of air inside the  $j^{\text{th}}$  cavity, where  $j = 0, 1, 2, \dots, J$ . The total

number of the equations is  $2(J + 1)$ . Each small cavity is bounded between the beams placed at  $y = jl, (j + 1)l$  along the  $y$  axis and by hard walls along the  $x$  axis at  $x = 0, A$ . The hard walls at  $x = 0, A$  correspond to the rigid baffle enclosing the whole panel structure, which was not the case for the infinite panel used by Brunskog (2005). Therefore, the pressure in each cavity must satisfy the hard wall boundary conditions given in Equation (2.36) at  $x = 0, A$  (Lin & Garrelick, 1977; Brunskog, 2005; Chung & Emms, 2008; Mosharrof et al., 2009). According to the Euler beam assumption mentioned in Section 2.1.1, beams' deflections and bending only act in the plane comprised of the transverse axis and the longitudinal axis, i.e.  $xz$  plane. Therefore, beams do not exhibit any deflection along the  $x$  and  $y$  axes, and cavities experience these beams as hard walls. Therefore, the cavity pressure also satisfies the hard wall conditions given by Equation (2.37) at the beam locations, i.e. at  $y = jl, (j + 1)l$  Brunskog (2005). The sound pressure in any cavity does not interact with the sound pressure in any other cavities. As given in Section 2.6.2, the cosine series satisfies these boundary conditions, and the pressure in each cavity is expressed as

$$p_c^j(x, y, z) = \sum_{m,n=0}^{\infty} p_z^j(z) \alpha_m(x) \beta_n^j(y), \quad j = 0, 1, 2, \dots, J, \quad (3.5)$$

where

$$\alpha_m(x) = \sqrt{2/A} \cos k_m x, \quad \beta_n^j(y) = \begin{cases} \sqrt{\frac{2}{l}} \cos \kappa_n (y - jl) & jl \leq y \leq (j + 1)l, \\ 0 & \text{elsewhere.} \end{cases}$$

$p_z^j(z)$  is the pressure along the  $z$  direction in the  $j^{\text{th}}$  cavity.  $p_z^j(z)$  at different cavities

are independent of each other. The cosine functions are orthogonal and thus,

$$\int_0^A \alpha_m(x)\alpha_n(x)dx = \begin{cases} 1 & m = n, \\ 0 & m \neq n, \end{cases} \quad (3.6)$$

$$\int_{jl}^{(j+1)l} \beta_m^j(y)\beta_n^j(y)dy = \begin{cases} 1 & m = n, \\ 0 & m \neq n. \end{cases} \quad (3.7)$$

The pressure in each cavity satisfies the Helmholtz equation and, following the same procedure as in Section 2.6.2, the pressure in the  $j^{\text{th}}$  cavity can be written as

$$p_c^j(x, y, z) = \sum_{m,n=0}^{\infty} (S_{mn}^j e^{\gamma_{mn}z} + T_{mn}^j e^{-\gamma_{mn}z}) \alpha_m(x) \beta_n^j(y), \quad j = 0, 1, 2, \dots, J, \quad (3.8)$$

where  $S_{mn}^j$  and  $T_{mn}^j$  are the sets of two coefficients that need to be determined. The corresponding sets of coefficients in different cavities are independent of each other. The upper limits of  $m$  and  $n$  are limited to finite values  $M_c$  and  $N_c$ , respectively, ensuring the convergence of the solution. The  $x$  and  $y$  dimensions of each cavity are  $A$  and  $l$ , respectively, making the side ratio of each cavity be  $A/l$ . The values of  $M_c$  and  $N_c$  are set in such a way that their ratio also match with the side ratio to hold the following relation,  $M_c/N_c = A/l$ . This relation is intuitive, and it is also shown in Section 3.5 that convergence of  $\mathcal{T}_L$  is achievable maintaining this relation. The width of any cavity is considered to be 600 mm for all panels in this thesis and the value of  $N_c$  is fixed, unless stated otherwise. When the panel dimension  $A$  increases the value of  $M_c$  is also increased in the same proportion.

The total cavity pressure acting on the plates is the sum of the pressures from all the cavities. Therefore, the pressures from the cavities acting on the incident and the

radiating plates are

$$p(x, y, 0) = \sum_{j=0}^J p_c^j(x, y, 0), \quad (3.9)$$

$$p(x, y, d) = \sum_{j=0}^J p_c^j(x, y, d). \quad (3.10)$$

Each beam exerts reaction line forces on the plates. Forces acting on a single beam, namely the  $j^{\text{th}}$  beam, is shown in the Fig. 3.1. Forces act in the vertical direction only, and the moment effects at the connections are ignored.  $F_{i,j}$  is the line force exerted from the  $j^{\text{th}}$  beam to the  $i^{\text{th}}$  plate, where  $i = 1, 2$  corresponds to the incident and the radiating plates, respectively. Therefore, the total reaction forces acting on the plates are the sum of all these reaction line forces from the individual beams as (Brunskog, 2005; Chung & Emms, 2008)

$$F_i(x, y) = \sum_{j=1}^J F_{i,j}(x) \delta(y - jl). \quad (3.11)$$

As shown in Section 2.2, the line forces exerted from the  $j^{\text{th}}$  beam to the incident and the radiating plates are respectively (Brunskog, 2005)

$$F_{1,j}(x) = (K + \mathcal{G})w_1(x, jl) - Kw_2(x, jl), \quad (3.12)$$

$$F_{2,j}(x) = K[w_1(x, jl) - w_2(x, jl)]. \quad (3.13)$$

The linear operator  $\mathcal{G} = E_b I_b \frac{d^4}{dx^4} - \rho_b A_b \omega^2$  is multiplied with  $w_1(x, y)$  which is approximated using sinusoidal basis functions  $\Phi_m = \sqrt{2/A} \sin k_m x$  as shown in Equation (2.21). Therefore, Equation (3.12) can be simplified as

$$F_{1,j}(x) = (K + G)w_1(x, jl) - Kw_2(x, jl), \quad (3.14)$$

where  $G = E_b I_b k_m^4 - \rho_b A_b \omega^2$ .

### 3.3.1 Solving the system of equations

Recalling Equation (2.21), the simply supported plate displacement is expressed using the two dimensional Fourier sine series as mentioned in section 2.4 as

$$w_i(x, y) = \sum_{m,n=1}^{\infty} C_{mn}^i \Phi_m(x) \Psi_n(y), \quad (3.15)$$

where  $\Phi_m(x) = \sqrt{2/A} \sin k_m x$  and  $\Psi_n(y) = \sqrt{2/B} \sin k_n y$ . The values of  $m$  and  $n$  are truncated at  $M$  and  $N$ , respectively, ensuring the convergence of the series. Therefore, the value of  $\mathcal{D}_i w_i(x, y)$  can be written as

$$\mathcal{D}_i w_i(x, y) = \sum_{m,n=1}^M \mathcal{D}_{mn}^i C_{mn}^i \Phi_m \Psi_n,$$

where

$$\mathcal{D}_{mn}^i = D_i (k_m^2 + k_n^2)^2 - \sigma_i \omega^2.$$

Inserting the force terms derived in the previous section and Equation (3.15) into Equations (3.1) to (3.4) and making use of the orthogonality of the Fourier sine and cosine terms given in Sections 2.4 and 3.3, respectively, a system of linear equations

can be derived as

$$\sum_{m,n=1}^M \left[ \mathcal{D}_{mn}^1 \delta_{mm'}^p \delta_{nn'}^p + \mathcal{P}_n (G + K) \delta_{mm'}^p \mathcal{J}_n^s \right] C_{mn}^1 - \sum_{m,n=1}^M \mathcal{P}_n K \delta_{mm'}^p \mathcal{J}_n^s C_{mn}^2 + \sum_{j=0}^J \sum_{m=0}^M \sum_{n=0}^{N_c} (S_{mn}^j + T_{mn}^j) \mathbf{I}_{mm'} \mathbf{I}_{nn'}^j = P_{m'n'}, \quad (3.16)$$

$$- \sum_{m,n=1}^M \mathcal{P}_n K \delta_{mm'}^p \mathcal{J}_n^c C_{mn}^{t,1} + \sum_{m,n=1}^M \left[ \mathcal{D}_{mn}^2 \delta_{mm'}^p \delta_{nn'}^p + \mathcal{P}_n K \delta_{mm'}^p \mathcal{J}_n^c \right] C_{mn}^{t,2} + \sum_{j=0}^J \sum_{m=0}^M \sum_{n=0}^{N_c} (S_{mn}^{t,j} e^{\gamma_{mn}d} + T_{mn}^{t,j} e^{-\gamma_{mn}d}) \mathbf{I}_{mm'} \mathbf{I}_{nn'}^j = 0, \quad (3.17)$$

$$\frac{1}{\gamma_{m''n''}} \sum_{m,n=1}^M C_{mn}^{t,1} \mathbf{I}_{mm'} \mathbf{I}_{nn'}^j - \sum_{j=0}^J \sum_{m=0}^M \sum_{n=0}^{N_c} (S_{mn}^{t,j} - T_{mn}^{t,j}) \delta_{mm''}^c \delta_{nn''}^c = 0, \quad (3.18)$$

$$\frac{1}{\gamma_{m''n''}} \sum_{m,n=1}^M C_{mn}^{t,2} \mathbf{I}_{mm'} \mathbf{I}_{nn'}^j - \sum_{j=0}^J \sum_{m=0}^M \sum_{n=0}^{N_c} (S_{mn}^{t,j} e^{\gamma_{mn}d} - T_{mn}^{t,j} e^{-\gamma_{mn}d}) \delta_{mm''}^c \delta_{nn''}^c = 0, \quad (3.19)$$

where

$$\delta_{mn}^p = \begin{cases} 1, & m = n, \\ 0, & m \neq n, \end{cases} \quad \delta_{mn}^c = \begin{cases} 1, & m = n \neq 0, \\ 0.5, & m = n = 0, \\ 0, & m \neq n, \end{cases}$$

$$\mathcal{P}_n = \begin{cases} \frac{4}{n\pi}, & n \text{ is odd,} \\ 0, & n \text{ is even,} \end{cases} \quad \mathcal{J}_n^s = \sum_{j=1}^J \sin(k_n j l),$$

$$\mathbf{I}_{mm'} = \begin{cases} \frac{4m}{\pi(m^2 - m'^2)} & m = m' \\ 0 & m \neq m' \end{cases}, \quad \mathbf{I}_{nn'}^j = \begin{cases} 0, & \frac{n}{A} = \frac{n'}{l}, \\ \mathbf{II}_{\text{cav}}^1, & n' = 0, \\ \mathbf{II}_{\text{cav}}^2 \text{ Otherwise,} \end{cases}$$

where

$$\begin{aligned}\Pi_{\text{cav}}^1 &= \frac{2}{n\pi} \sqrt{\frac{A}{l}} \sin \left[ (2j+1) \frac{n\pi A}{2l} \right] \sin \frac{n\pi l}{2B}, \\ \Pi_{\text{cav}}^2 &= \frac{2\sqrt{Al}}{\pi} \left[ \frac{1}{nl+n'A} \sin \left( \frac{(nl+n'A)n\pi}{2A} (2j+1) - n'j\pi \right) \sin \left( \frac{(nl+n'A)n\pi}{2A} \right) \right. \\ &\quad \left. + \frac{1}{nl-n'A} \sin \left( \frac{(nl-n'A)n\pi}{2A} (2j+1) + n'j\pi \right) \sin \left( \frac{(nl-n'A)n\pi}{2A} \right) \right], \\ P_{mn} &= 2p_e \mathcal{I}_m^{\text{sx}} \mathcal{I}_n^{\text{sy}}, \quad \text{and} \quad \mathcal{I}_m^{\text{sx}} = \int_0^A e^{ik_x x} \Phi_m(x) dx, \quad \mathcal{I}_n^{\text{sy}} = \int_0^B e^{ik_y y} \Psi_n(y) dy.\end{aligned}$$

The values of  $\mathcal{I}_m^{\text{sx}}$  and  $\mathcal{I}_n^{\text{sy}}$  depend on the choice of  $\Phi_m(x)$  and  $\Psi_n(x)$ , which depend on the boundary conditions. For the simply supported boundary conditions and with  $\Phi_m(x)$  and  $\Psi_n(y)$  selected in this chapter,  $\mathcal{I}_m^{\text{sx}}$  and  $\mathcal{I}_n^{\text{sy}}$  can be expressed as

$$\begin{aligned}\mathcal{I}_m^{\text{sx}} &= \left\{ \begin{array}{ll} i\sqrt{\frac{A}{2}}, & k_m = k_x, \\ \sqrt{\frac{2}{A}} \frac{k_m}{k_m^2 - k_x^2} (1 - (-1)^m e^{-ik_x A}), & \text{otherwise} \end{array} \right\}, \\ \mathcal{I}_n^{\text{sy}} &= \left\{ \begin{array}{ll} i\sqrt{\frac{B}{2}}, & k_n = k_y, \\ \sqrt{\frac{2}{B}} \frac{k_n}{k_n^2 - k_y^2} (1 - (-1)^n e^{-ik_y B}), & \text{otherwise} \end{array} \right\}.\end{aligned}$$

The matrix form of the system of equation is given as

$$Z[\mathbf{c}_1 \ \mathbf{c}_2 \ \mathbf{s} \ \mathbf{t}]^T = \mathbf{p}, \quad (3.20)$$

$$\mathbf{c}_i = \begin{bmatrix} C_{11}^i \\ C_{12}^i \\ \vdots \\ C_{M_p N_p}^i \end{bmatrix}, \quad \mathbf{s} = \begin{bmatrix} S_{11}^0 \\ S_{12}^0 \\ \vdots \\ S_{M_c N_c}^J \end{bmatrix}, \quad \mathbf{t} = \begin{bmatrix} T_{11}^0 \\ T_{12}^0 \\ \vdots \\ T_{M_c N_c}^J \end{bmatrix}, \quad \mathbf{p} = \begin{bmatrix} \mathbf{P} \\ 0 \\ \vdots \\ 0 \end{bmatrix},$$

where  $Z$  is the matrix formed from the system of equations, and  $c_i$ ,  $s$  and  $t$  are the coefficient vectors containing the unknown Fourier sine and cosine coefficients.  $\mathbf{P} = [P_{11}, P_{12}, \dots, P_{M_c M_c}]^T$ , and, when considering the high frequency region of large panels where the total number of elements of  $Z$  is large, the memory limit set by Matlab may be exceeded. Therefore, the solution is not derived by inverting the  $Z$  matrix directly. Instead, the method of substitution is applied here, where the unknown coefficient vectors  $c_1$ ,  $s$  and  $t$  are gradually eliminated from the 1<sup>st</sup> row of Equation (3.20) and solved for  $c_2$  only.

### 3.3.2 $\mathcal{T}_L$ calculation

$\mathcal{T}_L$  is calculated from the displacement of the radiating plate, i.e.  $w_2$ , by following the procedure in Section 2.7 and Section 2.8. Using the appropriate coefficients and the modal functions corresponding to the radiating plate used in this chapter, Equation (2.42) is rewritten as

$$p_t(R, \theta_t, \phi_t) = \frac{-\rho\omega^2}{2\pi R} e^{-ikR} \sum_{m=1}^M \sum_{n=1}^n C_{mn}^2 \mathcal{R}_m^{\text{sx}} \mathcal{R}_n^{\text{sy}}, \quad (3.21)$$

where

$$\mathcal{R}_m^{\text{sx}} = \left\{ \begin{array}{ll} i\sqrt{\frac{A}{2}}, & k_m = -ik \sin \theta_t \cos \phi_t x, \\ \sqrt{\frac{2}{A}} \frac{k_m (1 - (-1)^m e^{-ik \sin \theta_t \cos \phi_t A})}{k_m^2 - (k \sin \theta_t \cos \phi_t)^2}, & \text{otherwise,} \end{array} \right\},$$

$$\mathcal{R}_n^{\text{sy}} = \left\{ \begin{array}{ll} i\sqrt{\frac{B}{2}}, & k_n = -ik \sin \theta_t \cos \phi_t, \\ \sqrt{\frac{2}{B}} \frac{k_n (1 - (-1)^n e^{-ik \sin \theta_t \cos \phi_t B})}{k_n^2 - (k \sin \theta_t \cos \phi_t)^2}, & \text{otherwise,} \end{array} \right\}.$$

Inserting the expression of  $p_t$  in Equation (3.21) into Equation (2.45), the corresponding transmitted intensity becomes

$$I_t = \frac{\rho_0 \omega^4}{4c_0 \sqrt{AB} \pi^2 r^2} (|C_{mn}|^2 \mathcal{R}_m^{\text{sx}} \mathcal{R}_m^{*\text{sx}} \mathcal{R}_n^{\text{sy}} \mathcal{R}_n^{*\text{sy}}), \quad (3.22)$$

where  $\mathcal{R}_m^{*\text{sx}}$  and  $\mathcal{R}_n^{*\text{sy}}$  are the conjugate of  $\mathcal{R}_m^{\text{sx}}$  and  $\mathcal{R}_n^{\text{sy}}$ , respectively. The next step is to calculate  $\tau(\theta_i, \phi_i)$  from Equation (2.47), which is averaged over all incident angles using Equation (2.48). The integrations involved in Equation (2.47) and Equations (2.48) are performed by using the Matlab function 'Quad'. Finally,  $\mathcal{T}_L$  is calculated by using Equation (2.49).

### 3.4 Parameter values

The parameter values for the materials and dimensions of the panel components are taken from a paper, where applicable. Two 13 mm gypsum plates are used (Brunskog, 2005). The width of the beams attached between the plates and the depth of the cavity are 45 mm and 95 mm, respectively. The width of each cavity is  $l = 0.6$  m, which is the distance between the mid-sections of two adjacent beams. The mass per unit area  $\sigma_i$  for both the plates is 10.9 kg. The Young's modulus of both the plates is  $E_i^0 = 2.8402$  GPa. For the attached beams, the Young's modulus and the density are  $E_b^0 = 9.8$  GPa and  $\rho_b = 550$  kg/m<sup>3</sup>, respectively. The loss factor for timber materials  $\eta = 0.06$  is added to the Young's moduli of the plates and the beams as  $E_e = E_e^0(1 + i\eta)$ , where  $E_e$  is the effective values of the Young's moduli corresponding to the element e, where e = 1, 2 and b corresponds to the incident, radiating plates and the beams. The spring constant  $K$  of the supposed spring between the beams and the radiating plate is 10<sup>10</sup> Nm<sup>-2</sup> unless stated otherwise. The speed of sound in air is 330 m/sec and the mass density of air both outside and inside the cavity is 1.29 kg/m<sup>3</sup>.

### 3.5 Convergence check

In this section, the convergence of  $\mathcal{T}_L$  is checked. One approach is to calculate  $\mathcal{T}_L$  by gradually increasing the number of terms in the series and checking for the convergence of  $\mathcal{T}_L$ . Both the sine series representing the plates' vibration and the cosine series representing the cavities' pressure need to converge. Four different sized panels are used in this thesis with four different boundary conditions, and  $\mathcal{T}_L$  must converge for all cases. The number of terms required for convergence increases with the increase in the frequencies and in the panel dimensions. A comparatively large number of terms are required for a large panel in the higher frequencies. Therefore, it requires a huge amount of computation time and memory to find the right combinations of  $M$ ,  $N$ ,  $M_c$  and  $N_c$  for all cases. It will be much convenient if an alternative way can be found, which is more efficient and quicker. Such an alternative method of finding the convergence through mode counts ( $M_{ct}$ ) is explored and used in this thesis. The method is explained in Section 3.5.2.

#### 3.5.1 Convergence through repeated calculation of $\mathcal{T}_L$

The convergence of the computation of the solution is usually checked by varying the number of terms in the Fourier series and calculating the corresponding  $\mathcal{T}_L$ . The convergence corresponding to a 3 m  $\times$  3 m simply supported double-leaf panel is checked here. Since sine series is used for solid medium and cosine is used for the fluid medium, it is not necessary that both sine and cosine series converge with the same number of terms. The cosine begins with a zeroth term, and the total number of cosine terms along  $x$  and  $y$  directions are  $(M_c + 1)$  and  $(N_c + 1)$ , respectively.  $M_c$  is set equal to  $M$ , which gives  $N = N_c B/l$ . It will be shown later in Fig. 3.2 that  $\mathcal{T}_L$  converges with this relation. Therefore, the values of  $M_c$ ,  $N_c$ ,  $M$  and  $N$  are interrelated. If one of them is set to a specific number the remaining three values are also set. The dimensions are

chosen as multiples of  $l$  everywhere in this thesis, and number of the corresponding series terms ( $N_c$ ) is taken as the reference. Figure 3.2 compares  $\mathcal{T}_L$  calculated at seven different values of  $N_c$  between 4 and 14 as shown.  $\mathcal{T}_L$  is not shown for all frequency bands for all values of  $N_c$ . Once  $\mathcal{T}_L$  corresponding to an  $N_c$  get deviated, the calculation of  $\mathcal{T}_L$  is not continued further for the corresponding value of  $N_c$ . Figure 3.2 shows that  $N_c$  required for convergence increases with the frequency. For example,  $\mathcal{T}_L$  converges with  $N_c = 4$  for up to 315 Hz band, and  $\mathcal{T}_L$  converges with  $N_c = 6$  between 400 Hz and 800 Hz bands. The  $N_c$  required for convergence at different frequency bands are taken from Fig. 3.2 and are listed in Table 3.2.

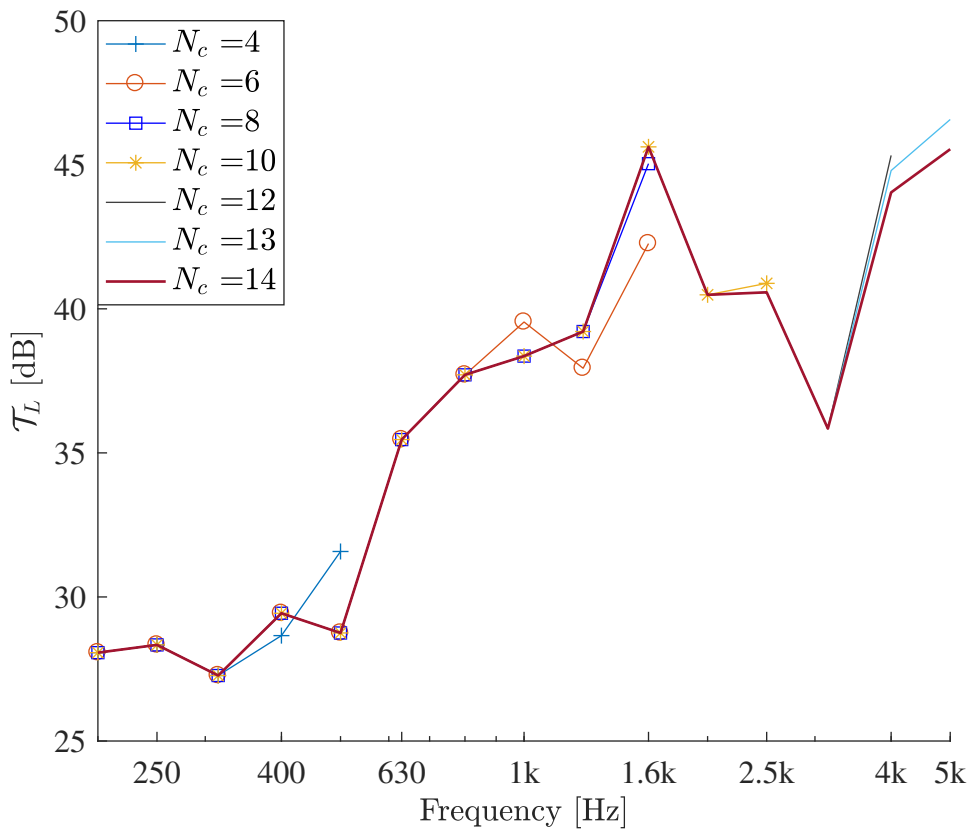


Figure 3.2:  $\mathcal{T}_L$  calculated for different values of  $N_c$  for the 3 m  $\times$  3 m panel.

### 3.5.2 Alternate method of convergence check

In this section, an alternate method of finding  $N_c$  for convergence is discussed. It is shown later in this section that the vibration field of the panel is related to the resonance modes of the plates. The resonance frequencies of a simply supported plate are calculated by Equation (2.13). Table 3.1 shows that ( $M_{ct}$ ) in each frequency band, and the corresponding values of  $N_c$  used. The values of  $M_{ct}$  in a band increase with  $N_c$  values.

Table 3.1:  $M_{ct}$  in each frequency band for the simply supported 3 m  $\times$  3 m panel.

Freq	$N_c=4$	$N_c=6$	$N_c=8$	$N_c=10$	$N_c=12$	$N_c=13$	$N_c=14$	$N_c=15$
20	2	2	2	2	2	2	2	2
25	1	1	1	1	1	1	1	1
31.5	3	3	3	3	3	3	3	3
40	3	3	3	3	3	3	3	3
50	3	3	3	3	3	3	3	3
63	5	5	5	5	5	5	5	5
80	7	7	7	7	7	7	7	7
100	6	6	6	6	6	6	6	6
125	10	10	10	10	10	10	10	10
160	12	12	12	12	12	12	12	12
200	15	15	15	15	15	15	15	15
250	19	19	19	19	19	19	19	19
315	24	24	24	24	24	24	24	24
400	30	30	30	30	30	30	30	30
500	32	37	37	37	37	37	37	37
630	20	49	49	49	49	49	49	49
800	11	60	60	60	60	60	60	60
1000	2	75	75	75	75	75	75	75
1250	0	55	97	97	97	97	97	97
1600	0	32	120	120	120	120	120	120
2000	0	12	123	154	154	154	154	154
2500	0	0	71	189	189	189	189	189
3150	0	0	39	186	243	243	243	243
4000	0	0	4	106	299	306	306	306
5000	0	0	0	51	189	309	342	342

Table 3.1 shows that the values of  $M_{ct}$  at different frequency bands converge at certain values. Increasing  $N_c$  beyond certain values does not add to the  $M_c$  value. For

example,  $M_c$  convergence at 60 in 800 Hz band, which is achieved at  $N_c = 6$ . It is also noticed that  $N_c$  required for  $M_{ct}$  convergence increase with frequency bands.  $N_c$  values corresponding to  $M_{ct}$  convergence are picked from Table 3.1, which are listed in Table 3.2. Table 3.2 shows that  $N_c$  values obtained from Fig. 3.2 and Table 3.1 are same in all frequency bands except in 4 kHz band.  $N_c$  obtained from Table 3.1 is greater than  $N_c$  from Fig. 3.2 in 4 kHz band, and convergence is attained for both values of  $N_c$ . Figure 3.2 shows that  $\mathcal{T}_L$  calculated using the  $N_c$  values according to Table 3.2 in 400 Hz and 600 Hz bands deviate by approximately 1 dB.  $N_c$  determined by Fig. 3.2 and Table 3.1 in the rest of the frequency bands are exactly the same. Therefore,  $N_c$  required for the series convergence can be determined either by the time and memory consuming method of calculating  $\mathcal{T}_L$  for various  $N_c$  or by checking the convergence of  $M_{ct}$  in each of the frequency bands at the cost of approximately 1 dB of accuracy in some frequency bands.

Table 3.2:  $M_{ct}$  in each frequency band for the simply supported 3 m  $\times$  3 m panel.

<b>Frequency bands</b>	<b><math>N_c</math> from Fig. 3.2</b>	<b><math>N_c</math> from Table 3.1</b>
100 Hz- 400 Hz	4	4
500 Hz- 1000 Hz	6	6
1250 Hz- 1600 Hz	8	8
2000 Hz- 2500 Hz	10	10
3150 Hz	12	12
4000 Hz	12	13
5000 Hz	14	14

The computation time depends on the number of terms in the Fourier series. Approximately 2 seconds is required to compute  $\mathcal{T}_L$  at four frequency points using 4 CPU core parallel computation, where  $M = M_c = 8$ . When  $M = M_c = 30, 40$  and  $50$  the computation times are 217 sec, 990 sec and 3450 sec, respectively. In all cases,  $N_c$  is set equal to 4. The number of terms increases with the increase in panel size and frequency. Therefore, finding the right combination of  $N_c, M_c, N$  and  $M$  by repeated

$\mathcal{T}_L$  calculations is time and memory consuming. Whereas, finding the right combination of  $N_c, M_c, N$  and  $M$  using the alternate method can be done without any simulation run. It only requires to fill up Table 3.1, which can be done by some hand calculations. Therefore, the alternate method of finding  $N_c, M_c, N$  and  $M$  (Section 3.5.2) is much faster compared to the method described in Section 3.5.1. Therefore, the alternate method of finding the right combinations of  $N_c, M_c, N$  and  $M$  is used in all panels at various boundary conditions. It is to be commented that the model is suitable for a small and medium sized panel (up to 3 m  $\times$  3 m panels corresponding to the parameter set up selected) or for the low frequency region of large panels because of the long computation time required otherwise.

### 3.6 $\mathcal{T}_L$ verification

The author searched the available literature for experimental data or theoretical prediction on  $\mathcal{T}_L$  through a similar double-leaf panel with beams. According to this research, the panel type considered by Brunskog (2005) is identical to the one considered here.  $\mathcal{T}_L$  calculated using the finite panel model is verified using the measurement data available in the paper by Brunskog (2005), and this is given in Section 3.6.2. The calculated results derived from the current model are also verified by comparing them with the calculated results presented by Brunskog (2005), which is given in Section 3.6.1. The measurement data is given in 1/3 octave band between 100 Hz and 3.15 kHz bands. The predicted  $\mathcal{T}_L$  is calculated for this frequency range as well and averaged over the 1/3 octave bands. The model is further verified using the results obtained from a renown software 'Insul' (Section 3.6.3). The consistency of the model is checked by comparing the calculated results with known lightweight characteristics, for example, the 1<sup>st</sup> resonance frequencies of rectangular plates.  $\mathcal{T}_L$  is calculated for various incident angles at 104 frequency points between 20 Hz and 5 kHz; this also verifies the consistency of the

model.

### 3.6.1 Comparison with infinite panel model

At first,  $\mathcal{T}_L$  is compared with the predicted results of an infinite panel model as shown in Fig. 3.4. The figure shows  $\mathcal{T}_L$  for 3 m  $\times$  3 m, 3.6 m  $\times$  3.6 m, 4.2 m  $\times$  4.2 m panels, and  $\mathcal{T}_L$  for the infinite panel. The results for the infinite panel used by Brunskog (2005) is reproduced to generate the corresponding  $\mathcal{T}_L$  curve. As discussed in Section 2.9.2, the effect of boundary conditions becomes insignificant when the panel size is sufficiently large, especially in the high frequency region. Therefore, it is expected that  $\mathcal{T}_L$  corresponding to the infinite panel is similar to  $\mathcal{T}_L$  predicted by the finite panel model with large panel size, which is apparent in Fig. 3.3. A negligible difference is seen between  $\mathcal{T}_L$  for finite panels and the infinite panel in the mid and high frequency region, above 250 Hz. The predicted  $\mathcal{T}_L$  exhibits a converging tendency with the increase in panel size and tends to converge to  $\mathcal{T}_L$  corresponding to the infinite panel model. Both the finite and the infinite panel models predict the peak at 1.6 kHz, which arises due to the valley corresponding to  $f_{cr}$  of the plates.  $f_{cr}$  depends on the panel materials, but not the panel size. Thus, the peak and the valley due to  $f_{cr}$  appears the same way for the panels with any dimensions.  $\mathcal{T}_L$  corresponding to the finite panels differs significantly with that corresponding to the infinite panel in the low frequency region below 250 Hz band. The set of boundary conditions is one of the dominating factors that governs  $\mathcal{T}_L$  in the low frequency region. Since the effects of the boundary conditions are completely ignored in the infinite panel model, the variation in  $\mathcal{T}_L$  in Fig. 3.3 below 250 Hz is well expected and it further shows the consistency of the model. The mass air mass resonance frequency ( $f_0$ ) is 85.5 Hz for the panel considered here, which falls in 80 Hz band.  $f_0$  is visible at 100 Hz band for the infinite panel but for the finite panels,  $f_0$  is not clearly visible and the dip varies with the panel size.  $f_0$  at 80 Hz band corresponds

to panels without the stiffeners, and the shift in  $f_0$  for the infinite panel is probably due to the added beams. The reason for not having the dip near  $f_0$  at a single band for the finite panels is that the finite panels experience structural resonances, which is a dominating factor in the low frequency region. It is not unlikely that some of the resonance frequencies occur near  $f_0$ , which causes the shifting of the dip at  $f_0$  when averaged in 1/3 octave bands. Variation of the dip in frequency indicates the dominance of the structural resonances near  $f_0$ . The low frequency characteristics of the panel will be further explored in Chapter 5.

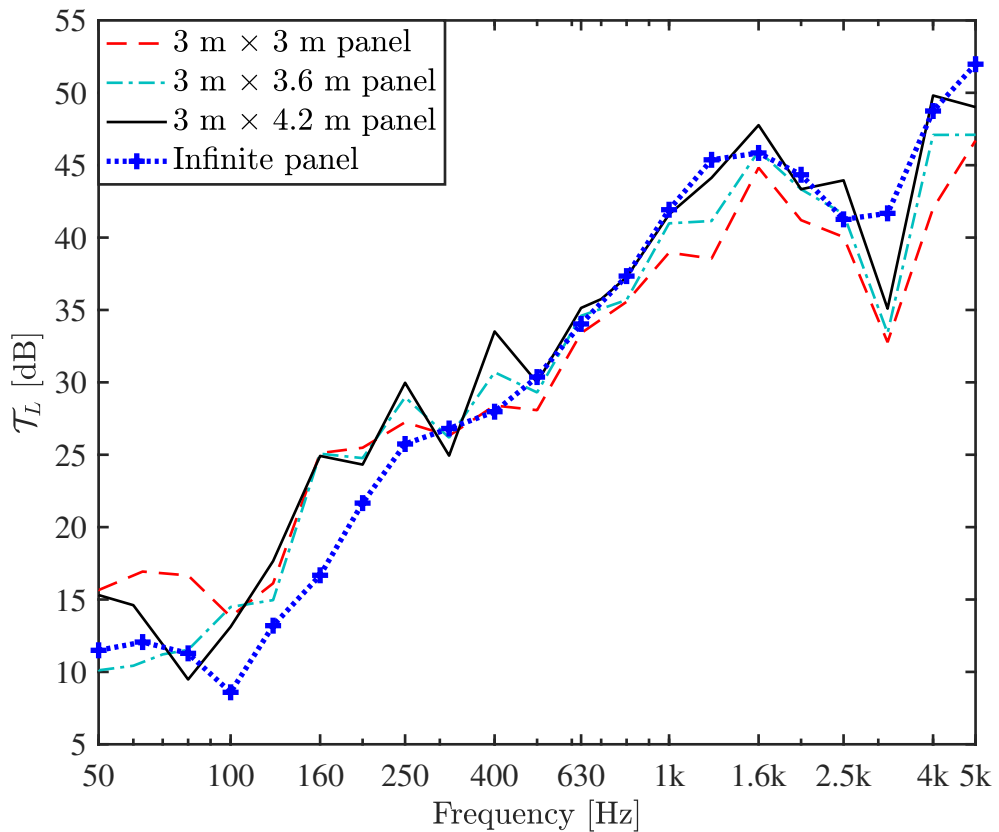


Figure 3.3: Comparison of  $\mathcal{T}_L$  between different finite sized panels and the infinite panel

### 3.6.2 Comparison with the measurement data

The exact dimension of the test panel was not given by Brunskog (2005), the detail of the test panel was collected by contacting the author Brunskog (2005). According to the author Brunskog (2005), the test was conducted in the acoustic lab of the Lund University in Sweden, which fulfils the requirement of ISO 140-2. The panel dimension was approximately  $3 \text{ m} \times 4 \text{ m}$ , with 3 m long beams.  $\mathcal{T}_L$  through a  $3 \text{ m} \times 4.2 \text{ m}$  panel is compared with the measurement data to verify the finite panel model results, as shown in Fig. 3.4. A slightly larger panel width compared to the width of the test panel (4 m) is selected to make the panel width an exact multiple of  $l$ . This modification is made to make all the cavity widths equal and to avoid the adjustment required for some cavity widths. This minor adjustment does not deviate the result significantly but makes the modelling more convenient.

The agreements between the predicted and the measurement are good in all frequency bands except at the 160 Hz band. The mean difference of  $\mathcal{T}_L$  in all frequency bands except 160 Hz band is 2 dB, and a difference of almost 10 dB is noticed at 160 Hz band. As discussed in Section 2.9.2, the boundary conditions and the cavity modes of the surrounding rooms play a significant role in the low frequency region. Therefore, it is hard to have an exact match between the predicted  $\mathcal{T}_L$  and the measurement in the low frequency region, without considering all the possible factors mentioned. Therefore, the discrepancy at 160 Hz band can be categorised as an expected discrepancy present in the low frequency region. Reasonably good agreements are noted in the higher frequencies, and both the graphs corresponding to the predicted result and the measurement data have similar shapes. The peak at 1.6 kHz band is visible in both the experimental and calculated curves. The peak arises due to the dip that follows, which occurs due to the coincidence.  $f_{cr}$  is 2.67 kHz for the plates of the lightweight panel considered here. It is normal that the dip does not show a sharp decrease in  $\mathcal{T}_L$  graph at  $f_{cr}$ .  $\mathcal{T}_L$  starts

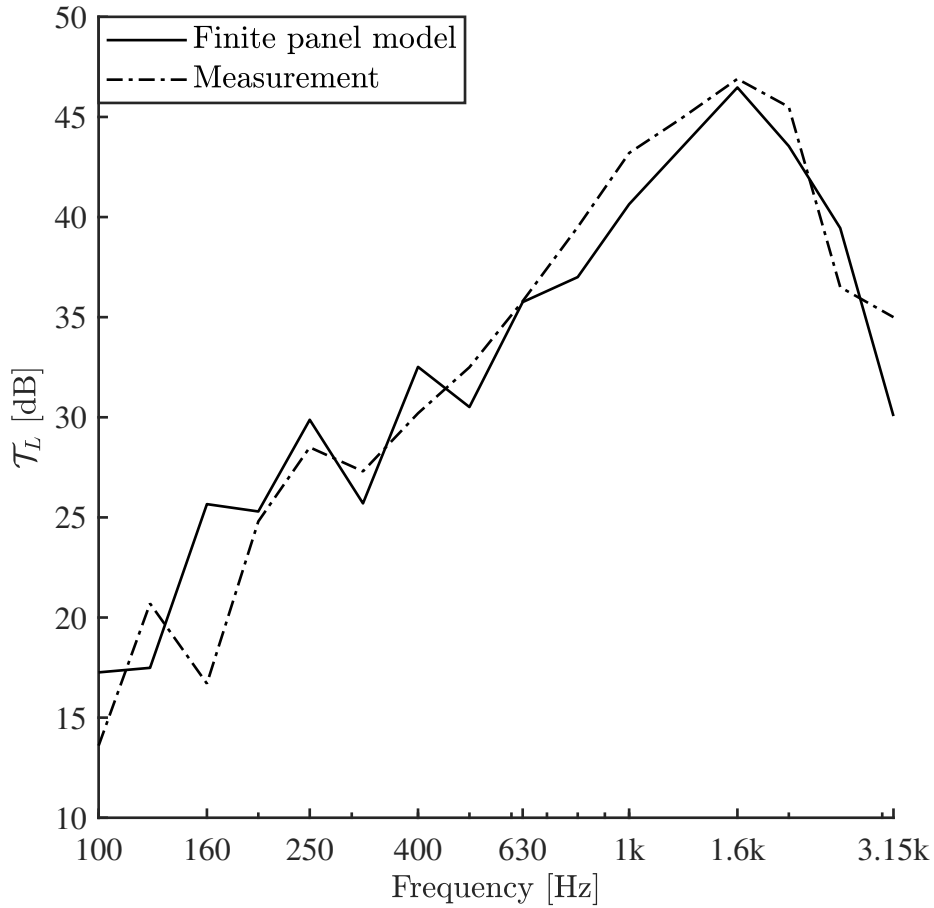


Figure 3.4: Comparison of  $\mathcal{T}_L$  calculated for 3 m  $\times$  4.2 m panel with the measured data.

decreasing gradually from a frequency below  $f_{cr}$  by one octave (Tadeu & Mateus, 2001). This explains the initiation of the dip at 1.6 kHz band. A dip is noticed at 2.5 kHz band for the infinite panel but the dip shifts to the 3.15 kHz band for both finite panel and measurement.  $\mathcal{T}_L$  graphs corresponding to both finite panels and experiment maintain the same shape around 3.15 kHz band. The finite panels (measurement and panel used in this model) experience complex structural resonances, where bending wave through different parts, i.e. beams and plates, interfere with each other resulting in shifting of the system resonance frequencies (Xin & Lu, 2010). This explains the shifting of the coincidence dips for  $\mathcal{T}_L$  corresponding to the finite panel and measurement.

### 3.6.3 Comparison with $\mathcal{T}_L$ generated by Insul

$\mathcal{T}_L$  calculated by the current model is further compared with  $\mathcal{T}_L$  generated using the software 'Insul'. Insul is built based on classic papers produced over the last 50 years. The results from Insul were verified using a number of empirical measurements obtained over thirty years.  $\mathcal{T}_L$  generated from Insul is considered to be accurate (within 2 or 3 dB) in the mid frequency region between 125 Hz and 3 kHz. Materials with the same parameter values described in Section 3.4 are considered for the Insul model.

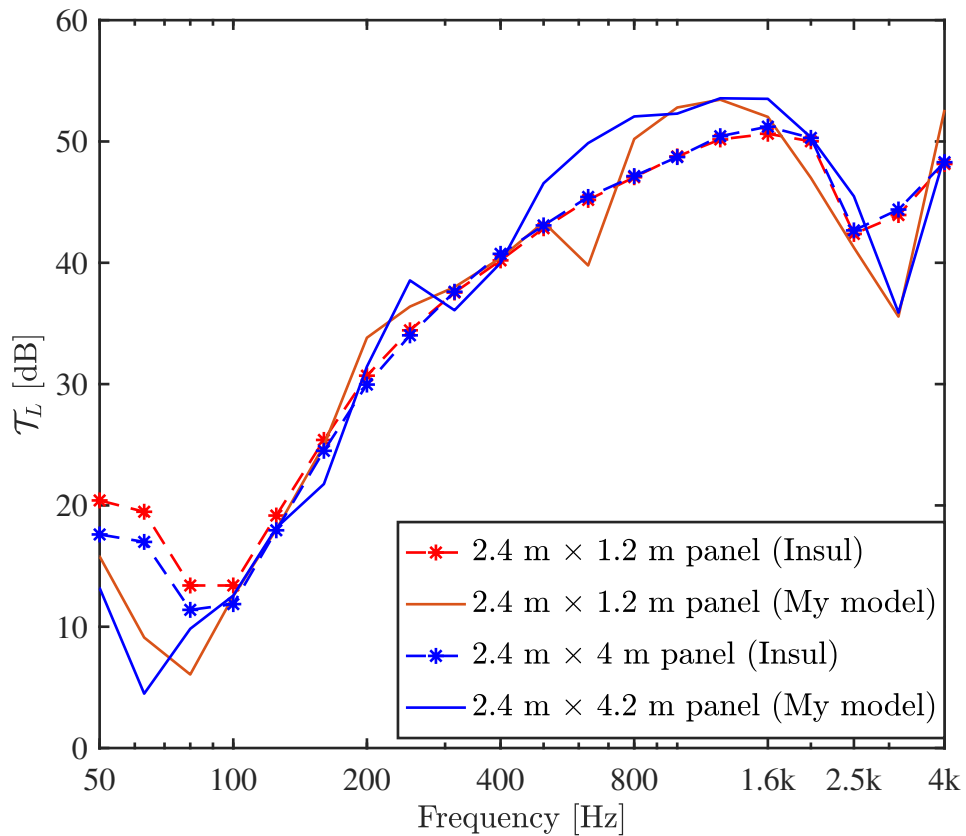


Figure 3.5:  $\mathcal{T}_L$  corresponding to the panels used in this model (1.2 m wide and 4.2 m wide) and in Insul (1.2 m wide and 4 m wide). The blue lines and the red lines correspond to the Insul model and the model used here, respectively, where the lines with markers correspond to the Insul model.

$\mathcal{T}_L$  is predicted using the Insul model for two panels, which are 2.4 m  $\times$  1.2 m and 2.4 m  $\times$  4 m. The panel dimensions used in the current model are 2.4 m  $\times$  1.2 m and 2.4

m × 4.2 m. The width of the 2<sup>nd</sup> panel is set equal to 4.2 m to make the panel width exact multiple of the beam spacings. As explained in Section 3.6.2, this slight modification in the panel size does not affect the result significantly but simplifies the modelling. The beams in the Insul model are assumed to connect rigidly to the plates. For the current model, the connection is modelled using  $K$ . As mentioned in Section 3.2, the value of  $K$  needs to be selected by trial and errors to best fit the results (from Insul). The value of  $K$  is chosen as  $3 \times 10^5 \text{ Nm}^{-2}$  in this case, and the comparison is shown in Fig. 3.5. The agreement is reasonably well between the corresponding panels, and  $\mathcal{T}_L$  predicted by this model for both panels falls within the 3 dB limit of  $\mathcal{T}_L$  generated by Insul. The pattern of the corresponding graphs (predicted by this model and Insul) for both panels are similar between 100 Hz and 2.5 kHz bands. Below 100 Hz band, the agreement is poor and  $\mathcal{T}_L$  dips vary with the panel size in case of  $\mathcal{T}_L$  corresponding to the current model. This is consistent with observation in Section 3.6.1 that the structural resonances are the most significant parameter in the low frequency region.

Figure 3.5 shows that similar to  $\mathcal{T}_L$  corresponding to Insul,  $\mathcal{T}_L$  (this model) does not vary much with the panel size with an exception in the 630 Hz band. This further indicates that the model is capable of predicting  $\mathcal{T}_L$  with reasonable accuracy when appropriate values of  $K$  are selected. A dip is seen in the 630 Hz band for the smaller panel, which is the reason for the discrepancy in this band. A similar dip is seen in the 250 Hz band for the larger panel. These dips may have occurred due to the triggering of structural resonances. The dips corresponding to the coincidence predicted by this model and by Insul are different, which occur in 3.15 kHz and 2.5 kHz bands, respectively. As explained in Section 3.6.2, the bending waves propagated through different panel component interfere with each other and it is often the case that the system resonance frequencies shift. Fig. 3.4 shows the  $\mathcal{T}_L$  graph given by Brunskog (2005) corresponding to the measurement taken on a test panel with the same material properties. The dips predicted by this model in Fig. 3.5 is consistent with the dip seen

in Fig. 3.4 for the test panel, which proves the accuracy of the prediction of this model.

### 3.6.4 Model consistency check

Two of the main features of double-leaf panels in the low frequency region are the 1<sup>st</sup> structural resonance frequency ( $f_1$ ) and the mass air mass resonance frequency  $f_0$ . In this section, these two frequencies corresponding to four sized panels are explored. The capability of the model for identifying these two frequencies with reasonable accuracy is checked, which is crucial for the consistency of the model. The effect of the resonance is perceived as sharp dips in the  $\mathcal{T}_L$  curve.  $f_1$  corresponding to a single simply supported plate can be calculated using Equation (2.13), and Equation (2.56) can be used to calculate  $f_0$  for double-leaf panels without any beam stiffeners. None of these equations correspond to the case for the double-leaf panels considered here. Therefore, the model is modified by setting the beam parameters including  $K$  as zero so that Equation (2.13), and Equation (2.56) become more applicable.  $\mathcal{T}_L$  is calculated for 1.2 m  $\times$  1.2 m, 1.8 m  $\times$  1.8 m, 2.4 m  $\times$  2.4 m and 3 m  $\times$  3 m simply supported panels for two conditions, 1. plates are attached with the beams, and 2. double plates without any beam, which are shown in Fig. 3.6. In both cases, panels are placed inside an infinite baffle and closed cavities are considered. A single incident at  $\theta_i = \pi/4$  is considered for all cases.

Sharp dips are noticed for all cases, where the 1<sup>st</sup> dips occur at 15 Hz, 7 Hz, 4 and 2 Hz corresponding to 1.2 m  $\times$  1.2 m, 1.8 m  $\times$  1.8 m, 2.4 m  $\times$  2.4 m and 3 m  $\times$  3 m panels, respectively, when no beams are considered. For the case of panels without any beam, the dips exactly coincide with the 1<sup>st</sup> resonance of the individual plates given by Equation (2.13). Whereas for the panels with attached beams, these peaks are noticed at higher frequencies. The structural resonance is dependent on the stiffness and mass per unit area of the panel. When no beams are considered, the overall stiffness of the panel

is the same as the stiffness of the identical plates. Addition of the beams significantly increases the overall stiffness of the structure, and Equation (2.13) loses its applicability. It is intuitive to state that the added stiffness due to the attached beams is the main reason for the increase in  $f_1$ . Equation (2.13) needs to be modified for the double-leaf panel attached by the beams. This indicates that the model is accurately considering the effects of all the structural components on the resonances, which exhibits the consistency of the model.

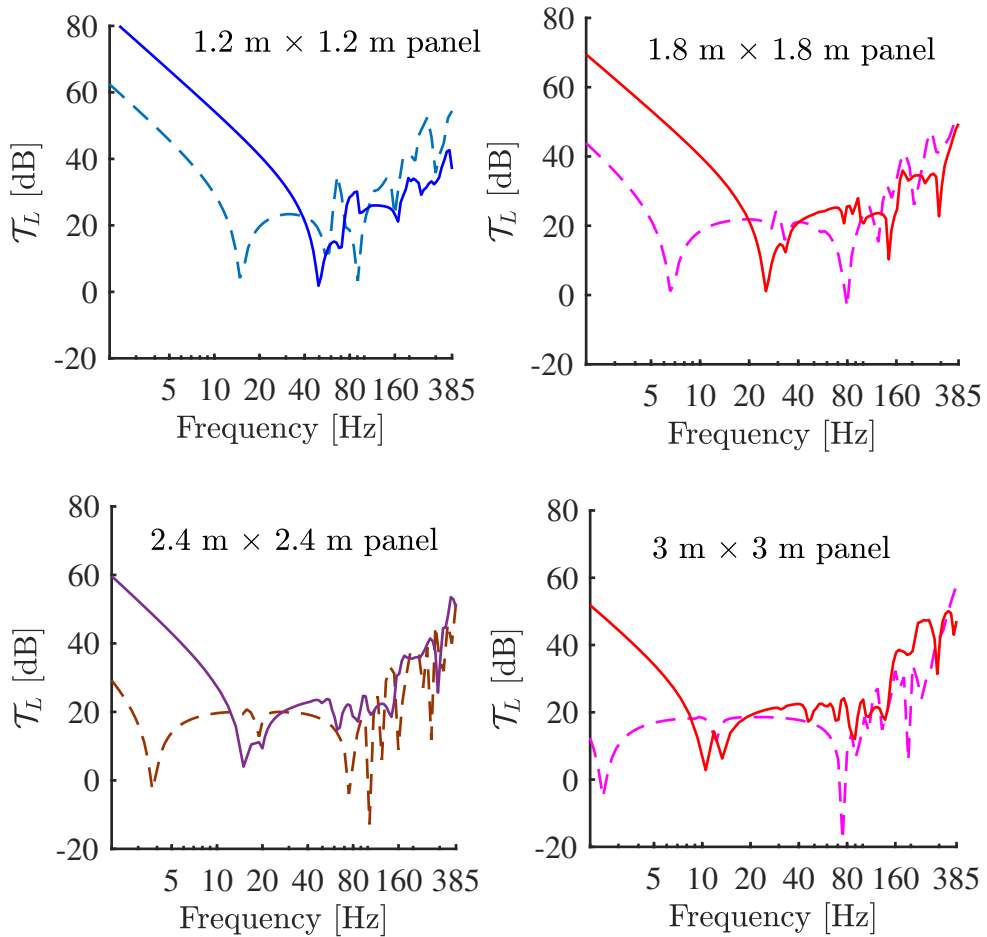


Figure 3.6:  $\mathcal{T}_L$  through four different sized simply supported panels when  $\theta_i, \phi_i = \pi/4$ . The dashed lines (---) and the solid lines (—) corresponding to panels without stiffeners and panels with stiffeners, respectively.

To explore more, the mode shapes of the 1<sup>st</sup> modes for 1.2 m × 1.2 m simply

supported panels corresponding to two previously mentioned beam conditions are shown in Fig. 3.7, where a) corresponds to a panel without any beam, and b) corresponds to a panel with the beams attached. The addition of beams gives rise to the structure-borne path, and vibration can pass through the beams. Figure 3.7 shows that the addition of the beams increases the vibration amplitude of the 1<sup>st</sup> mode of the 1.2 m × 1.2 m panel, which will cause the  $\mathcal{T}_L$  to decrease.

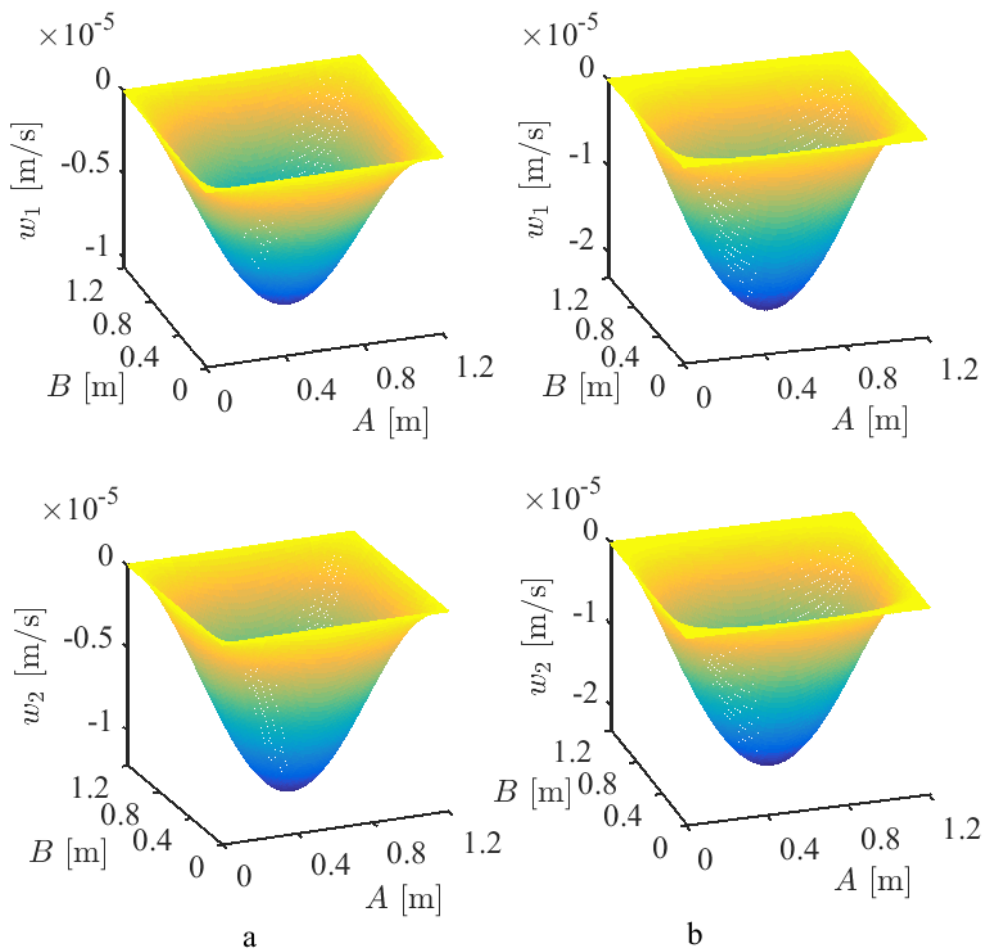


Figure 3.7: 1<sup>st</sup> mode of 1.2 m × 1.2 m panels, a) without the stiffeners (15 Hz), and b) with the stiffeners (50 Hz).

$f_0$  calculated using Equation (2.56) is 85.5 Hz for all panels without the attached beams, and sharp dips are clearly visible near 80 Hz in the  $\mathcal{T}_L$  curves corresponding

to any panel without the beam. Whereas, the dips are not seen at 85.5 Hz for panels with the beams. Instead, smaller dips are noticed near 85.5 Hz for the case of beam stiffened panels. Double-leaf panels with attached beams no longer fulfil the condition of Equation (2.56) and this may shift  $f_0$ . The finite beam stiffened double-leaf panels experience complex structural resonances, and the system resonances interfere with each other, which may cause  $f_p, f_0, f_{cr}$  to shift (Xin & Lu, 2010). As will be seen in Chapter 3 that resonance does not occur in all the cavities at a single frequency. Instead, partial resonances occur in different cavities and give rise to few dips near calculated  $f_0$ .

### 3.6.5 Effect of the incident angles

$\mathcal{T}_L$  calculated in Section 3.6.1 is done by considering the average transmission coefficient  $\tau_{ave}$ . These results do not show the variation in  $\mathcal{T}_L$  present at various incident angles. In this section, the effects of these incident angles are studied, which help to further verify the consistency of the model. Figure 3.8 shows the variation of  $\mathcal{T}_L$  at four elevation angles  $\theta_i = \pi/18, \pi/6, \pi/4$  and  $\pi/3$ . The value of  $\sin \theta_i$  changes with  $\theta_i$ , and so does the trace wavenumber of the incident wave  $k \sin \theta_i$ . As discussed in Section 2.9.2, waves get reflected at the boundaries and give rise to the resonant field. Structural resonance happens when the phase coincidence occurs between the incident and the reflected waves at the boundaries. The wavelengths of these incident and the reflected waves vary with the incident angle.

According to Fig. 3.8, the high frequency region is affected the most by  $\theta_i$  variation with almost no effect in the low frequency region. In the low frequency region, the wavelength is large and the resonance frequencies are widespread. Variation in the incident and the reflected wavelengths (at the boundaries) due to the variation in  $\theta_i$  is insignificant compared the actual wavelengths. As a result, the resonance takes place at same frequencies. For the case of higher frequencies, the wavelengths are small.

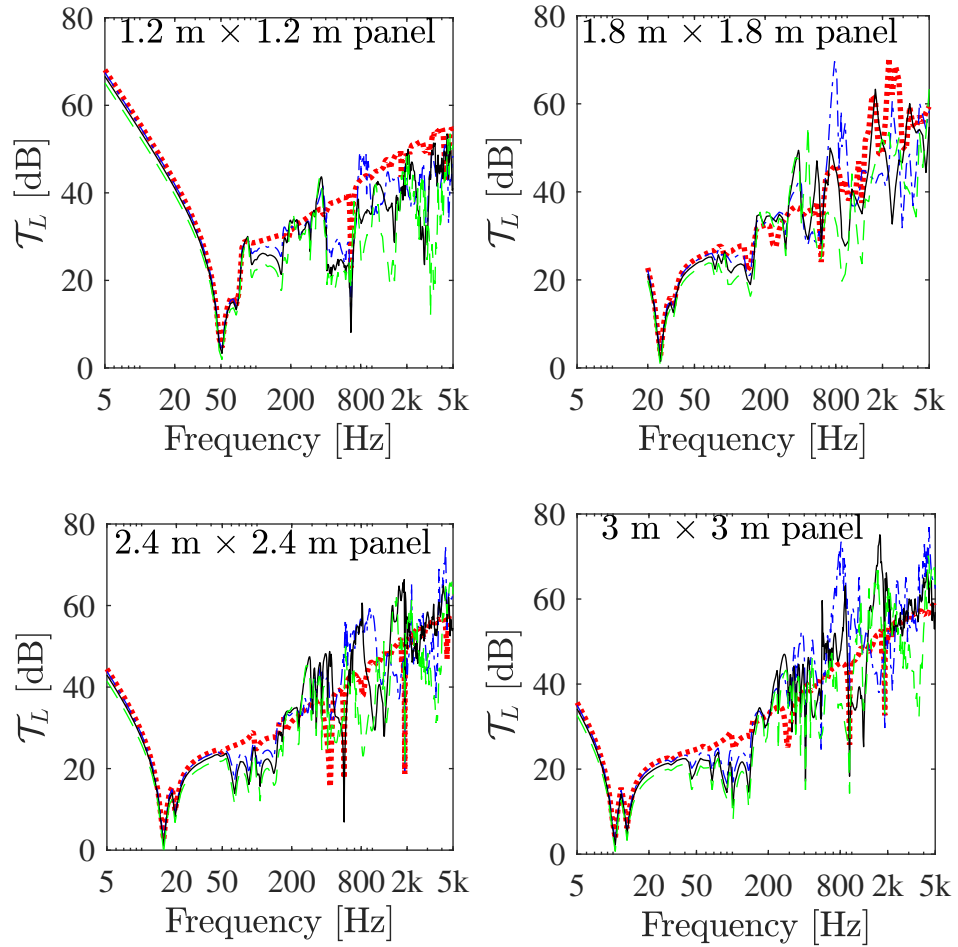


Figure 3.8:  $\mathcal{T}_L$  at different  $\theta_i$ . Red dotted line ( $\cdots$ ), blue dash-dotted line ( $-\cdot-$ ), solid line ( $—$ ) and brown dashed line ( $- - -$ ) corresponding to  $\theta_i = \pi/18, \pi/6, \pi/4$  and  $\pi/3$ , respectively.

A little variation in the wavelength becomes significant enough to break the phase coincidence. Moreover, the resonance frequencies are close in the higher frequencies. A little variation in the wavelength is enough to cause the resonance to occur at a different frequency. This results in frequent shifting of the resonance frequencies in the higher frequency region as seen in Fig. 3.8. Therefore, it can be said that the model is consistent with existing knowledge about the lightweight double-leaf panels.

## Chapter 4

### Effects of boundary conditions

In this chapter, the effects of various boundary conditions on a lightweight panel are discussed. As explained in Section 1.8, it is hard to have the real panels fully simply supported or fully clamped. Fully simply supported and fully clamped boundary conditions are the two extremes of the real scenario and the author found it useful to explore both these extremes. Indeed, the real panels can be even more complicated, but an attempt is made in this thesis to get as close as possible to the real panels within the capacity of the model. With this in mind, mixed boundary conditions are included to introduce variations to the extreme boundary conditions. In total, four types of boundary conditions are considered, where all edges simply supported and all edges clamped are two of the four types. The remaining two types are the mixture of the simply supported and the clamped boundary conditions, which are denoted as Type 1 and Type 2 boundary conditions. The type 1 boundary condition corresponds to the case where two opposite edges parallel to the beams are simply supported and the remaining two are clamped. Type 2 has the simply supported and the fully clamped edges swapped. The boundary conditions are applied at the four edges of the plates, i.e. at  $x = 0, A$  and  $y = 0, A$ . The same boundary conditions apply for the corresponding edges of both plates. The  $xy$  cross-section of the panel is illustrated in Fig. 4.1 to show the mixed

boundary conditions.

The same exact double-leaf panel considered in Chapter 3 is also considered here. Likewise, the model remains the same for any boundary condition, except for the necessary modifications for the respective boundary condition. The same panel orientation as considered in Chapter 3 is maintained here as well, where plates are placed parallel to the  $xy$  plane and the beams are placed parallel to the  $x$  axis. Multiple cavities are considered as before, and the depth of the cavities varies along the  $z$  axis. The incident and the radiating plates are situated at  $z = 0$  and  $z = d$ , respectively. The schematic diagram of the panel with the clamped boundary conditions are shown in Fig. 4.2.

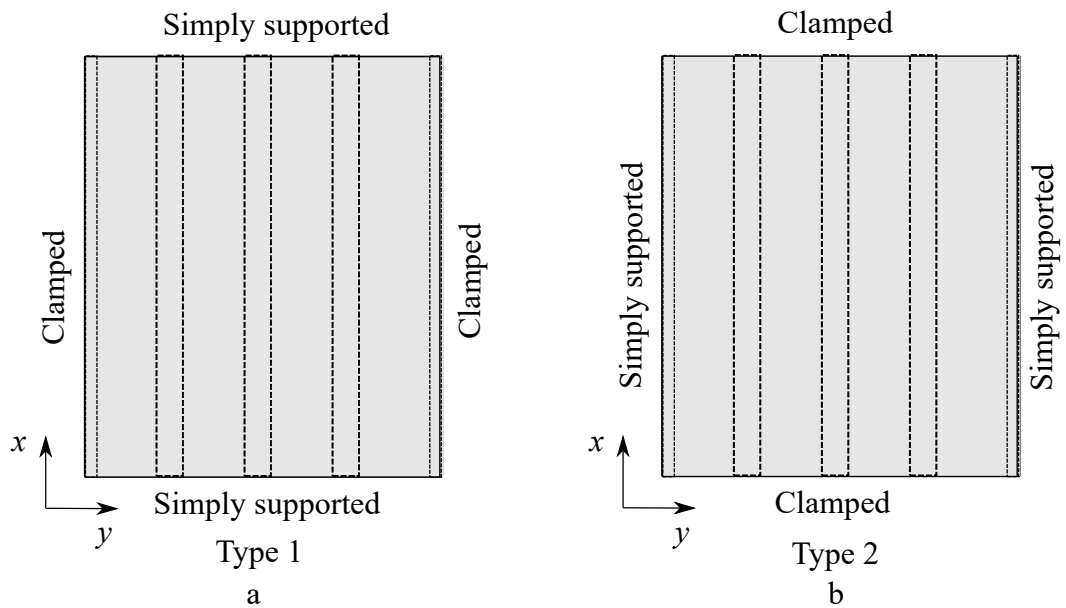


Figure 4.1: Mixed boundary conditions. a) Type 1 boundary conditions, b) Type 2 boundary conditions.

The derivation of the model with the simply supported boundary conditions is given in Chapter 3, and the derivation of the model with the clamped and mixed boundary conditions are presented in Section 4.1 in this chapter. The model for the clamped boundary conditions is verified using the measurement data from an article (Xin & Lu, 2009). The panel used by Xin & Lu (2009) is little different from the one considered

here. The model considered in this thesis with the clamped boundary conditions was modified to correspond to the panel is used by Xin & Lu (2009) for verification purposes and this is discussed in Section 4.3. The effects of the boundary conditions on four different sized square panels are also discussed. The panel sizes are 1.2 m  $\times$  1.2 m, 1.8 m  $\times$  1.8 m, 2.4 m  $\times$  2.4 m and 3 m  $\times$  3 m.  $\mathcal{T}_L$  is calculated for the four sets of boundary conditions per panel.  $\mathcal{T}_L$  is averaged over the 1/3 octave bands between 20 Hz and 5 kHz. The effect of variation in the incident angle on panels under various boundary conditions is studied. The effect of the attached beams on the 1<sup>st</sup> resonance mode of the panel is discussed.

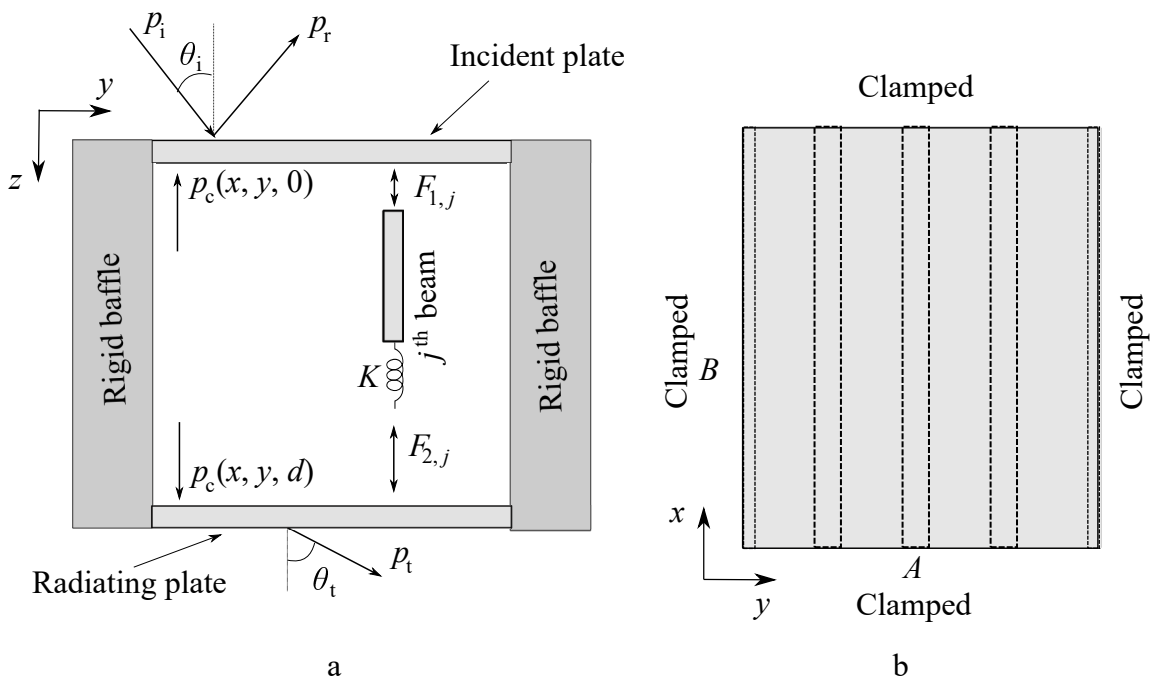


Figure 4.2: Floor panel, a) Schematic diagram of the panel, and b) clamped boundary conditions.

## 4.1 Solving the system of equations

The solution method corresponding to any boundary condition is the same and is done in three steps, first, the appropriate modal functions which satisfy the corresponding boundary conditions for the plate displacements are selected. Second, the appropriate weighting functions are then selected and the system of equations is generated from the governing equations, which are the Kirchhoff plate equations for two plates, i.e. Equation (3.1), Equation (3.2), and two equations for the cavity pressure corresponding to each cavity, i.e. Equation (2.34) and Equation (2.35). The system of equations is solved for the plate displacements and the cavity pressure. Finally,  $\mathcal{T}_L$  is calculated from the plate displacements.

### 4.1.1 Selecting the appropriate modal function

The general equations for of the plate displacements for the clamped and the mixed boundary conditions are expressed in terms of series as

$$w_i(x, y) = \sum_{m,n=1}^{\infty} C_{mn}^{b,i} \mathcal{A}_m(x) \mathcal{B}_n(y), \quad (4.1)$$

where  $C_{mn}^{b,i}$  is the set of unknown coefficients corresponding to the boundary condition 'b', which needs to be determined and  $i = 1, 2$  represents the two plates, respectively.  $b = ['c', 't', 'q']$  represents the boundary conditions, where 'c', 't' and 'q' correspond to the clamped, type1 and type 2 boundary conditions, respectively. The modal functions  $\mathcal{A}_m(x)$  and  $\mathcal{B}_n(y)$  are chosen so that the corresponding boundary conditions are satisfied. The appropriate modal functions for four different boundary conditions, which satisfy the corresponding boundary conditions are given in Table 4.1.

Only square panels are considered in this chapter, which means  $A = B$  and the modal functions are the same in both directions when all edges have the same boundary

conditions. As an example, the plates' displacements corresponding to the type 1 boundary conditions are

$$w_i(x, y) = \sum_{m,n=1}^{\infty} \frac{2}{\sqrt{3A}} \sin(k_m x)(1 - \cos(2k_n y)),$$

which satisfy the simply supported boundary conditions at  $x = 0, A$  and the clamped conditions at  $y = 0, A$ .

Table 4.1: Modal functions for different boundary conditions.

Boundary conditions	$\mathcal{A}_m(x)$	$\mathcal{B}_n(y)$
Simply supported	$\sqrt{\frac{2}{A}} \sin k_m x$	$\sqrt{\frac{2}{A}} \sin k_n y$
Clamped	$\sqrt{\frac{2}{3A}} (1 - \cos 2k_m x)$	$\sqrt{\frac{2}{3A}} (1 - \cos 2k_n y)$
Type 1	$\sqrt{\frac{2}{A}} \sin k_m x$	$\sqrt{\frac{2}{3A}} (1 - \cos 2k_n y)$
Type 2	$\sqrt{\frac{2}{3A}} (1 - \cos 2k_m x)$	$\sqrt{\frac{2}{A}} \sin k_n y$

#### 4.1.2 Selecting the appropriate weighting function and generating the system of equations

The modal functions corresponding to the simply supported edges are orthogonal, and the solution method corresponding to the simply supported boundary conditions is as given in Chapter 3. Whereas, the modal functions for the clamped edges are not orthogonal and the Galerkin method is used to generate the system of equations. In the Galerkin method, the governing equations are multiplied by a set of functions known as the weighting functions and then integrated over the plate surface (Fletcher, 2012). The modal functions corresponding to any boundary conditions are selected to be the weighting functions for the respective boundary conditions.

The governing equations are the same as the ones in Chapter 3, i.e. Kirchhoff plate equations for two plates given by Equations (4.7) and (4.8) and the continuity conditions at  $z = 0, d$  between the cavity air particle velocity and the plate displacements given by Equations (4.5) and (4.6). All the cavities between the plates and the beams are considered to be isolated from each other as before, and two continuity conditions corresponding to two plates are derived for each cavity. Equation (3.8) used in Chapter 3 can be used as the general expression for the pressure in each cavity for any boundary conditions, which is

$$p_c(x, y, z) = \sum_{m,n=0}^M \left( \mathcal{S}_{mn}^{b,j} e^{\gamma_{mn} z} + \mathcal{T}_{mn}^{b,j} e^{-\gamma_{mn} z} \right) \alpha_m(x) \beta_n^j(y). \quad (4.2)$$

The same cosine series for the cavity pressure is used here. The expressions of  $\alpha_m(x) = \sqrt{2/A} \cos(k_m x)$  and  $\beta_n^j(y) = \sqrt{2/l} \cos(\kappa_n(y - jl))$  remain the same. Similar to  $\mathcal{C}_{mn}^{b,i}$ , the sets of coefficients  $\mathcal{S}_{mn}^{b,j}$  and  $\mathcal{T}_{mn}^{b,j}$  depend on the type of boundary conditions 'b', and need to be solved for each type of boundary conditions. Similarly, the expression for the forces from the beams and the coupling conditions between the plates and the beams are the same as given in Equations (2.3) to (2.7). The only differences are the displacement functions  $w_i(x, y)$ , and the associated modal functions. Inserting the force terms and the cavity pressure terms into Equation (3.1), (3.2), (2.34) and (2.35), it can be written as

$$\sum_{m,n=1}^M \mathcal{C}_{mn}^{b,1} \left[ (\mathcal{G} + K) \mathcal{A}_m(x) \mathcal{J}_n + \mathcal{D}_1 \mathcal{A}_m(x) \mathcal{B}_n(y) \right] - \sum_{m,n=1}^M \mathcal{C}_{mn}^{b,2} K \mathcal{A}_m(x) \mathcal{J}_n + p_c(x, y, 0) - 2p_e = 0, \quad (4.3)$$

$$\sum_{m,n=1}^M \mathcal{C}_{mn}^{b,1} K \mathcal{A}_m(x) \mathcal{J}_n - \sum_{m,n=1}^M \mathcal{C}_{mn}^{b,2} \left[ K \mathcal{A}_m(x) \mathcal{J}_n + \mathcal{D}_2 \mathcal{A}_m(x) \mathcal{B}_n(y) \right] - p_c(x, y, d) = 0, \quad (4.4)$$

$$\left. \frac{\partial p_c(x, y, z)}{\partial z} \right|_{z=0} - \omega^2 \rho_0 \sum_{m,n=1}^M C_{mn}^{b,1} \mathcal{A}_m(x) \mathcal{B}_n(y) = 0, \quad (4.5)$$

$$\left. \frac{\partial p_c(x, y, z)}{\partial z} \right|_{z=d} - \omega^2 \rho_0 \sum_{m,n=1}^M C_{mn}^{b,2} \mathcal{A}_m(x) \mathcal{B}_n(y) = 0, \quad (4.6)$$

where

$$\mathcal{G} = \left( E_b I_b \frac{d^4}{dx^4} - \rho_b A_b \omega^2 \right), \quad \mathcal{D}_i = \left( D_i \nabla^4 - \sigma_i \omega^2 \right), i = 1, 2, \quad \mathcal{J}_n^b = \sum_{j=1}^J \mathcal{B}_n(jl).$$

$\mathcal{J}_n^b$  varies deepening on the boundary conditions 'b'. The symbols used in the above equations correspond to the same parameters as described in Section 2.1.1 to 2.2.

The Galerkin method is used to derive the system of equations as described in Section 2.5. Multiplying both sides of Equations (4.3) and (4.4) by the selected modal functions (depending on the boundary conditions)  $\mathcal{A}_{m'}(x)$  and  $\mathcal{B}_{n'}(y)$ , where  $m', n' = 1, 2, 3, \dots, M$ , and multiplying both sides of Equations (4.5) and (4.6) by the  $\alpha_{m'}(x)$  and  $\beta_{n'}^j(y)$ , where  $m' = 0, 1, 2, \dots, M$ ,  $n'' = 0, 1, 2, \dots, N_c$  and integrating over the plate surfaces, the following equations are found

$$\int_0^A \int_0^A \left[ \sum_{m,n=1}^M C_{mn}^{b,1} [(\mathcal{G} + K) \mathcal{J}_n + \mathcal{D}_1 \mathcal{B}_n(y)] \mathcal{A}_m(x) - \sum_{m,n=1}^M C_{mn}^{b,2} K \mathcal{A}_m(x) \mathcal{J}_n + \sum_{j=0}^J \sum_{m=0}^M \sum_{n=0}^{N_c} \left( \mathcal{S}_{mn}^{b,j} + \mathcal{T}_{mn}^{b,j} \right) \alpha_m(x) \beta_n^j(y) \right] \mathcal{A}_{m'}(x) \mathcal{B}_{n'}(y) dx dy - P_{m'n'}^b = 0, \quad (4.7)$$

$$\int_0^A \int_0^A \left[ \sum_{m,n=1}^M C_{mn}^{b,1} K \mathcal{A}_m(x) \mathcal{J}_n - \sum_{m,n=1}^M C_{mn}^{b,2} [K \mathcal{J}_n + \mathcal{D}_2 \mathcal{B}_n(y)] \mathcal{A}_m(x) - \sum_{j=0}^J \sum_{m=0}^M \sum_{n=0}^{N_c} \left( \mathcal{S}_{mn}^{b,j} e^{\gamma_{mn}d} + \mathcal{T}_{mn}^{b,j} e^{-\gamma_{mn}d} \right) \alpha_m(x) \beta_n^j(y) \right] \mathcal{A}_{m'}(x) \mathcal{B}_{n'}(y) dx dy = 0, \quad (4.8)$$

$$\int_0^A \int_0^A \left[ \sum_{j=0}^J \sum_{m=0}^M \sum_{n=0}^{N_c} \gamma_{mn} \left( \mathcal{S}_{mn}^{b,j} - \mathcal{T}_{mn}^{b,j} \right) \alpha_m(x) \beta_n^j(y) - \omega^2 \rho_0 \sum_{m,n=1}^M \mathcal{C}_{mn}^{b,1} \mathcal{A}_m(x) \mathcal{B}_n(y) \right] \alpha_{m'}(x) \beta_{n''}^j(y) dx dy = 0, \quad (4.9)$$

$$\int_0^A \int_0^A \left[ \sum_{j=0}^J \sum_{m=0}^M \sum_{n=0}^{N_c} \gamma_{mn} \left( \mathcal{S}_{mn}^{b,j} e^{\gamma_{mn} d} + \mathcal{T}_{mn}^{b,j} e^{-\gamma_{mn} d} \right) \alpha_m(x) \beta_n^j(y) - \omega^2 \rho_0 \sum_{m,n=1}^M \mathcal{C}_{mn}^{b,2} \mathcal{A}_m(x) \mathcal{B}_n(y) \right] \alpha_{m'}(x) \beta_{n''}^j(y) dx dy = 0, \quad (4.10)$$

where

$$P_{m'n'}^b = 2p_c \mathcal{I}_{m'}^{sx} \mathcal{I}_{n'}^{sy}, \quad \text{and} \quad \mathcal{I}_{m'}^{sx} = \int_0^A e^{ik_x x} \mathcal{A}_{m'}(x) dx, \quad \mathcal{I}_{n'}^{sy} = \int_0^A e^{ik_y y} \mathcal{B}_{n'}(y) dy,$$

where,  $m', n' = 1, 2, 3, \dots, M$ ,  $n'' = 0, 1, 2, \dots, N_c$ . The terms of the governing equations are basically the integration between the different combinations of the terms of  $\mathcal{A}_m(x)$ ,  $\mathcal{B}_n(y)$ ,  $\alpha_m(x)$ , and  $\beta_n^j(y)$ , which are

$$I_{mm'}^{b,x} = \int_0^A \mathcal{A}_m(x) \mathcal{A}_{m'}(x) dx, \quad (4.11)$$

$$I_{nn'}^{b,y} = \int_0^A \mathcal{B}_n(y) \mathcal{B}_{n'}(y) dy, \quad (4.12)$$

$$I_{mm'}^x = \int_0^A \alpha_m(x) \alpha_{m'}(x) dx, \quad (4.13)$$

$$I_{nn'}^{y,j} = \int_{j_l}^{(j+1)l} \beta_n(y)^j \beta_{n'}(y)^j dy, \quad (4.14)$$

$$II_{mm'}^{b,x} = \int_0^A \mathcal{A}_m(x) \alpha_{m'}(x) dx, \quad (4.15)$$

$$II_{nn'}^{b,j} = \int_{j_l}^{(j+1)l} \mathcal{B}_n(y) \beta_{n'}^j(y) dy, \quad (4.16)$$

The above integrals need to be evaluated separately for different boundary conditions represented by 'b'. The values of the integrals and the solution procedure corresponding to the clamped boundary conditions are shown in this chapter. The integral values and the final form of the governing equations for the mixed boundary conditions are

presented in Appendix A.

The step by step procedure for finding the solution is the same up to Equation (4.10) for any boundary conditions. The difference begins from Equation (4.11) because the above integrals vary with the boundary conditions. The values of the integrals depend on the choice of the weighting functions, i.e.  $\mathcal{A}_m(x)$  and  $\mathcal{B}_n(y)$ , for any the boundary conditions. At this point, the task is to evaluate these integrals with the appropriate modal functions  $\mathcal{A}_m(x)$ ,  $\mathcal{B}_n(y)$  selected for the corresponding boundary conditions, and insert them back to Equations (4.7) to Equation (4.10). The modal functions corresponding to the clamped boundary condition are

$$\mathcal{A}_m(x) = \sqrt{\frac{2}{3A}}(1 - \cos 2k_m x), \mathcal{B}_n(y) = \sqrt{\frac{2}{3A}}(1 - \cos 2k_n y),$$

and with these modal functions, the plate displacements take the form

$$w_i(x, y) = \frac{2}{3A} \sum_{m,n=1}^M \mathcal{C}_{mn}^{c,i} (1 - \cos 2k_m x)(1 - \cos 2k_n y). \quad (4.17)$$

The terms  $\mathcal{G}\mathcal{A}_m(x)$  and  $\mathcal{D}_i\mathcal{A}_m(x)\mathcal{B}_n(y)$  corresponding to the selected  $\mathcal{A}_m(x)$  and  $\mathcal{B}_n(y)$  (clamped boundary condition) are expressed as

$$\begin{aligned} \mathcal{G}\mathcal{A}_m(x) &= -\sqrt{\frac{2}{3A}} E_b I_b (2k_m)^4 \cos 2k_m x - A_b \rho_b \omega^2 \mathcal{A}_m(x) \\ \mathcal{D}_i\mathcal{A}_m(x)\mathcal{B}_n(y) &= -\sqrt{\frac{2}{3A}} D_i \left( (2k_m)^4 \cos 2k_m x \mathcal{B}_n(y) + (2k_n)^4 \cos 2k_n y \mathcal{A}_m(x) \right. \\ &\quad \left. - 2\sqrt{\frac{2}{3A}} (2k_m)^2 (2k_n)^2 \cos 2k_m x \cos 2k_n y \right) - \sigma_i \omega^2 \mathcal{A}_m(x)\mathcal{B}_n(y). \end{aligned}$$

Inserting  $\mathcal{A}_m(x)$ ,  $\mathcal{B}_n(y)$ ,  $\alpha_m(x)$  and  $\beta_n^j(y)$  in Equation (4.11) to Equation (4.16) the

integrals corresponding to the clamped boundary condition are evaluated as

$$\begin{aligned}
 I_{mm'}^{c,x} &= \begin{cases} 1 & m = m', \\ \frac{2}{3} & m \neq m', \end{cases}, & I_{nn'}^{c,y} &= \begin{cases} 1 & n = n', \\ \frac{2}{3} & n \neq n', \end{cases}, \\
 I_{mm'}^x &= \begin{cases} 1 & m = m' \neq 0, \\ 0.5 & m = m' = 0, \\ 0 & m \neq m', \end{cases}, & I_{nn'}^{y,j} &= \begin{cases} 1 & n = n' \neq 0, \\ 0.5 & n = n' = 0, \\ 0 & n \neq n', \end{cases}, \\
 II_{mm'}^{c,x} &= \begin{cases} -\frac{1}{\sqrt{3}} & 2m = m', \\ \frac{1}{\sqrt{3}} & m' = 0, \\ 0 & \text{Otherwise,} \end{cases}, & II_{nn'}^{c,j} &= \begin{cases} \sqrt{\frac{l}{3A}} & n' = 0, \\ -(-1)^{n'j} \sqrt{\frac{l}{3A}} & 2n = n', \\ \Pi_{\text{cav}} & \text{Otherwise,} \end{cases}.
 \end{aligned}$$

where

$$\begin{aligned}
 \Pi_{\text{cav}} &= \frac{2\sqrt{Al}}{\pi} \left[ \frac{1}{nl + n'A} \sin\left(\frac{(nl + n'A)n\pi}{2A}(2j + 1) - n'j\pi\right) \sin\left(\frac{(nl + n'A)n\pi}{2A}\right) \right. \\
 &\quad \left. + \frac{1}{nl - n'A} \sin\left(\frac{(nl - n'A)n\pi}{2A}(2j + 1) + n'j\pi\right) \sin\left(\frac{(nl - n'A)n\pi}{2A}\right) \right].
 \end{aligned}$$

Having these integrals evaluated, Equations (4.7) to (4.10) can be simplified as the

followings,

$$\begin{aligned} & \sum_{m,n=1}^M \left[ \frac{D_1}{9} (3\zeta_{mm'}^4 + 2\zeta_{mm'}^2 \zeta_{nn'}^2 + 3\zeta_{nn'}^4 - \sigma_1 \omega^2) I_{mm'}^{c,x} I_{nn'}^{c,y} + \frac{2}{3} \left( \frac{E_b I_b \zeta_{mm'}^4}{3} \right. \right. \\ & \quad \left. \left. - A_b \rho_b \omega^2 I_{mm'}^{c,x} + K I_{mm'}^{c,x} \right) \mathcal{J}_n \right] \mathcal{C}_{mn}^{c,1} - \sum_{m,n=1}^M \frac{2}{3} K I_{mm'}^{c,x} \mathcal{J}_n \mathcal{C}_{mn}^{c,2} \\ & + \sum_{j=0}^J \sum_{m=0}^M \sum_{n=0}^{N_c} (\mathcal{S}_{mn}^{c,j} + \mathcal{T}_{mn}^{c,j}) I I_{m'm}^{c,x} I I_{n'n}^{c,j} = 2p_e \mathcal{I}_m^{cx} \mathcal{I}_n^{cy}, \end{aligned} \quad (4.18)$$

$$\begin{aligned} & - \sum_{m,n=1}^M \frac{2}{3} K I_{mm'}^{c,x} \mathcal{J}_n \mathcal{C}_{mn}^{c,1} + \sum_{m,n=1}^M \left[ \frac{D_2}{9} (3\zeta_{mm'}^4 + 2\zeta_{mm'}^2 \zeta_{nn'}^2 + 3\zeta_{nn'}^4 - \sigma_2 \omega^2) I_{mm'}^{c,x} I_{nn'}^{c,y} \right. \\ & \quad \left. + \frac{2}{3} K I_{mm'}^{c,x} \mathcal{J}_n \right] \mathcal{C}_{mn}^{c,2} + \sum_{j=0}^J \sum_{m=0}^M \sum_{n=0}^{N_c} (\mathcal{S}_{mn}^{c,j} e^{\gamma_{mn}d} + \mathcal{T}_{mn}^{c,j} e^{-\gamma_{mn}d}) I I_{m'm}^{c,x} I I_{n'n}^{c,j} = 0, \end{aligned} \quad (4.19)$$

$$\frac{1}{\gamma_{m''n''}} \sum_{m,n=1}^M \mathcal{C}_{mn}^{c,1} I I_{mm''}^{c,x} I I_{nn''}^{c,j} - \sum_{j=0}^J \sum_{m=0}^M \sum_{n=0}^{N_c} (\mathcal{S}_{mn}^{c,j} - \mathcal{T}_{mn}^{c,j}) I_{mm''}^{c,x} I_{nn''}^{c,j} = 0, \quad (4.20)$$

$$\begin{aligned} & \frac{1}{\gamma_{m''n''}} \sum_{m,n=1}^M \mathcal{C}_{mn}^{c,2} I I_{mm''}^{c,x} I I_{nn''}^{c,j} \\ & - \sum_{j=0}^J \sum_{m=0}^M \sum_{n=0}^{N_c} (\mathcal{S}_{mn}^{c,j} e^{\gamma_{mn}d} - \mathcal{T}_{mn}^{c,j} e^{-\gamma_{mn}d}) I_{mm''}^{c,x} I_{nn''}^{c,j} = 0, \end{aligned} \quad (4.21)$$

where

$$\zeta_{mm'} = \begin{cases} 2k_m & m = m', \\ 0 & m \neq m', \end{cases}, \quad \zeta_{nn'} = \begin{cases} 2k_n & n = n', \\ 0 & n \neq n', \end{cases},$$

$$\mathcal{I}_m^{cx} = \begin{cases} \sqrt{\frac{2}{3A}} \left( \frac{1 - e^{-ik_m A}}{ik_m} - \frac{A}{2} \right), & k_m = -ik \sin \theta_i \cos \phi_i x, \\ \sqrt{\frac{2}{3A}} \frac{ik_m (1 - e^{-ik \sin \theta_i \cos \phi_i A})}{(k \sin \theta_i \cos \phi_i)^2 - k_m^2}, & \text{otherwise} \end{cases},$$

$$\mathcal{I}_n^{cy} = \begin{cases} \sqrt{\frac{2}{3A}} \left( \frac{1 - e^{-ik_n A}}{ik_n} - \frac{A}{2} \right), & k_n = -ik \sin \theta_i \cos \phi_i, \\ \sqrt{\frac{2}{3A}} \frac{ik_n (1 - e^{-ik \sin \theta_i \sin \phi_i A})}{(k \sin \theta_i \sin \phi_i)^2 - k_n^2}, & \text{otherwise} \end{cases}.$$

$m', n' = 1, 2, 3, \dots, M$ ,  $m'' = 0, 1, 2, \dots, M$ ,  $n'' = 0, 1, 2, \dots, N_c$  and  $j = 0, 1, 2, \dots, J$ . The total number of equations is Thus  $2[MN + (M+1)(N_c+1)(J+1)]$ , which equals the

total number of unknowns in the system of equations. The system of equations is then solved for the coefficient sets  $[\mathbf{c}_1 \ \mathbf{c}_2 \ \mathbf{s}_j \ \mathbf{t}_j]$ , where

$$\mathbf{c}_i = \begin{bmatrix} \mathcal{C}_{11}^{c,i} \\ \mathcal{C}_{12}^{c,i} \\ \vdots \\ \mathcal{C}_{MN}^{c,i} \end{bmatrix}, \mathbf{s}_j = \begin{bmatrix} \mathcal{S}_{00}^{c,j} \\ \mathcal{S}_{01}^{c,j} \\ \vdots \\ \mathcal{S}_{MN_c}^{c,j} \end{bmatrix}, \mathbf{t}_j = \begin{bmatrix} \mathcal{T}_{00}^{c,j} \\ \mathcal{T}_{01}^{c,j} \\ \vdots \\ \mathcal{T}_{MN_c}^{c,j} \end{bmatrix},$$

where  $i = 1, 2$  and  $j = 0, 1, 2, \dots, J$ .

Finally,  $\tau(\theta_i, \phi_i)$  is calculated for all incident angles following the procedure in Section 2.8, where  $\theta_i$  is restricted to  $0.433\pi$  radian. Equation (3.22) for  $I_t$  needs to be revised for the clamped boundary conditions, and becomes

$$I_t = \frac{\rho_0 \omega^4}{8C_0 \pi^2 r^2} (|\mathcal{C}_{mn}^{c,2}|^2 \mathcal{R}_m^{\text{cx}} \mathcal{R}_m^{*\text{cx}} \mathcal{R}_n^{\text{cy}} \mathcal{R}_n^{*\text{cy}}), \quad (4.22)$$

where

$$\mathcal{R}_m^{\text{cx}} = \begin{cases} \sqrt{\frac{2}{3A}} \left( \frac{1 - e^{-ik_m A}}{ik_m} - \frac{A}{2} \right), & k_m = -ik \sin \theta_t \cos \phi_t x, \\ \sqrt{\frac{2}{3A}} \frac{ik_m (1 - e^{-ik \sin \theta_t \cos \phi_t A})}{(k \sin \theta_t \cos \phi_t)^2 - k_m^2}, & \text{otherwise} \end{cases},$$

$$\mathcal{R}_n^{\text{cy}} = \begin{cases} \sqrt{\frac{2}{3A}} \left( \frac{1 - e^{-ik_n A}}{ik_n} - \frac{A}{2} \right), & k_n = -ik \sin \theta_t \cos \phi_t, \\ \sqrt{\frac{2}{3A}} \frac{ik_n (1 - e^{-ik \sin \theta_t \sin \phi_t A})}{(k \sin \theta_t \sin \phi_t)^2 - k_n^2}, & \text{otherwise} \end{cases}.$$

## 4.2 Convergence

Convergence of  $\mathcal{T}_L$  in each frequency band is related to the number of terms in the series representing the plate displacements and the cavity pressure. As discussed in Chapter 3,  $M_{ct}$  in each frequency band converges for certain values of  $N_c$ , and  $\mathcal{T}_L$  also

converges when these values of  $N_c$  are used. The same procedure for determining the  $N_c$  value required for  $\mathcal{T}_L$  convergence is followed here as well. Table 4.3 shows  $M_{ct}$  corresponding to four different sized clamped panels in each band and also the value of  $N_c$  corresponding to the convergence of  $M_{ct}$ . The table shows four values for  $N_c$  corresponding to the four panels in each frequency bands. The maximum values of  $N_c$ , i.e. the  $N_c$  value corresponding to the largest panel is considered for all panels in the respective bands. Similar to Chapter 3, the same relationship between  $M_c$ ,  $M$ ,  $N_c$ ,  $N$  is maintained, where  $M_c = M$ , and  $M_c = N_c A/l$ .

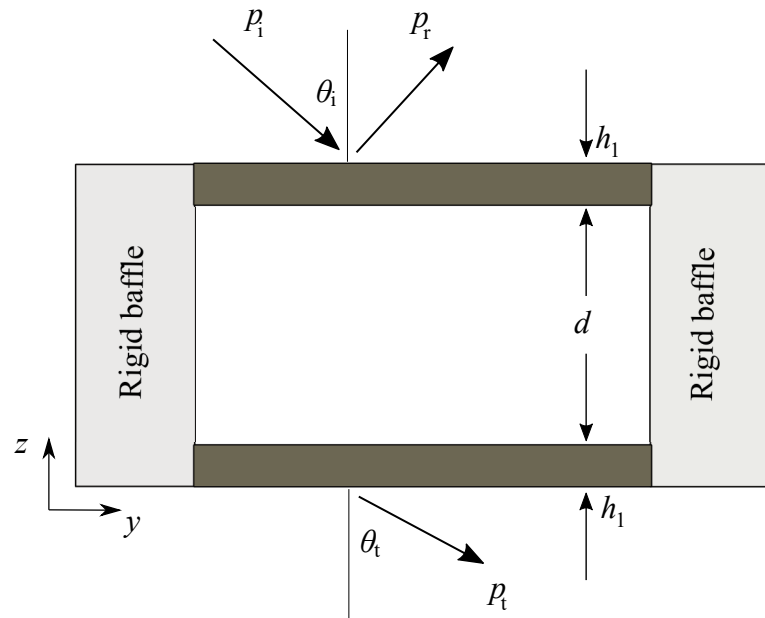


Figure 4.3: The schematic diagram of the panel used by Xin & Lu (2009).

### 4.3 Model verification

It is hard to find in the available literature some experiment data or theoretical results corresponding to the exact clamped panel considered here, i.e. double-leaf panels with attached beams. The closest match is the panel considered by Xin & Lu (2009), a fully clamped double panel with only two plates are considered. No beams are placed

between the plates as stiffeners, and the plates are located on an infinite acoustic rigid baffle. Air is trapped inside the closed cavity formed between the plates. The schematic of the panel is shown in Fig. 4.3. The measurement data available in (Xin & Lu, 2009) is used to verify  $\mathcal{T}_L$  predicted by the model here. The test panel used by Xin & Lu (2009) was made of two identical 1 mm thick 0.3 m  $\times$  0.3 m panels with an 8 cm gap between them. The material properties of the plates and the air cavity considered are given in Table 4.2.

Table 4.2: Material and cavity properties of the double-leaf panel used by Xin & Lu (2009).

Parameters	Value
$E_1$	2700 Gpa
$\rho_1$	2700 kg/m <sup>3</sup>
$\eta$	0.01
$\rho_0$	1.21 kg/m <sup>3</sup>
$c_0$	343 m/s

The double-leaf panel considered in this thesis includes attached beams as stiffeners that give rise to multiple cavities between the two plates and the beams.  $\mathcal{T}_L$  is calculated by setting the values of  $h_b$ ,  $K$ ,  $E_b$ ,  $J$ ,  $\rho_b$  in the current model as zero, correspond to the panel used by Xin & Lu (2009). The calculated  $\mathcal{T}_L$  is then compared with the theoretical results and the measurement data shown by Xin & Lu (2009) in Fig. 4.4. Reasonably good agreement between  $\mathcal{T}_L$  predicted by the current model and the measured  $\mathcal{T}_L$  is observed except in the frequency range between 150 Hz and 300 Hz. The model predicts the 2<sup>nd</sup> dip at a different frequency compared to the measurement data, which causes the deviation in  $\mathcal{T}_L$  between 150 Hz and 300 Hz. All the remaining dips corresponding to the measurement data are well predicted by the model. The 2<sup>nd</sup> dips in the graphs correspond to  $f_0$ , which are calculated as 182 Hz according to Equation (2.56).  $f_0$  correspond[ing] to the current model, the model by Xin & Lu (2009); Daudin & Liu (2016) and the experiment are 156 Hz, 215 Hz and 215 Hz, respectively.  $f_0$  is underestimated by the

current model and is overestimated by the experiment. This indicates the values of the parameter controlling  $f_0$  may not be selected accurately while modelling.

Table 4.3:  $M_{ct}$  and number of terms in the displacements series per cavity width for four clamped panels

Freq band	1.2 m × 1.2 m		1.8 m × 1.8 m		2.4 m × 2.4 m		3 m × 3 m	
	$M_{ct}$	$N_p$	$M_{ct}$	$N_p$	$M_{ct}$	$N_p$	$M_{ct}$	$N_p$
20	0	4	0	4	0	4	1	4
25	0	4	0	4	2	4	1	4
31.5	1	4	1	4	1	4	2	4
40	0	4	1	4	1	4	3	4
50	0	4	1	4	2	4	3	4
63	1	4	1	4	3	4	4	4
80	0	4	3	4	3	4	5	4
100	2	4	2	4	4	4	8	4
125	1	4	2	4	6	4	9	4
160	1	4	4	4	7	4	11	4
200	2	4	5	4	9	4	14	4
250	3	4	7	4	11	4	17	4
315	3	4	7	4	16	4	24	4
400	4	4	11	4	16	4	29	4
500	6	4	13	4	24	6	36	6
630	7	6	16	6	29	6	47	6
800	9	6	20	6	38	6	58	6
1000	11	6	26	6	47	6	77	6
1250	16	8	34	8	60	8	90	8
1600	16	8	42	8	75	8	120	8
2000	24	10	52	10	96	10	150	10
2500	29	10	68	10	122	10	190	10
3150	38	12	85	12	152	12	240	12
4000	47	12	108	12	193	13	297	13
5000	53	14	120	14	215	14	340	14

The vibrations of the plates radiate sound to both sides of the panels and thus reactions are experienced from both sides. These reactions were considered by Xin & Lu (2009); Daudin & Liu (2016) but are ignored in the current thesis. The current model is focused on the building industry, where thicker panels attached with beams are used. Neglecting the fluid loading is not expected to have significant effects on overall

$\mathcal{T}_L$  (Roussos, 1984). Ignoring the reaction pressures is the only significant difference between the modelling approach adopted by Xin & Lu (2009); Daudin & Liu (2016) and the author. This difference in modelling the reaction pressure (due to sound radiation), may add to the discrepancy near  $f_0$ .  $f_0$  also depends on  $\theta$ , i.e. the trace of the incident wave, and one possible parameter that controls  $f_0$  is the pressure field in the incident side. This further indicates the influence of ignoring the reaction pressures on  $f_0$  in this context.

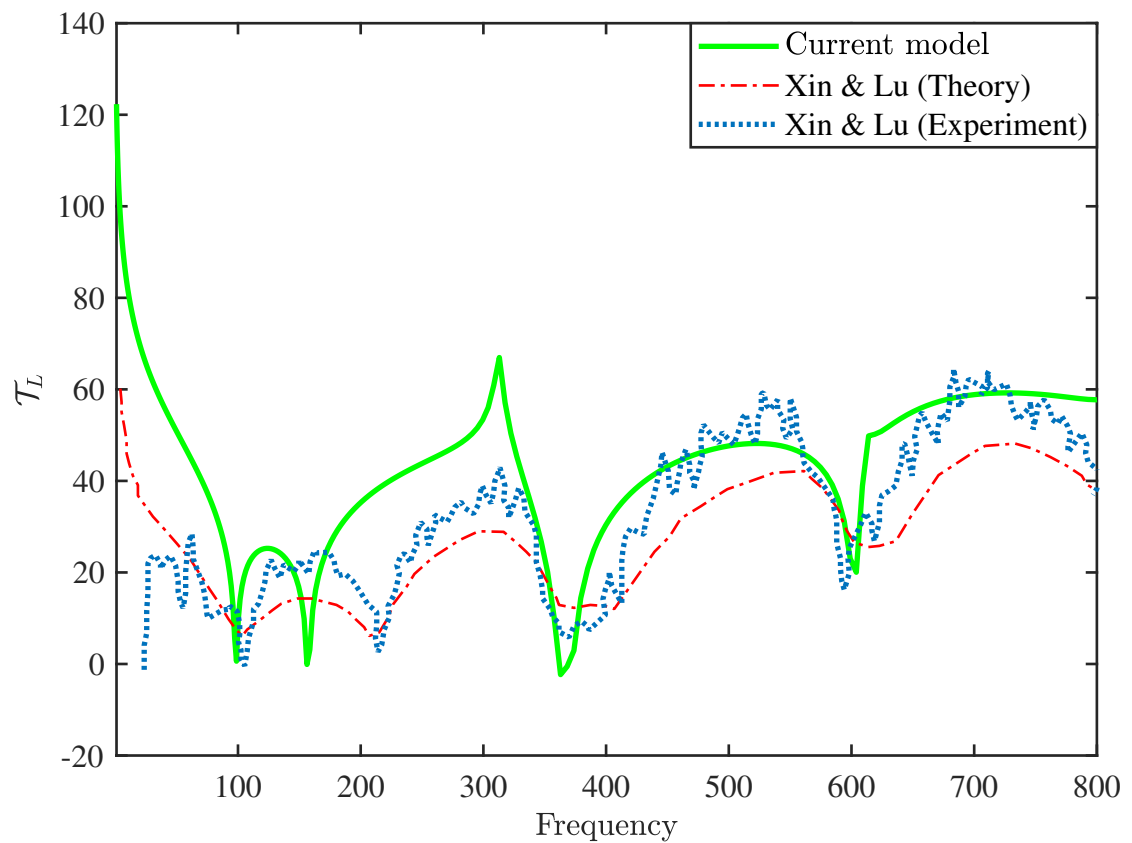


Figure 4.4: Comparison of  $\mathcal{T}_L$  with the measured data corresponding to a  $1 \text{ m} \times 1 \text{ m}$  double panel without any beam stiffener.

### 4.3.1 Model consistency check

$f_1$  of each of the clamped panels is calculated in this section to check the consistency of the model. The default parameter values given in Section 3.4 are used. As shown in Section 3.6.4,  $f_1$  of a double-leaf panel without any stiffener can be calculated with reasonable accuracy using the resonance frequency equation corresponding to a single panel, and attachment of beams shifts the resonance frequency towards higher frequencies. The 1<sup>st</sup> resonance frequency corresponding to the panels without the stiffener beams are predicted using the model. These predicted resonance frequencies are then compared with the resonance frequency calculated using Equation (2.20).  $\mathcal{T}_L$  is calculated for four clamped double-leaf square panels with side lengths 1.2 m, 1.8 m, 2.4 m and 3 m; these are shown in Fig 4.5. The 1<sup>st</sup> resonance frequencies corresponding to the panels with side lengths 1.2 m, 1.8 m, 2.4 m and 3 m based on Fig 4.5 are 27.6 Hz, 12 Hz, 7 and 4.5 Hz, respectively, and according to Equation (2.20) are 34 Hz, 15 Hz, 8.5 Hz and 5.5 Hz, respectively. The corresponding values of the resonance frequencies according to Fig 4.5 and Equation (2.20) are similar, which indicates the consistency of the model. To check the consistency further, the mode shape of the 1<sup>st</sup> resonance for the  $2.4 \times 2.4$  m panel is shown in Fig. 4.6. The panel dimensions are selected randomly to show the comparison.

The author could not find any experimental data or theoretical predictions about  $\mathcal{T}_L$  for these panels under the mixed boundary conditions and therefore it was not possible to make any comparison. The  $\mathcal{T}_L$  values for the simply supported and the clamped boundary conditions are verified by the measurement data, and the same model is used for the mixed boundary conditions. It is therefore reasonable to claim that the model is equally valid for the mixed boundary conditions.

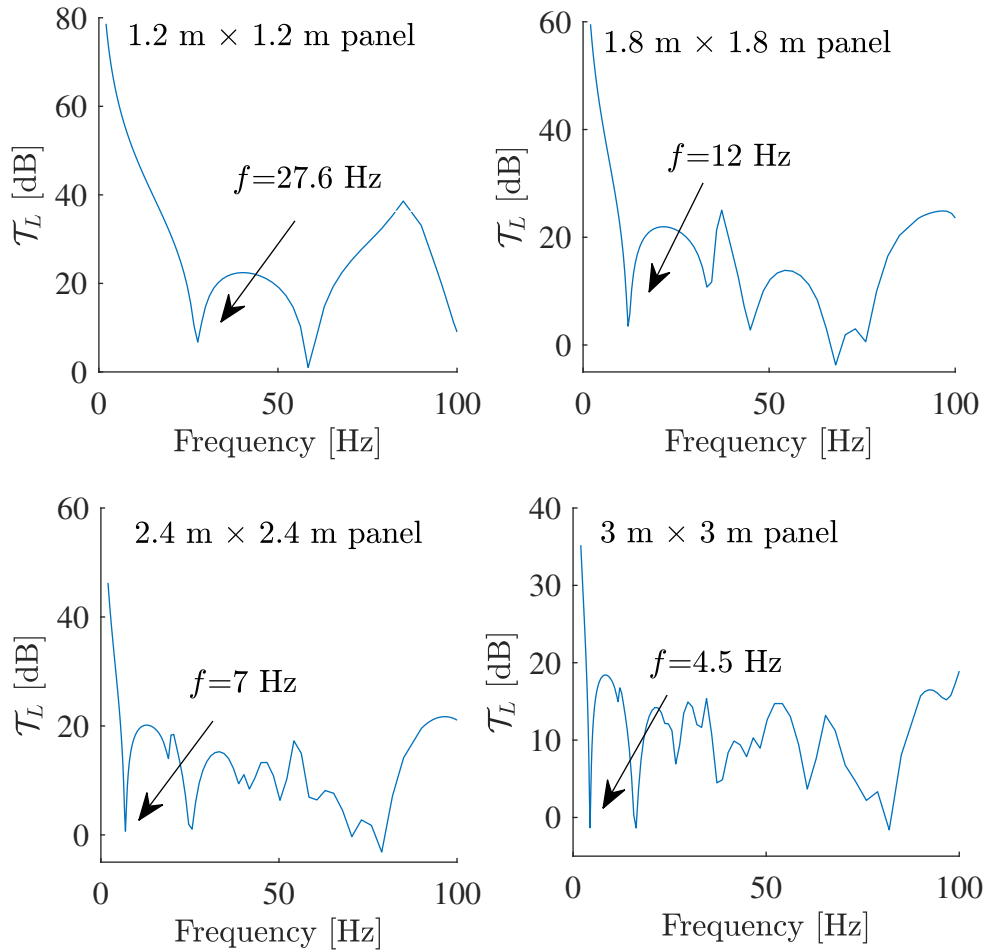


Figure 4.5: Predicated  $\mathcal{T}_L$  corresponding four sized square double-leaf panels without any beam stiffener. Material data given in Section 3.4 are used.

## 4.4 Effects of boundary conditions on different sized panels

In this section,  $\mathcal{T}_L$  is computed for different boundary conditions and the results are compared and discussed. As seen in Chapter 3, the plate vibration is strongly influenced by the structural resonances. The structural resonances are dependent on the boundary conditions and on the panel size. The effect of boundary conditions on four different sized square panels having side lengths 1.2 m, 1.8 m, 2.4 m and 3 m are discussed in

the following subsections. The results are plotted in 1/3 octave bands between 20 Hz and 5 kHz bands. In Section 4.4.3,  $\mathcal{T}_L$  is calculated at a single incident angle and is plotted against single frequency points between 20 Hz and 5 kHz to study the effect of the structural resonances at different frequency regions.

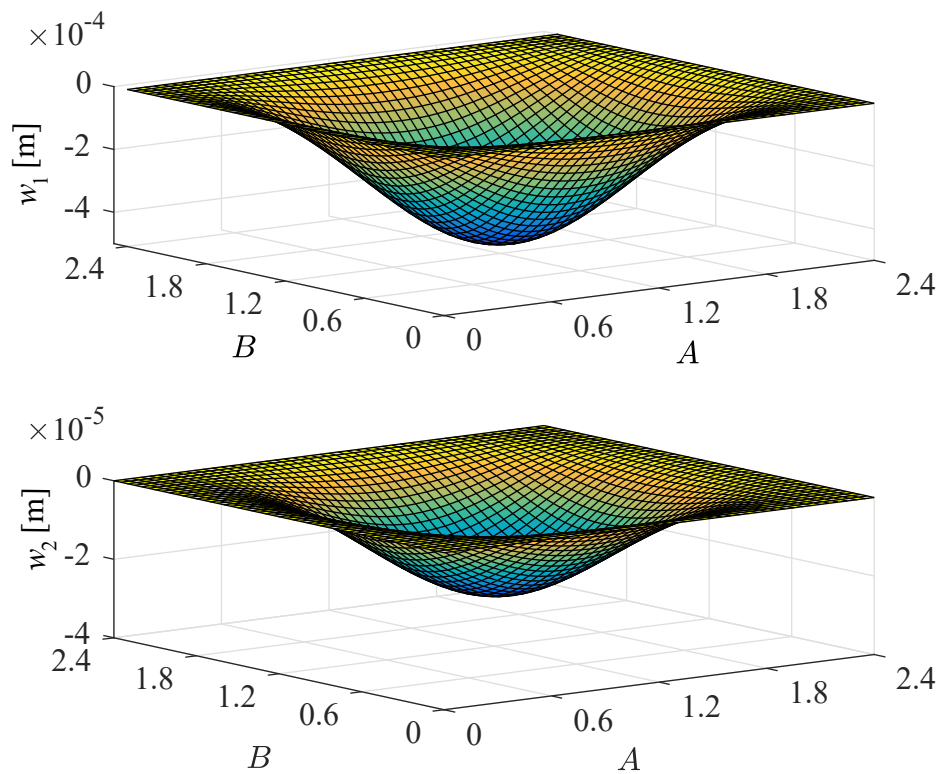


Figure 4.6: Mode shape corresponding to the 1<sup>st</sup> resonance frequency of the 2.4 m  $\times$  2.4 m clamped double-leaf panel without any beam stiffener. Material data given in Section 3.4 are used. Top and bottom graphs correspond to the mode shape of the incident and radiating plates, respectively.

#### 4.4.1 Comparison between the simply supported and clamped boundary conditions

The  $\mathcal{T}_L$  values corresponding to the simply supported and clamped boundary conditions are compared here for four sized square panels and are shown in Fig. 4.7.  $\mathcal{T}_L$  variation

is higher in the low frequency region compared to the variation in the high frequency region for all panels. Sharp dips due to the structural resonances are observed in the low frequency region for the two smallest panels corresponding to both boundary conditions. Shifting of these resonance dips due to the change in the boundary conditions is the main reason for the differences in  $\mathcal{T}_L$  in the low frequency region.  $\mathcal{T}_L$  corresponding to these two boundary conditions are similar in the higher frequency region.

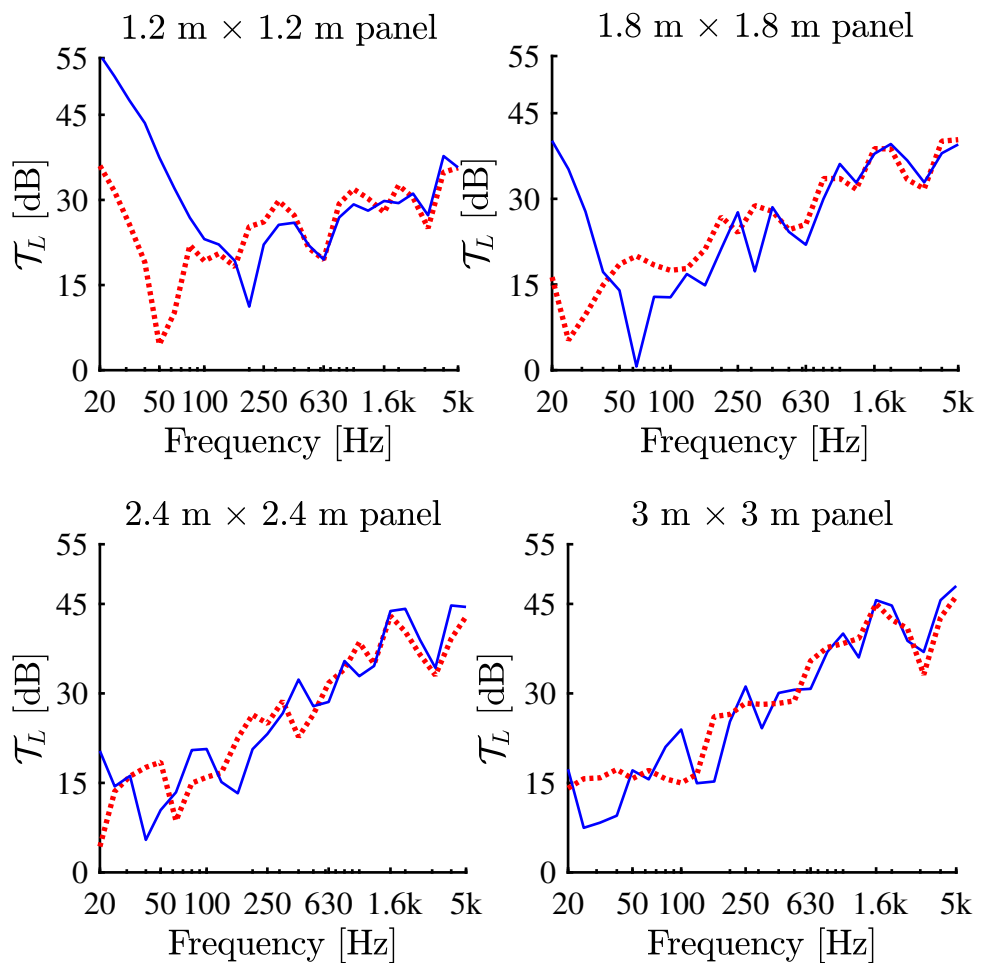


Figure 4.7:  $\mathcal{T}_L$  for different boundary conditions. Red dotted line ( $\cdots$ ) and blue solid line ( $—$ ) correspond to the simply supported and the clamped boundary conditions, respectively.

Table 4.4 shows the number of resonance modes in each frequency band corresponding to clamped and simply supported panels of four different sizes.  $M_{ct}$  are similar in

all frequency bands for both these boundary conditions for all sized panels. In the low frequency bands,  $M_{ct}$  is low and the resonance frequencies ( $f_p$ ) are widely spread and the corresponding wavelengths are also large. As a result, the shifting of  $f_p$  due to the change in boundary conditions becomes significant in the low frequency region, which is shown in Fig. 4.7. The effect is maximum for the smallest panel because of the low  $M_{ct}$  and  $f_p$  shifting. The 1<sup>st</sup> resonance of 1.2 m  $\times$  1.2 m simply supported and clamped panels fall in 50 Hz and 160 Hz bands, respectively, which contradicts the values shown in Table 4.4. This is because Table 4.4 lists the  $M_{ct}$  corresponding to single plates whereas Fig. 4.7 corresponds to the double-leaf panels with attached beams. Therefore,  $f_p$  may shift in frequencies because of the interference of the bending waves through the plates and the beams Xin & Lu (2010).

Minor differences in  $\mathcal{T}_L$  corresponding to the simply supported and the clamped boundary conditions are shown in Fig. 4.7 after a frequency band ( $f_b$ ) which depends on the panel size.  $f_b$  for 3 m  $\times$  3 m, 2.4 m  $\times$  2.4 m, 1.8 m  $\times$  1.8 m and 1.2 m  $\times$  1.2 m panels correspond to approximately 160 Hz, 500 Hz, 400 Hz and 400 Hz bands, respectively. The minor differences in  $\mathcal{T}_L$  in the higher frequencies and similarity in the  $M_{ct}$  corresponding to the simply supported and the clamped boundary conditions indicate that despite the resonance frequencies shift in the frequencies, the resonance modes corresponding to these two boundary conditions are not very different, which will be further explored in Section 4.4.3. Xin & Lu (2009) showed that the mode shape of a fully clamped and fully simply supported double-leaf panels (see Fig. 4.3) without any stiffeners are similar in case of the normal incidence, but that the mode shapes differ for oblique incidences. Figure 4.7 corresponding to the double-leaf panels considered here shows that, when the number of modes is sufficiently large in a band, the differences in the individual mode shapes corresponding to these two boundary conditions are reduced with the averaging of  $\mathcal{T}_L$ .  $f_b$  is the minimum frequency band corresponding to this case. Since the  $M_{ct}$  are higher for the larger panels, the  $\mathcal{T}_L$  values

of large simply supported panels provide good approximations of the corresponding clamped panels in the higher frequencies.

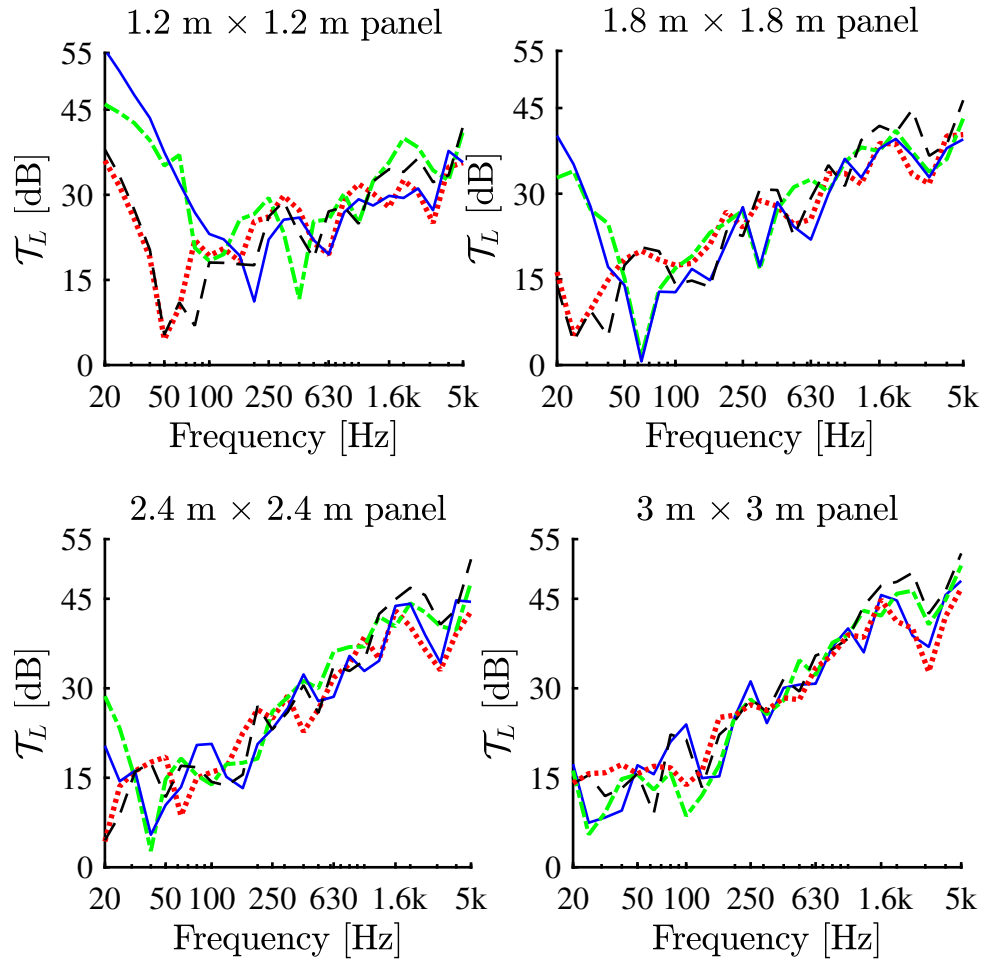


Figure 4.8:  $\mathcal{T}_L$  for different boundary conditions. Red dotted line (···), blue solid line (—), dashed line (- -) and green dash-dotted line (-.-), correspond to the simply supported, clamped, type 1 and type 2 boundary conditions, respectively.

The mode-count corresponding to  $f_b$  are 12, 25, 10, 5 for the simply supported 3 m x 3 m, 2.4 m x 2.4 m, 1.8 m x 1.8 m and 1.2 m x 1.2 m panels, respectively. These  $M_{ct}$  are based on single simply supported plates, but plates attached with beams are considered here. These  $M_{ct}$  are useful to make some comparisons between the boundary conditions. The reason that  $f_b$  is not a fixed value but varies with the panels' dimensions is because the plates' vibrations depend on many factors, such as the boundary conditions and the

resonance frequencies, which are related to the panel size. The placement of the beams is also crucial because that affects the plates' vibrations and the mode shapes. 1.2 m  $\times$  1.2 m panel has only one beam placed in the middle whilst larger panels have more beams with different configurations.

Table 4.4:  $M_{ct}$  in each band for clamped (CCCC) and simply supported (SSSS) boundary conditions.

Freq band	A=1.2m		A=1.8m		A=2.4m		A=3m	
	CCCC	SSSS	CCCC	SSSS	CCCC	SSSS	CCCC	SSSS
20	0	0	0	0	0	1	1	2
25	0	0	0	1	2	1	1	1
31.5	1	0	1	1	1	2	2	3
40	0	1	1	1	1	1	3	3
50	0	0	1	0	2	3	3	3
63	1	1	1	3	3	3	4	5
80	0	1	3	2	3	3	5	7
100	2	1	2	2	4	5	8	6
125	1	2	2	4	6	7	9	10
160	1	1	4	5	7	6	11	12
200	2	3	5	4	9	10	14	15
250	3	3	7	6	11	13	17	19
315	3	3	7	10	16	14	24	24
400	4	5	11	10	16	19	29	30
500	6	7	13	13	24	25	36	37
630	7	6	16	18	29	31	47	49
800	9	10	20	22	38	36	58	60
1000	11	13	26	27	47	50	77	75
1250	16	14	34	35	60	62	90	97
1600	16	19	42	42	75	75	120	120
2000	24	25	52	54	96	99	150	154
2500	29	31	68	71	122	123	190	189
3150	38	36	85	86	152	152	240	243
4000	47	50	108	108	193	197	297	306
5000	53	55	120	123	215	218	340	342

#### 4.4.2 Comparison between the identical and mixed boundary conditions between the edges

In this section, the  $\mathcal{T}_L$  values corresponding to the mixed boundary conditions, i.e. Type 1 and Type 2 boundary conditions, are compared with the  $\mathcal{T}_L$  values shown in the previous section. The comparison is shown in Fig. 4.8 for the same four sized square panels used in Section 4.4.1. Figure 4.8 shows that  $\mathcal{T}_L$  varies a lot with the mixed boundary conditions in all frequency bands. It is hard to find a region in the frequency where large and small variations in  $\mathcal{T}_L$  can be distinguished. This indicates that the  $M_{ct}$  and the natural frequencies corresponding to the mixed boundary conditions are significantly different from those corresponding to the other two boundary conditions. For example, the 1<sup>st</sup> resonance frequencies corresponding to the mixed boundary conditions are approximately 22 Hz, 10 Hz, 5.5 Hz and 3.5 Hz for square panels with sides 1.2 m, 1.8 m, 2.4 m and 3 m, respectively. The resonance frequencies are calculated from the non-dimensional frequency parameter listed in Table A2 in the Appendix of the paper by Leissa (1973).

The  $M_{ct}$  in the 20 Hz band for  $2.4 \times 2.4$  m panels are 2, 1 and 5 corresponding to the simply supported, clamped and mixed boundary conditions. These large differences in the natural frequencies and in the  $M_{ct}$  are the main cause of the discrepancies in the low frequency region. The differences in the resonance frequencies and in the  $M_{ct}$  are expected to be even more in the higher frequencies, which is one of the possible reasons for the differences in the higher frequencies. Similar to the resonance frequencies, the corresponding mode shapes may also vary, and this is explored in the next section. It is observed that  $\mathcal{T}_L$  increases in the case of mixed boundary conditions and this may resemble the real panels more closely. This is because, as mentioned earlier in Section 1.8, it is not possible to have the panel fully clamped or fully simply supported and the boundary conditions of the real panels are therefore a mixture of both.

### 4.4.3 Effects of structural resonances

As discussed in Section 2.9, the vibration field in a finite panel is composed of forced and resonant vibration fields and the resonant vibration is related to the boundary conditions (Brunskog, 2012). Therefore, when identical panels are subjected to different boundary conditions, it is the variation in the resonant field that causes the variation in  $\mathcal{T}_L$ . Although resonances are noticed as dips in  $\mathcal{T}_L$  curve, it is not so apparent in Fig. 4.8 because of the 1/3 octave bands average.  $\mathcal{T}_L$  is calculated from  $\tau_{\text{ave}}$ , which is the average transmission coefficient corresponding to different incident waves. Therefore,  $\mathcal{T}_L$  is calculated for single incident angles to have a closer look at the resonance effects.

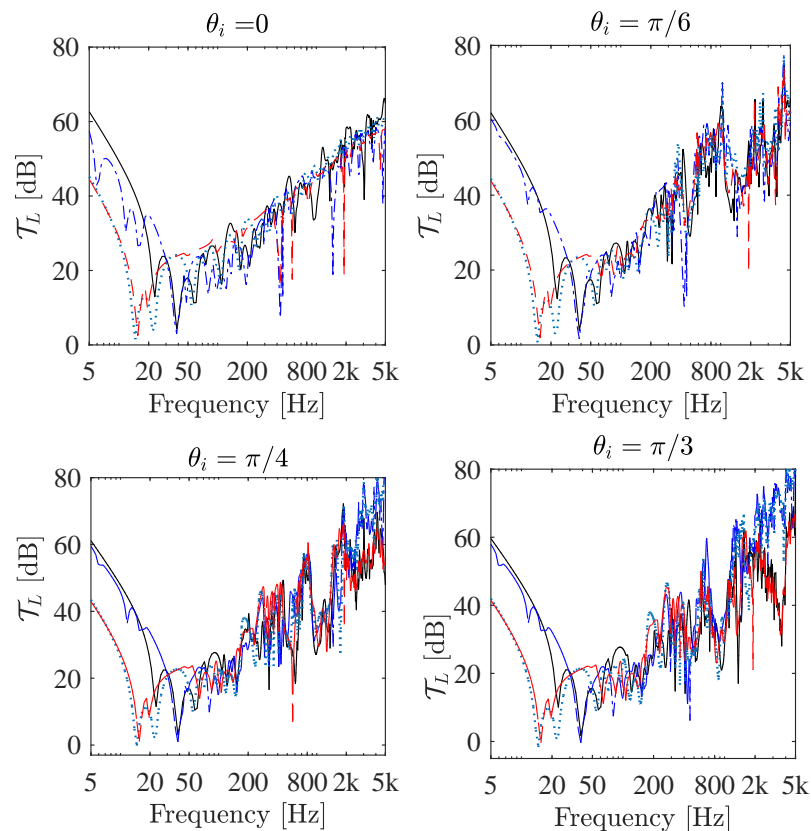


Figure 4.9:  $\mathcal{T}_L$  2.4 m  $\times$  2.4 m panel under different boundary conditions for four different  $\theta_i$ . Solid line (—), blue dashed line (- - -), blue dash-dotted line (-.-) and red solid line (—) correspond to the clamped, Type 1, Type 2 and simply supported boundary conditions, respectively.

Figure 4.9 shows  $\mathcal{T}_L$  at various boundary conditions for a 2.4 m  $\times$  2.4 m panel at four different elevation angles ( $\theta_i$ ), where the azimuth angle ( $\phi_i$ ) is kept constant at  $\pi/4$ .  $\mathcal{T}_L$  is plotted at 445 frequencies between 5 Hz and 5 kHz instead of 1/3 octave bands.

The dips due to the resonance frequencies are clearly visible in Fig 4.9. Shifting of  $f_1$  due to the change in the boundary conditions is the main reason for the large variations in the low frequency region, which is also seen in Fig. 4.8.  $\mathcal{T}_L$  corresponding to simply supported and clamped boundary conditions have distinct patterns in the low frequency region, where 1<sup>st</sup> resonance corresponding to the clamped panel occurs at a higher frequency. This is because the panel becomes more stiff with the edges clamped (Xin & Lu, 2009). Often the factor  $\sqrt{2}$  is multiplied with the plate stiffness to account for the added stiffness (Carneal & Fuller, 2004). Type 1 boundary condition exhibits resonances at  $f_1$  for both simply supported and clamped boundary conditions. Whereas, the 1<sup>st</sup> resonance corresponding to the Type 2 boundary condition occurs at a lower frequency. In general,  $\mathcal{T}_L$  pattern corresponding to the Type 1 and Type 2 boundary conditions are more similar to the simply supported and clamped boundary conditions, respectively below 100 Hz. The boundary conditions of the edges having the beams' ends, i.e. edges at  $x = 0, A$ , for the Type 1 and Type 2 boundary conditions are identical to the boundary conditions of the corresponding edges for the simply supported and clamped boundary conditions, respectively. This indicates that the mode shapes and the natural frequencies are highly influenced by the attached beams, and the boundary conditions at their ends are the most significant.

As mentioned earlier that the resonance frequency equations given in Section 2.3 correspond to a single plate. Therefore, the resonance frequencies corresponding to the panels used in this thesis can not be directly derived from those equations. Those equations are used to make a comparison between the resonance frequencies and  $M_{ct}$  corresponding to different boundary conditions. Resonances frequencies corresponding to the panels considered in this thesis are picked from dips in the  $\mathcal{T}_L$  graphs shown

in Fig. 4.9. The 1<sup>st</sup> dip corresponding to the simply supported, Type 1 and clamped boundary conditions for 2.4 m  $\times$  2.4 m panels occur at 15.5 Hz, 14.5 Hz and 23 Hz respectively. For the Type 2 boundary condition, some minor dips are noticed in the low frequency region, which does not affect or reduce the overall  $\mathcal{T}_L$  much, and also diminish with the increase in  $\theta_i$ . The 1<sup>st</sup> significant resonance corresponding to Type 2 boundary condition occurs at 38.5 Hz.

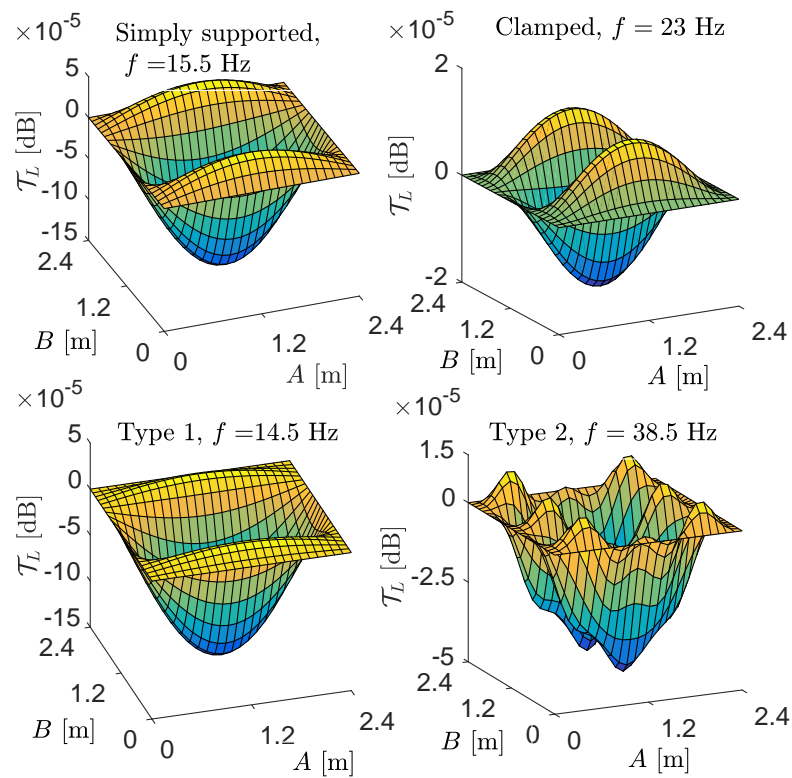


Figure 4.10: Comparison of the mode shape of the incident plate corresponding to the clamped, Type 1, Type 2 and simply supported boundary conditions.

The corresponding mode shapes of the 1<sup>st</sup> dips corresponding to the four boundary conditions are compared in Fig. 4.10. The mode shapes and the natural frequencies are similar corresponding to the simply supported and the type 1 boundary condition. This explains the similar  $\mathcal{T}_L$  for the simply supported and the type 1 boundary conditions in the low frequency region. Although the first mode shape for the clamped boundary

conditions are not very different, the difference in the natural frequency causes  $\mathcal{T}_L$  to be significantly different in the low frequency region. The mode shapes corresponding to the type 2 boundary conditions are significantly different from the remaining ones ( see Fig 4.10 ). This is one of the main reasons for the differences in  $\mathcal{T}_L$  for different boundary conditions in the low frequency region. As the frequency increases,  $M_{ct}$  in the frequency bands also increase, and the resonance frequencies come closer to each other. Another observation from Table 4.4 is that the  $M_{ct}$  for these two boundary conditions are similar in all bands. A possible explanation of similar  $\mathcal{T}_L$  values for the simply supported and the clamped boundary conditions in the higher frequencies shown in Fig. 4.7 is the similarities in  $M_{ct}$  values and the mode shapes corresponding to these two boundary conditions (see Fig. 4.10). The effects of the differences in the individual mode shapes corresponding to the simply supported and the clamped boundary conditions get reduced when averaged in 1/3 octave bands, provided that the  $M_{ct}$  are high in the frequency bands.

Figure 4.9 shows that  $\mathcal{T}_L$  corresponding to different boundary conditions follow the same increasing trend with the frequency, but dips occur at different frequencies corresponding to different boundary conditions. This variations in the resonance frequencies with the boundary conditions causes the differences in  $\mathcal{T}_L$  observed in Figure 4.8. Figure 4.9 shows that  $\mathcal{T}_L$  values corresponding to any set of boundary conditions are similar at the higher frequencies for smaller values of  $\theta_i = 0, \pi/6$ . Despite some shifting of dips, the overall  $\mathcal{T}_L$  does not vary much. Whereas, two  $\mathcal{T}_L$  graphs corresponding to the mixed boundary conditions deviate from the remaining two graphs in Fig. 4.9 corresponding to higher values of  $\theta_i$ , i.e.  $\theta_i = \pi/4, \pi/3$ . A similar observation was made by Xin & Lu (2009) regarding simply supported and clamped double-leaf 1 m  $\times$  1 m aluminium panels as shown in Fig. 4.3. Xin & Lu (2009) found that mode shapes corresponding to these two boundary conditions were similar for  $\theta_i = 0$ , which resulted in similar  $\mathcal{T}_L$  corresponding to both these boundary conditions at  $\theta_i = 0$ . The mode shapes varied at

higher values of  $\theta_i$  and resulted in significant variation in  $\mathcal{T}_L$  in the higher frequencies corresponding to both boundary conditions. Therefore, it can be deduced, based on the differences in  $\mathcal{T}_L$  observed in Fig. 4.9 for higher values of  $\theta_i$  in the higher frequencies that the variation in  $\mathcal{T}_L$  between the identical and mixed boundary conditions are due to the significant variations in the corresponding mode shapes in the higher frequencies.

## Chapter 5

### Effects of varying parameters

Lightweight double-leaf panels are used in a variety of applications and the panel design varies depending on the application. For example, the panel dimensions vary with the size of the room. The differences in the component dimensions and material properties influence the overall  $\mathcal{T}_L$ . Depending on the design objectives, the dimensions and the material properties of the double-leaf panel components need to be selected properly to keep the sound level within limits. Therefore, a double-leaf panel designed for high sound transmission differs from a double-leaf panel used for minimising the sound transmission in terms of material properties and dimensions of the panel components, which are termed as parameters. Understanding the relative influence of each parameter is crucial for making an optimum design of a double-leaf panel for a particular application. Lin & Garrelick (1977) examined the relative influence of the number of frames attached to plates on the sound pressure level and Brunskog & Hammer (2003) made a parametric study on infinite double-leaf panels. Both Brunskog & Hammer (2003); Lin & Garrelick (1977) considered infinite double-leaf panels but did not consider multiple cavities. Xin et al. (2008) used a clamped double-leaf panel without any beam and made some parametric analyses.

In this thesis, varying effects of different parameters on  $\mathcal{T}_L$  are analysed using the

modified model described in Chapter 3. The same simply supported panels described in Chapter 3 are considered here, for readers' convenience, the panel orientation and the boundary conditions are shown again in Fig. 5.1. Similar to practice in the previous chapters, the dimensions  $A$  and  $B$  correspond to the sides parallel to the beams and across the beams, respectively. To maintain the consistency with the previous chapters, sides corresponding to  $A$  and  $B$  are placed along  $x$  and  $y$  axes, respectively. The  $z$  axis lies perpendicular to the paper, where the positive direction points towards the paper. One of the contributions of this thesis is the inclusion of considering multiple cavities between the plates and the beams in the finite panel model. The effects of this improvement are analysed in Section 5.3 by comparing  $\mathcal{T}_L$  computed for two cases, (i) where a single large cavity is used and (ii) where multiple cavities are considered.  $\mathcal{T}_L$  is then compared for the four different sized square double-leaf panels ranging between  $1.2 \text{ m} \times 1.2 \text{ m}$  and  $3 \text{ m} \times 3 \text{ m}$ . Thus, the effects of considering the multiple cavities on both smaller and larger double-leaf panels are understood. The goal is to identify the frequency range and the panel dimensions at which the effect of the multiple cavities become significant. Multiple cavities are considered in all other places.

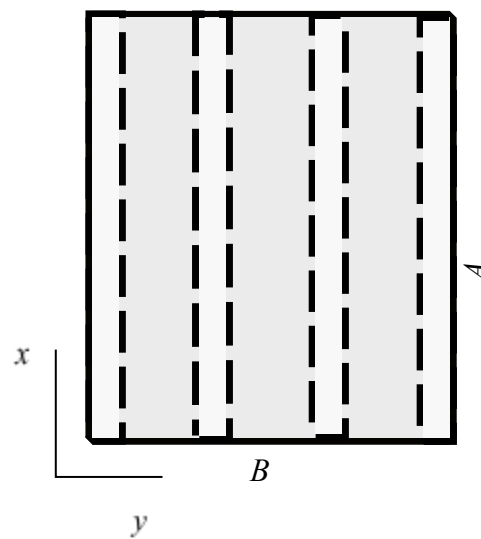


Figure 5.1: Double-leaf panel.

There are many double-leaf panel parameters and it is not possible to consider them all in this thesis. The material and geometric parameters of the double-leaf panel components, i.e. the plates and the beams, are considered in this thesis, which are  $\rho_i, E_i, h_i, d, A$  and  $B$ , where  $i = 1, 2, b$  correspond to the incident plate, the radiating plate and the beams. The effects of  $A$  and  $B$  are discussed in Section 5.2, and the effects of the remaining ten parameters of comparatively large  $3 \text{ m} \times 3 \text{ m}$  double-leaf panels are discussed in Section 5.4. Effects of  $K$  representing the coupling condition on  $\mathcal{T}_L$  are discussed in Section 5.1 by calculating  $\mathcal{T}_L$  at three different values of  $K$  for different sized double-leaf panels. The values of  $K$  selected are  $K = [7, 70, 1000] \times 10^7 \text{ Nm}^{-2}$ . The largest value of  $K = 10^{10} \text{ Nm}^{-2}$  is considerably high, which corresponds to rigid connection, and this was also used by Brunskog (2005). The two smaller values of  $K$  are randomly selected to explore the effects of  $K$ . A prior knowledge through making measurements would be helpful for accurate predictions of  $\mathcal{T}_L$ , which can be crucial for the smaller panels but no such measurements have been carried out here. Instead, the same value used by Brunskog (2005), i.e. ( $K = 10^{10} \text{ Nm}^{-2}$ ), is used throughout unless otherwise stated.

The effects of different parameter variations are understood by calculating  $\mathcal{T}_L$  at different values of the corresponding parameter. Therefore, the range of the values of different parameters needs to be set first. The range of  $K$  is mentioned earlier and the panel size varies between  $1.2 \text{ m} \times 1.2 \text{ m}$  and  $3 \text{ m} \times 3 \text{ m}$ . Catalogues of some of the panel manufacturers and the available literature are used as sources of information regarding the range of values for the ten remaining parameters. The author could not find the range of all the parameters in the catalogues, but the ranges of some parameters found in the catalogues are given in Table 5.1.

Brunskog (2002) added a section with a parametric survey in his thesis paper, where he varied each parameter by multiplying  $[0.25 \ 0.5 \ 1 \ 1.5 \ 2 \ 4]$  with their respective predetermined nominal values. which are the parameter values used in Section 3.4. The

nominal values and the corresponding ranges of various parameters used by Brunskog (2002) cover the ranges found in the catalogues. Ranges set for some parameters are unrealistic compared to actual practice because multiplying the factors  $[0.25, 4]$  often makes the range unrealistically large. For example, the range for the plate thickness would be between 3.25 mm and 52 mm, which is extremely wide for the case of building industries. Therefore, the same nominal values for different parameters considered by Brunskog (2002) are also considered but a narrower range is used in this thesis. Each parameter except the panel dimensions and  $K$  is varied by multiplying the factors  $[0.5, 1, 1.5, 2]$  by its nominal values given in section 3.4. In every case, only one parameter is varied at a time.

Table 5.1: Parameter data from the manufacturers' catalog

Manufacturer	$h_i$ (mm)		$h_b$ (mm)		$d$ (mm)		$\rho_i$ (kg/m <sup>3</sup> )	
	min	max	min	max	min	max	min	max
Gyp rock	6	16	27	68	70	140		
USG Boral	6.5	25					4.1	20.5
Kanauf	6.5	25					4.9	20.5
Gtek	6.5	25					4.5	21.9
British Gypsum	9.5	15					6.3	9.8

## 5.1 Effects of the plate-beam-plate coupling

In this section,  $\mathcal{T}_L$  is calculated for three values of  $K = [7, 70, 1000] \times 10^7 \text{ Nm}^{-2}$  for four different sized double-leaf panels. The length of all the panels is kept at  $A = 3$  m, and the width is varied as  $B = [1.2, 1.8, 2.4, 3]$  m. The beams are placed at a fixed distance of  $l = 0.6$  m and thus, the number of beams increases with the increase in  $B$ . Figure 5.2 shows that  $\mathcal{T}_L$  for all double-leaf panels remains almost unchanged for all values of  $K$  below the 250 Hz band. This further confirms that the low frequency region is mostly dominated by the boundary conditions at the edges. Above 250 Hz up to 1

kHz, there is a minor variation in  $\mathcal{T}_L$  with  $K$  for all double-leaf panels, although there is a sharp dip at 400 Hz band for the 3 m  $\times$  1.2 m and 3 m  $\times$  1.8 m panels, which may have occurred due to the triggering of structural resonances in this frequency band. The effect of  $K$  is significant in the frequency region above 1 kHz band. Fig. 5.2 shows that above 1 kHz band,  $\mathcal{T}_L$  is maximum for the smallest value of  $K$ , and it decreases with an increase in  $K$  for all double-leaf panels. This is because a high value of  $K$  corresponds to a rigid connection and the beams act as efficient sound bridges. In this case, the vibration propagates from the incident plate to the radiating plate through the beams without much loss. For lower values of  $K$ , the coupling is comparatively loose and each plate can vibrate more independently causing better vibration isolation. The spring makes the system behave as a mass-spring-mass system, where both masses vibrate in harmony in the lower frequencies but at the higher frequencies, vibrations of both masses get isolated. The degree of vibration isolation depends on the  $K$  value, which causes significant variations of  $\mathcal{T}_L$  with  $K$  for the higher frequencies.

Another observation is that  $\mathcal{T}_L$  converges with  $K$  for the largest double-leaf panel in the high frequency region. This indicates that after a certain value of  $K$  the connections correspond to almost rigid, and further increase in  $K$  does not significantly increase the rigidity of the connection. This is only true for the largest double-leaf panel, and for the smaller panels, does not show the converging tendency in the higher frequencies. This shows that the effectiveness of  $K$  in the higher frequencies above 1 kHz band depends on the panel width. Figure 5.2 shows that  $K$  is more effective above 1 kHz band for the smaller panels, causing higher variation compared to variation for the larger panels. This is counter intuitive because in the higher frequencies,  $\mathcal{T}_L$  is expected to be independent of the panel dimension. As pointed out in Section 3.2, the value of  $K$  needs to be selected so that  $\mathcal{T}_L$  best fit any relevant measurement data. Figure 5.2 shows that  $\mathcal{T}_L$  prediction can be wrong above 1 kHz if the value of  $K$  is selected randomly. Therefore, an accurate knowledge of coupling conditions is necessary for predicting  $\mathcal{T}_L$ ,

especially for comparatively smaller panels.

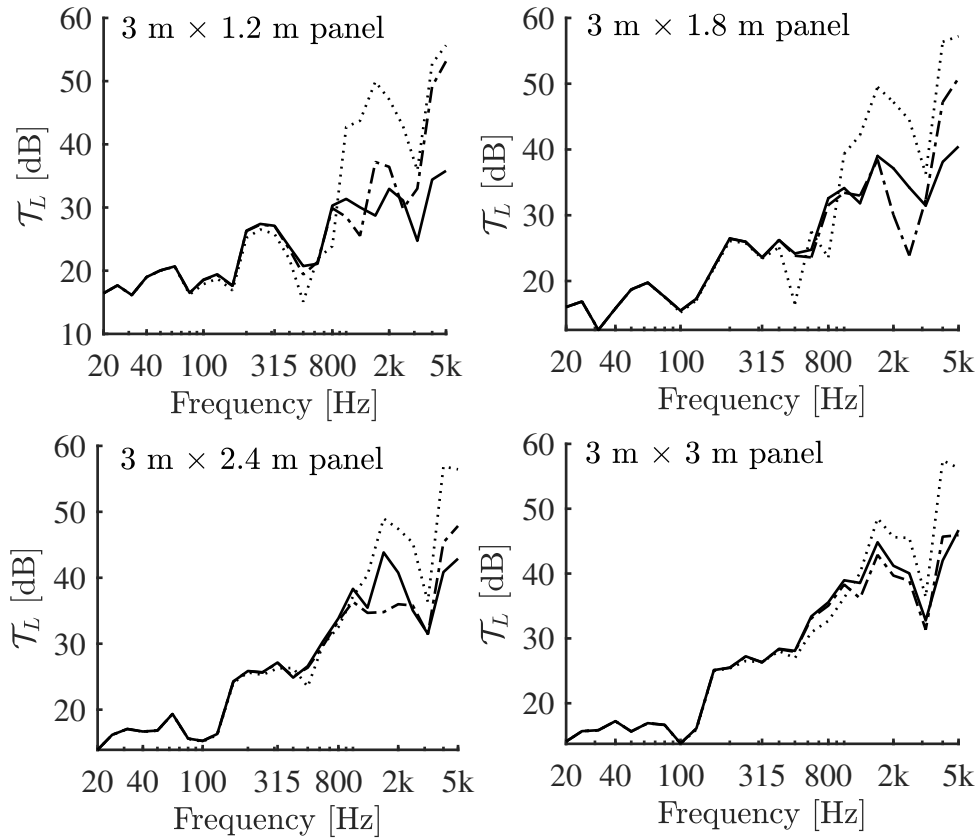


Figure 5.2:  $\mathcal{T}_L$  calculated for three different  $K = [7, 70, 1000] \times 10^7 \text{ Nm}^{-2}$  for double-leaf panels with various  $B = [12, 1.8, 2.4, 3] \text{ m}$  and fixed  $A = 3 \text{ m}$ . Dotted line ( $\cdots$ ), solid line ( $\text{—}$ ) and dash-dotted lines ( $\text{--}\cdot\text{--}$ ) correspond to  $K = [7, 70, 1000] \times 10^7 \text{ Nm}^{-2}$ , respectively.

## 5.2 Effects of the dimension of the panel

The effects of the length ( $A$ ) and the width ( $B$ ) of the panel are analysed in this section.

When the panel size increases along the  $x$  direction, the number of beams remains the same but the number of beams may increase as the size along the  $y$  axis increases. In each case, the width of all the cavities is set to be  $l = 0.6 \text{ m}$ .  $\mathcal{T}_L$  is computed for various values of  $A$  and  $B$ . When  $A$  is varied and  $B$  is fixed to its nominal value  $3 \text{ m}$ , and vice versa. The effects of varying  $A$  and  $B$  are given in separate sections below.

### 5.2.1 Effect of varying panel length $A$

$\mathcal{T}_L$  characteristics of a panel is influenced by the boundary conditions and the panel parameters, for example,  $\sigma_i$ ,  $D_i$  and  $K$ . None of these panel parameters vary significantly with the variations in  $A$ . As a result, the boundary conditions act as the only significant parameter related to  $A$  variation. Therefore, variation in  $\mathcal{T}_L$  due to the variation in  $A$  are expected to be influenced highly by the boundary conditions. Figure 5.3 shows the comparison between  $\mathcal{T}_L$  computed for various values of  $A$  (length), while  $B$  (width) is fixed to its nominal value 3 m. Fig. 5.3 shows that variation in  $A$  highly affects  $\mathcal{T}_L$  in the low frequency region below the 125 Hz band, where structural resonances are dominant. An increase in  $A$  causes the fundamental resonance frequencies of these panels to decrease and to shift toward the left on the frequency axis. Since  $(M_{ct})$  is lower in the lower frequency bands, shifting in the 1st resonance frequency causes significant variations in  $\mathcal{T}_L$ , which was also noticed in Chapter 4. It is also noted in Chapter 4 that the boundary conditions at  $x = 0, A$ , where the beams' ends are located, are the most effective regarding panel resonances. This explains the large shifting of  $\mathcal{T}_L$  dips below 125 Hz band.

Above the 125 Hz band,  $\mathcal{T}_L$  follows a trend without much shifting of frequencies. As discussed in Chapter 4,  $(M_{ct})$  increase with the higher frequency bands, and the gap between the natural frequencies gradually gets narrower. It is likely that an overlap of resonance frequencies takes place in each band. This minimises the effects of shifting of individual resonance frequency when  $\mathcal{T}_L$  is averaged over 1/3 octave bands. Between the 160 Hz and 1.6 kHz bands, the level of  $\mathcal{T}_L$  increases with the decrease in  $A$ , because the boundary conditions are most significant for the smallest panels. The boundary conditions act as constraints to plates' vibrations, which gradually decreases with the increase in  $A$ . The variations in  $\mathcal{T}_L$  becomes negligible above the 1.25 kHz band. This indicates that the effect of boundary conditions become negligible even for the smallest

panel in the high frequency region above 1.25 kHz band, which agrees with the findings in Chapter 4. The boundary conditions become negligible for the three larger panels at a lower frequency band of 500 Hz. This further agrees with the findings in Chapter 4 that the larger panels are less affected by the boundary conditions. All these results indicate that the variation in  $\mathcal{T}_L$  due to the variation in panel dimension parallel to the beams is mainly related to the boundary conditions.

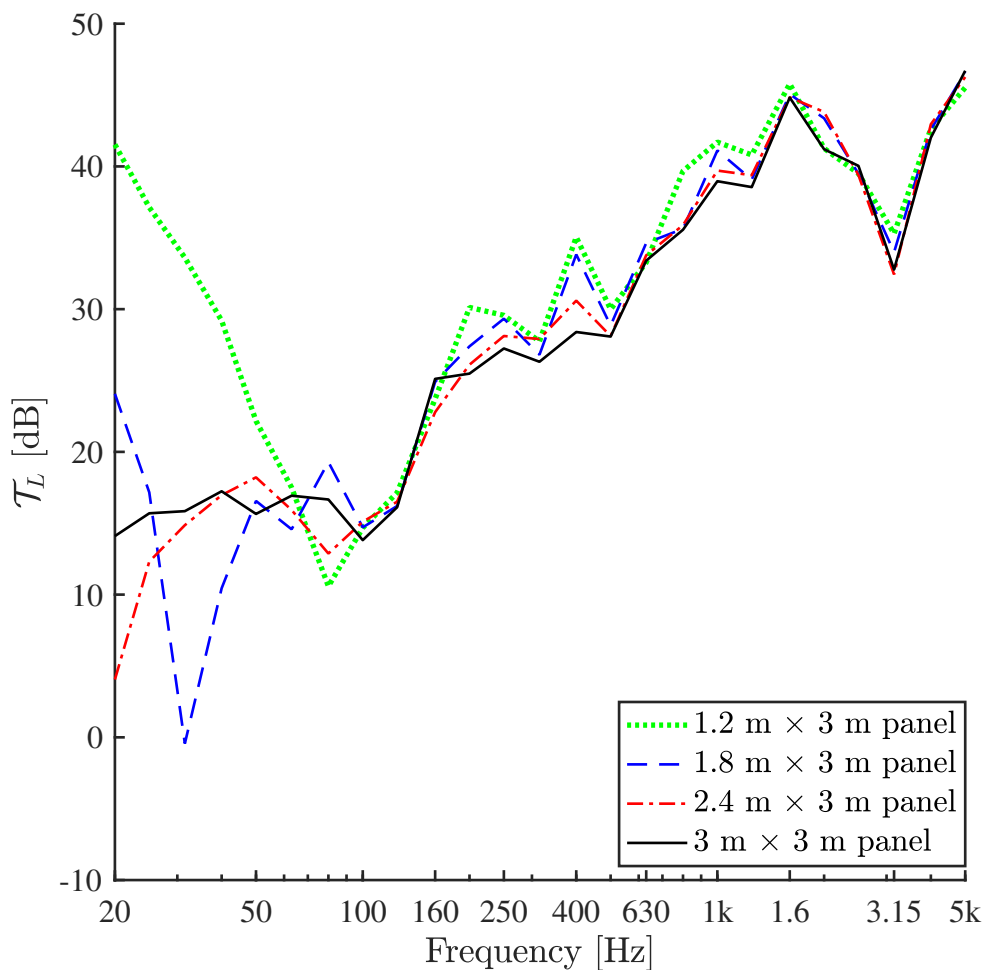


Figure 5.3:  $\mathcal{T}_L$  calculated for different panel length  $A$ , when panel width is fixed at  $B = 3$  m.

## 5.2.2 Effect of varying panel width $B$

Similar to the case for  $A$  variation, the boundary conditions are effective in this case. Likewise, variations in the panel parameters are expected to be ineffective, except for  $K$ , which is found to be highly effective above 1 kHz band in Section 5.1. The effect of varying  $B$  is analysed for three different values of  $K = [7, 70, 1000] \times 10^7 \text{ Nm}^{-2}$ , which are shown in Figs. 5.4 to 5.6, respectively. The same results shown in Fig. 5.2 are shown differently in Figs. 5.4 to 5.6, where  $\mathcal{T}_L$  is plotted against  $B$  corresponding to a fixed value of  $K$ . As noted in Section 5.1, the  $\mathcal{T}_L$  characteristics are independent of  $K$  below 250 Hz band, where boundary conditions are the most significant constraint.

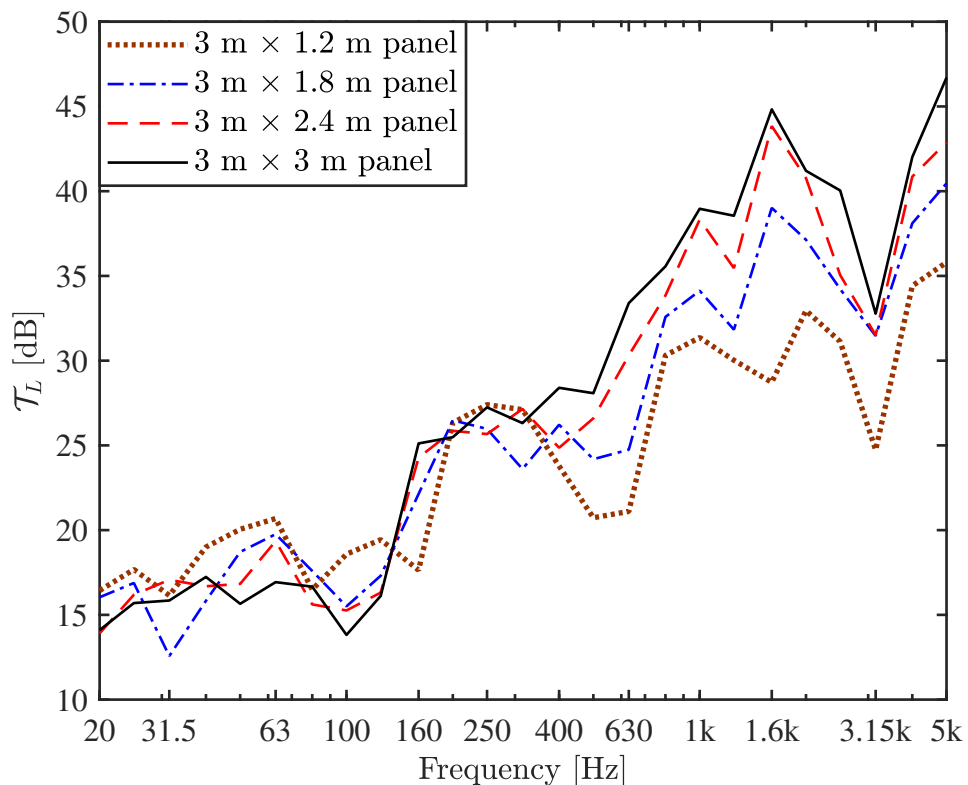


Figure 5.4:  $\mathcal{T}_L$  calculated for different panel width  $B$ , when panel length is fixed at  $A = 3 \text{ m}$  and  $K = 10^{10} \text{ Nm}^{-2}$ .

Therefore, the corresponding graphs in Figs. 5.4 to 5.6 are almost the same below

250 Hz band. Shifting of  $\mathcal{T}_L$  dips in frequencies are noticed in this frequency region, which corresponds to the occurrence of resonance at different frequencies depending on  $B$ . Variations in  $B$  do not shift the  $\mathcal{T}_L$  dips much compared to the variations in  $A$  because, as explained in Chapter 4, the boundary conditions at  $x = 0, A$ , where the beams' ends are located, are most significant regarding panel resonances.  $\mathcal{T}_L$  is maximum for the smallest panel in most frequency bands below the 250 Hz band, illustrating the maximum effects of the boundary conditions on the smaller panels.

As seen in Section 5.1, the effects of  $K$  begin to show from the 250 Hz band and become most significant above the 1 kHz band. It is also noted that variation in  $K$  does not affect  $\mathcal{T}_L$  in the same order for all sized panels. The smallest panel is affected the most by the variation in  $K$  compared to the larger panels above 1 kHz band. Figs. 5.4 to 5.6 shows that variation in  $\mathcal{T}_L$  is independent of  $B$  for  $K = 7 \times 10^{10} \text{ Nm}^{-2}$  whereas,  $\mathcal{T}_L$  varies significantly with  $B$  for higher values of  $K$ , which is counter-intuitive. This is probably because of a limitation in modelling the coupling condition. Equation (2.7) shows that a very large value of  $K$  will result in a large value of  $F_{2,j}$  even for a small difference in plates' displacements, which results in a large value for  $F_{1,j}$ . The forces exerted by the beams are mainly governed by the Euler equation, and  $K$  only controls the coupling between the beams and the plates. With a large value of  $K$ , the dominance of the Euler equation may get reduced, which may lead to incorrect solution. This is only a possibility, which is not verified in this thesis but this indicates a necessity of introducing a limiting conditions for the value of  $K$ . Therefore, the value of  $K$  needs to be selected with great care, e.g. finding the best fit to any relevant measurement data. Some prior knowledge of the coupling condition can be helpful in this regard. Otherwise, if the  $K$  value is set too high, there is a possibility of underestimating  $\mathcal{T}_L$  for the smaller panels.

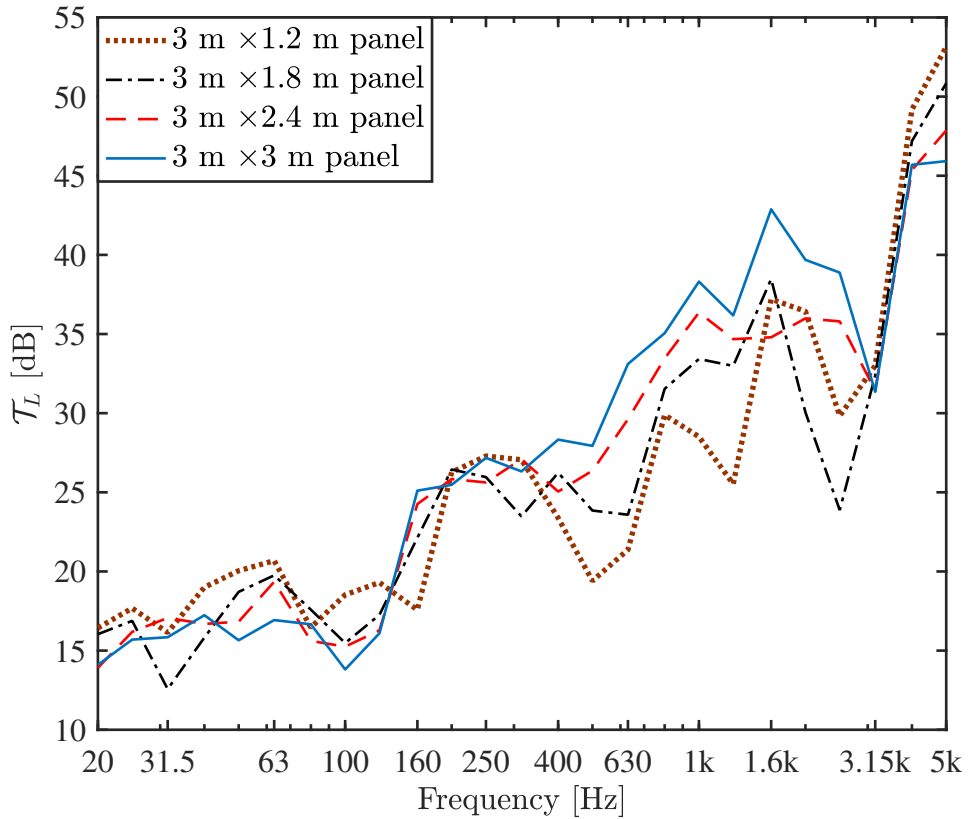


Figure 5.5:  $\mathcal{T}_L$  calculated for different panel width  $B$ , when panel length is fixed at  $A = 3$  m and  $K = 70 \times 10^7$   $\text{Nm}^{-2}$ .

### 5.3 Effect of multiple cavities

The effect of modelling multiple cavities is analysed in this section. This is done by comparing  $\mathcal{T}_L$  corresponding to two cavity conditions, 1. considering a single cavity and 2. considering multiple cavities. Beams are paced parallel to  $x$  axis, and the distance between two adjacent beams is  $l$ . For the single cavity case, a single large cavity spanning between  $y = 0$  and  $y = B$  is considered ignoring the beams. For the multiple cavity case, effect of the beams are included by considering the space between two adjacent beams as a separate cavity. The multiple cavities formed between different beams are numbered as  $j = 0, 1, 2, \dots, J$ , where the  $j^{\text{th}}$  cavity spans between  $j l$  and  $(j + 1) l$  along the  $y$  axis. For example, the  $0^{\text{th}}$  cavity spans between  $y = 0$  and  $y = l$ . The

pressure field inside the cavity/cavities is approximated differently in these two cases. When a single cavity is considered, the incident plate is treated as a single unit by the single large cavity, which results in a continuous pressure field over the entire cavity. In a similar manner, the single cavity treats the radiating plate as a single unit and transmits the sound. On the other hand, the pressure fields in each cavity are independent of each other and are discontinuous over the cavities when multiple cavities are considered. This discontinuity was also observed by Brunskog (2005). Each cavity is only affected by the vibration of the fraction of the plates attached to it.

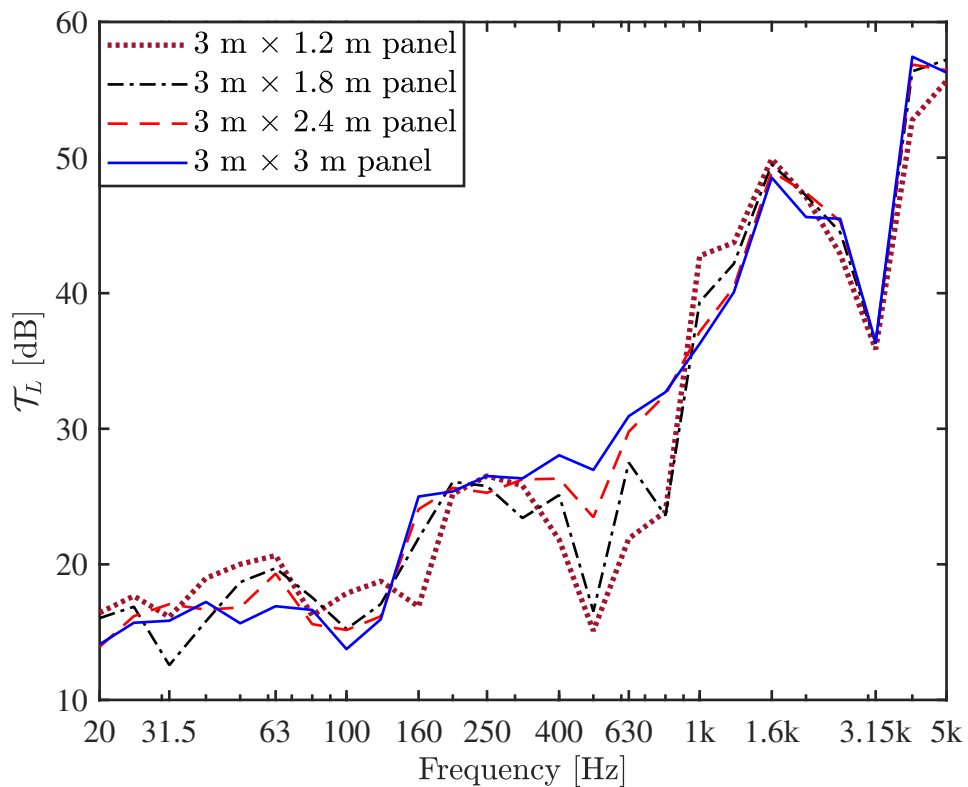


Figure 5.6:  $\mathcal{T}_L$  calculated for different panel width  $B$ , when panel length is fixed at  $A = 3$  m and  $K = 7 \times 10^7$   $\text{Nm}^{-2}$ .

To visualize the pressure fields inside the cavities,  $p_c$  is compared for 3 different conditions, 1. infinite panel, 2. finite panel with single cavity, and 3. finite panel with multiple cavities.  $3 \text{ m} \times 3 \text{ m}$  panels are considered for the finite panel model, and the

infinite panel is cut at  $x = 3$  m for making the comparison. 600 mm beam spacing ( $l$ ) is set and the default parameter values given in Section 3.4 are used in all cases. Figure 5.7 shows the pressure field inside the cavity at  $z = 0$ . Only the 0<sup>th</sup> and the 1<sup>st</sup> cavity pressure are shown for the infinite panel condition and the multiple cavity condition. Pressure in other cavities mainly differ by phase (as observed between the 0<sup>th</sup> and the 1<sup>st</sup> cavities).

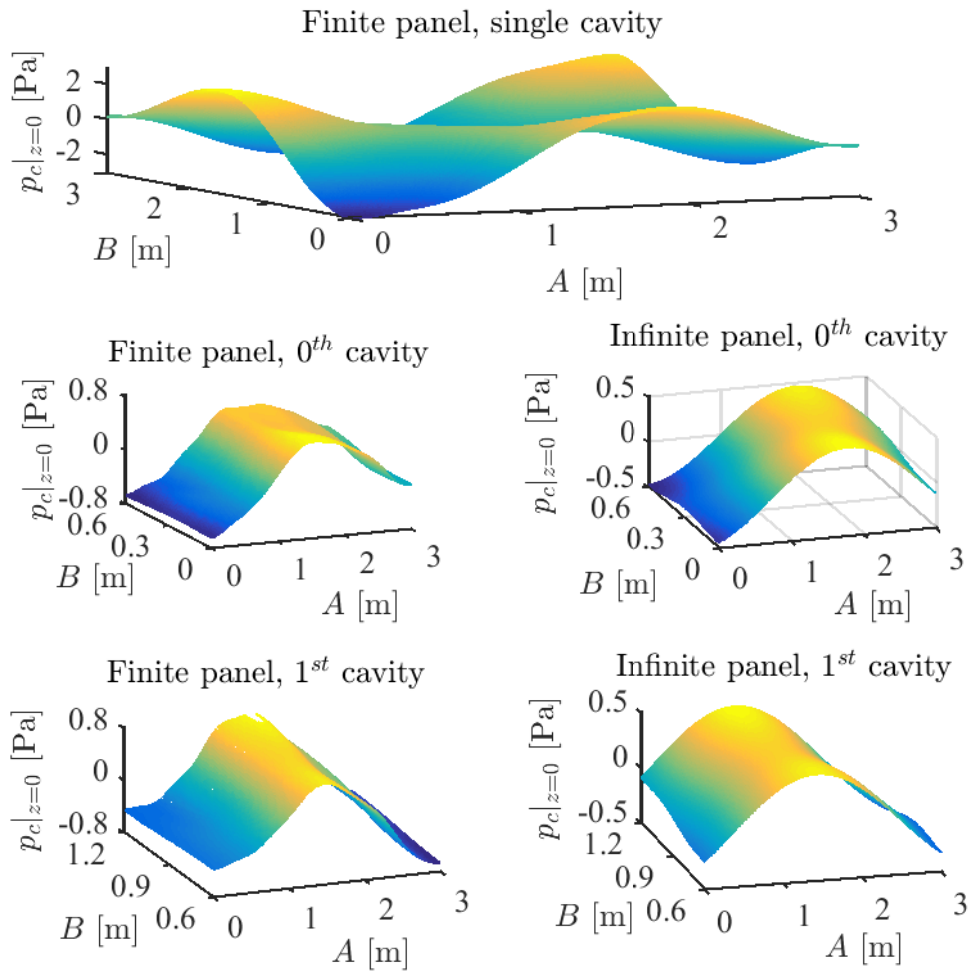


Figure 5.7:  $\mathcal{T}_L$  calculated for different finite panels and different cavity conditions. Red (—) and blue (---) lines correspond to single cavity and multiple cavities, respectively.  $\mathcal{T}_L$  is averaged in 1/3 octave bands over all incident angles.

When single cavity is considered, pressure is effected by the reflections in the boundaries in both  $x$  and  $y$  directions. The pressure field in the finite and the infinite

panels are similar because  $3\text{ m} \times 3\text{ m}$  panel is large enough to ignore the boundary effects at  $x = 0, A$  and  $y = 0, B$ , and both panels have similar cavity boundaries along the  $y$  direction. Pressure in the 0<sup>th</sup> and in the 1<sup>st</sup> cavities mainly differ by phase for both finite and infinite panels. This again shows the consistency of the model. For the frequencies having wave length much larger than  $l$ , which is the case in Fig 5.7, the pressure amplitude is higher for the single cavity case compared to the multiple cavity conditions. For wave length much larger than  $l$ , the plate vibration are easily transmitted to the pressure inside the single cavity. For simplicity, plate vibration with large wave lengths are named as global vibration. The global vibration of the plates can not transmit through the multiple cavities because of the parting of the cavities. Air between the multiple cavities (both for finite and infinite panels) become discontinuous resulting in significant reduction in the amplitude of  $p_c$  compared to the pressure amplitude in the single cavity, as noticed in Fig 5.7. As the frequency increases, the wave length of the pressure field gets reduced and becomes comparable with  $l$ . Thus, the difference in the pressure amplitude for the single and the multiple cavity conditions are expected to be minor in the higher frequencies.

$\mathcal{T}_L$  with and without multiple cavities are presented in Fig. 5.8 for four different panel sizes between  $3\text{ m} \times 1.2\text{ m}$  and  $3\text{ m} \times 3\text{ m}$ . The results are compared in 1/3 octave bands. Splitting the single cavity into multiple ones does not affect the very low frequency region below 50 Hz band. In this region, the structural modes are the dominating factor rather than transmission mechanism through the cavities. The structural resonances depend on the boundary conditions and thus the boundary conditions are the dominant factor in this low frequency region. Consideration of multiple cavities does not affect  $\mathcal{T}_L$  through the smallest  $1.2\text{ m} \times 1.2\text{ m}$  panel, since boundary conditions are more significant on the smallest panel. As the panel gets larger, the boundary effect gets reduced and gradually the effects of multiple cavities become evident. The choice of the cavity configurations is more prominent for the larger panels.

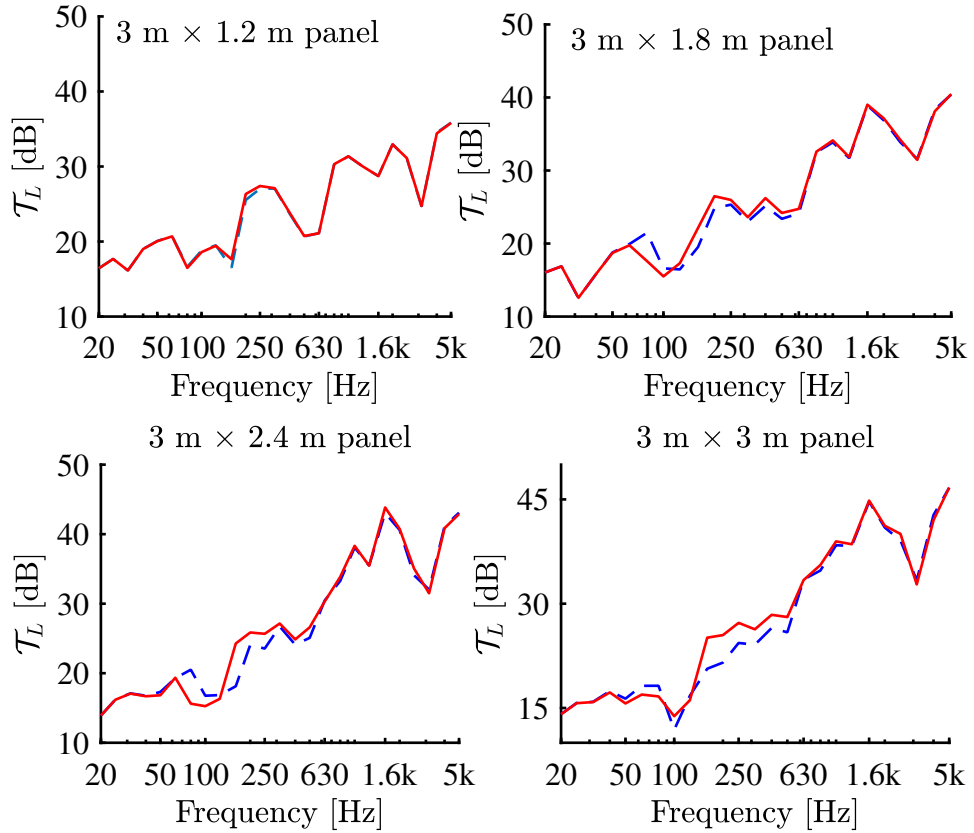


Figure 5.8:  $\mathcal{T}_L$  calculated for different finite panels and different cavity conditions. Red (—) and blue (---) lines correspond to single cavity and multiple cavities, respectively.  $\mathcal{T}_L$  is averaged in 1/3 octave bands over all incident angles.

The consideration of multiple cavities begins to have effects above 50 Hz and reduction in  $\mathcal{T}_L$  is observed near 100 Hz band. The low frequency characteristics will be discussed in more detail in the following section. After the decrease,  $\mathcal{T}_L$  increases when the multiple cavities are considered up to a certain frequency band ( $f_t$ ) depending on the panel size and, above this frequency, the differences in  $\mathcal{T}_L$  corresponding to two-cavity conditions are negligible. This is consistent with the observation in Fig 5.7.

As  $B$  increases, this range of frequency bands extends. This agrees with the findings in Chapter 4 that the boundary conditions are the main factors that govern  $\mathcal{T}_L$  for smaller panels. As long as the boundary conditions are effective, any other constraints, such as the splitting of the cavities, are insignificant.  $f_t$  divides the whole frequency region

as two, 1. below  $f_t$ , where choice of cavity conditions is significant, and 2. above  $f_t$ , where choice of cavity conditions are not significant.  $f_t$  is expected to be related to the cavity parameters, and the dependency of the  $f_t$  on  $l$  is given later in Section 5.3.3.

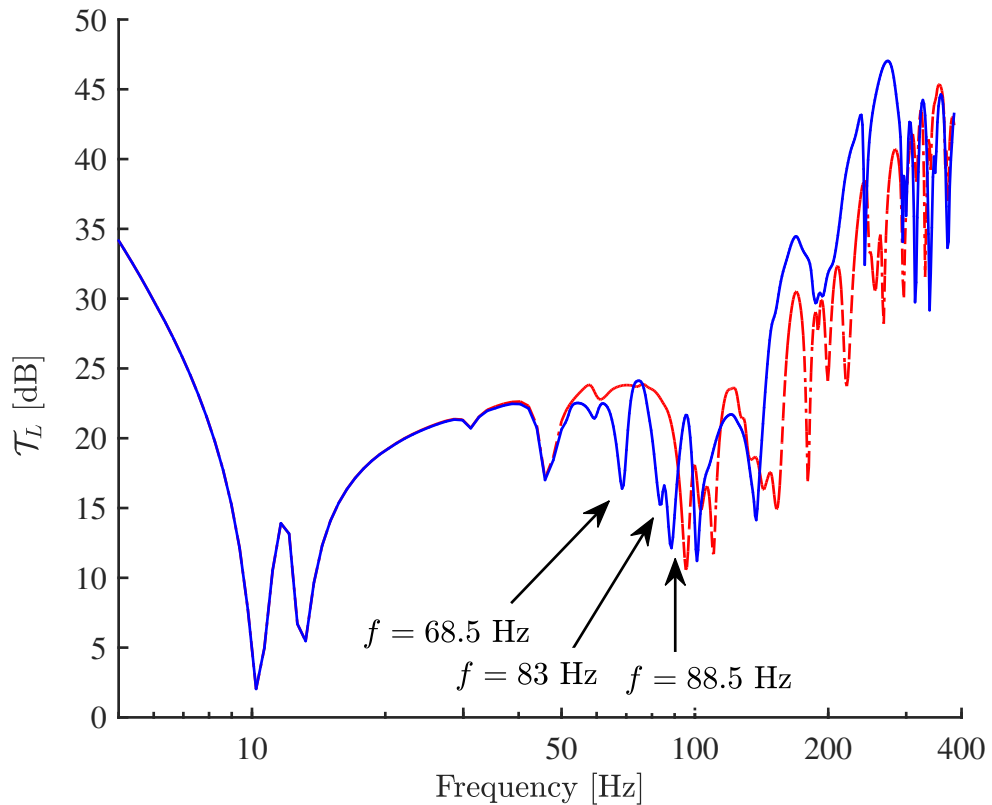


Figure 5.9: Transmission loss calculated for a  $3 \text{ m} \times 3 \text{ m}$  panel at  $\theta_i, \phi_i = \pi/4$  with (—) and without (- - -) considering multiple cavities, respectively.

### 5.3.1 Low frequency characteristics

$\mathcal{T}_L$  below 400 Hz is plotted in Fig. 5.9 for a single incident of  $\theta_i, \phi_i = \pi/4$  corresponding to a  $3 \text{ m} \times 3 \text{ m}$  panel for two cavity conditions. Between 50 Hz and close to  $f_0 = 88$  Hz, some dips show up when multiple cavities are considered, and  $\mathcal{T}_L$  decreases in this frequency region. The reason for these dips is that splitting the cavities makes the cavities independent of each other and it is possible that each cavity may undergo

resonance separately at different frequencies. Each time resonance takes place, it reduces the overall  $\mathcal{T}_L$  significantly. Figure 5.9 shows that  $\mathcal{T}_L$  dip occur at 68.5 Hz, 83 Hz and 88.5 Hz when multiple cavities are considered. The cavity pressures at  $z = 0$  for two cavity conditions are compared at 88.5 Hz, which is displayed in Fig. 5.10.

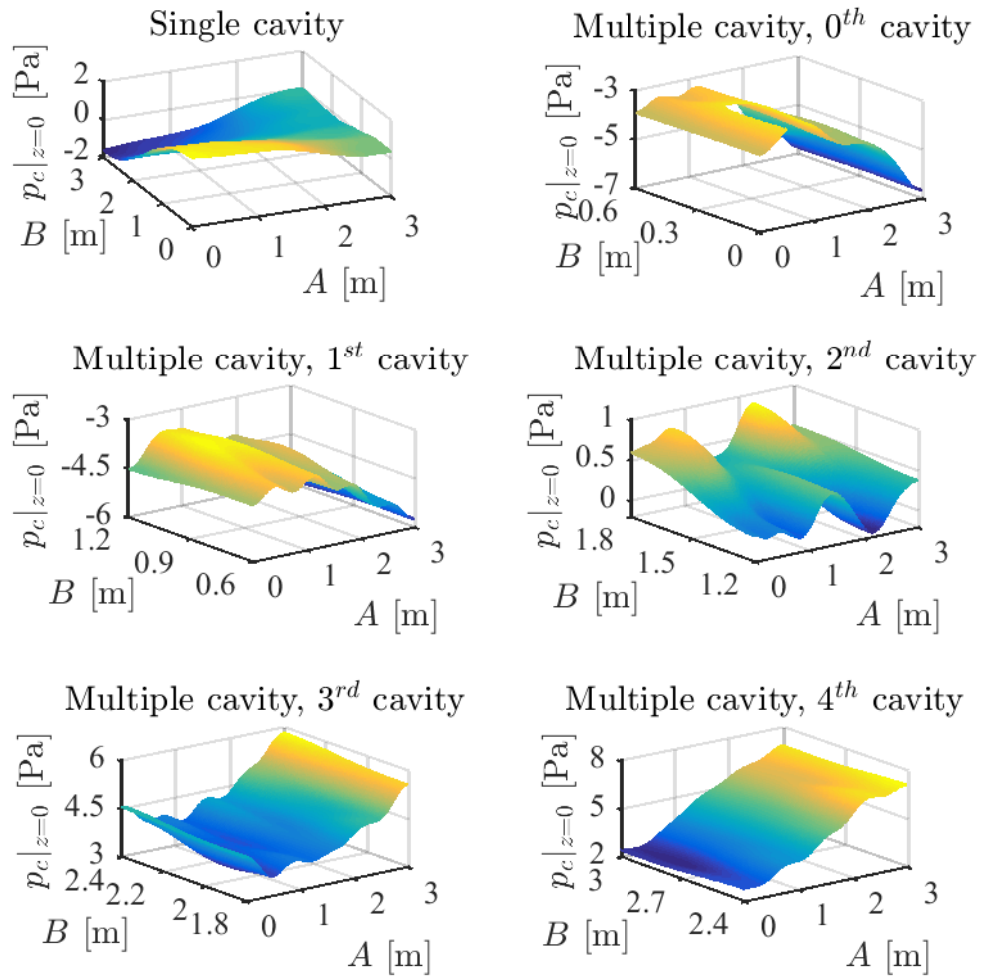


Figure 5.10: Comparison of  $\mathcal{T}_L$  for two cavity conditions at  $\theta_i, \phi_i = \pi/4$  and at  $f = 88$  Hz. Top and bottom figures correspond to the single cavity and the multiple cavity conditions, respectively.

Fig. 5.10 shows that the pressure amplitude of 0<sup>th</sup>, 1<sup>st</sup>, 3<sup>rd</sup> and 4<sup>th</sup> cavities are high (approximately 7 Pa, 6 Pa, 6 Pa and 8 Pa, respectively) at 88.5 Hz. The pressure corresponding to the single cavity case is much smaller, approximately 2 dB. This confirms that the dips near  $f_0$  are due to the local resonances of the individual cavities.

### 5.3.2 $\mathcal{T}_L$ characteristics above $f_0$

For the frequencies above  $f_0$ ,  $f_t$  divides  $\mathcal{T}_L$  graphs into two frequency regions, 1.  $f_0 < f < f_t$ , where  $\mathcal{T}_L$  corresponding to the multiple cavities is higher, and 2.  $f > f_t$ , where the difference between  $\mathcal{T}_L$  corresponding to the two-cavity conditions is negligible. The pressure inside the cavities at 180 Hz and 3 kHz are compared and plotted in Fig. 5.11 and Fig. 5.13, respectively, which corresponds to two previously mentioned frequency regions (below and above  $f_t$ , respectively). In all these figures, 3 m  $\times$  3 m panel with nominal parameter values as given in Section 3.4 is considered and a single incident wave ( $\theta_i, \phi_i = \pi/4$ ) is considered. The angles are chosen arbitrarily to demonstrate the pressure comparison between the two cavity conditions. Figure 5.11 shows the pressure inside the cavities at frequency region 1 (at 180 Hz), where the pressure inside the single cavity is continuous and the pressure for the multiple cavities are discontinuous over the cavities. The wavelength corresponding to the single cavity is comparable to the panel dimension. In this case, the panel can be considered to vibrate globally, where the vibration of any part of the panel differs from the vibration of another part by a phase. This results in similar characteristics to the pressure field inside the single cavity, through which the sound propagates to the radiating plate. Therefore, any disturbance in any part of the panel or in the cavity affects the vibration propagation.

Splitting of the single cavity into multiple cavities breaks the global effect. Each cavity now only interacts with the part of the plates attached to it. As a result, the continuity in the pressure over the cavities is broken and the pressure amplitude is reduced. Thus, the propagation of sound in this frequency region is disturbed, which results in an increase of  $\mathcal{T}_L$ . This is what is seen in Fig. 5.8, namely that  $\mathcal{T}_L$  increases in the this frequency region ( $f_0 < f < f_t$ ) when multiple cavities are considered. With the increase in frequencies, the wavelength gradually decreases and the interdependence of

the vibration of different parts of the panel reduces. As the frequency approaches  $f_t$ , the vibration of different parts no longer differ by phase only, and the panel vibration can no longer be considered as global.

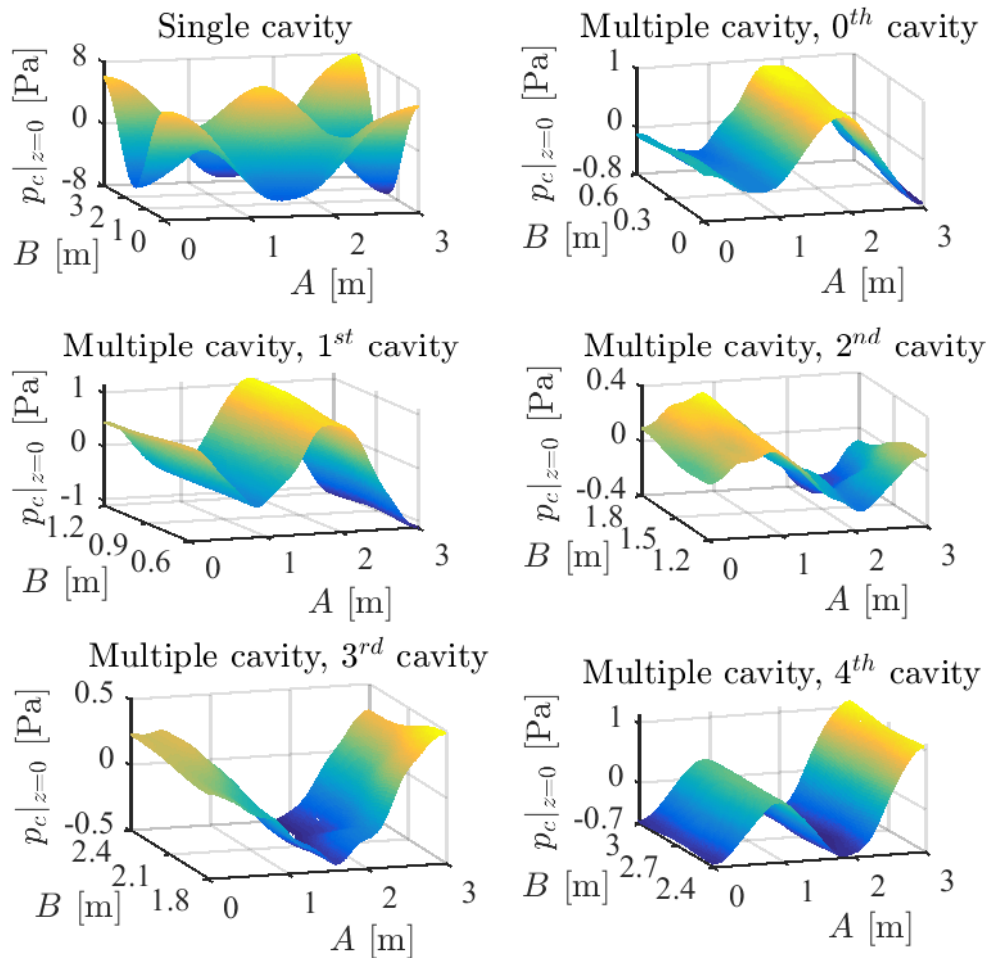


Figure 5.11: Comparison of  $p_c(x, y, 0)$  for two cavity conditions at  $\theta_i, \phi_i = \pi/4$  for 180 Hz. Top and bottom figures correspond to the single cavity and the multiple cavity conditions, respectively.

Fig. 5.12 shows the pressure comparison at 395 Hz. Although the pressures in two cavity conditions are not exactly the same, the pressure amplitudes are similar in both cases. The reason is as stated earlier that the plates tend to vibrate locally, and each part of the panel tends to vibrate independently with different amplitudes. Therefore, in the frequency region near  $f_t$  (e.g. 395 Hz), cavity pressure is largely affected by the

local characteristics of the plate vibration with a little effect of global characteristics.

Disturbance in one part does not affect the vibration of other parts significantly.

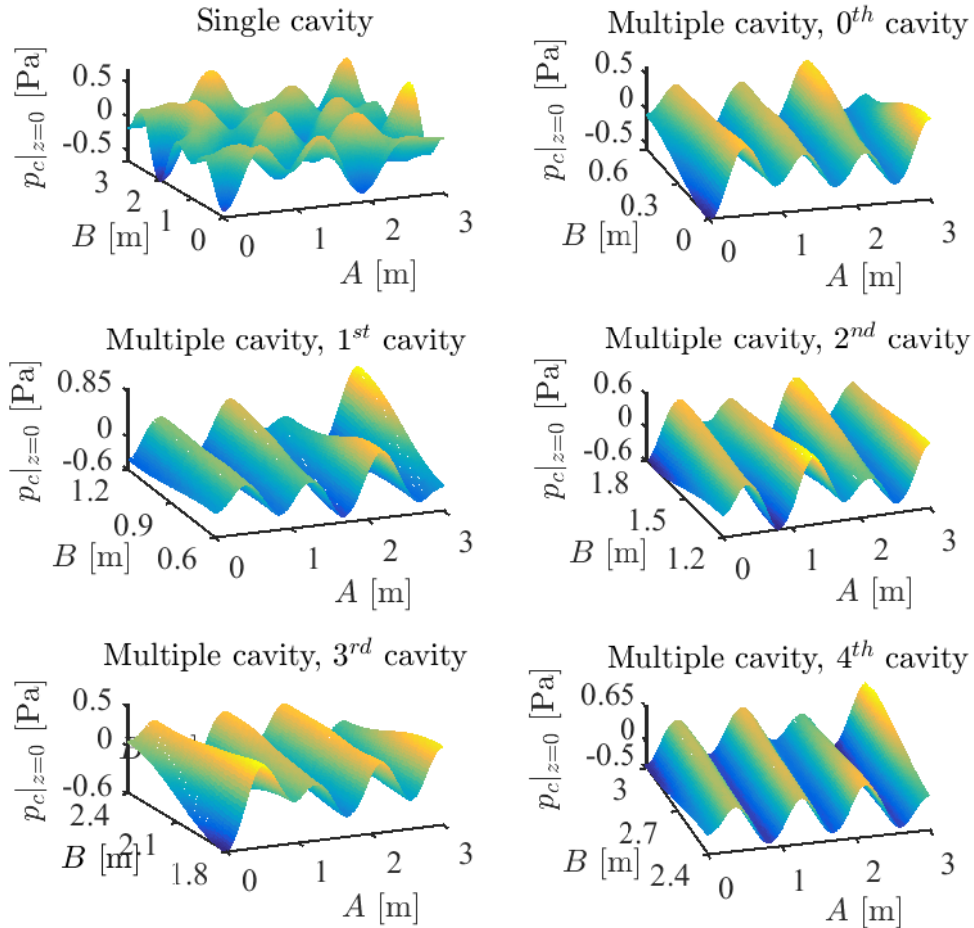


Figure 5.12: Comparison of  $p_c(x, y, 0)$  for two cavity conditions at  $\theta_i, \phi_i = \pi/4$  for 395 Hz. Top and bottom figures correspond to the single cavity and the multiple cavity conditions, respectively.

Therefore, the effects of considering multiple cavities are reduced, and differences between  $\mathcal{T}_L$  corresponding to both cavity conditions are minor near  $f_i$ . With further increases in frequency, the wavelengths become so small that the plate vibration becomes highly localised and so does the resulting cavity pressure as shown in Fig. 5.13. There remain not much correlations between the pressures in different location in the cavities for both cavity conditions. Therefore, it makes a little difference whether the sound is

propagating through a single cavity or multiple cavities. The frequency band  $f_t$ , above which a minor difference between  $\mathcal{T}_L$  corresponding to two different cavity conditions occur, is the frequency band where the plate vibration characteristics shifts from global to local. Figure 5.8 shows that the value of  $f_t$  varies with the panel width ( $B$ ), where effect is maximum for the larger 3 m  $\times$  3 m panel.

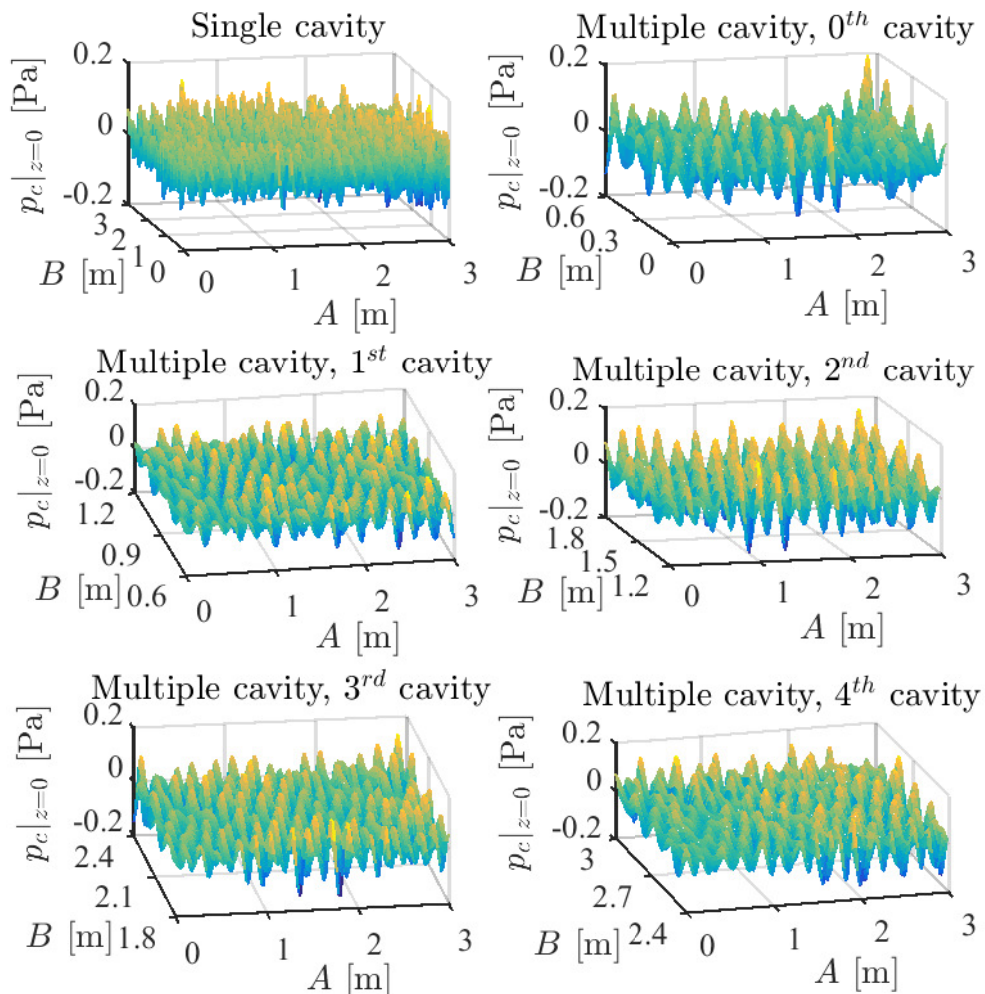


Figure 5.13: Comparison of  $p_c(x, y, 0)$  for two cavity conditions at  $\theta_i$ ,  $\phi_i = \pi/4$  for 3 kHz. Top and bottom figures correspond to the single cavity and the multiple cavity conditions, respectively.

### 5.3.3 Relationship of $f_t$ with the cavity parameter $l$

The vibration field of the plates is largely composed of the free bending waves of the panel. When a single cavity is considered, all these bending waves can propagate through the single cavity undisturbed. On the contrary, when multiple cavities are considered, the bending waves larger than  $l$  get split. A fraction of these bending waves propagates through different cavities. For the frequencies where the bending wavelength is smaller than  $l$ , splitting of the cavities does not necessarily break the propagation of these waves through the cavities. As a result, choice of the cavity conditions is not expected to make much difference to  $\mathcal{T}_L$ . Therefore, it is intuitive that  $f_t$  has some dependency on  $l$ . In this section, the relationship of  $f_t$  with  $l$  is discussed corresponding to  $3\text{ m} \times 3\text{ m}$  panels.  $\mathcal{T}_L$  is calculated to various  $l$  for  $3\text{ m} \times 3\text{ m}$  panels and are plotted in Fig. 5.14. Figure 5.14 shows that  $f_t$  occurs at different frequencies depending on  $l$ ; these are listed in Table 5.2. The corresponding values of the wavelength ( $\lambda_t$ ) and ( $l/\lambda_t$ ) ratio are also given in Table 5.2.  $f_t$  is maximum for smallest value of  $l$ , because the bending wavelength needs to be sufficiently small compared to a smaller  $l$ .

It is noticed in Table 5.2 that  $f_t$  corresponds to the frequency where the ( $l/\lambda_t$ ) ratio is greater than 2. This further indicates that the propagation of the sound waves through the cavity is not disturbed by the cavity conditions when  $\lambda_t$  is smaller than  $l$ . Table 5.2 also shows that ratio is not a fixed value, which indicates that  $f_t$  does not depend on  $l$  only and that some other constraints are also significant. For example, wavelength  $\lambda$  corresponding to  $\lambda = l/2$  for  $l = B/2 = 1.5\text{ m}$  is comparable with  $B$ . The corresponding frequency ( $f$ ) is 77 Hz, which falls in the frequency region where boundary conditions are dominant and plates' vibrations are global.  $f_t$  occurs in comparatively higher frequency (in the 160 Hz band) where  $\lambda_t$  is small enough for plates to exhibit local vibration. From Table 5.2, it can be said that  $f_t$  is expected to occur in a frequency band, where the corresponding  $\lambda_t$  is between half and one-third of  $l$ .

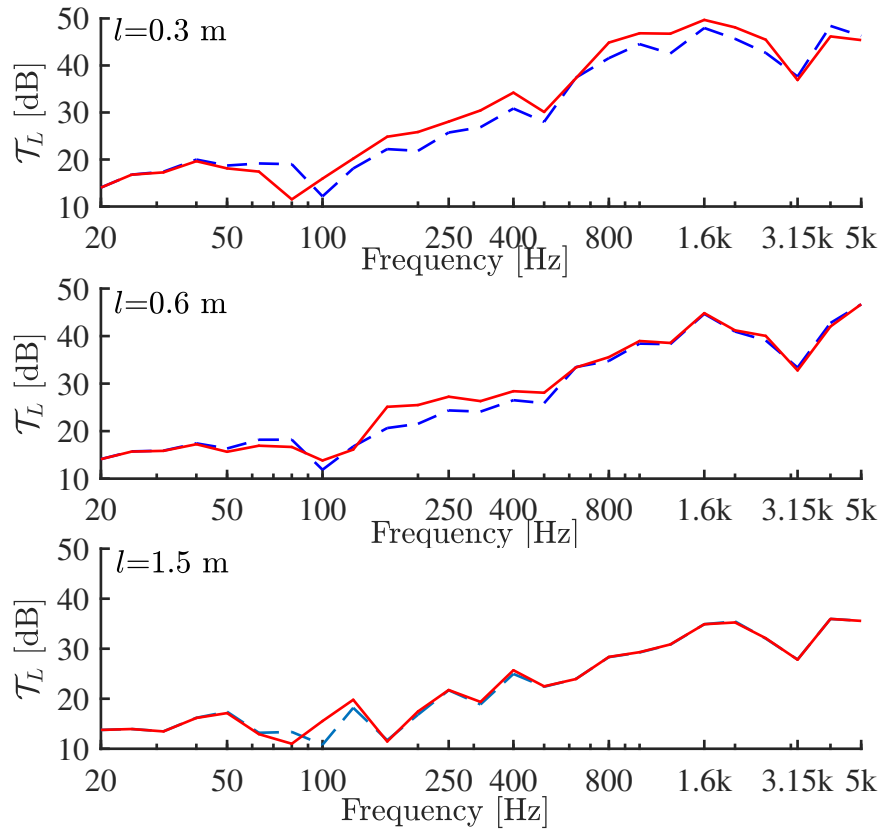


Figure 5.14: Comparison of  $\mathcal{T}_L$  for  $3 \text{ m} \times 3 \text{ m}$  panels at various  $l$  with (—) and without (---) considering multiple cavities, respectively.

## 5.4 Parametric analysis

The effects of previously mentioned ten varying parameters  $h_b, \rho_b, E_b, h_i, \rho_i, E_i$  and  $d$ , where  $i = 1, 2$ , on  $\mathcal{T}_L$  are analysed in this section for  $3 \text{ m} \times 3 \text{ m}$  panels.  $\mathcal{T}_L$  is calculated for different values of the parameters. When a single parameter is varied, the remaining parameters are assigned their respective nominal values given in Section 3.4.

Table 5.2: Ratio of  $l/\lambda_t$  at  $f_t$  for various cavity width of  $3 \text{ m} \times 3 \text{ m}$  panels

$l$	$f_t$	$\lambda_t$	$l/\lambda_t$
0.3 m	3150 Hz	0.12	2.88
0.6 m	630 Hz	0.26	2.28
1.5 m	160 Hz	0.52	2.55

As mentioned earlier, parameters are varied by multiplying the factors [0.5, 1, 1.5, 2] with the nominal values. The simply supported boundary conditions and the multiple cavities are considered throughout this section. The mass and the stiffness are two key properties of a panel structure, and  $\mathcal{T}_L$  is sensitive to variation in any of these two. The overall mass and stiffness of the double-leaf panel are both dependent on the material properties of the components. For example, any variation in plates' mass densities will vary the overall mass, and thus will affect the  $\mathcal{T}_L$ . Likewise, variation in  $h_b$  will cause the stiffness to vary and thus, affects  $\mathcal{T}_L$ . The effects of different parameters are understood in terms of the overall mass and stiffness of the double-leaf panel. Discussions on the plate parameters, the beam parameters and one cavity parameter are presented in separate subsections.

### 5.4.1 Effect of the plate parameters

In this section, the effects of both the incident and the radiating plates' parameters are discussed. Firstly, the effects of three incident plate parameters  $\rho_1$ ,  $E_1$  and  $h_1$ , are discussed. Then the effects of the corresponding radiating plate parameters are discussed. Figure 5.15 shows the comparison between  $\mathcal{T}_L$  calculated at four different values of  $\rho_1$ . As discussed earlier,  $\rho_1$  affects the panel mass positively and thus, an increase  $\rho_1$  increases  $\mathcal{T}_L$  according to the 'Mass law'. Figure 5.15 shows the increasing trend of  $\mathcal{T}_L$  with the increase of  $\rho_1$  up to the 1.2 kHz band, despite some overlap of the peaks in some frequency bands. The peaks and the dips are related to the complex structural resonances (Xin & Lu, 2009). Although the resonance peaks are more pronounced in narrow frequency bands, their presence can be noticed in the 1/3 octave bands as well. As explained in Section 2.9.2, the structural resonances occur when phase coincidence between the free reflected waves takes place. This phase coincidence depends on the free bending wave and the geometry of the plate. For a simply supported beam, the

condition for resonance is given as (Fahy, 2007)

$$\left(\frac{\omega^2 \sigma_b}{E_b I_b}\right) = \frac{n\pi}{l_b}, \quad (5.1)$$

where  $\sigma_b$  and  $l_b$  are the beam mass per unit length and length, respectively, and  $n = 1, 2, 3, \dots$ . Therefore, resonances occur at lower frequencies as the beam mass increases. This understanding is applicable to a plate as well. Therefore, with the increase of  $\rho_1$ , the resonance frequencies shift towards the lower frequencies, and this explains the peaks visible at different frequencies in Fig. 5.15.

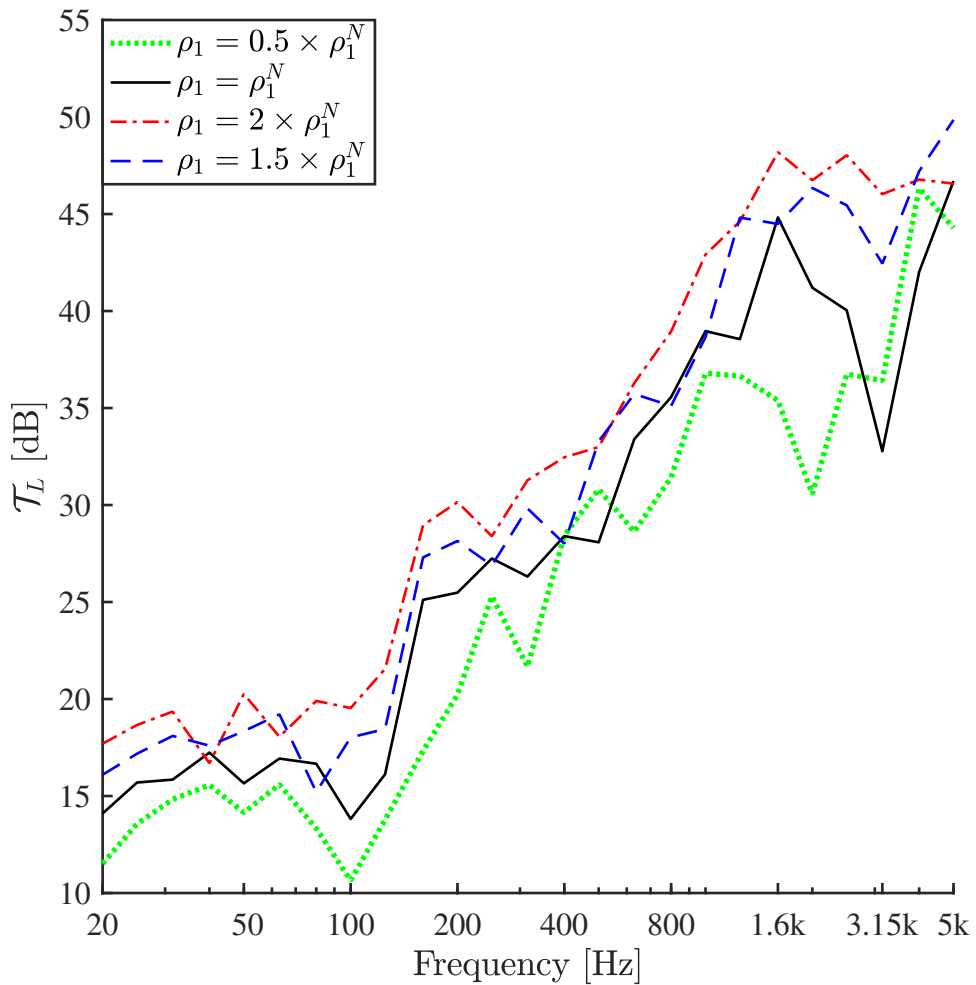


Figure 5.15: Transmission loss calculated for different  $\rho_1$ , where the nominal value  $\rho_1^N = 838.46 \text{ kg/m}^3$ .

Similarly,  $\rho_1$  affects the critical frequency, and recalling Equation (2.52), the critical frequency is

$$f_{cr} = \frac{1}{2\pi} \sqrt{\frac{m_1 c_0^4}{D_1}}.$$

As discussed in Section 3.6.2, the peak at 1.6 kHz band for  $\rho_1 = \rho_1^N$  is due to the coincidence effect and the corresponding value of  $f_{cr}$  falls in 2.5 kHz band. Equation (2.52) shows that  $f_{cr}$  increases with the increase in  $\rho_1$  i.e.  $m_1$ , which agrees with Fig. 5.15. The peaks due to the coincidence effect for  $\rho_1 = [0.5, 1.5, 2] \times \rho_1^N$  occur at the 1 kHz, 2 kHz and 2 kHz bands, respectively and the corresponding values of  $f_{cr}$  are 1.88 kHz, 3.26 kHz and 3.76 kHz, respectively. The coincidence dips for the two heaviest panels are so close that the corresponding peaks for both these panels occur in the same frequency band.

In reality, both of the plates undergo the coincidence, but it is hard to get a clear picture of the coincidence effect of the radiating plate from the graphs. This is partly because the frequency resolution is not high enough in the high frequency region. The effect of coincidence of both plates can be perceived by making a closer observation on the depth of the coincidence dips corresponding to the incident plate. A severe coincidence with a sharp dip takes place when both the plates have equal masses, i.e.  $\rho_1 = \rho_2$ . In this case, coincidence takes place at the same frequencies, and the sharp dip occur due to the superposition of the dips caused by both plates separately. For  $\rho_1 \neq \rho_2$ , coincidences for both plates take place at different frequencies and the resulting dips are not combined. In this case, the dips have depth approximately half the depth corresponding to  $\rho_1 = \rho_2$ , as shown in Fig. 5.15.  $f_{cr}$  and the corresponding peak can be pushed to higher frequencies and be kept outside the frequency range of interest by increasing the plates' densities. Therefore, it is recommended that denser plates within the limit set for lightweight plates should be used. Also it is recommended to have the plates' masses different to avoid the sharp reduction in  $\mathcal{T}_L$  at the coincidence.

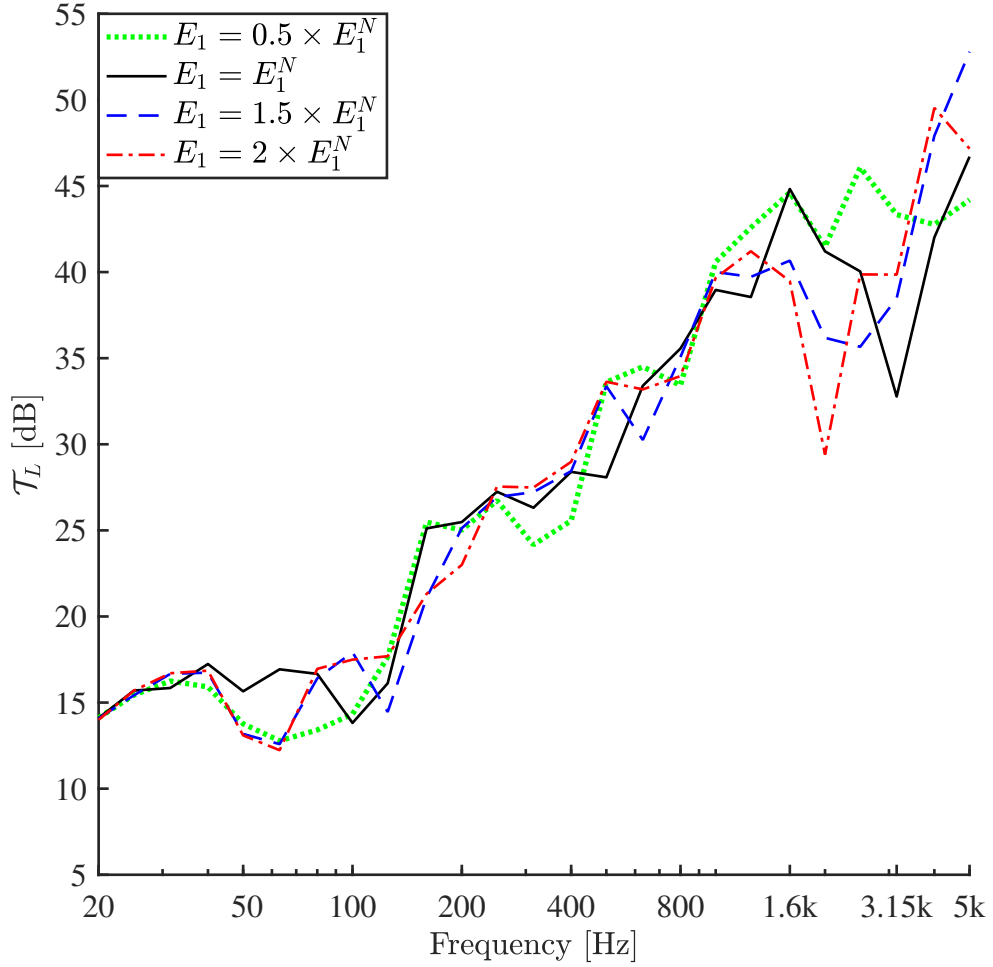


Figure 5.16: Transmission loss calculated for different  $E_1$ , where the nominal value  $E_1^N = 2.840$  GPa.

$\mathcal{T}_L$  at four different  $E_1$  values is presented in Fig. 5.16. Figure 5.16 shows that  $\mathcal{T}_L$  does not vary much with the variation in  $E_1$  at frequencies below 1 kHz band except between the 50 Hz and 100 Hz bands. As discussed in Section 2.9.1,  $\mathcal{T}_L$  below  $f_{cr}$  mainly follows the mass. Since  $E_1$  contributes solely to  $D_1$  without any contribution to  $\sigma_1$ ,  $\mathcal{T}_L$  does not vary much with  $E_1$  below  $f_{cr}$ , which is observed in Fig. 5.16.  $E_1$  also affects the resonance and coincidence, and this explains the shifting of some peaks in frequencies below 1 kHz band in Fig. 5.16. Shifting of the resonance and coincidence frequencies are the primary reason for some variations in  $\mathcal{T}_L$  in some frequency bands.

For example, between the 50 Hz and 100 Hz bands. ( $M_{ct}$ ) in the lower frequency bands are fewer and the resonance frequencies are widely spread. This makes the shifting of the frequencies more prominent in these low frequency bands.

The coincidences occur above 1 kHz band, and significant variations in  $\mathcal{T}_L$  is observed because of the shifting of the coincidence peaks. From Equation (5.1), it can be deduced that the effect of  $E_1$  to structural resonances is opposite to the effects of  $\rho_1$ , i.e. structural resonance frequencies increase with the increase in  $E_1$ . Increasing  $E_1$  contributes to an increase of  $D_1$ , which causes the coincidence to take place at lower frequencies. The peak at 1.6 kHz band, corresponding to  $E_1 = E_N$ , shifts towards lower frequencies with the increase in  $E_1$ . Similar to Fig. 5.15, the coincidence effect of the lower plate can be perceived from the depth of the coincidence dips. The depth of the dip corresponding to  $E_1 = E_2$  is the largest compared to the others, although the dip for  $E_1 = 2E_1^N$  is of equal depth. The possible explanation for this large dip for  $E_1 = 2E_1^N$  is that the coincidence occurred at one of the natural frequencies. Unlike  $\rho_1$ , the material with lower Young's modulus is preferable for a panel so that  $f_{cr}$  is pushed outside of the frequency range of interest.

Figure 5.17 shows  $\mathcal{T}_L$  calculated for four different  $h_1$ .  $h_1$  affects both  $\sigma_1$  and  $D_1$ . Therefore, variation in  $h_1$  has the combined effects of variations in  $\sigma_1$  and  $D_1$ . Variation in  $\sigma_1$  increases  $\mathcal{T}_L$  according to the mass law, and also decreases the resonance frequencies and increases  $f_{cr}$ . On the other hand,  $D_1$  increases the panel stiffness, which increases the resonance frequencies and decreases  $f_{cr}$ . These variations in the resonance frequencies and  $f_{cr}$  due to the variations in  $\rho_1$  and  $E_1$  explain the peaks and dips arising at different frequencies depending on  $h_1$ .

Figure 5.17 shows that  $\mathcal{T}_L$  increases with the increase in  $h_1$  in the lower frequencies, and agrees with the mass law.  $\mathcal{T}_L$  for  $h_1 = 2 \times h_1^N$  is 10 dB more than  $\mathcal{T}_L$  for  $h_1 = 0.5 \times h_1^N$  at the 100 Hz band. This difference gradually decreases with the increase in frequency until 1 kHz band. The effectiveness of stiffness in the higher frequencies is the reason

for this decrease. Similar to Fig. 5.15 and Fig. 5.16, the graphs overlap and thus lose their trend above 1 kHz band because of shifting of  $f_{cr}$ . Since  $\mathcal{T}_L$  corresponding to the thickest panel is maximum until the 800 Hz band despite some overlap in few bands, it is desirable to have the plate as thick as possible without making the panel too heavy.

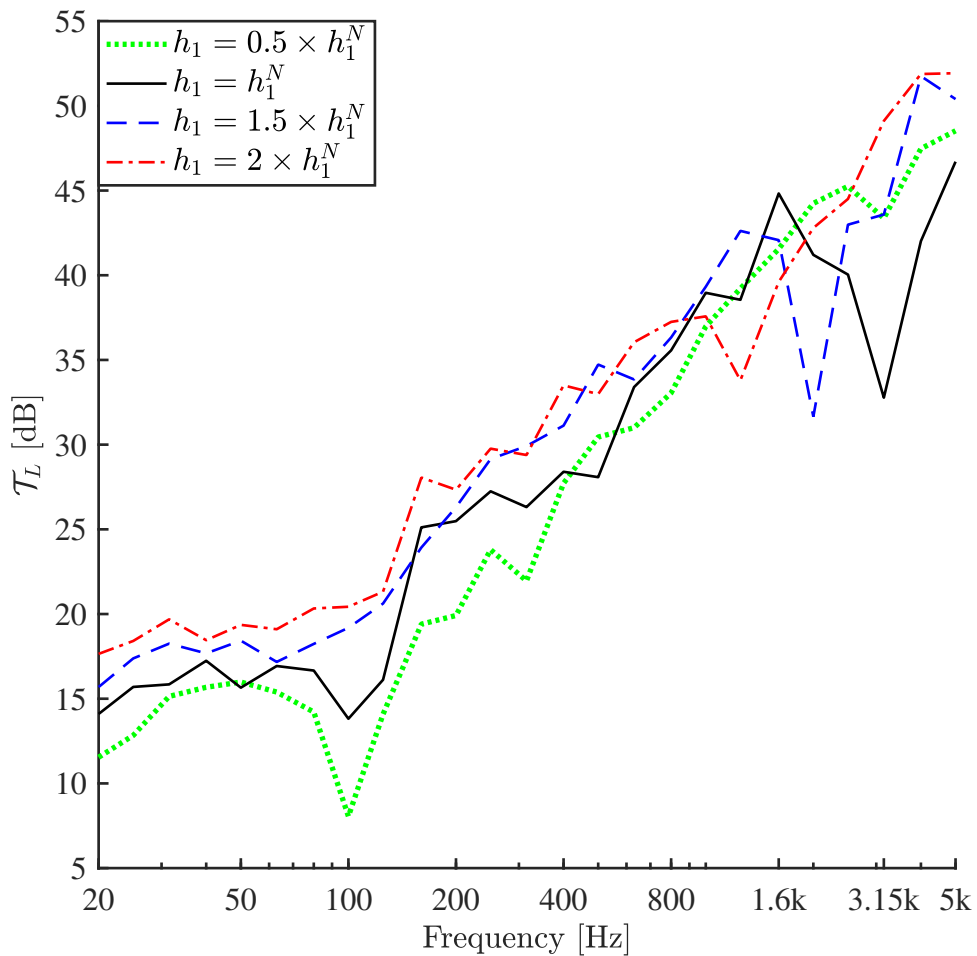


Figure 5.17: Transmission loss calculated for different  $h_1$ , where the nominal value  $h_1^N = 0.013$  m.

Figure 5.18 shows the comparison of  $\mathcal{T}_L$  at four different  $\rho_2$ . The effect of  $\rho_2$  on  $\mathcal{T}_L$  is almost identical to the effect of  $\rho_1$  up to the 1 kHz band.  $\mathcal{T}_L$  increases with the increase in  $\rho_2$ , in accordance with the mass law. The peaks are noticed at different frequencies depending on  $\rho_2$ , which is the case for  $\rho_1$  as well, as is shown in Fig. 5.15.

The peak due to coincidence shifts with the variation in  $\rho_1$  in Fig. 5.15, whereas in Fig. 5.18, the maximum  $\mathcal{T}_L$  occurs at the 1.6 kHz band for all values of  $\rho_2$ . Similar to Fig. 5.15, here also the coincidence effect of the radiating plate is not clearly visible. Like before, the effect of the coincidence of the radiating plate can be perceived by observing the comparatively shallow dips for  $\rho_2 \neq \rho_2^N$ . This is the main cause of the difference between Fig. 5.15 and Fig. 5.18 above 1 kHz band.

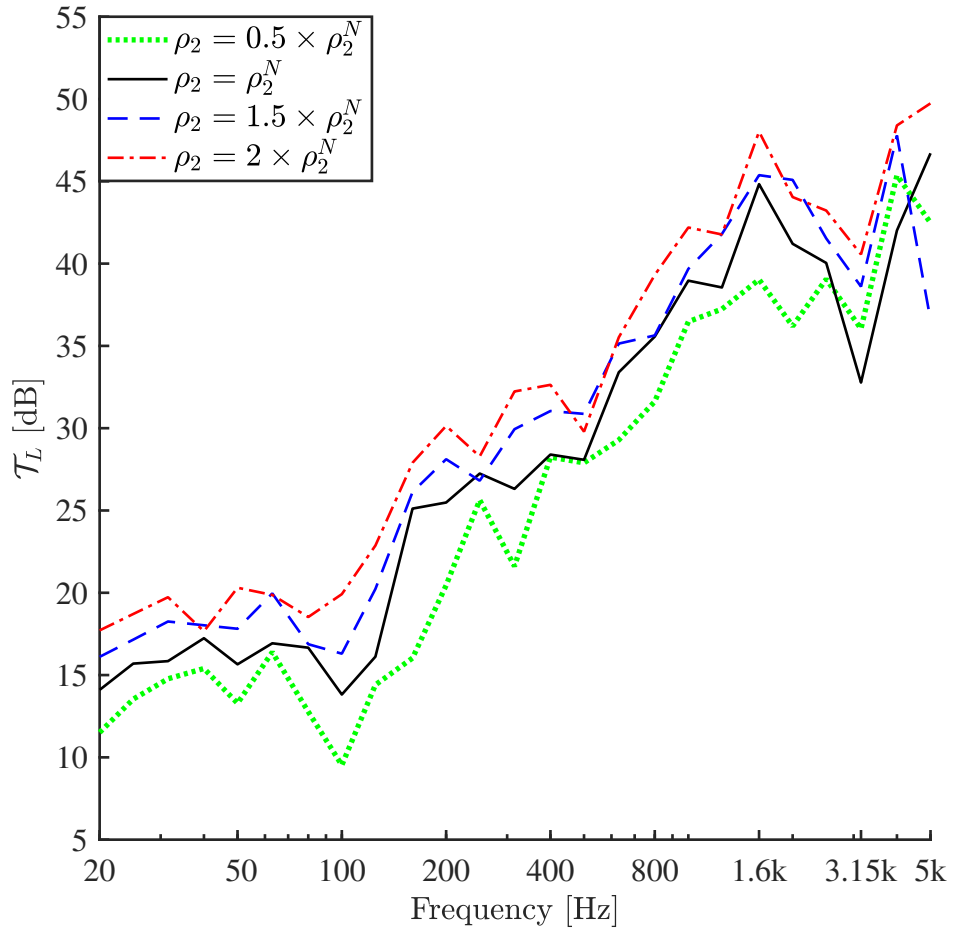


Figure 5.18: Transmission loss calculated for different  $\rho_2$ , where the nominal value  $\rho_2^N = 838.46 \text{ kg/m}^3$ .

The assumed coupling spring between the radiating plate and the beams is also one of the reasons for the non-symmetric behaviour of  $\mathcal{T}_L$  with respect to  $\rho_1$  and  $\rho_2$

variations. Because, as seen in Section 5.1,  $K$  is more effective above the 1 kHz band, where the non-symmetry is noticed. Although a high value of  $K$  is considered to make the connection close to rigid, there still remains some flexibility between the plates. The coupling between the plates is strong in the lower frequencies, resulting in a strong correlation between the plates' vibration whereas the coupling is comparatively less at the higher frequencies and plates vibrations become isolated from each other. As a result, the effect of the parameters of the two plates on  $\mathcal{T}_L$  show variation above 1 kHz band. Therefore, if the plates and beams are connected rigidly without the springs, vibrations of the plates are likely to be more correlated to each other. In that case,  $\mathcal{T}_L$  profiles with respect to the corresponding parameters of two plates are expected to be more symmetric.

Figure 5.19 and Fig. 5.20 show the variation in  $\mathcal{T}_L$  with the variation in the other two radiating plate parameters  $E_2$  and  $h_2$ , respectively. The effects of variations in these two parameters is similar to the effect of  $\rho_2$  variation that the structural resonances are shifted with the variations in the parameters. Similar to Fig. 5.18, the peak at 1.6 kHz band corresponding to the incident plate coincidence is seen for all values of  $E_2$  and  $h_2$ . Similarly, the coincidence effects of the radiating plates are not clearly visible except as the shallow dips when  $E_2$  and  $h_2$  take values other than their respective nominal values. A single peak and dip is noticed for  $E_2 = 1.5E_2^N$ , where the corresponding  $f_{cr}$  values for the incident and the radiating plates are 2.66 kHz and 2.17 kHz, respectively. These frequencies are not far apart to appear as two distinct peaks and dips in a 1/3 octave band representation. Variations in  $\mathcal{T}_L$  with  $E_1$  and  $E_2$  are almost identical below 1 kHz band and same is true regarding the variations of  $\mathcal{T}_L$  with  $h_1$  and  $h_2$ . Similar to  $E_1$ ,  $E_2$  does not contribute to varying the  $\mathcal{T}_L$  level, but shifts the resonance frequencies.

Similar to  $h_1$ ,  $h_2$  positively increase  $\mathcal{T}_L$  below the 1 kHz band because of the increase in overall panel mass, as shown in Fig. 5.20.  $h_2$  also contributes to  $D_2$ , and therefore affects structural resonances of the radiating plate and causes some peaks to shift in

frequency. Comparing Fig. 5.17 and Fig. 5.17, it is noted that shifting of peaks is more frequent in the case of  $h_1$  variation. This indicates that the structural resonances of the incident plate are more effective than those of the radiating plate.

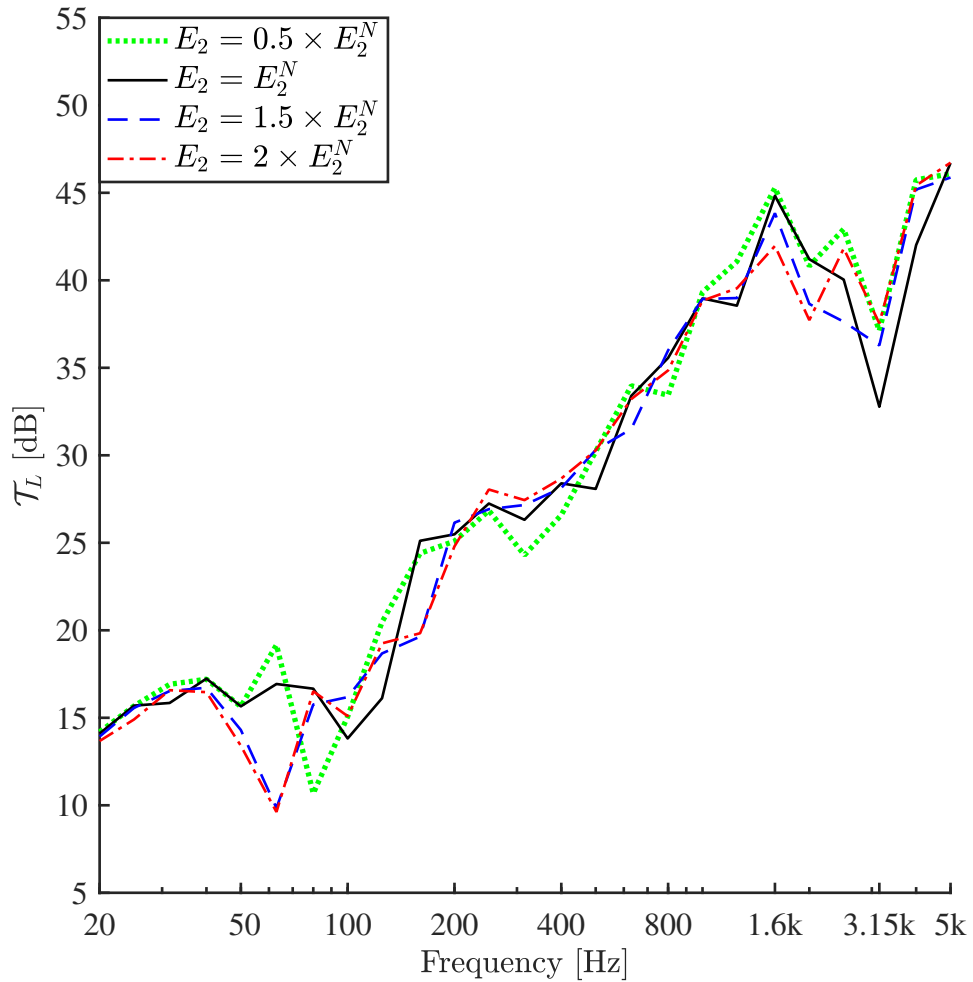


Figure 5.19: Transmission loss calculated for different  $E_2$ , where the nominal value  $E_2^N = 2.8457$  GPa.

## 5.4.2 Effects of the beam parameters

The effects of variations in three beam parameters are considered in this thesis, which are  $\rho_b$ ,  $E_b$  and  $h_b$ . Figure 5.21 shows the variation in  $\mathcal{T}_L$  with the variation in  $\rho_b$ . As explained at the beginning of this section, the masses of the beams are small compared

to the mass of the plates. Therefore, increasing  $\rho_b$  causes only a minor increase in the panel mass and increases  $\mathcal{T}_L$  according to the mass law. Despite this minor increase in panel mass,  $\mathcal{T}_L$  increases significantly in the lower frequency below the 50 Hz band to such an extent that the effects of  $\rho_b$  and  $\rho_1$  on  $\mathcal{T}_L$  are almost the same below 50 Hz band.

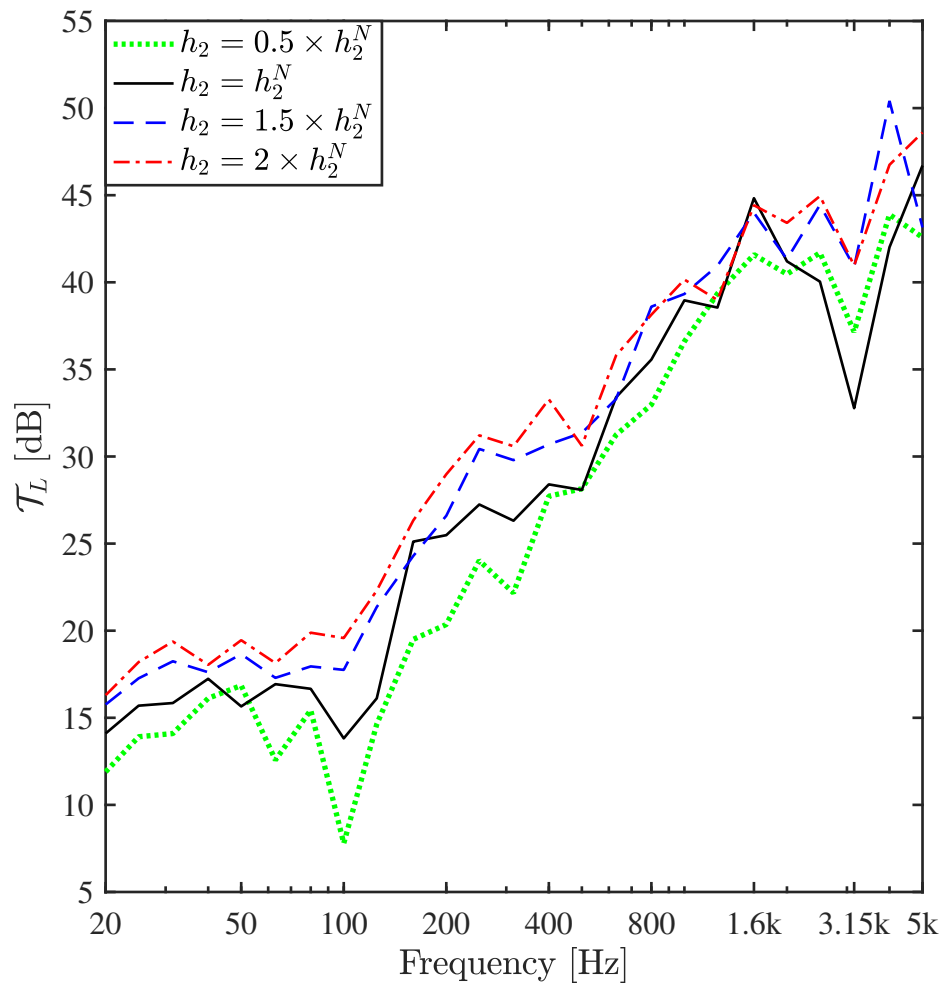


Figure 5.20: Transmission loss calculated for different  $h_2$ , where the nominal value  $h_2^N = 0.013$  m.

Beams act as constraint to plate vibrations, and the heavier the beam is, the greater is the constraint, which results in higher  $\mathcal{T}_L$ . As explained in Section 5.3 that at very low frequencies, the plate vibration is global, and constraint in any part of the plate affects

the overall vibration. Therefore, constraints caused by the beams are most effective below the 50 Hz band. It is noted that  $\mathcal{T}_L$  varies in the below 50 Hz band without any shift in peaks. This further indicates that the variation in  $\mathcal{T}_L$  is not due to the beam resonance frequencies ( $f_{bm}$ ), rather it is due to the constraint by the beams. Significant increase in  $\mathcal{T}_L$  is also noticed between 160 Hz and 500 Hz bands. Because  $f_t = 630$  Hz and below 630 Hz band, the plate vibration is still global. Another observation between 160 Hz and 500 Hz bands is that  $\mathcal{T}_L$  dips shift in frequency with the variation in  $\rho_b$ . This indicates some effectiveness of the beam resonances in this frequency range. Beam resonances do not necessarily affect the plate vibrations directly. Beam resonances can affect the plate resonance indirectly by increasing the plate vibration amplitude when  $f_{bm}$  coincides with the plate resonance frequencies ( $f_p$ ). The higher ( $M_{ct}$ ) values corresponding to the plates between 160 Hz and 500 Hz bands as shown in Table 4.10 is also an indication that beam resonance indirectly affect the plate vibration. Because higher ( $M_{ct}$ ) values increase the possibility of coincidence between  $f_{bm}$  and  $f_p$ .

Conversely, the shifting of  $\mathcal{T}_L$  dips is not perceived above the 500 Hz band because with the increase in frequencies,  $f_{bm}$  become widely spread. For example, approximately 200 Hz gap between two consecutive  $f_{bm}$  occur between 500 Hz and 1 kHz bands. ( $M_{ct}$ ) corresponding to the beams are too small in these frequency bands and the possibility of coincidence between  $f_{bm}$  and  $f_p$  is low. This further supports that shifting of the dips between 160 Hz and 500 Hz bands is due to the coincidence between  $f_{bm}$  and  $f_p$ . Above  $f_t = 630$  Hz, the plate vibration is local, and the effectiveness of the beams' constraints are reduced. This explains the minor  $\mathcal{T}_L$  variation due to  $\rho_b$  between the 630 Hz and 3.15 kHz bands. Significant variation in  $\mathcal{T}_L$  is observed in the 4 kHz band and one possible reason for this is the low frequency resolution because only two frequency points are considered in this band and also in the 5 kHz band. This saves computation time at the expense of some accuracy. It is also noticed from Fig. 5.21 that variation in  $\rho_b$  does not shift the coincidence peak, and dips are of the same depth for all cases.

This shows that the coincidence does not depend on beam mass.

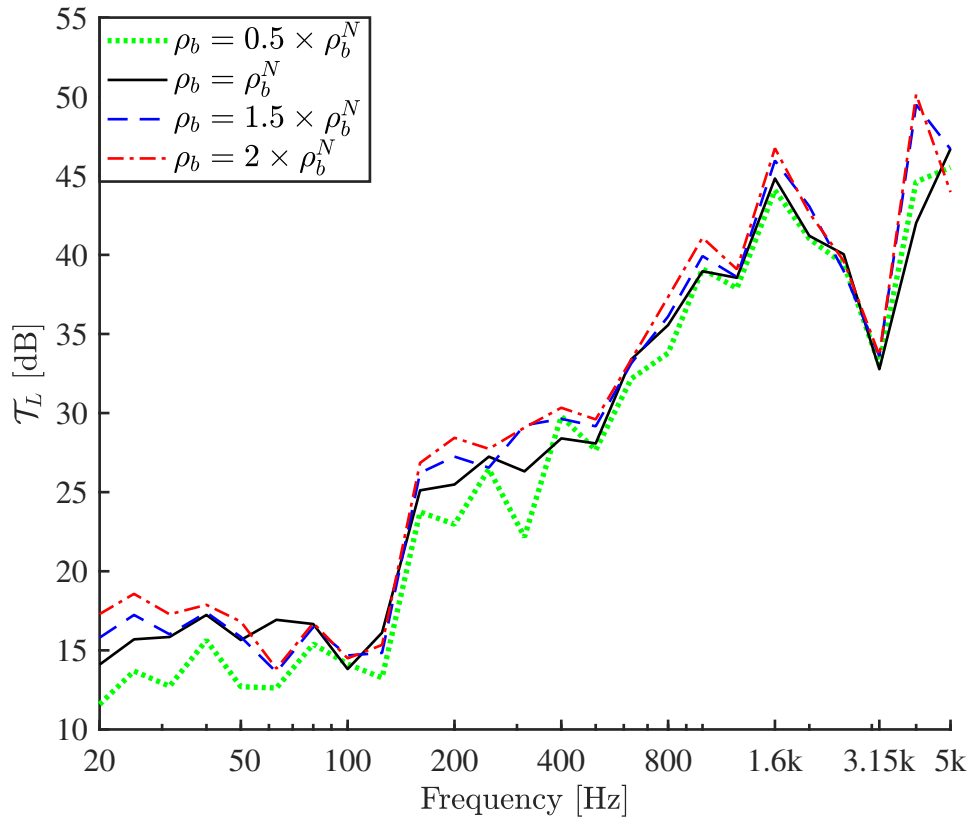


Figure 5.21: Transmission loss calculated for different  $\rho_b$ , where the nominal value  $\rho_b^N = 550 \text{ kg/m}^3$ .

Figure 5.22 shows the variation in  $\mathcal{T}_L$  for different values of the Young's modulus of the beams  $E_b$ . Figure 5.22 can be explained in terms of the explanation given for Fig. 5.21.  $f_t$  (630 Hz band) divides the figure into two regions, and the beams' constraints are more effective below 630 Hz band. This makes  $\mathcal{T}_L$  to be more affected by  $E_b$  below 630 Hz band compared to  $f > 630 \text{ Hz}$ . As explained earlier,  $E_b$  mainly contributes to increasing the panel stiffness without increasing the panel mass, which causes the resonance peaks to shift in frequencies without causing much variance of  $\mathcal{T}_L$  levels. As explained earlier, the variation in  $\mathcal{T}_L$  below the 50 Hz band is due to the constraint caused by the beams. The constraint put by the beams is experienced by the plates as reaction forces given by Equation (3.12). The terms containing  $\rho_b$  and  $E_b$  in

these equations are of opposite signs. Therefore,  $\mathcal{T}_L$  significantly decreases with the increase in  $E_b$ , which is opposite to the case corresponding to  $\rho_b$  variation as shown in Fig. 5.21. Similar to the case for  $\rho_b$  variation, peaks and dips are not shifted below 160 Hz band corresponding to  $E_b$  variation as well, and the exception with the peak in the 63 Hz band corresponding to  $\rho_b = \rho_b^N$  is also there.

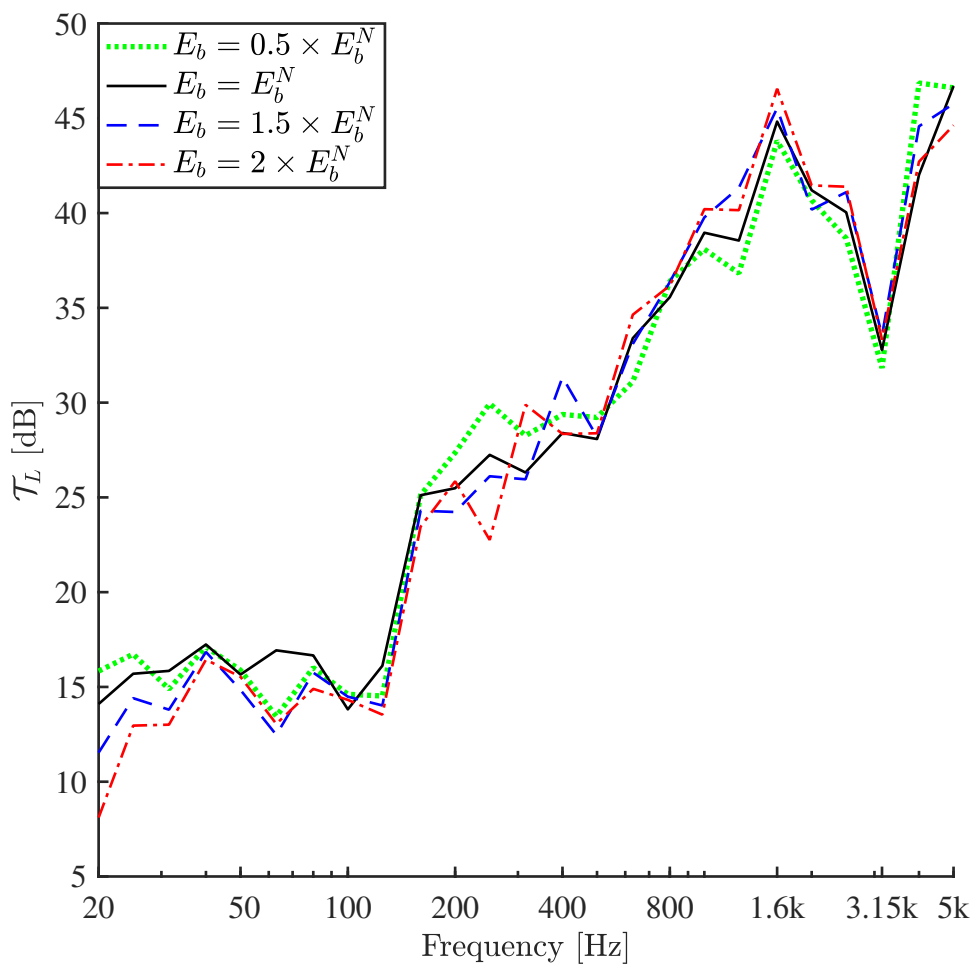


Figure 5.22: Transmission loss calculated for different  $E_b$ , where the nominal value  $E_b^N = 9.8$  GPa.

Similarly to  $\rho_b$ ,  $E_b$  is most effective between the 160 Hz and 500 Hz bands in terms of shifting of peaks and dips for reasons explained earlier. Similar to  $\rho_b$ ,  $\mathcal{T}_L$  shows an increasing trend above the 500 Hz band with an increase in  $E_b$ . Above the 1 kHz

band,  $\mathcal{T}_L$  variation due to  $E_b$  variations is greater compared to that corresponding to  $\rho_b$  variation, which indicates the changes in overall panel stiffness with the increase in  $E_b$ . The coincidence dips are located in the same frequency corresponding to all panels, which indicates that the incident plate is not affected by the  $\rho_b$  variations. New additional dips emerge at comparatively lower frequencies for the two largest values of  $E_b$ . This indicates that the overall stiffness of the panel increases with the increase in  $E_b$ , which affects the coincidence of the radiating plate.

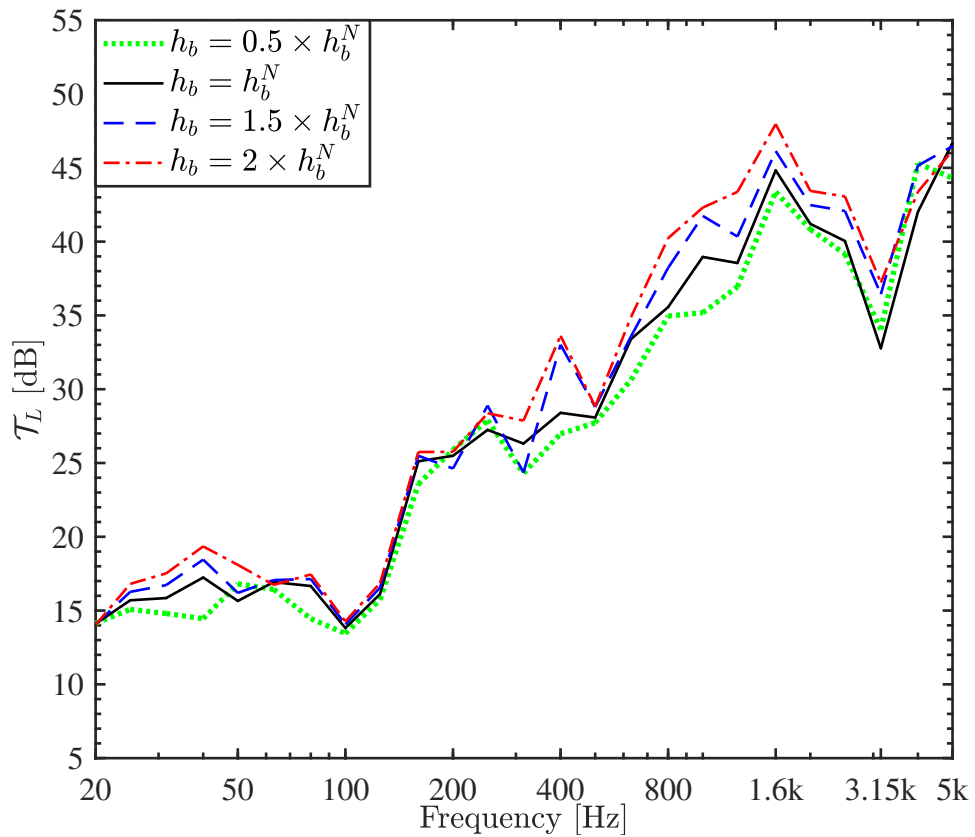


Figure 5.23: Transmission loss calculated for different  $h_b$ , where the nominal value  $h_b^N = 0.045$  m.

Figure 5.23 shows the variation in  $\mathcal{T}_L$  for different beam thickness  $h_b$ . An increase in  $h_b$  causes both beam mass and inertia, i.e.  $I_b$ , to increase. Increase in  $I_b$  makes the beam stiffer and thus, the effect of  $I_b$  variation is similar to the effect of  $E_b$  variation on  $\mathcal{T}_L$ . Therefore, the effect of  $h_b$  variation on  $\mathcal{T}_L$  can be treated as the combination of

the variational effects of both  $\rho_b$  and  $E_b$  on  $\mathcal{T}_L$  in all frequency bands. Starting from a low frequency below 50 Hz band,  $\rho_b$  and  $E_b$  have opposite effects on  $\mathcal{T}_L$ . As a result,  $\mathcal{T}_L$  does not show any variation with  $h_b$  at the 20 Hz band. As the frequency increases, the effect of  $\rho_b$  prevails and  $\mathcal{T}_L$  increases with  $h_b$  up to the 50 Hz band. Similar to the cases for  $\rho_b$  and  $E_b$  variations, peaks and dips are not shifted below 160 Hz band significantly with few exceptions. Likewise, the effects of  $h_b$  variation are maximum between the 160 Hz and 500 Hz bands, and the graphs correspond to the combined effects of  $\rho_b$  and  $E_b$  variations. The opposite effects of  $\rho_b$  and  $\rho_b$  variations on  $\mathcal{T}_L$  are also observed between the 50 Hz and 500 Hz bands with some overlap between 160 Hz and 500 Hz bands. The variation in both  $\rho_b$  and  $E_b$  positively affect  $\mathcal{T}_L$  above 500 Hz band, which explains the significant increase in  $\mathcal{T}_L$  with the increase in  $h_b$  between the 500 Hz and 3.15 kHz bands. Therefore, the effects of  $E_b$  on  $\mathcal{T}_L$  shifts from negative to positive with frequency, and  $\mathcal{T}_L$  varies positively with  $\rho_b$  in all frequency bands. This is perceived in Fig. 5.23 as a gradual increase in  $\mathcal{T}_L$  variation with frequency. The coincidence peaks and dips do not vary with  $h_b$ , and  $\mathcal{T}_L$  does not show significant variation above the 3.15 kHz band. This indicates that the net contribution of increased panel mass and stiffness due to  $h_b$  increment is not large enough to have any significant effect on the coincidence.

### 5.4.3 Effects of the cavity parameters

$\mathcal{T}_L$  for 3 m  $\times$  3 m panel at different cavity depths  $d$  is shown in Fig. 5.24. Similar to  $h_b$ , an increase in  $d$  causes mass and stiffness of the beam to increase. Therefore,  $\mathcal{T}_L$  variation due to  $d$  variation is similar to the  $\mathcal{T}_L$  variations due to  $\rho_b$  and  $E_b$  variations.  $f_t$  divides the graphs into two regions in frequency, where shifting of frequencies are seen below  $f_t$ , and graphs do not show any specific trend.  $\mathcal{T}_L$  increases significantly with  $d$  in most of the frequency bands above  $f_t$ .

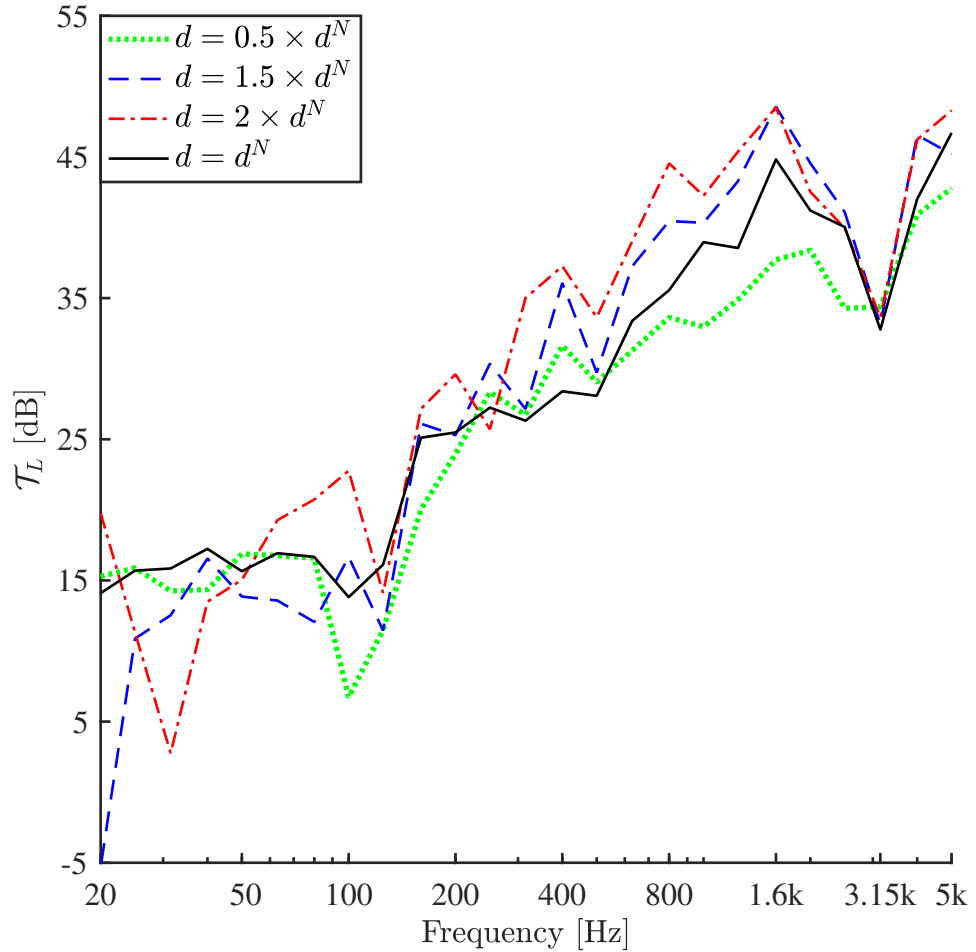


Figure 5.24: Transmission loss calculated for different  $d$ , where the nominal value  $d^N = 0.095$  m.

An increase in  $d$  varies the beam characteristics by increasing the beam height and also varies the air characteristics inside the cavities. Both these effects have significant influence in the low frequency region.  $\mathcal{T}_L$  is calculated between 2 Hz and 200 Hz with high frequency resolution (151 frequency points) corresponding to four different values of  $d$ , which are  $[0.5, 1, 1.5, 2] \times 0.095$  m, the corresponding graphs are displayed in Fig. 5.25. Increasing the beam height makes the beams heavier and also increases the inertia of the beams ( $I_b$ ) as  $I_b = h_b d^3 / 12$ . Since  $I_b$  varies in cubic order with  $d$ , the panel gets much stiffer with a comparatively small increase in  $d$ . As a result, the overall

stiffness of the panel increases, which shifts the structural resonances in the higher frequencies. It is apparent from Fig. 5.25 that  $f_1$  shifts in the higher frequencies with an increase in  $d$ .

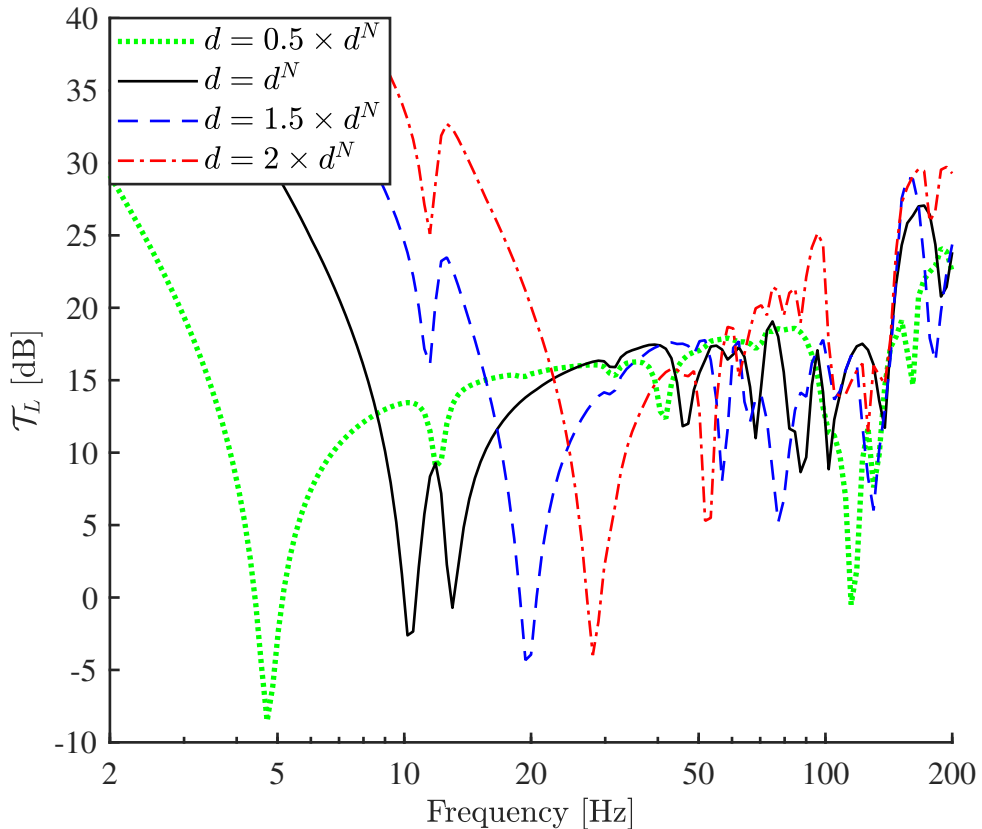


Figure 5.25: Transmission loss calculated for different  $d$  at 151 frequency points below 200 Hz, where the nominal value  $d^N = 0.095$  m.

An increase in  $d$  takes the plates farther apart from each other and sound pressure needs to travel a longer distance to transmit to the radiating plate, which adds to  $\mathcal{T}_L$ .  $f_0$  reduces in frequency with the increase in  $d$ . Ignoring the attached beams,  $f_0$  for  $d = [0.5, 1, 1.5, 2] \times d^N$  are calculated based on Equation (2.56) as 121 Hz, 85 Hz, 70 Hz and 60 Hz, respectively. The four corresponding  $f_0$  predicted by the model are selected by observing the dips in Fig. 5.25, which are 115 Hz, 87 Hz, 77 Hz and 52 Hz respectively. The discrepancies in the frequencies are expected because of the attached beams. As discussed in Section 5.3, multiple cavity consideration gives rise to partial

resonance, where the air inside some cavities undergoes resonance whilst the others may not. As a result, some additional dips are also seen besides  $f_0$ .

At the higher frequencies above  $f_t$ , the effect of  $d$  variation is similar to the effect of  $h_b$  variation so that  $\mathcal{T}_L$  rises significantly with  $d$ . Because similar to  $h_b$ , an increase in  $d$  also increases the weight and stiffness of the beams resulting in increase in  $\mathcal{T}_L$ . As pointed out earlier that  $I_b$  increases as a cubic order of  $d$ . Therefore, the beams' stiffness rises to a much higher magnitude with  $d$  variation compared to  $h_b$  variation. This agrees with the result shown in Fig. 5.24 up to the 2.5 kHz band for  $d = [0.5, 1, 1.5] \times d^N$ .  $\mathcal{T}_L$  does not increase as expected for  $d = 2d^N$  above 1 kHz band, and  $\mathcal{T}_L$  for various  $d$  overlaps at 2.5 kHz band. This behaviour is because of the changes in cavity characteristics with the increase in  $d$ .

Recalling Equation (2.57), cavity resonances due to standing wave take place at  $f_{cav} = nc_0/2d$ , where  $n$  is a positive integer.  $f_{cav}$  for  $n = 1$  corresponding to  $d = [0.5, 1, 1.5, 2] \times d^N$  are 3.56 kHz, 1.79 kHz, 1.20 kHz and 895 Hz, respectively.  $f_{cav}$  begins from a comparatively lower frequency and the next two  $f_{cav}$  values for  $d = 2d^N$  are 1.79 kHz and 2.68 kHz. This indicates that  $\mathcal{T}_L$  reduction corresponding to  $d = 2d^N$  and the overlapping of  $\mathcal{T}_L$  above 2.5 kHz band are both due to  $f_{cav}$ . By controlling the cavity resonances, it is possible to increase in  $\mathcal{T}_L$  considerably in the higher frequencies. Therefore, increasing  $d$  in the presence of absorbing material inside the cavity is expected to increase  $\mathcal{T}_L$  considerably at the higher frequencies. Brunskog (2002) studied the effects of  $d$  on impact sound level in the presence of partially filled mineral wool on similar panels, and found considerable reduction in sound pressure level compared to the case where no mineral wool is used. This agrees with the prediction made here that a considerable increase in  $\mathcal{T}_L$  can be achieved at the higher frequencies by increasing  $d$  in the presence of some absorbing materials partially filling the cavities.

## Chapter 6

# Effects of minor variations in panel parameters

The design of a lightweight panel depends on the use and purpose of the panel. The parameter values of a panel used for ensuring high sound insulation differ from the parameter values of panel used for enhancing the sound transmission. Multiple panels may be manufactured based on a single design, and these panels are called nominal identical panels. It is found from experiment that  $\mathcal{T}_L$  corresponding to these nominally identical panels show variations (Craig & Steel, 1989; Johansson, 2000; Öqvist, 2010). These variations in  $\mathcal{T}_L$  are due to the variations in the individual parameters. For example, thicknesses of the plates and the beams or beam spacings are not exact values in all panels; some variations are expected in these dimensions due to workmanship (Craig & Steel, 1989). Another variation is the properties of timber materials, which depend on the environmental conditions the raw timber grew in (Machado et al., 2014; Gerhards, 2007). Depending on the loading and boundary conditions, both the material and dimensional properties of the panel may deteriorate and cause deviations in  $\mathcal{T}_L$  over time.

As discussed in Section 1.4 that the material properties exhibit some variations due

to some internal and external factors. For example, the grain orientation in wood causes the strength of the timber material to vary. Likewise, variation in the environmental factors (temperature, moisture content) and loading conditions causes the material properties to vary. As mentioned in Section 1.4 that although variation due to these external and internal factors may be minor for individual parameter and thus, resulting variations in  $\mathcal{T}_L$  are expected to be small. Despite this, the cumulative effects of variations in many parameters on  $\mathcal{T}_L$  variation can be significant. This chapter and the following one are focused on the variation in  $\mathcal{T}_L$  due to this small-scale variation in the individual panel parameters. The panel parameters are many but only the three most important parameters are considered in this chapter because of the large computation time required. The three varying parameters are thickness of the incident plate, thickness of the beams, and the cavity depth. In the next chapter, a regression model, which reduces the computation time significantly, will be used to study the effects of variations of more parameters. One of the main purposes of this chapter is to generate some results based on the analytical model for validating the regression model used in the next chapter. In both these chapters, it is not intended to make exact representations of the variation in the individual parameters. The main focus of this chapter and Chapter 7 is the method. The range of the variations in the parameters used in these two chapters is only to demonstrate the method. Therefore, the variation found in these two chapters may not correspond to the real double-leaf panels, but the analytical method used in this chapter and the regression model of the next chapter can be useful.

Arbitrary ranges of parameter values are selected as examples to demonstrate the method. The parameter values in Section 3.4 are set as the nominal values for different parameters, and a  $\pm 5\%$  variation in each parameter is considered. The expected variation in each parameter may vary depending on the applications. The method can be used for any selected ranges. Therefore, once some ideas of the exact variations in the panel parameters are known, the method in this chapter and in the next chapter (for many

parameters and at the high frequencies) can be used to predict the expected variations in  $\mathcal{T}_L$ . This knowledge can work as feedback to the main design, which is useful for the proper design of the panel. Some modifications in the main design may be necessary if the expected variation in  $\mathcal{T}_L$  turns out to be too large or the minimum  $\mathcal{T}_L$  is below the tolerable limit.

The physical mechanisms of  $\mathcal{T}_L$  variations due to large scale variations in parameter values are discussed in Chapter 5. Therefore, the physical mechanisms behind the results are not highlighted much in this chapter and in the next one. The author's opinion is that it is more helpful to have some idea about the magnitude of  $\mathcal{T}_L$  variations caused by the minor variations in individual parameters, rather than to explore the physical mechanism behind it. Therefore, more attention is given to the methods applied in this chapter and in the next one for evaluating the expected variation in  $\mathcal{T}_L$  due to the minor variations in the parameters.

## 6.1 Methods

In this thesis, two methods are adopted for analysing the sensitivity of the parameters. The first method is described in this chapter; it uses the analytical model to calculate  $\mathcal{T}_L$  for a number of combinations of different parameter values. The three varying parameters, i.e.  $h_1$ ,  $h_b$  and  $d$ , vary within the specified  $\pm 5\%$  range around the nominal values given in Section 3.4. The maximum or minimum  $\mathcal{T}_L$  is then identified from the set of calculated  $\mathcal{T}_L$  at various parametric combinations. Obviously, the greater the number of combinations is, the better the  $\mathcal{T}_L$  variation prediction will be. The number of combinations needs to be limited to keep the computation time from becoming too high. For that reason, 11 evenly spaced values are set for each varying parameter within the specified range. 11 points in a  $\pm 5\%$  range is adequate for capturing the  $\mathcal{T}_L$  variation. Three varying parameters considered here are the incident plate thickness, the beam

thickness and the cavity depth.

The total computation time can still become too long with the analytical model for many parameters and higher frequency bands. In that case, the second method is adopted, which is described in Chapter 7. In Chapter 7 a regression model is set based on RSM. The model is derived from fewer results calculated from the analytical model. The model can predict  $\mathcal{T}_L$  with reasonable accuracy for small variations in panel parameters. Therefore, the model is suitable for a higher number of parameters and for higher frequencies.

## 6.2 Sensitivity analysis for three parameters

The sensitivity of  $\mathcal{T}_L$  is analysed for two cases. First, a single parameter is varied, while the others are fixed. Second, two parameters are varied and the third remains constant. Similar to Chapter 5, a set of  $\mathcal{T}_L$  is calculated for sets of varying parameters when single parameter is varied. For two parameter varying case, a set of  $\mathcal{T}_L$  is calculated for all combinations of two varying parameter values. Therefore, 11 calculations are required in each frequency points for a single parameter variation case, and 121 calculations are required when two parameters are varied.

For each parametric combination,  $\mathcal{T}_L$  is calculated at four 1/3 octave frequency bands at 125 Hz, 250 Hz, 400 Hz and 800 Hz bands. Five frequency points are considered in each band, which increases the computation 5 times. The relative difference of the sound transmission loss  $\Delta\mathcal{T}_L = \mathcal{T}_L - \mathcal{T}_{\min}$  is then calculated for each band, where  $\mathcal{T}_{\min}$  is the minimum sound transmission loss corresponding to the frequency band. The expected variation in  $\Delta\mathcal{T}_L$  due to the variation in a parameter or variations in two parameters are quantified from the calculated  $\Delta\mathcal{T}_L$ . In Section 6.2.1 a single parameter is varied and in Section 6.2.2 two parameters are varied. The results in Section 6.2.1 will be used in Chapter 7 to validate the RSM based model.

### 6.2.1 Varying one parameter

The sets of  $\Delta\mathcal{T}_L$  corresponding to three parameters are plotted against the percentage change of each parameter in Fig. 6.1.  $\Delta\mathcal{T}_L$  increases steadily with  $h_b$  at all frequency bands, but  $\Delta\mathcal{T}_L$  is least sensitive to  $h_b$  variations. Maximum  $\Delta\mathcal{T}_L$  is noticed in the 250 Hz band and 400 Hz band, and in both cases  $\Delta\mathcal{T}_L$  is little more than 0.5 dB.  $\Delta\mathcal{T}_L$  is more sensitive to  $h_1$  in most frequency bands, with a maximum  $\Delta\mathcal{T}_L$  value of approximately 1 dB at the 400 Hz band. Variation  $\Delta\mathcal{T}_L$  is less in the 125 Hz and 800 Hz bands with respect to  $d$  and  $h_b$ , which shows  $\Delta\mathcal{T}_L$  to be the most sensitive to  $h_1$  variations.  $\Delta\mathcal{T}_L$  increases almost linearly with  $h_1$  in the 125 Hz band.  $\Delta\mathcal{T}_L$  variation is nonlinear with  $h_1$  in the remaining frequency bands, maintaining an increasing trend. Comparatively large variations in  $\Delta\mathcal{T}_L$  are observed for  $d$  variations in 250 and 400 Hz bands, which are approximately 1.25 and 2 dB, respectively. The variation in  $\Delta\mathcal{T}_L$  with respect to  $d$  is nonlinear in all bands, and similar to  $h_1$ ,  $\Delta\mathcal{T}_L$  follows an increasing trend in all bands.

The results given in the previous paragraph correspond to a  $\pm 5\%$  variation for all parameters, whereas, in reality, each parameter may vary with a different range. Fig. 6.1 can be useful to predict the variation in  $\Delta\mathcal{T}_L$  corresponding to any of these three parameters. For any variation range below  $\pm 5\%$ ,  $\Delta\mathcal{T}_L$  can be extracted directly from Fig. 6.1. For variation ranges slightly above  $\pm 5\%$ ,  $\Delta\mathcal{T}_L$  can be extrapolated based on the results given in Fig. 6.1. Otherwise, results need be recalculated corresponding to the new ranges following the same procedure.

### 6.2.2 Varying two parameters

The sets of varying parameters are normalised by their respective nominal values for convenience thus:  $\bar{h}_b = h_b/0.045$ ,  $\bar{d} = d/0.095$  and  $\bar{h}_1 = h_1/0.013$ . Three sets of  $\Delta\mathcal{T}_L$  are calculated corresponding to three pairs of normalised parameter sets, namely  $\{\bar{h}_b, \bar{d}\}$ ,  $\{\bar{d}, \bar{h}_1\}$  and  $\{\bar{h}_b, \bar{h}_1\}$  shown in Figures 6.2, 6.3 and 6.4.

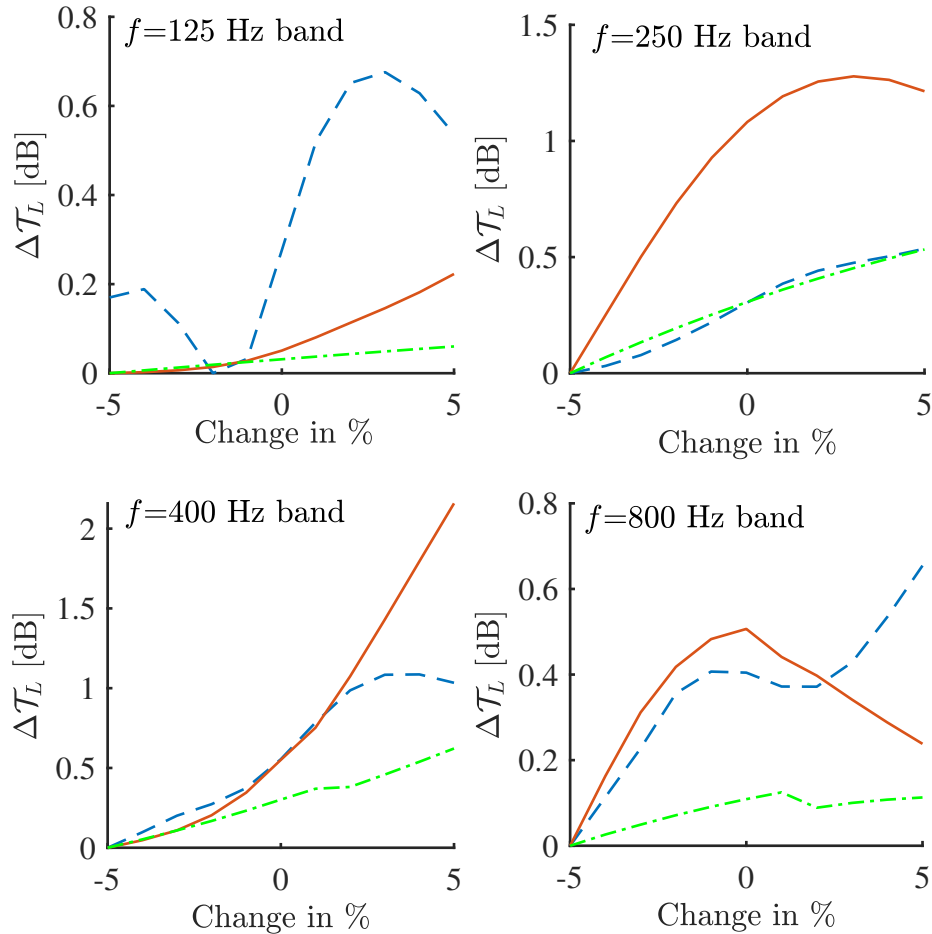


Figure 6.1:  $\Delta\mathcal{T}_L$  is plotted against the percentage change of three parameters. Blue dashed line (- - -), red solid line (—) and green dotted line (· · ·) represent the  $\Delta\mathcal{T}_L$ , corresponding to the variations in  $h_1$ ,  $d$  and  $h_b$ , respectively.

The variation in  $\Delta\mathcal{T}_L$  due to the combined effects of  $\bar{h}_1$  and  $\bar{h}_b$  in Fig. 6.2 is similar to the variation of  $\Delta\mathcal{T}_L$  due to the variational effect of  $h_1$  and  $h_b$  separately in Fig 6.1. The variation in  $\Delta\mathcal{T}_L$  due to the variation in  $\bar{h}_1$  is nonlinear for most values of  $\bar{h}_b$  at the 125 Hz band whereas the variation in  $\Delta\mathcal{T}_L$  with respect to  $\bar{h}_b$  is linear for most values of  $\bar{h}_1$  at the 125 Hz band with an exception when  $\bar{h}_1$  is close to its minimum. The response surfaces are flat in the 250 Hz band, which indicates a linear relationship between  $\Delta\mathcal{T}_L$  and the two parameters in this band. Both these parameters positively affect  $\Delta\mathcal{T}_L$  causing the maximum  $\Delta\mathcal{T}_L$  of 1 dB to occur when both these parameters are

at their maximum.

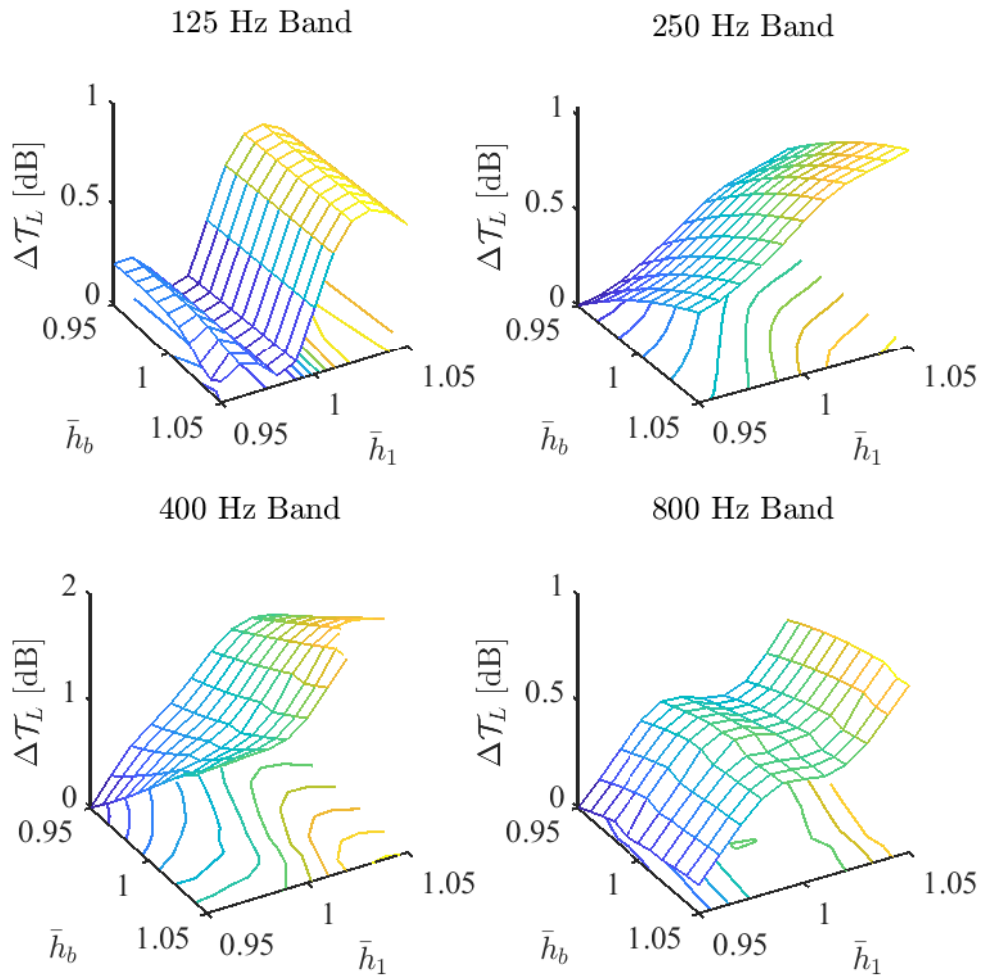


Figure 6.2: Variation of  $\Delta\mathcal{T}_L$  due to the variations in  $\bar{h}_b$  and  $\bar{h}_1$ , when  $\bar{d} = 1$ .

The same increasing trend in  $\Delta\mathcal{T}_L$  is seen while varying  $\bar{h}_1$  and  $\bar{h}_b$  separately in Fig 6.1. At 400 Hz, the variation of  $\Delta\mathcal{T}_L$  with respect to  $\bar{h}_1$  is nonlinear, and linear with respect to  $\bar{h}_b$ . As shown in Fig 6.1, despite the linear or nonlinear relationship, the maximum values of  $\Delta\mathcal{T}_L$  due to the variation in  $\bar{h}_1$  and  $\bar{h}_b$  are not high. The maximum values of  $\Delta\mathcal{T}_L$  due to the combined variations in  $\bar{h}_1$  and  $\bar{h}_b$  are approximately 1 dB in all bands except in the 400 Hz band, where the maximum  $\Delta\mathcal{T}_L$  is approximately 2 dB. The variation in  $\Delta\mathcal{T}_L$  is higher along the  $\bar{h}_1$  direction compared to the variation along the  $\bar{h}_b$  direction in all frequency bands. The panel stiffness increases with the increase

in  $\bar{h}_b$ , and the mass of the panel increases strongly with the increase in  $\bar{h}_1$ . Results show that  $\Delta\mathcal{T}_L$  is more sensitive to the variation in panel mass compare to the panel stiffness in these frequency bands.

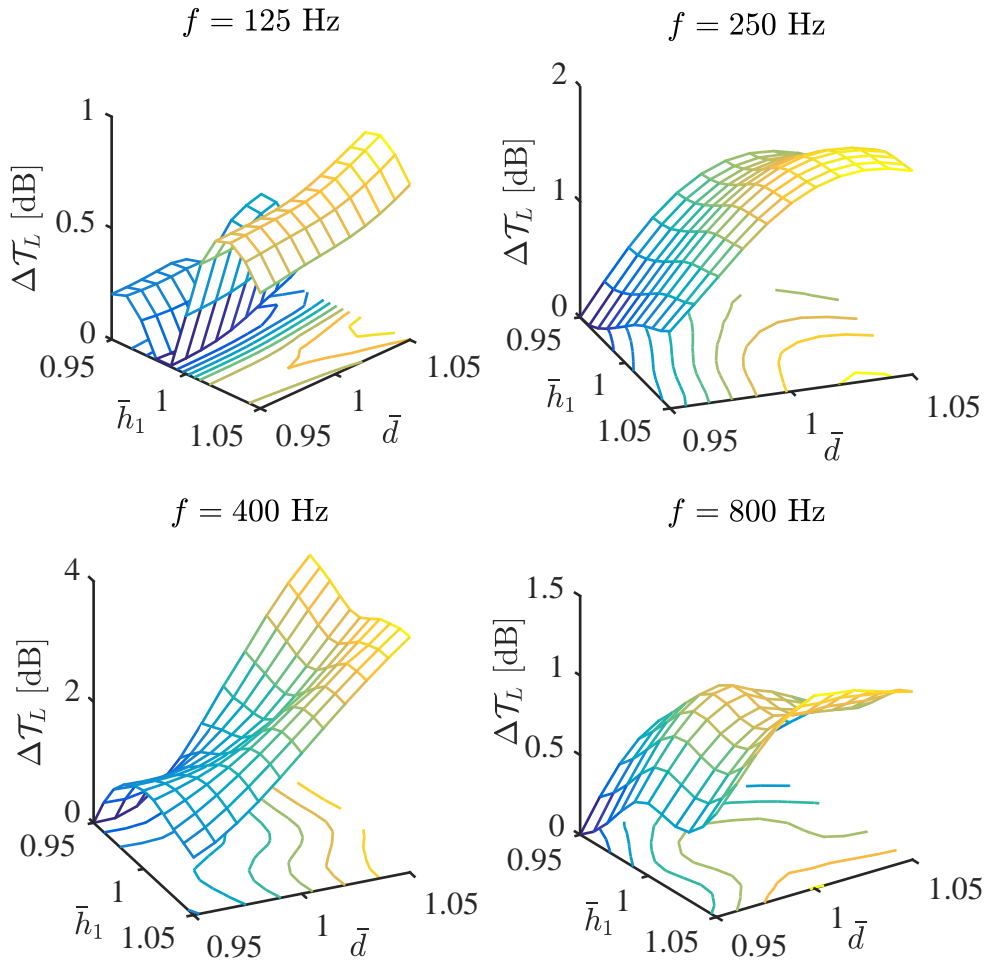


Figure 6.3: Variation of  $\Delta\mathcal{T}_L$  due to the variations in  $\bar{d}$  and  $\bar{h}_1$ , when  $\bar{h}_b = 1$ .

Figure 6.3 shows how  $\Delta\mathcal{T}_L$  varies with  $\bar{d}$  and  $\bar{h}_1$  when  $\bar{h}_b$  is fixed at 1.  $\Delta\mathcal{T}_L$  is maximum at the 400 Hz band, which is approximately 4 dB. The maximum values for  $\Delta\mathcal{T}_L$  at the 125 Hz, 250 Hz and 800 Hz bands are 1 dB, 2 dB and 1 dB, respectively. At the 400 Hz band, maximum  $\Delta\mathcal{T}_L$  along  $\bar{d}$  and  $\bar{h}_1$  direction are approximately 4 dB and 1.2 dB, respectively.  $\Delta\mathcal{T}_L$  increases nonlinearly with  $d$  for any value of  $\bar{h}_1$ , and maximum and minimum  $\Delta\mathcal{T}_L$  occur when  $\bar{d}$  is maximum and minimum, respectively.

$\Delta\mathcal{T}_L$  variation is parabolic with  $\bar{h}_1$ , where  $\Delta\mathcal{T}_L$  is convex upward and downward for  $\bar{h}_1$  below and above the nominal value, respectively.  $\Delta\mathcal{T}_L$  is more sensitive to  $\bar{d}$  than  $\bar{h}_1$  in the 400 Hz band. With the change in  $\bar{d}$ , the height of the beams along the  $z$  axis also changes, which changes the panel stiffness. Variation in  $\bar{d}$  also causes the cavity characteristics to vary. Comparing the graphs corresponding to the 400 Hz band in Fig. 6.2 and Fig. 6.3, it can be seen that variation in cavity characteristics is the key factor for  $\bar{d}$  to be most sensitive in this band.

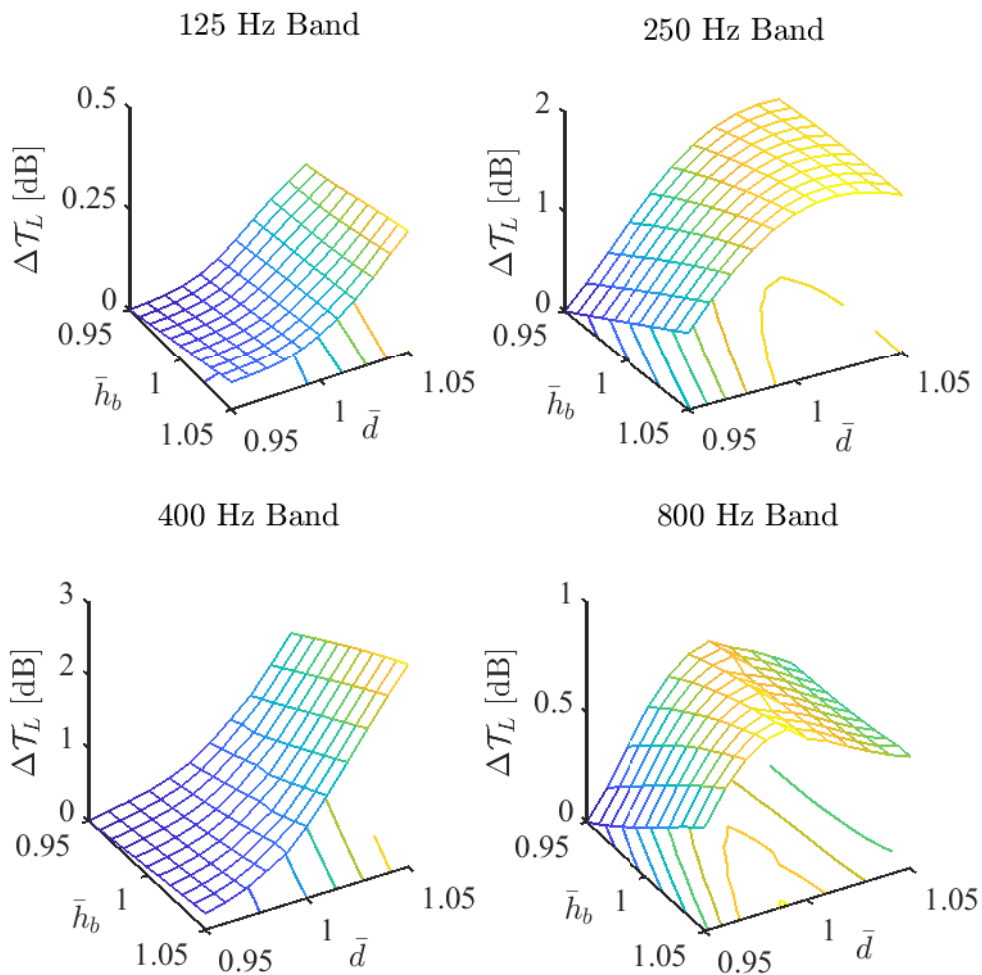


Figure 6.4: Variation of  $\Delta\mathcal{T}_L$  due to the variations in  $\bar{h}_b$  and  $\bar{d}$ , when  $\bar{h}_1 = 1$ .

Figure 6.4 shows the variation in  $\Delta\mathcal{T}_L$  due to the variations in  $\bar{h}_b$  and  $\bar{d}$  when  $\bar{h}_1 = 1$ .  $\Delta\mathcal{T}_L$  increases linearly with the variation in  $\bar{h}_b$  in all frequency bands except for a case

in the 250 Hz band, when  $\bar{d}$  is close to its maximum.  $\Delta\mathcal{T}_L$  variation is nonlinear with  $\bar{d}$  in all bands. The maximum  $\Delta\mathcal{T}_L$  is determined for the 125 Hz, 250 Hz, 400 Hz and 800 Hz bands, where maximum  $\Delta\mathcal{T}_L$  values are approximately 0.5 dB, 1 dB, 2 dB and 3 dB, respectively.  $\Delta\mathcal{T}_L$  is more sensitive to  $\bar{d}$  compared to  $\bar{h}_b$  in all bands except for the case when  $\bar{d}$  is minimum at the 800 Hz band. Variation in  $\bar{h}_b$  varies the stiffness and mass of the panel, whereas, variation in  $\bar{d}$  varies the stiffness and mass of the panel and also causes the cavity conditions to vary. This makes  $\Delta\mathcal{T}_L$  more sensitive to  $\bar{d}$ .

## Chapter 7

# Variation in $\mathcal{T}_L$ using the Response Surface Method

The variations in  $\mathcal{T}_L$  through the nominally identical lightweight structures are evident from measurement data (Craik & Steel, 1989; Johansson, 2000; Öqvist, 2010). As pointed out in Chapter 6 that one possible source of these variations is workmanship (Craik & Steel, 1989). Some environmental factors may also cause these variations (Machado et al., 2014; Gerhards, 2007). Both Chapter 6 and Chapter 7 are about the variations in  $\mathcal{T}_L$  due to the small scale variations in the panel parameters. In the previous chapter, the method of studying the effects of small scale variations of three parameters on  $\mathcal{T}_L$  using the analytical model of Chapter 3 was described. Time and memory consumptions increase with the increase in parameters and frequency bands. Therefore, using the method in Chapter 6 becomes unrealistic in case of many parameters. In this chapter, a regression model based on Response Surface Method used by Ganguli (2002); Myers et al. (2016) is implemented for estimating the variations in  $\mathcal{T}_L$ , which is much efficient in terms of time and memory consumption. The effects of variations in seven parameters are demonstrated at the same four frequency bands considered in Chapter 6, which are 125 Hz, 250 Hz, 400 Hz and 800 Hz bands. RSM is described in

Section 7.1. Once the regression model is derived, the analysis becomes much feasible and convenient.

Similar to Chapter 6, the exact representation of the random nature of each parameter is not intended here. The same  $\pm 5\%$  variation in parameter values as considered in Chapter 6 is also used here. Each varying parameter is varied around its respective nominal value given in Section 3.4. The focus here is to generate the regression model applicable within the  $\pm 5\%$  range near the specified nominal values. This model is only to be used for predicting  $\mathcal{T}_L$  for parameter values within this range. One use of this regression model is to have some idea about the trend of  $\mathcal{T}_L$  variation with respect to the parametric variations. Despite the variation in the parameters may not correspond to the reality, the model is still useful. Once the model is set, the expected variation in  $\mathcal{T}_L$  for any other ranges (within  $\pm 5\%$ ) of variations in the parameters can be predicted. Similar to Chapter 6, the physical mechanisms for the results are not explored here, which is not within the scope of this model.

The regression model is derived from the results calculated by the analytical model. Therefore, the regression model can only be derived when either some results from a theoretical model exist or some data from measurement is available. RSM uses a second order equation to predict  $\mathcal{T}_L$ , where the normalised parameters' values are set as the input variables. Therefore, it is possible to identify the stationary points of the quadratic surface. This could lead to estimating the absolute maximum ( $\mathcal{T}_L^{\max}$ ) and the absolute minimum ( $\mathcal{T}_L^{\min}$ ) within the interval. The expected maximum variation in  $\mathcal{T}_L$  due to the variations in the parameters can also be derived, which can be helpful to optimize the panel design.

## 7.1 Model based on RSM

The model is an algebraic equation with many constants. Once the coefficients are known, the model is set. The values of the parameters are not used in the model directly. Instead, the actual parameter values are first converted into the level values, and then inserted to the model equations. The conversion between the level values and the parameter values is given later in this section. The level values of each parameter are considered as the variable of the model equation. The seven parameters considered in this chapter are  $[h_1, h_2, h_b, \rho_1, \rho_2, \rho_b, d]$ . For the convenience of display, a different set of notation for the level values of each parameter is used in the model equation as  $t_n$ , where  $n = 1, 2, 3, \dots, 7$  correspond to the parameters  $[h_1, h_2, h_b, \rho_1, \rho_2, \rho_b, d]$ , respectively. The range of  $t_n$  varies between -1 and 1. For the convenience of display, a different set of notation ( $t_n^p$ ) is used to represent the actual values of different parameters. In the RSM model, three levels are set for each parameter as low, middle and high, which corresponding to the parameter  $t_n^p$  are denoted by  $t_n^l, t_n^m, t_n^h$ , respectively, and the corresponding level values are -1, 0 and 1, respectively. The middle level  $t_n^m$  corresponds to the nominal value corresponding to  $t_n^p$ , and  $t_n^l$  and  $t_n^h$  correspond to the lowest and the highest values of  $t_n^p$  at a  $\pm 5\%$  range. The three values of the varying parameters corresponding to the three levels are given in Table 7.1. The conversion of the parameter values  $t_n^p = [t_n^l, t_n^m, t_n^h]$ , to the level values  $t_n = [-1, 0, 1]$  is as follows

$$t_n = \frac{t_n^p - t_n^m}{t_n^h - t_n^m}. \quad (7.1)$$

$t_n$  according to Equation (7.1) is inserted to the second order model equation, which is written as (Cheng & Xiao, 2005, 2007; Li & Liang, 2007)

$$\mathcal{T}_L = b_0 + \sum_{n=1}^7 b_n t_n + \sum_{n=1}^7 b_{nn} t_n^2 + \sum_{n>m}^7 b_{mn} t_m t_n, \quad (7.2)$$

where  $b_n, b_{nn}$  and  $b_{mn}$  are the coefficients to be determined. As mentioned earlier, the notation  $t_n$  is used instead of the parameter notation just for simplicity and for the convenience of display but the discussion and results are presented using the usual notations. Once the unknown coefficients are known, the range of  $t_n$  does not need to be restricted to the three level values -1, 0 and 1, as mentioned earlier. Any other level values within the range or slightly outside the range can also be inserted in the model equation to calculate  $\mathcal{T}_L$ .

Table 7.1: Values of 7 selected parameters.

<b>Parameter</b>	Low	Middle	High
$h_1$	12.35 mm	13 mm	13.65 mm
$h_2$	12.35 mm	13 mm	13.65 mm
$h_b$	42.75 mm	45 mm	47.25 mm
$\rho_1$	796.54 kg/m <sup>3</sup>	838.46 kg/m <sup>3</sup>	880.38 kg/m <sup>3</sup>
$\rho_2$	796.54 kg/m <sup>3</sup>	838.46 kg/m <sup>3</sup>	880.38 kg/m <sup>3</sup>
$\rho_b$	522.50 kg/m <sup>3</sup>	550 kg/m <sup>3</sup>	577.5 kg/m <sup>3</sup>
$d$	90.25 mm	95 mm	99.75 mm

The first summation in the model includes the linear effects of each parameter and the second summation includes the non-linear effects of the parameters. The third summation corresponds to the combined effects of any pair of parameters. The coefficients are calculated using a software **R** package `rsm`. The limitation of the model is that it considers up to the 2<sup>nd</sup> order effects. This is justified because this model is used to study the effects of small scale variations of the input parameters on  $\mathcal{T}_L$ . Therefore, the expected variation in  $\mathcal{T}_L$  is assumed to be small enough not to exhibit any 3<sup>rd</sup> or higher order effects. The goal of using this method is not to predict  $\mathcal{T}_L$  with high accuracy but to estimate the effects of variation of each parameter on  $\mathcal{T}_L$ . Another important aspect of this model is that the stationary points corresponding to an optimum  $\mathcal{T}_L$ , or the direction towards the stationary points can be identified. Comparing  $\mathcal{T}_L$  at the stationary points and at the simulation points, the absolute maximum ( $\mathcal{T}_L^{\max}$ ) and

the absolute minimum ( $\mathcal{T}_L^{\min}$ ) within the interval can be evaluated corresponding to a frequency band.

## 7.2 Simulation design

The constants of any algebraic equation are determined by deriving an equal number of independent equations based on some known points. Similarly, a known set of  $\mathcal{T}_L$  corresponding to different known sets of parametric combinations are required to solve the constants in Equation (7.2). Although the constants are derived using the software 'R', the input needs to be calculated from outside and inserted into the software. Therefore, the set of  $\mathcal{T}_L$  and the sets of parametric combinations need to be evaluated from an outside source. One way of finding the results is to calculate  $\mathcal{T}_L$  using the analytical model at some parametric combinations, which is implemented here. Alternatively,  $\mathcal{T}_L$  can also be measured for various panels representing a range of parametric combinations. In both cases, selecting the appropriate parametric combinations is crucial, which is termed as 'Design of experiment'. There are several design options available and a brief overview of different design options is explained below.

### 7.2.1 Full Factorial Design

The Full Factorial Design (FFD) considers all the combinations of the parameters with all the levels. The total parametric combination of 7 parameters with 3 levels is  $3^7$ , which is a huge number and requires a long computation time. Each parametric combination of the level values is referred to as a point. The points where the level values of all parameters are non-zero are termed as the corner points. The total number of such points are  $2^{\mathcal{N}}$ , where  $\mathcal{N}$  is the number of parameters. The number of corner points for three parameters is 8, which is shown in Table 7.2. The points where only one parameter has non zero level value are termed as the axial points, which are located

at the centre of each side. The total number of such points is  $2\mathcal{N}$ , and the points are shown in Table 7.3. The points where the level value of any one parameter is zero are named as the edge points. The total number of the edge points for  $\mathcal{N}$  parameters with three levels is  $\mathcal{N} \times 2(\mathcal{N} - 1)$ . The parametric combinations of the edge points for 3 parameters are shown in Table 7.4. The centre point is the one with level values set to zero for all parameters. In the full factorial design, the corner points, the axial points, the edge points, the centre point and other points (if available) are included.

Table 7.2: Corner points of the design with 3 parameters and 3 levels.

Run	$t_1$	$t_2$	$t_3$
1	1	1	1
2	1	1	-1
3	1	-1	1
4	1	-1	-1
5	-1	1	1
6	-1	1	-1
7	-1	-1	1
8	-1	-1	-1

Table 7.3: Axial points of the design with 3 parameters and 3 levels.

Run	$t_1$	$t_2$	$t_3$
1	0	0	1
2	0	0	-1
3	0	1	0
4	0	-1	0
5	1	0	0
6	-1	0	0

### 7.2.2 Box-Behnken Design

In the Box-Behnken Design (BBD), the centre point and the edge points are included but not the corner and the axial points (Myers et al., 2016). The number of points for

BBD is less than the points in CCD. The total number of points in BBD for 7 parameters and considering one centre point is 57.

Table 7.4: Edge points of the design with 3 parameters and 3 levels.

Run	$t_1$	$t_2$	$t_3$
1	1	1	0
2	1	-1	0
3	1	0	1
4	1	0	-1
5	-1	1	0
6	-1	-1	0
7	-1	0	1
8	-1	0	-1
9	0	1	1
10	0	1	-1
11	0	-1	1
12	0	-1	-1

### 7.2.3 Central Composite Design

The Central Composite Design (CCD) includes a fewer number of points than the FFD (Ganguli, 2002; Myers et al., 2016). The corner points and the centre point are included in CCD. There are other points similar to the axial points included in CCD, where the non-zero level values of the axial points are set to a value larger than unity. CCD for 7 parameters with 3 levels is used here, and the design is given in Table 7.5. The design is set using the Matlab command 'ccdesign', where the extreme level values are set as  $\pm 2.83$  (rounded to 3 significant figures). Often more than one centre points are used for a smooth response surface when measurement data is considered. Here only one centre points is considered. The total number of point used in this chapter corresponding to 7 parameters with 3 levels having one centre point is 79. As mentioned earlier, four frequency bands are considered in this thesis and model equations differ between the frequency bands.

### 7.2.4 Model verification

Results from the regression model for variation analysis are verified using the results from the analytical model given in Chapter 3. In this regard,  $\mathcal{T}_L$  is calculated for various combinations of parameter level values to reproduce the graphs in Fig 6.1 in Chapter 6. The range of level values is limited to  $\pm 1$ , which corresponds to  $\pm 5\%$  variations in the parameters as considered in Chapter 6. A single parameter is varied keeping the remaining ones fixed and a set of  $\mathcal{T}_L$  is calculated for a set of a single parameter values. Similar to Section 6.2.1, the corresponding  $\Delta\mathcal{T}_L = \mathcal{T}_L - \mathcal{T}_L^{\min}$  is then calculated, where  $\mathcal{T}_L^{\min}$  is the minimum  $\mathcal{T}_L$  in the corresponding frequency band.  $\Delta\mathcal{T}_L$  calculated by the regression model is compared with the corresponding  $\Delta\mathcal{T}_L$  calculated using the analytical model in Chapter 6. The comparison of the graphs generated using the RSM model and the graphs in Fig 6.1 is given in Fig. 7.1.

Although the corresponding graphs are not identical, the range of  $\Delta\mathcal{T}_L$  variations is not far different. As mentioned earlier, predicting the exact value of  $\mathcal{T}_L$  corresponding to a given parametric combination is not the scope of this model. The graphs in Fig 7.1 corresponding to both models show similar trends, and similar conclusions can be made regarding the effects of different parameters on  $\Delta\mathcal{T}_L$  from the corresponding sets of graphs in Fig 7.1. Three colours are used to represent three-parameter variations, where green, blue and red correspond  $h_b$  variation,  $h_1$  variation and  $d$  variation, respectively. The graphs with and without the marker represent the analytical model and the RSM model, respectively.

Figure 7.1 shows that RSM can replicate the graphs that are mostly linear corresponding to the analytical model with higher accuracy. For example, the agreements between the pairs of green graphs at 125 Hz, 250 Hz and 400 Hz bands and the blues graphs at 250 Hz band are good. Each of these graphs exhibits a strong linear relationship between  $\Delta\mathcal{T}_L$  and the corresponding parameter. The curves for RSM deviate from

the original analytical curves having higher order tendencies. This is because the RSM ignores the 3<sup>rd</sup> and higher order effects. The trends of  $\mathcal{T}_L$  corresponding to both models remain the same. The deviations in all cases are less than a dB. Therefore, the model can be used to predict the trend of  $\mathcal{T}_L$  variation for small variations in the parameter values.

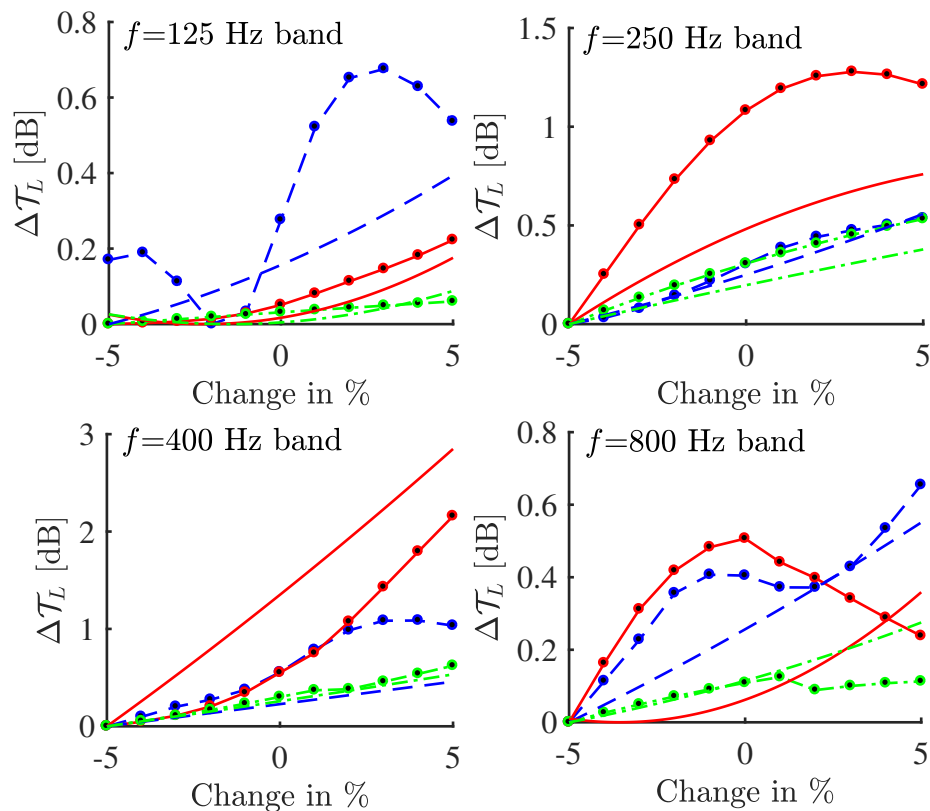


Figure 7.1: Comparison between  $\Delta\mathcal{T}_L$  calculated by RSM (lines with no marker) and the analytical model (lines with marker).  $\Delta\mathcal{T}_L$  values are plotted against the percentage change of each parameter. Dashed line (---), solid line (—) and dotted line (⋯) represent the  $\Delta\mathcal{T}_L$ , corresponding to the variations in  $h_1$ ,  $d$  and  $h_b$ , respectively.

### 7.3 Results

$\mathcal{T}_L$  values corresponding to all the simulations in Table 7.5 are calculated using the analytical model for the four frequency bands, which are given in Table 7.6. The

level data and the calculated  $\mathcal{T}_L$  in each frequency band are inserted separately into the statistical **rsm** package and the unknown coefficients corresponding to each frequency band are derived. The results from the software **R** are displayed in Tables 7.7, 7.8, 7.9 and 7.10 for 125 Hz, 250 Hz, 400 Hz and 800 Hz bands, respectively. The second column of each table shows the values of the unknown coefficients listed in the first column. The third column gives the standard error, and the last two columns correspond to the effectiveness of each parameter on the output. The most effective parameters are marked by  $\star$  signs, and only the coefficients with  $\star$  are displayed in the tables. The coefficients that are not displayed in the tables are insignificant, which are set equal to zero. Inserting the coefficients to Equation (7.2) the model is completed and  $\mathcal{T}_L$  can be calculated for different parameter level values. Finally, a set of parametric values corresponding to the optimum  $\mathcal{T}_L$  is presented in Subsection 7.3.2.

The results from the software **R** are displayed in Tables 7.7, 7.8, 7.9 and 7.10 for 125 Hz, 250 Hz, 400 Hz and 800 Hz bands, respectively. The second column of each table shows the values of the unknown coefficients listed in the first column. The third column gives the standard error, and the last two columns correspond to the effectiveness of each parameter on the output. The most effective parameters are marked by  $\star$  signs, and only the coefficients with  $\star$  are displayed in the tables. The coefficients that are not displayed in the tables are insignificant, which are set equal to zero. Inserting the coefficients to Equation (7.2) the model is completed and  $\mathcal{T}_L$  can be calculated for different parameter level values. Finally, a set of parametric values corresponding to the optimum  $\mathcal{T}_L$  is presented in Subsection 7.3.2.

### 7.3.1 Discussion

In this section, discussions on some results obtained from the regression model are presented. Two types of variation of  $\Delta\mathcal{T}_L$  are discussed here. The first discussion

includes the variation of  $\Delta\mathcal{T}_L$  with respect to the variation of a single parameter, where the level values of the remaining parameters are kept at zero. The second discussion is about the combined effects of any two parameters on  $\Delta\mathcal{T}_L$ , if found significant from the corresponding table.

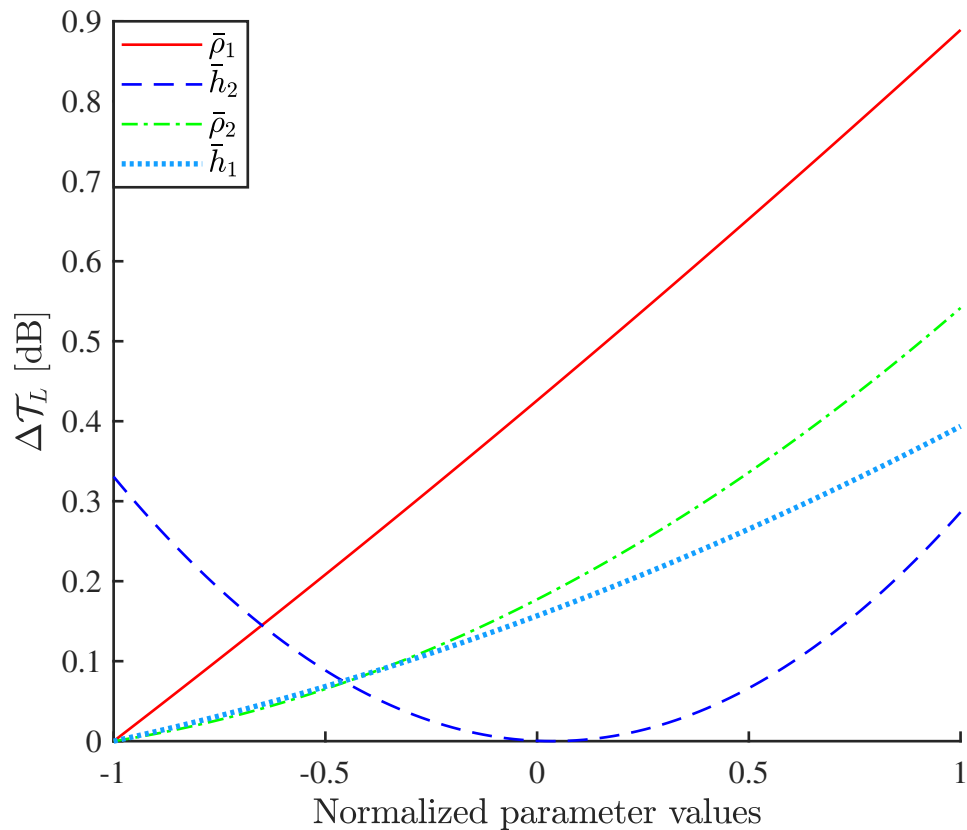


Figure 7.2: Variation in  $\Delta\mathcal{T}_L$  due to the variation in significant parameters at 125 Hz, predicted using RSM. When a single parameter values are varied, the remaining parameters take their respective nominal values.

Table 7.7 shows the results corresponding to 125 Hz band. Ignoring the intercept and the coefficients representing the combined effects, the highest coefficient value at 125 Hz band is  $b_4 = 0.444$  followed by  $b_{22}, b_5$ , and  $b_1$ . This means that the maximum variation in  $\Delta\mathcal{T}_L$  is caused by the variation in  $\rho_1$  followed by the variation in  $h_2, \rho_1$  and  $h_1$ . The effects of the variations of  $h_1, \rho_1$ , and  $\rho_2$  are mainly linear, since only the coefficients corresponding to the linear effects of these parameters are significant.

Whereas, the effect of  $h_2$  variation is mainly non-linear, since only  $b_{22}$  is significant. The positive signs for all these coefficients indicate the increasing trend of  $\Delta\mathcal{T}_L$  with respect to the increase in all these parameters.

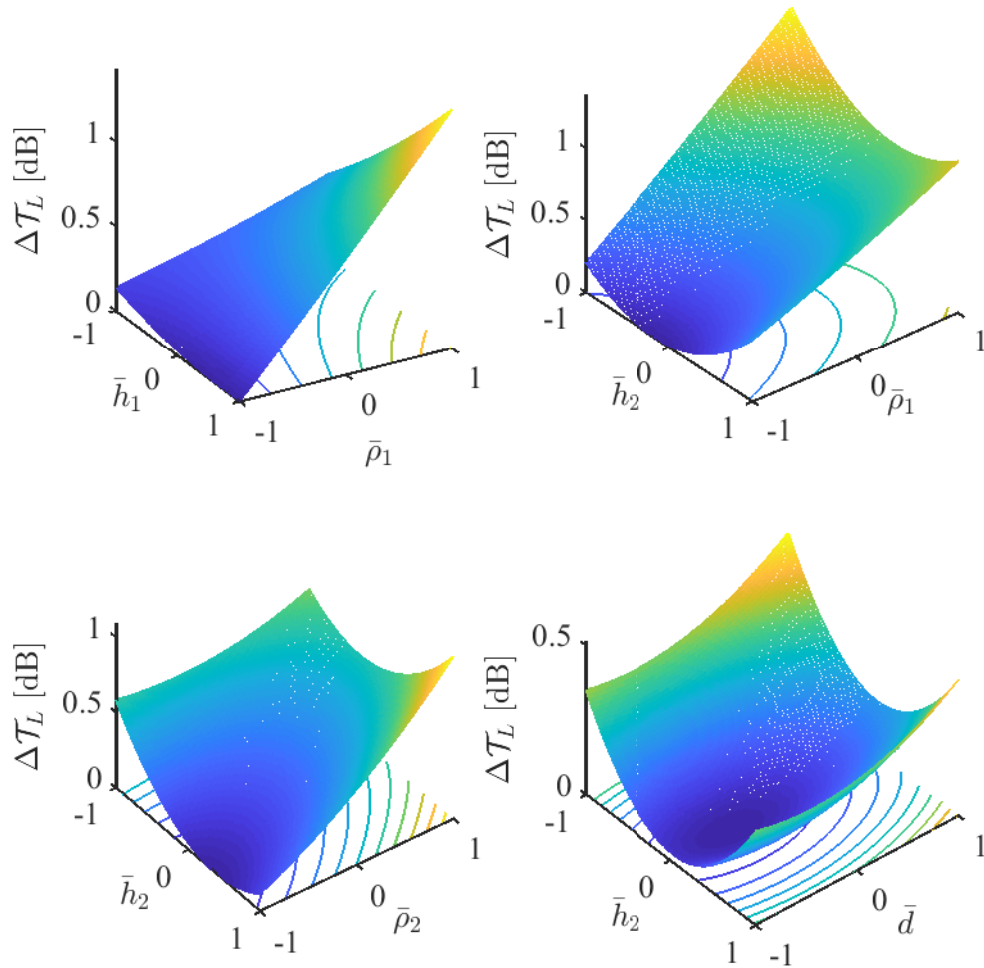


Figure 7.3: Variation in  $\Delta\mathcal{T}_L$  due to the variations in significant parameter pairs at 125 Hz, predicted using RSM. When the values of a parameter pair are varied, the remaining parameters take their respective nominal values.

The pattern of  $\Delta\mathcal{T}_L$  variation is not visible by the results displayed in the tables. The variations in  $\Delta\mathcal{T}_L$  with the variations in each significant parameters are plotted in Fig. 7.2. The level values ranging for -1 to 1 in the figure correspond to a  $\pm 5\%$  variation in the parameters. The figure confirms that the variation of  $\Delta\mathcal{T}_L$  is highly non-linear with respect to  $h_2$ , and  $\Delta\mathcal{T}_L$  variations have some degree of non-linearity with the

variations in  $h_1$  and  $\rho_2$ . The maximum value of  $\Delta\mathcal{T}_L$  for  $\rho_1$  variation is approximately 1 dB, and this is less than 0.5 dB for the variations in the remaining parameters. Due to the parabolic shape of  $\Delta\mathcal{T}_L$  graph corresponding to  $h_2$ , the minimum value of  $\Delta\mathcal{T}_L$  occurs when  $h_2$  level value is located at both ends of the curve with the minimum at its nominal value.

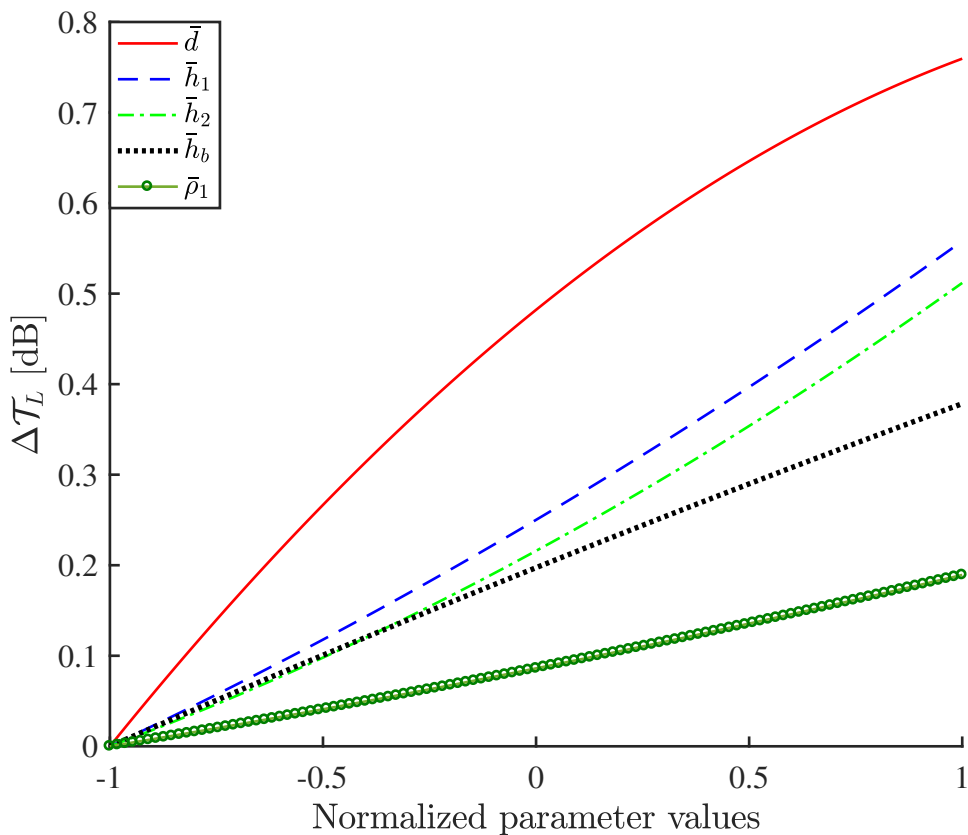


Figure 7.4: Variation in  $\Delta\mathcal{T}_L$  due to the variation in significant parameters at 250 Hz, predicted using RSM. When a single parameter value is varied, the remaining parameters take their respective nominal values.

According to Table 7.7, the combined effects of four parameter pairs are significant in 125 Hz band, which are  $h_1, \rho_1$ ,  $h_2, \rho_1$ ,  $h_2, \rho_2$  and  $h_2, d$ . Figure 7.3 shows the combined effects of these significant pair of parameters, where  $\Delta\mathcal{T}_L$  is plotted against the variation in parameter pairs. Figure 7.3 shows that the combined effects of  $h_1, \rho_1$  have maximum effects on  $\mathcal{T}_L$  and causes a 2 dB variation in  $\Delta\mathcal{T}_L$  when both parameters

take the highest values. Variation in  $\mathcal{T}_L$  with respect to the combined effects of other parameter pairs are approximately less than 1 dB.

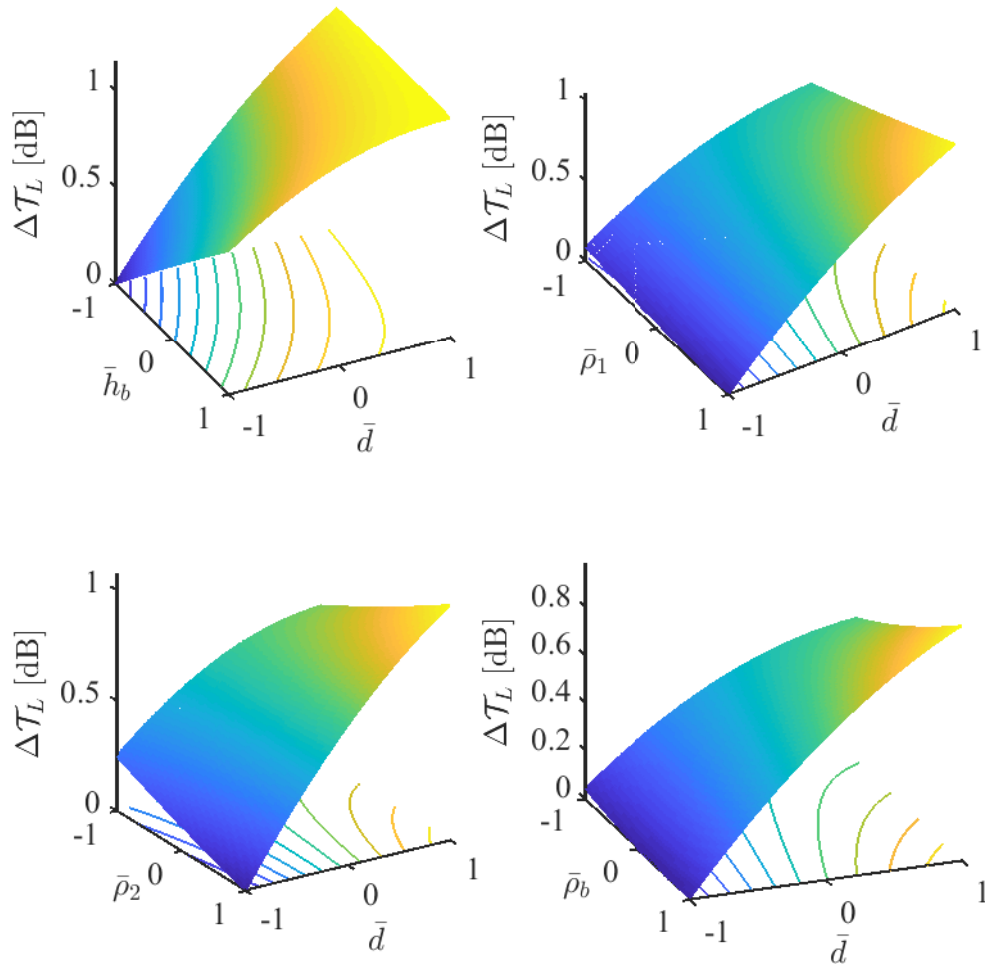


Figure 7.5: Variation in  $\Delta\mathcal{T}_L$  due to the variations in significant parameter pairs at 250 Hz, predicted using RSM. When the values of a parameter pair are varied, the remaining parameters take their respective nominal values.

Table 7.8 shows that the most effective parameter at a  $\pm 5\%$  in 250 Hz band is  $d$  followed by  $h_1, h_2, h_b$  and  $\rho_1$ .  $\Delta\mathcal{T}_L$  varies linearly with all these parameters since the coefficients corresponding to quadratic effects are not significant. The positive signs of the linear coefficient indicate the positive variations of  $\Delta\mathcal{T}_L$  with the parameters. The corresponding graphs are shown in Fig. 7.4. Fig. 7.4 confirms that  $\Delta\mathcal{T}_L$  varies almost positively linearly with all the effective parameters. The maximum variation in

$\Delta\mathcal{T}_L$  with respect to any of these parameter variation is less than a dB. Table 7.8 also shows that the combined effects of the parameter pairs  $h_b, d$ ,  $\rho_1, d$ ,  $\rho_2, d$  and  $\rho_b, d$  are significant. The effects of these significant parameter pairs are shown in Fig. 7.5. The maximum  $\Delta\mathcal{T}_L$  is approximately 1 dB or less in all frequency bands. Variations in  $d$  cause most of the variations in  $\Delta\mathcal{T}_L$ . Therefore,  $d$  is the most significant parameter in this band, and  $\Delta\mathcal{T}_L$  is less sensitive to the remaining parameters.

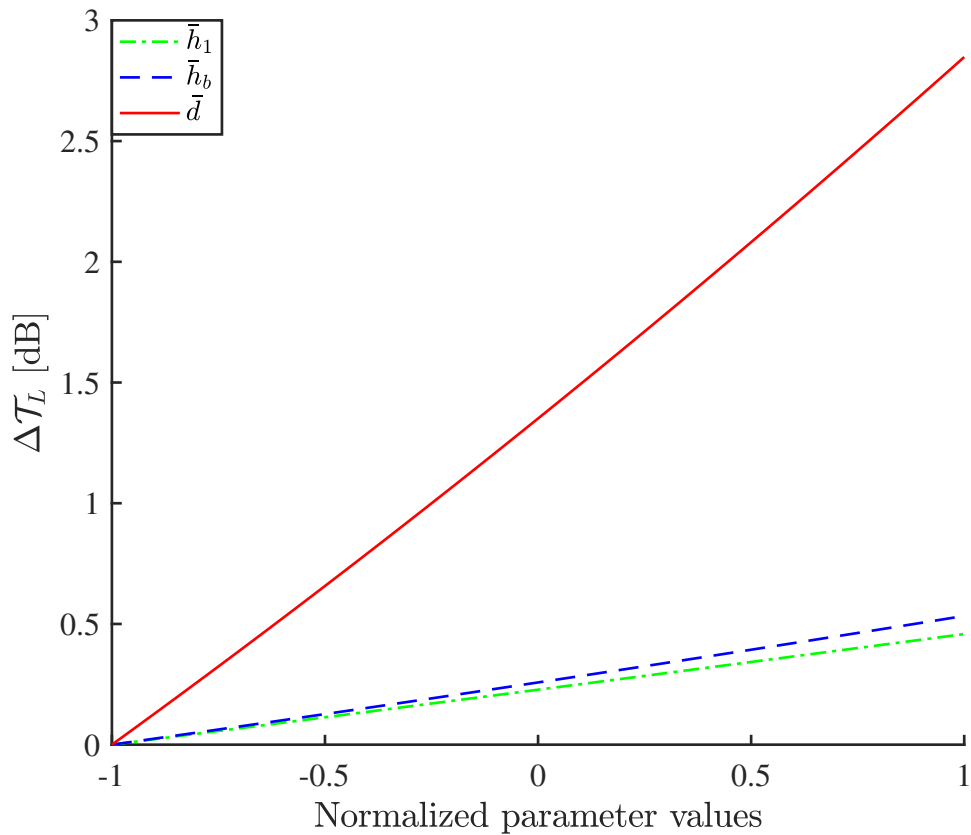


Figure 7.6: Variation in  $\Delta\mathcal{T}_L$  due to the variation in significant parameters at 400 Hz, predicted using RSM. When a single parameter value is varied, the remaining parameters take their respective nominal values.

Table 7.9 shows that  $d$  is the most effective parameter in 400 Hz band, with two more effective parameters  $h_b$  and  $h_1$ . The variations of  $\Delta\mathcal{T}_L$  with respect to these three parameters are positively linear. Figure 7.6 shows the variations of  $\Delta\mathcal{T}_L$  when the effective parameters are varied. A maximum of 3 dB variation in  $\Delta\mathcal{T}_L$  is shown when  $\bar{d}$

is varied and this occurs when  $\bar{d} = 1$  corresponding to +5% variation. The maximum value for  $\Delta\mathcal{T}_L$  is less than one dB for the remaining parameters. Table 7.9 shows that the combined effects of no two parameters are significant at a  $\pm 5\%$  variation.

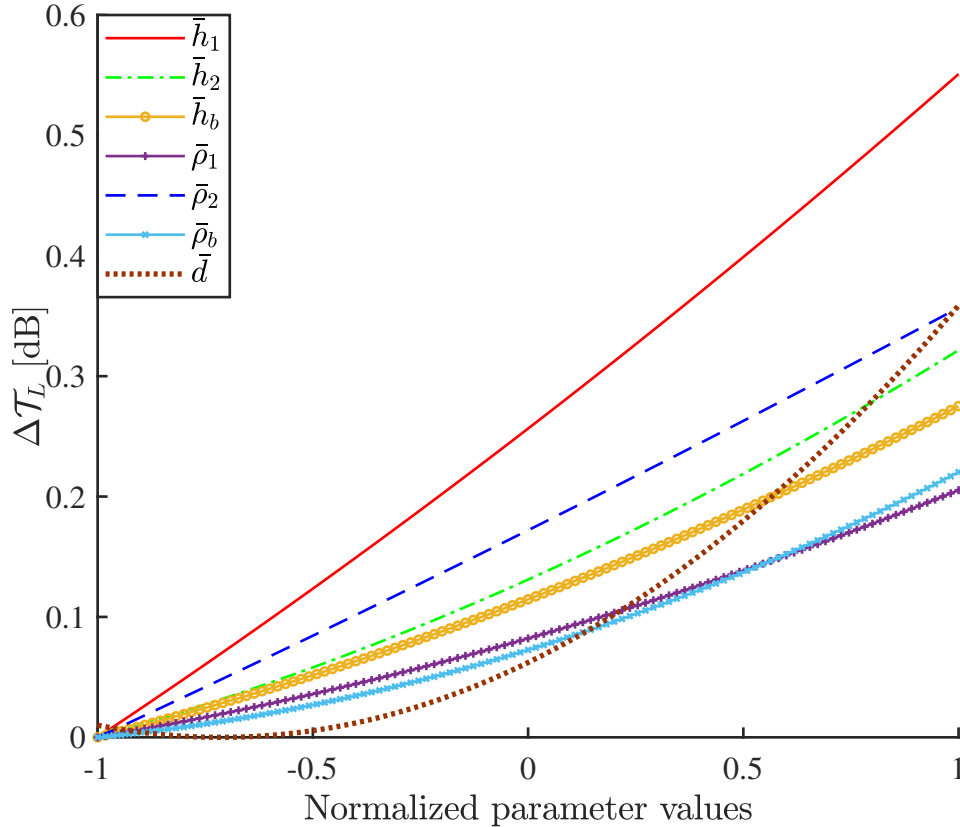


Figure 7.7: Variation in  $\Delta\mathcal{T}_L$  due to the variation in significant parameters at 800 Hz, predicted using RSM. When single parameter values are varied, the remaining parameters take their respective nominal values.

The model considers all the parameters to be significant in 800 Hz band. The most effective parameter in 800 Hz band according to Table 7.10 is  $h_1$  followed by  $\rho_2, d, h_2, h_b, \rho_b$  and  $\rho_2$ . Variation in all these parameters positively affect  $\Delta\mathcal{T}_L$ .  $\Delta\mathcal{T}_L$  variation with  $d$  also have some non-linearity since coefficient term  $b_{77}$  is significant. Only the linear coefficient terms corresponding to the remaining parameters are significant. Therefore,  $\Delta\mathcal{T}_L$  varies mainly linearly with the remaining parameters. The corresponding graph of the variation in  $\Delta\mathcal{T}_L$  with the variation in the parameters is

shown in Fig. 7.10, where a single parameter is varied at a time. The variation in  $\Delta\mathcal{T}_L$  is never more than 0.6 dB for any parameter, although all the parameters are considered as significant. The model makes a relative comparison between the parameters. Therefore, all parameters are treated as significant when their relative effects are of the same order. For that reason, it is always recommended to check the outcome graphically. Despite the maximum  $\Delta\mathcal{T}_L$  is low for a single parameter variation, it could add up to a big number when many parameters are varied simultaneously. The combined effects of the parameter pairs  $h_b d$ ,  $h_2 d$  and  $\rho_2 h_2$  are significant according to Table 7.10, and the corresponding effects are plotted in Fig. 7.8. Figure 7.8 shows that  $\Delta\mathcal{T}_L$  is less sensitive to all these parameter pairs, with combined effects not exceeding 0.6 dB.

### 7.3.2 Optimization

In this section, the stationary point located on the response surface and the corresponding  $\mathcal{T}_L$  are calculated. Comparing  $\mathcal{T}_L$  corresponding to the stationary points and the terminal points,  $\mathcal{T}_L^{\min}$  and  $\mathcal{T}_L^{\max}$  are evaluated. The difference in  $\mathcal{T}_L^{\max}$  and  $\mathcal{T}_L^{\min}$  gives the maximum expected variation ( $\Delta\mathcal{T}_L^{\max}$ ) corresponding to  $\pm 5\%$  variations in the panel parameters. The informations are helpful because in reality,  $\mathcal{T}_L^{\min}$  is always expected to be above a tolerable limit.

The level values at the stationary points are calculated using `rsm` package of **R** in different frequency bands, and are given in Table 7.11. The level values corresponding to the stationary point are often outside the range of  $\pm 1$ , which means that the stationary point lies outside the range of interest of the corresponding parameter. In that case, the level values more than 1 and less than -1 are replaced by  $\pm 1$ , respectively to keep the range within the specified limit. The amended level values are shown in Table 7.11 beside the actual level values given by the software **R**.

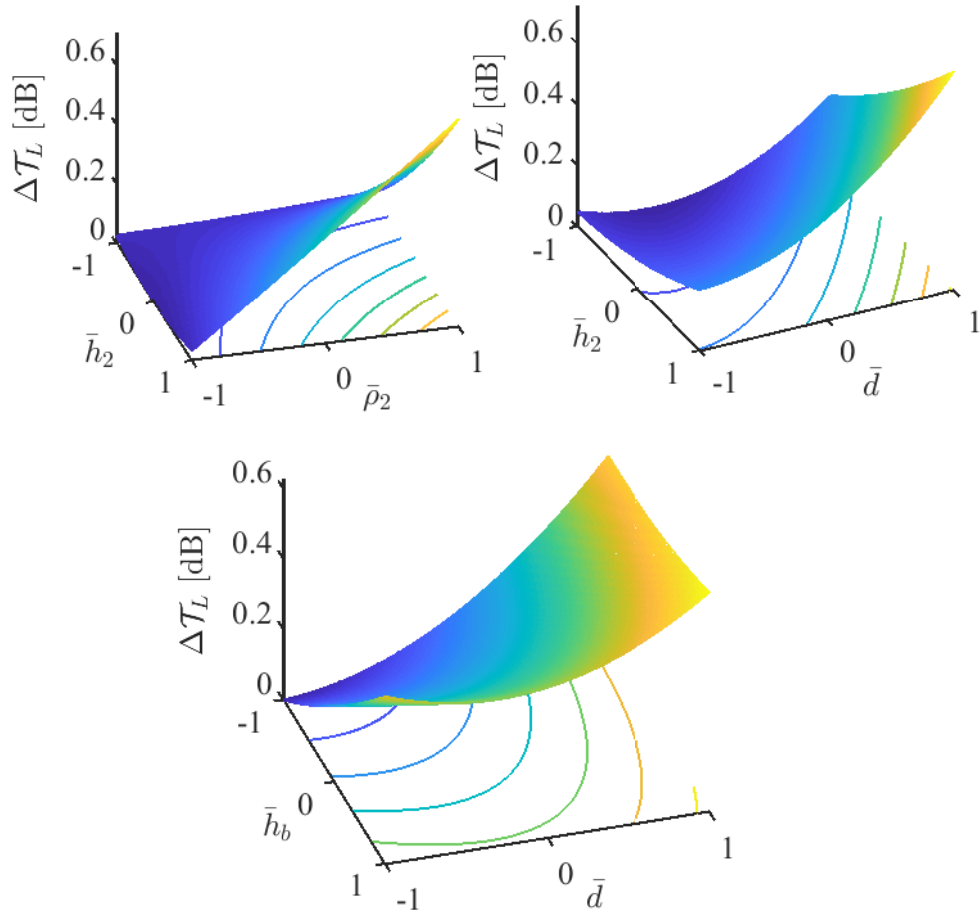


Figure 7.8: Variation in  $\Delta\mathcal{T}_L$  due to the variations in significant parameter pairs at 800 Hz, predicted using RSM. When the values of a parameter pair are varied, the remaining parameters take their respective nominal values.

The corresponding  $\mathcal{T}_L$  in each frequency band is calculated using the model equation of the respective bands. The level values kept within  $\pm 1$  and the coefficients corresponding to a frequency band are inserted into Equation (7.2) to predict  $\mathcal{T}_L$  at the corresponding frequency band. The optimum  $\mathcal{T}_L$  values at four frequency bands calculated using RSM are shown in Table 7.12, which is denoted as  $\mathcal{T}_L^{\text{sta}}$ . The corresponding parameter values are also shown in Table 7.12. Comparing  $\mathcal{T}_L^{\text{sta}}$  with  $\mathcal{T}_L$  for the terminal points,  $\mathcal{T}_L^{\text{min}}$  and  $\mathcal{T}_L^{\text{max}}$  are calculated, and are shown in Table 7.12.  $\Delta\mathcal{T}_L^{\text{max}}$  in different frequency bands are also calculated, which are given in the last row of Table 7.12.

As mentioned earlier that the ranges of parameters do not represent the actual variations in the parameters but the model used here can be useful. The derived model equations are useful when the nominal values set for the parameters are the same and the real variations in the parameters are below the ranges set here. Otherwise, the model equation and the expected variations in  $\mathcal{T}_L$ , i.e.  $\Delta\mathcal{T}_L^{\max}$ ,  $\mathcal{T}_L^{\min}$  and  $\mathcal{T}_L^{\max}$  for any other known variation ranges can be evaluated following the same procedure. It is desirable to keep  $\mathcal{T}_L$  as high as possible. Some adjustment needs to be made when  $\mathcal{T}_L^{\min}$  is too low. Some changes in the panel parameters may be required to increase the overall  $\mathcal{T}_L$ . For example, with  $\pm 5\%$ ,  $d$  is found to increase  $\mathcal{T}_L$  in all frequency bands and thus,  $\mathcal{T}_L$  can be created by increasing the value of  $d$ .

Table 7.5: Design of simulation using CCD for 7 parameters.

Simulation run	$t_1$	$t_2$	$t_3$	$t_4$	$t_5$	$t_6$	$t_7$
1	-1	-1	-1	-1	-1	-1	1
2	-1	-1	-1	-1	-1	1	-1
3	-1	-1	-1	-1	1	-1	-1
4	-1	-1	-1	-1	1	1	1
5	-1	-1	-1	1	-1	-1	-1
6	-1	-1	-1	1	-1	1	1
7	-1	-1	-1	1	1	-1	1
8	-1	-1	-1	1	1	1	-1
9	-1	-1	1	-1	-1	-1	-1
10	-1	-1	1	-1	-1	1	1
11	-1	-1	1	-1	1	-1	1
12	-1	-1	1	-1	1	1	-1
13	-1	-1	1	1	-1	-1	1
14	-1	-1	1	1	-1	1	-1
15	-1	-1	1	1	1	-1	-1
16	-1	-1	1	1	1	1	1
17	-1	1	-1	-1	-1	-1	-1
18	-1	1	-1	-1	-1	1	1
19	-1	1	-1	-1	1	-1	1
20	-1	1	-1	-1	1	1	-1
21	-1	1	-1	1	-1	-1	1
22	-1	1	-1	1	-1	1	-1
23	-1	1	-1	1	1	-1	-1
24	-1	1	-1	1	1	1	1
25	-1	1	1	-1	-1	-1	1
26	-1	1	1	-1	-1	1	-1
27	-1	1	1	-1	1	-1	-1
28	-1	1	1	-1	1	1	1
29	-1	1	1	1	-1	-1	-1
30	-1	1	1	1	-1	1	1
31	-1	1	1	1	1	-1	1
32	-1	1	1	1	1	1	-1
33	1	-1	-1	-1	-1	-1	-1
34	1	-1	-1	-1	-1	1	1
35	1	-1	-1	-1	1	-1	1
36	1	-1	-1	-1	1	1	-1
37	1	-1	-1	1	-1	-1	1
38	1	-1	-1	1	-1	1	-1
39	1	-1	-1	1	1	-1	-1
40	1	-1	-1	1	1	1	1

41	1	-1	1	-1	-1	-1	1
42	1	-1	1	-1	-1	1	-1
43	1	-1	1	-1	1	-1	-1
44	1	-1	1	-1	1	1	1
45	1	-1	1	1	-1	-1	-1
46	1	-1	1	1	-1	1	1
47	1	-1	1	1	1	-1	1
48	1	-1	1	1	1	1	-1
49	1	1	-1	-1	-1	-1	1
50	1	1	-1	-1	-1	1	-1
51	1	1	-1	-1	1	-1	-1
52	1	1	-1	-1	1	1	1
53	1	1	-1	1	-1	-1	-1
54	1	1	-1	1	-1	1	1
55	1	1	-1	1	1	-1	1
56	1	1	-1	1	1	1	-1
57	1	1	1	-1	-1	-1	-1
58	1	1	1	-1	-1	1	1
59	1	1	1	-1	1	-1	1
60	1	1	1	-1	1	1	-1
61	1	1	1	1	-1	-1	1
62	1	1	1	1	-1	1	-1
63	1	1	1	1	1	-1	-1
64	1	1	1	1	1	1	1
65	-2.83	0	0	0	0	0	0
66	2.83	0	0	0	0	0	0
67	0	-2.83	0	0	0	0	0
68	0	2.83	0	0	0	0	0
69	0	0	-2.83	0	0	0	0
70	0	0	2.83	0	0	0	0
71	0	0	0	-2.83	0	0	0
72	0	0	0	2.83	0	0	0
73	0	0	0	0	-2.83	0	0
74	0	0	0	0	2.83	0	0
75	0	0	0	0	0	-2.83	0
76	0	0	0	0	0	2.83	0
77	0	0	0	0	0	0	-2.83
78	0	0	0	0	0	0	2.83
79	0	0	0	0	0	0	0

Table 7.6: Input  $\mathcal{T}_L$  inserted to  $\mathbf{R}$  corresponding to all simulation run at 4 frequency bands, calculated using the analytical model.

Simulation run	125 Hz band	250 Hz band	400 Hz band	800 Hz band
1	13.14	26.17	29.60	33.89
2	13.37	25.70	27.49	33.98
3	13.58	25.44	26.52	33.92
4	13.91	26.90	29.96	34.53
5	13.98	25.73	26.17	33.90
6	14.23	27.03	29.99	34.57
7	14.25	26.97	30.25	34.22
8	14.13	25.28	26.56	33.96
9	13.23	26.46	27.03	34.63
10	13.35	26.51	30.46	34.44
11	13.89	26.28	31.06	34.23
12	13.71	26.23	26.75	34.64
13	14.21	26.39	30.84	34.30
14	14.12	26.49	26.58	34.62
15	13.70	26.22	25.89	34.55
16	14.42	27.36	31.02	34.65
17	13.64	26.07	27.02	33.78
18	13.46	27.28	30.04	34.60
19	14.00	27.37	29.48	34.97
20	14.01	25.88	28.31	34.31
21	13.34	27.33	30.66	34.45
22	13.28	26.07	26.53	33.87
23	14.26	25.82	27.24	34.34
24	14.66	27.97	29.51	35.29
25	13.35	26.65	31.08	34.23
26	13.84	26.77	27.47	34.38
27	13.97	26.72	28.46	34.71
28	14.18	27.76	30.30	35.43
29	13.28	26.84	26.66	34.38
30	13.54	27.68	31.38	34.82
31	14.61	27.77	30.88	35.15
32	14.43	26.54	27.58	34.83
33	13.58	26.31	26.82	34.42
34	13.49	27.28	30.20	34.90
35	13.41	27.17	31.03	34.59
36	13.07	26.05	26.88	34.40
37	14.94	27.47	29.94	35.09
38	15.04	26.31	27.98	34.56
39	15.05	25.93	27.62	34.52
40	15.49	27.94	29.92	35.42
41	13.53	26.60	31.23	34.65
42	13.77	26.96	27.41	35.05
43	13.09	26.75	26.87	34.92

Simulation run	125 Hz band	250 Hz band	400 Hz band	800 Hz band
44	13.61	27.53	31.81	34.99
45	15.01	27.01	28.38	34.94
46	15.14	27.85	30.74	35.53
47	15.34	27.73	31.43	35.17
48	15.22	26.62	27.93	35.03
49	12.90	27.51	30.95	34.64
50	13.04	26.79	27.43	34.18
51	13.71	26.56	27.69	34.85
52	14.20	28.14	30.17	35.64
53	13.89	26.60	27.80	34.25
54	14.10	28.23	30.42	35.31
55	15.50	28.29	30.58	35.65
56	14.99	26.60	28.52	35.53
57	13.10	27.37	27.88	34.67
58	13.10	27.84	31.65	34.97
59	14.18	27.85	31.12	35.46
60	13.89	27.15	28.16	35.31
61	14.06	27.96	31.31	35.18
62	14.09	27.20	28.29	34.71
63	14.96	27.08	28.92	35.29
64	15.65	28.75	31.21	36.08
65	13.39	27.01	29.16	34.29
66	15.05	27.92	28.73	35.95
67	16.17	27.08	30.19	34.35
68	16.55	28.03	28.52	36.06
69	14.23	26.39	28.49	34.87
70	14.41	27.94	29.51	35.43
71	12.82	27.20	28.76	34.71
72	15.28	27.40	27.97	35.55
73	13.83	27.29	28.62	34.38
74	15.47	27.34	28.10	35.65
75	14.15	27.27	28.61	34.87
76	14.49	27.53	29.09	35.67
77	14.42	26.70	27.65	35.53
78	14.72	26.13	31.38	36.36
79	14.32	27.48	28.85	35.37

Table 7.7: Estimation for 125 Hz.

Coefficient	Estimate	Std. Error	t value	Pr(> t )
$b_0$	13.47692	0.329751	40.87	<2.2E-16 ***
$b_1$	0.196848	0.040758	4.8296	1.77E-05 ***
$b_4$	0.444583	0.040756	10.9085	5.77E-14 ***
$b_5$	0.270798	0.040756	6.6445	4.22E-08 ***
$b_{14}$	0.265428	0.045566	5.8251	6.56E-07 ***
$b_{24}$	-0.13208	0.045566	-2.8987	0.005878 **
$b_{25}$	0.210253	0.045566	4.6143	3.54E-05 ***
$b_{27}$	0.092485	0.045566	2.0297	0.048606 *
$b_{22}$	0.308037	0.054959	5.6049	1.37E-06 ***

Table 7.8: Estimation for 250 Hz.

Coefficient	Estimate	Std. Error	t value	Pr(> t )
$b_0$	26.98714	0.36543	73.8503	<2.2E-16 ***
$b_1$	0.278987	0.045168	6.1766	2.02E-07 ***
$b_2$	0.255893	0.045168	5.6653	1.12E-06 ***
$b_3$	0.189202	0.045168	4.1888	0.000137 ***
$b_4$	0.094619	0.045165	2.095	4.21E-02 *
$b_7$	0.379743	0.045168	8.4073	1.27E-10 ***
$b_{37}$	-0.18459	0.0505	-3.6552	0.000695 ***
$b_{47}$	0.137476	0.050496	2.7225	0.009321 **
$b_{57}$	0.153172	0.050496	3.0333	0.004091 **
$b_{67}$	0.106637	0.0505	2.1116	0.040568 *

Table 7.9: Estimation for 400 Hz.

Coefficient	Estimate	Std. Error	t value	Pr(> t )
$b_0$	29.01337	0.735657	39.4387	<2.2E-16 ***
$b_1$	0.229096	0.09093	2.5195	1.55E-02 *
$b_3$	0.266587	0.09093	2.9318	0.005381 **
$b_7$	1.423988	0.09093	15.6603	2.20E-16 ***

Table 7.10: Estimation for 800 Hz.

Coefficient	Estimate	Std. Error	t value	Pr(> t )
$b_0$	34.56802	0.298516	115.7996	< 2.20E-16 ***
$b_1$	0.275459	0.036898	7.4655	2.74E-09 ***
$b_2$	0.160796	0.036898	4.3579	8.02E-05 ***
$b_3$	0.137568	0.036898	3.7284	0.000559 ***
$b_4$	0.102648	0.036895	2.7822	7.99E-03 **
$b_5$	0.178424	0.036895	4.836	1.73E-05 ***
$b_6$	0.110119	0.036898	2.9845	0.004671 **
$b_7$	0.174331	0.036898	4.7247	2.48E-05 ***
$b_{25}$	0.158174	0.04125	3.8345	4.06E-04 ***
$b_{27}$	0.084029	0.041253	2.0369	0.047842 *
$b_{37}$	-0.09935	0.041253	-2.4084	0.020382 *
$b_{77}$	0.122237	0.049753	2.4569	0.018126 *

Table 7.11: Optimum level values of the parameters derived from R. Level values more than 1 and less than -1 are rounded as 1 and -1, respectively to keep the parameter variations within the limit.

	125 Hz band		250 Hz band		400 Hz band		800 Hz band	
	R	Rounded	R	Rounded	R	Rounded	R	Rounded
$h_1$	-0.63	-0.63	-9.07	-1	1.13	1	3.45	1
$h_2$	1.06	1	-9.32	-1	0.17	0.17	-1.91	-1
$h_b$	-0.71	-0.71	-14	-1	-3.8	-1	-2.62	-1
$\rho_1$	-0.33	-0.33	-10	-1	0	0	-9.64	-1
$\rho_2$	-3.35	-1	2.12	1	-0.08	-0.08	-1.02	-1
$\rho_b$	-0.23	-0.23	-6.12	-1	5.85	1	-2.56	-1
$d$	1.61	1	1.45	1	-0.97	-0.97	1.46	1

Table 7.12: Optimum  $\mathcal{T}_L$  and the parameter values at the stationary point with the extreme values of  $\mathcal{T}_L$ .

		125 Hz band	250 Hz band	400 Hz band	800 Hz band
Parameters	$h_1$ (mm)	12.59	12.35	13.65	13.65
	$h_2$ (mm)	13.65	12.35	13.11	12.35
	$h_b$ (mm)	43.40	42.75	42.75	42.75
	$\rho_1$ (kg/m <sup>3</sup> )	824.62	796.54	838.46	796.54
	$\rho_2$ (kg/m <sup>3</sup> )	796.54	880.38	835.11	795.87
	$\rho_b$ (kg/m <sup>3</sup> )	543.67	522.5	577.5	522.5
	$d$ (mm)	99.75	99.75	90.39	99.75
Transmis- sion loss	$\mathcal{T}_L^{\text{sta}}$ (dB)	13.56	26.88	29.09	34.69
	$\mathcal{T}_L^{\text{min}}$ (dB)	12.82	24.50	25.89	27.83
	$\mathcal{T}_L^{\text{max}}$ (dB)	17.05	29.03	31.81	36.36
	$\Delta\mathcal{T}_L^{\text{max}}$ (dB)	4.23	4.52	5.93	8.53

# Chapter 8

## Concluding remarks

### 8.1 Conclusion

In this research, the effects of varying parameters on  $\mathcal{T}_L$  of lightweight double-leaf panels are studied theoretically. The study is carried out using a modified analytical model and a regression model based on RSM. An important feature of the analytical model is that it includes multiple cavities formed between the plates and the beams of a finite double-leaf panel.  $\mathcal{T}_L$  corresponding to the parametric combinations are calculated using the analytical model for 3 m  $\times$  3 m simply supported panels. The effects of the multiple cavities are discussed. The effects of the varying dimensions of the panel are also studied.  $\mathcal{T}_L$  is computed for various boundary conditions. Variations in  $\mathcal{T}_L$  due to minor, e.g.  $\pm 5\%$ , variations in the panel parameters are investigated.

At first, the  $\mathcal{T}_L$  values from the analytical model are verified by the measurement data given by Brunskog (2005), and the agreement between the analytical and measurement is reasonably good. The results are also verified using the theoretical results given by Brunskog (2005). The model is further verified by comparing the first resonance frequencies predicted by the model and the first resonance frequencies calculated using the standard equation. With the panel parameters selected in this thesis, the computation

time is long for frequencies above 3.15 kHz band with a standard pc for a comparatively large panel (surface area above 10 m<sup>2</sup>). Therefore, the infinite panel model by Brunskog (2005) probably is a better option for predicting  $\mathcal{T}_L$  at high frequencies when large panels are considered. In all other cases, the proposed analytical model is recommended.

The model is capable of identifying the structural resonances and cavity resonances. It is observed that  $\mathcal{T}_L$  characteristics in a frequency band is highly dependent on the mode counts. The Fourier sine series is used to describe the plates' displacement. A minimum number of terms in the series is required for the convergence of  $\mathcal{T}_L$ . The convergence of  $\mathcal{T}_L$  and mode counts in a frequency band are found to be closely related. The number of terms required to approximate all the modes in a frequency band is the same as the number of terms required for  $\mathcal{T}_L$  convergence in that band. This indicates the vibration profile of the finite plates is strongly influenced by the resonance vibration field. From the perspective of computation time, it saves a huge amount of time, because the number of terms for  $\mathcal{T}_L$  convergence is easily determined by simply checking for the mode counts in a particular band.

In Chapter 4, the effects of different boundary conditions are studied.  $\mathcal{T}_L$  is calculated for simply supported, clamped and mixed boundary conditions. Two opposite sides parallel to the beams are clamped and the remaining two sides are simply supported in Type 1 boundary condition, whereas, the boundary conditions of the corresponding sides are opposite in the Type 2 boundary condition. Comparisons of  $\mathcal{T}_L$  for these boundary conditions are presented for four square panels. The effects of the boundary conditions are significant in the lower frequency region, where the maximum difference in  $\mathcal{T}_L$  corresponding to different boundary conditions exceeds 7 dB. It is explained that the mode counts in the low frequency regions are less and are widely spread. Therefore, any difference in mode shapes due to difference in the boundary conditions makes  $\mathcal{T}_L$  significantly different. It is noticed that the 1<sup>st</sup> resonance mode of the panel is the most dominating factor that reduces  $\mathcal{T}_L$  in this frequency range. The attached beams

make the panel stiffer, which causes the 1<sup>st</sup> resonance frequency ( $f_1$ ) to shift toward the higher frequencies. Therefore, there is a possibility that  $f_1$  falls within the operating frequency range. The first resonance can be pushed in the lower frequency region and possibly outside the operating frequency range by increasing the panel size. It may not be the case for smaller panels, where the first resonance may well be within the operating range. Therefore, by designing a mechanism for blocking the modal vibration in the lower frequencies would increase  $\mathcal{T}_L$  dramatically. The scope of this thesis is not to propose any such mechanisms, and further studies are recommended on this topic. A parametric analysis is carried out in this thesis, from which some ideas of  $\mathcal{T}_L$  enhancement can be derived.

The effects of the boundary conditions of the panels get reduced as the panel gets larger. Therefore, accurate understanding of the panel details is crucial for the prediction of  $\mathcal{T}_L$  for the smaller panels. The structural resonances are most affected by the boundary conditions at the edges containing the beams' ends. Therefore,  $\mathcal{T}_L$  is more sensitive to variation in  $A$  compared to the variation in  $B$  in the lower frequencies.

The difference in  $\mathcal{T}_L$  decreases with the increase in panel size corresponding to the simply supported and the clamped boundary conditions, which become negligible above a certain frequency band ( $f_b$ ) depending on the size of the panel.  $f_b$  depends on mode count, and beam orientations are also crucial in this regard. Interestingly,  $f_b$  can no longer be identified when the mixed boundary conditions are compared.  $\mathcal{T}_L$  for the mixed boundary conditions is significantly higher than  $\mathcal{T}_L$  corresponding to the remaining two types of boundary conditions. The boundary conditions of real panels are expected to be more complex than the mixed boundary conditions. Therefore,  $\mathcal{T}_L$  for real panels are expected to be significantly higher compared to  $\mathcal{T}_L$  for the fully simply supported or fully clamped boundary conditions corresponding to ideal laboratory conditions.

The value of  $K$  corresponding to the spring constant of the springs assumed between

the beams and the radiating plate is very crucial and needs to be selected accurately. Any incorrect value of  $K$  may lead to significant error in  $\mathcal{T}_L$  prediction. At the moment,  $K$  is selected by trial and error to best fit any relevant measurement data or reliable  $\mathcal{T}_L$  predictions. The low frequency region is not affected by the coupling conditions, the structural resonances, i.e. the boundary conditions, are the most significant parameter in this region.  $\mathcal{T}_L$  characteristics vary in the higher frequency region depending on the choice of  $K$  value. Therefore, correct values of  $K$  are necessary for making accurate conclusion.

One of the core contributions of this thesis is the consideration of the multiple cavities for the finite panel model. The effects of multiple cavities are analysed in detail. The findings are given in this paragraph and in the next few paragraphs. The cavity conditions have no effects in the very low frequency region around the first resonance frequency. The parameters that influence the structural resonances are significant in this region. Therefore, a proper design of the panel to suppress or weaken the 1<sup>st</sup> resonance can increase  $\mathcal{T}_L$  considerably in this region. Another option could be to push the frequency down outside of the operating range by proper selection of the panel dimension and material parameters.

The effects of multiple cavities begin around  $f_0$ . Separate resonances take place in different cavities causing multiple mass-air-mass resonance dips in  $\mathcal{T}_L$  curve compared to a single dip corresponding to the single cavity case. As a result,  $\mathcal{T}_L$  decreases in this frequency region in multiple cavity case. This characteristic can be utilized where low  $\mathcal{T}_L$  is desired. Otherwise, these dips are expected to be suppressed or minimized in the presence of the absorbing materials in the cavities.

A rise in  $\mathcal{T}_L$  occurs after  $f_0$  up to a certain frequency  $f_t$ , beyond which a minor differences in  $\mathcal{T}_L$  are noticed. Multiple cavity consideration is most effective in the frequency range between  $f_0$  and  $f_t$ , and the range gets wider as the panel size increases. In this range, the plate vibration is mainly global, meaning the vibrations of different

area of the plates are correlated. Disturbance in any part of the panel causes disturbance to the entire vibration profile.  $f_t$  is dependent on the panel dimension, cavity width and the bending wavelength of the panel.  $f_t$  is found between the frequency bands, where the corresponding wavelength ( $\lambda_t$ ) and  $l$  maintain the following relation  $2\lambda_t < l < 3\lambda_t$ . Therefore, it is possible to control the location of  $f_t$  by varying the wavelength or the cavity width, i.e. by a proper design of the panel.

The two key features of the panel are the mass and the stiffness. The variation of different parameters affect the overall mass and stiffness. Therefore, the effects of different parameters are understood in terms of the variation in panel mass and panel stiffness. Increase in  $h_1, h_2, \rho_1$  and  $\rho_2$  increase the plate mass and causes  $\mathcal{T}_L$  to increase according to mass law. Increase in these parameters also decrease the resonance frequencies and increase  $f_{cr}$  of the corresponding plates. Therefore, thickening the plates and/or using denser material for plates,  $\mathcal{T}_L$  can be increased and the  $f_{cr}$  can be pushed out of the operating frequency range. The values of all these parameters need to be within the limit for lightweight panels.  $E_1$  and  $E_2$  increase the panel stiffness without any contribution to the panel mass. Therefore,  $\mathcal{T}_L$  does not increase much with the increase in  $E_1$  or  $E_2$ . The main contributions of an increase in  $E_1$  or  $E_2$  is in an increase in  $f_p$  and a decrease in  $f_{cr}$  of the corresponding plate. Therefore, materials with comparatively less Young's moduli are more appropriate for the plates.

The beams act as an obstacle to the panel vibration, and  $\mathcal{T}_L$  can be increased by increasing these obstacles. Two beam parameters  $E_b$  and  $\rho_b$  act in opposite manner below 500 Hz, and  $\mathcal{T}_L$  increase with both these parameters above 500 Hz.  $h_b$  positively affects  $\mathcal{T}_L$  in all frequency bands. Therefore, making beams with material having higher Young's modulus will boost  $\mathcal{T}_L$  above 500 Hz. Thick and massive beams will increase  $\mathcal{T}_L$  in all frequency region and also will compensate for the negative effects of having higher  $E_b$  in the lower frequency. Therefore, higher values for  $h_b$  and  $\rho_b$  are recommended, and  $E_b$  needs to be selected depending on the frequency range of interest.

When the frequency range is broad, higher values for all these beam parameters within the allowable limits are recommended.

Increase in  $d$  increases  $\mathcal{T}_L$  because higher values of  $d$  mean that the beam heights are larger, which adds to the stiffness of the beams. Increase in  $d$  also lowers  $f_{\text{cav}}$ , which occurs in the higher frequency region. As a result,  $\mathcal{T}_L$  decreases in the higher frequencies with considerably large values of  $d$ . It is expected that the positive effects of  $d$  on  $\mathcal{T}_L$  can be retained by restricting the cavity resonances. One option of restricting these cavity resonances is the use of absorbing materials in the cavities. Therefore, it is recommended that the optimum value of  $d$  should be selected so that  $f_{\text{cav}}$  becomes high and falls outside the operating frequency range when no absorbing materials are used.

Chapters 6 and 7 deal with the variations in  $\mathcal{T}_L$  between the nominally identical panels caused by small scale variations in the panel parameters. Understanding the physical mechanisms has not been the primary objective here. The goal is to demonstrate a method and a regression model for making such analysis. Chapter 6 considers the analytical model for making the analysis, where three parameters are considered. The regression model in Chapter 7 is useful when many parameters are considered or frequencies of interest are high. The expected variations of  $\mathcal{T}_L$  through a 3 m  $\times$  3 m panel due to a  $\pm 5\%$  variation in parameters are studied in both Chapter 6 and Chapter 7 just as an example, and may not be the case in reality. The results in Chapter 6 and Chapter 7 are still useful. Once the exact ranges of variation for the corresponding panel parameters are known, the expected variations in  $\mathcal{T}_L$  can be derived by interpolation or extrapolation if the ranges are not very different from  $\pm 5\%$ . The regression model in Chapter 7 uses an algebraic equation to predict  $\mathcal{T}_L$  for any small scale variations within a tolerable limit. The regression model is useful to estimate the maximum expected variations in  $\mathcal{T}_L$  due to different variations in the panel parameters.

## 8.2 Future works

No measurements of test panels have been carried out for this research. Therefore, experiment-based research works on different panels are recommended as future works. The same panels with different materials and designs are used in other industries, such as aerospace, marine, railway. The analytical model is capable of simulating  $\mathcal{T}_L$  of panels used for various applications and it can be used as a supporting tool for analyzing the measurement data.

The finite panel model is suitable for the smaller panels and the infinite panel model is appropriate for the large panels. It is hard to classify the small and large panels based on the size only. The transition from a small panel to a large panel depends on material properties and the geometry of the panel. Panels with dimensions  $3 \text{ m} \times 3 \text{ m}$  and larger can be considered as large panels for the panels studied in this thesis. This dimension values may differ for panels with different parametric values. I propose as a future work to determine the critical dimension  $\mathcal{D}_{cr}$  irrespective of the material properties and the dimension of the panel.  $\mathcal{D}_{cr}$  represents the transition from the small to large panel and will be of the form

$$\mathcal{D}_{cr} = f(A, B, \rho_i, h_i, E_i).$$

It will then be easier to predict  $\mathcal{T}_L$  with the appropriate model.

In this thesis, I have used a regression model and made some discussions on the trend of the  $\mathcal{T}_L$  with respect to the variations in the panel parameters. This method of deriving a regression model can be tried for analysing more complex structures. Some structures are too complex for deriving a mathematical model. RSM based regression model can be an option for such panels. The regression model requires some output values at various parametric combinations, either from models or through taking measurements. The outputs for the complex structures can be found by taking measurements on various panels of different parametric combinations. I propose to

keep the number of parameters small. Otherwise, the number of required test panels with different parametric combinations will be large.

## References

- Beranek & Work. (1949). Sound transmission through multiple structures containing flexible blankets. *The Journal of the Acoustical Society of America*, 21(4), 419–428.
- Bradley & Birta. (2001). A simple model of the sound insulation of gypsum board on resilient supports. *Noise Control Engineering Journal*, 49(5), 216–223.
- Brunskog. (2002). *Acoustic excitation and transmission of lightweight structures*. Div. Engineering Acoustics, LTH.
- Brunskog. (2005). The influence of finite cavities on the sound insulation of double-plate structures. *The Journal of the Acoustical Society of America*, 117(6), 3727–3739.
- Brunskog. (2012). The forced sound transmission of finite single leaf walls using a variational technique. *The Journal of the Acoustical Society of America*, 132(3), 1482–1493.
- Brunskog & Hammer. (2003). Prediction model for the impact sound level of lightweight floors. *Acta acustica united with acustica*, 89(2), 309–322.
- Carneal & Fuller. (2004). An analytical and experimental investigation of active structural acoustic control of noise transmission through double panel systems. *Journal of Sound and Vibration*, 272(3-5), 749–771.
- Chen & Soares. (2008). Spectral stochastic finite element analysis for laminated composite plates. *Computer Methods in Applied Mechanics and Engineering*, 197(51), 4830–4839.
- Cheng & Xiao. (2005). Probabilistic free vibration and flutter analyses of suspension bridges. *Engineering structures*, 27(10), 1509–1518.
- Cheng & Xiao. (2007). Probabilistic free vibration analysis of beams subjected to axial loads. *Advances in Engineering Software*, 38(1), 31–38.
- Chung. (2012). Vibration field of a double-leaf plate with random parameter functions. *Acoustics Australia*, 40(3), 203–210.
- Chung & Emms. (2008). Fourier series solutions to the vibration of rectangular lightweight floor/ceiling structures. *ACTA Acustica united with Acustica*, 94(3), 401–409.

- Chung, Emms & Fox. (2014). Vibration reduction in lightweight floor/ceiling systems with a sand-sawdust damping layer. *Acta Acustica united with Acustica*, 100(4), 628–639.
- Craik & Smith. (2000). Sound transmission through double leaf lightweight partitions part i: airborne sound. *Applied Acoustics*, 61(2), 223–245.
- Craik & Steel. (1989). The effect of workmanship on sound transmission through buildings: Part 1—airborne sound. *Applied Acoustics*, 27(1), 57–63.
- Cremer. (1942). Theory of the sound attenuation of thin walls with oblique incidence. *Architectural Acoustics, Benchmark Papers in Acoustics*, 10, 367–399.
- Cremer & Heckl. (2013). *Structure-borne sound: structural vibrations and sound radiation at audio frequencies*. Springer Science & Business Media.
- Crocker & Price. (1969). Sound transmission using statistical energy analysis. *Journal of Sound and Vibration*, 9(3), 469–486.
- Cummings & Mulholland. (1968). The transmission loss of finite sized double panels in a random incidence sound field. *Journal of Sound and Vibration*, 8(1), 126–133.
- Daudin & Liu. (2016). Vibroacoustic behaviour of clamped double-wall panels lined with poroelastic materials. In *Proceedings of the 23rd international congress on sound and vibration* (Vol. 341).
- Davy. (2009). Predicting the sound insulation of single leaf walls: Extension of cremer's model. *The Journal of the Acoustical Society of America*, 126(4), 1871–1877.
- Delaney & Bazley. (1969). Acoustical characteristics of fibrous absorbent materials. *Aero Report Ac37, National Physical Laboratory*.
- Dym & Shames. (2013). *Solid mechanics*. Springer.
- Fahy. (2007). *Sound and structural vibration: radiation, transmission and response*. Academic Press.
- Fletcher. (2012). *Computational galerkin methods*. Springer Berlin Heidelberg.
- Ford, Lord & Walker. (1967). Sound transmission through sandwich constructions. *Journal of Sound and Vibration*, 5(1), 9–21.
- Ganguli. (2002). Optimum design of a helicopter rotor for low vibration using aeroelastic analysis and response surface methods. *Journal of Sound and Vibration*, 258(2), 327–344.
- Gao, Song & Tin-Loi. (2010). Probabilistic interval analysis for structures with uncertainty. *Structural Safety*, 32(3), 191–199.

- Gardonio & Elliott. (1999). Active control of structure-borne and airborne sound transmission through double panel. *Journal of Aircraft*, 36(6), 1023–1032.
- Gerhards. (2007). Effect of moisture content and temperature on the mechanical properties of wood: an analysis of immediate effects. *Wood and Fiber Science*, 14(1), 4–36.
- Gupta. (1970). Natural flexural waves and the normal modes of periodically-supported beams and plates. *Journal of Sound and Vibration*, 13(1), 89–101.
- Hațiegan, Hațiegan, Gillich, Hamat, Vasile & Stroia. (2018). Natural frequencies of thin rectangular plates clamped on contour using the finite element method. In *Iop conference series: Materials science and engineering* (Vol. 294, p. 012033).
- Johansson. (2000). Field measurements of 170 nominally identical timber floors: a statistical analysis. In *International congress on noise control engineering: 27/08/2000-30/08/2000* (pp. 330–334).
- Kinsler, Frey, Coppens & Sanders. (1999). *Fundamentals of acoustics*. Wiley-VCH.
- Kropp & Rebillard. (1999). On the air-borne sound insulation of double wall constructions. *Acta Acustica united with Acustica*, 85(5), 707–720.
- Legault & Atalla. (2009). Numerical and experimental investigation of the effect of structural links on the sound transmission of a lightweight double panel structure. *Journal of Sound and Vibration*, 324(3-5), 712–732.
- Legault, Mejdı & Atalla. (2011). Vibro-acoustic response of orthogonally stiffened panels: The effects of finite dimensions. *Journal of Sound and Vibration*, 330(24), 5928–5948.
- Leissa. (1973). The free vibration of rectangular plates. *Journal of Sound and Vibration*, 31(3), 257–293.
- Leppington, Heron, Broadbent & Mead. (1987). Resonant and non-resonant acoustic properties of elastic panels. ii. the transmission problem. *Proceedings of the Royal Society of London. Series A, Mathematical and Physical Sciences*, 309–337.
- Li & Cheng. (2008). Mechanisms of active control of sound transmission through a linked double-wall system into an acoustic cavity. *Applied Acoustics*, 69(7), 614–623.
- Li & Liang. (2007). Vibro-acoustic analysis and optimization of damping structure with response surface method. *Materials & design*, 28(7), 1999–2007.
- Li, Zhang, Cheng & Yu. (2010). Effectiveness of t-shaped acoustic resonators in low-frequency sound transmission control of a finite double-panel partition. *Journal of Sound and Vibration*, 329(22), 4740–4755.

- Liang, Lin & Zhu. (2007). Acoustic analysis of damping structure with response surface method. *Applied Acoustics*, 68(9), 1036–1053.
- Lin & Garrelick. (1977). Sound transmission through periodically framed parallel plates. *The Journal of the Acoustical Society of America*, 61(4), 1014–1018.
- Liu & Catalan. (2017). External mean flow influence on sound transmission through finite clamped double-wall sandwich panels. *Journal of Sound and Vibration*, 405, 269–286.
- Liu & Daudin. (2017). Analytical modelling of sound transmission through finite clamped double-wall sandwich panels lined with poroelastic materials. *Composite Structures*, 172, 359–373.
- Lodygowski & Sumelka. (2006). Limitations in application of finite element method in acoustic numerical simulation. *Journal of Theoretical and Applied Mechanics*, 44(4), 849–865.
- London. (1949). Transmission of reverberant sound through single walls. *J. Research Nat. Bur. of Stand*, 42(605), 2.
- London. (1950). Transmission of reverberant sound through double walls. *The Journal of the Acoustical Society of America*, 22(2), 270–279.
- Loucks, Beek, V., Stedinger, Dijkman & Villars. (2005). *Water resources systems planning and management: an introduction to methods, models and applications*. Paris: Unesco.
- Mace. (1980a). Periodically stiffened fluid-loaded plates, i: Response to convected harmonic pressure and free wave propagation. *Journal of Sound and Vibration*, 73(4), 473–486.
- Mace. (1980b). Sound radiation from a plate reinforced by two sets of parallel stiffeners. *Journal of Sound and Vibration*, 71(3), 435–441.
- Machado, Louzada, Santos, Nunes, Anjos, Rodrigues, . . . Pereira (2014). Variation of wood density and mechanical properties of blackwood (acacia melanoxylon r. br.). *Materials and Design (1980-2015)*, 56, 975–980.
- Manohar & Adhikari. (1998). Dynamic stiffness of randomly parametered beams. *Probabilistic Engineering Mechanics*, 13(1), 39–51.
- Mao & Pietrzko. (2005). Control of sound transmission through double wall partitions using optimally tuned helmholtz resonators. *Acta Acustica united with Acustica*, 91(4), 723–731.
- Mazur-Śniady, Misiurek, Szyłko-Bigus & Śniady. (2013). Fuzzy stochastic vibrations of double-beam complex system as model sandwich beam with uncertain parameters. *ISRN Applied Mathematics*, 2013.

- Mead. (1975). Wave propagation and natural modes in periodic systems: I. mono-coupled systems. *Journal of Sound and Vibration*, 40(1), 1–18.
- Mead & Pujara. (1971). Space-harmonic analysis of periodically supported beams: response to convected random loading. *Journal of Sound and Vibration*, 14(4), 525–541.
- Memmo, Ricci, Boffa, Maio & Monaco. (2016). Statistical recognition of structural health in composites through ultrasonic testing. In *19th world conference on non-destructive testing* (Vol. 21).
- Moore & Lyon. (1991). Sound transmission loss characteristics of sandwich panel constructions. *The Journal of the Acoustical Society of America*, 89(2), 777–791.
- Mosharrof, Brunskog, Ljunggren & Ågren. (2011). An improved prediction model for the impact sound level of lightweight floors: Introducing decoupled floor-ceiling and beam-plate moment. *Acta Acustica united with Acustica*, 97(2), 254–265.
- Mosharrof & Chung. (2016). Effects of finite cavities within a finite double-leaf panel on sound transmission loss. *Proceedings of ACOUSTICS 2016*.
- Mosharrof, Ljunggren, Ågren & Brunskog. (2009). Prediction model for the impact sound pressure level of decoupled lightweight floors. In *International congress and exposition on noise control engineering: 23/08/2009-26/08/2009* (pp. 2038–2046).
- Mulholland, Parbrook & Cummings. (1967). The transmission loss of double panels. *Journal of Sound and Vibration*, 6(3), 324–334.
- Myers, Montgomery & Anderson-Cook. (2016). *Response surface methodology: Process and product optimization using designed experiments*. John Wiley Sons, Incorporated.
- Onkar & Yadav. (2005). Forced nonlinear vibration of laminated composite plates with random material properties. *Composite Structures*, 70(3), 334–342.
- Öqvist. (2010). *Variations in sound insulation in lightweight timber constructions*. Luleå University of Technology.
- Roussos. (1984). Noise transmission loss of a rectangular plate in an infinite baffle. *The Journal of the Acoustical Society of America*, 75(S1), S2–S3.
- Sewell. (1970). Transmission of reverberant sound through a single-leaf partition surrounded by an infinite rigid baffle. *Journal of Sound and Vibration*, 12(1), 21–32.
- Sharp. (1978). Prediction methods for the sound transmission of building elements. *Noise Control Engineering*, 11(2), 53–63.

- Shen, Xin & Lu. (2012). Theoretical model for sound transmission through finite sandwich structures with corrugated core. *International Journal of Non-Linear Mechanics*, 47(10), 1066–1072.
- Smith. (2012). *An investigation into the strength properties of reclaimed timber joists* (Unpublished doctoral dissertation). Northumbria University.
- Sun & Richards. (1985). Prediction of total loss factors of structures, i: Theory and experiments. *Journal of Sound and Vibration*, 103(1), 109–117.
- Sun, Sun, Chow & Richards. (1986). Predictions of total loss factors of structures, part ii: Loss factors of sand-filled structure. *Journal of Sound and Vibration*, 104(2), 243–257.
- Sung & Jan. (1997). The response of and sound power radiated by a clamped rectangular plate. *Journal of Sound and Vibration*, 207(3), 301–317.
- Tadeu & Mateus. (2001). Sound transmission through single, double and triple glazing. experimental evaluation. *Applied Acoustics*, 62(3), 307–325.
- Takahashi. (1983). Sound radiation from periodically connected double-plate structures. *Journal of Sound and Vibration*, 90(4), 541–557.
- Timoshenko & Woinowsky-Krieger. (1940). *Theory of plates and shells, by s. timoshenko*,. McGraw-Hill Book Company.
- Trevathan & Pearse. (2008). The effect of workmanship on the transmission of airborne sound through light framed walls. *Applied Acoustics*, 69(2), 127–131.
- Vaicaitis. (1974). Free vibrations of beams with random characteristics. *Journal of Sound and Vibration*, 35(1), 13–21.
- Ventsel & Krauthammer. (2001). *Thin plates and shells: Theory: Analysis, and applications*. CRC Press.
- Vigran. (2008). *Building acoustics*. CRC Press.
- Wang, Lu, Woodhouse, Langley & Evans. (2005). Sound transmission through lightweight double-leaf partitions: theoretical modelling. *Journal of Sound and Vibration*, 286(4-5), 817–847.
- White & Powell. (1966). Transmission of random sound and vibration through a rectangular double wall. *The Journal of the Acoustical Society of America*, 40(4), 821–832.
- Xin & Lu. (2009). Analytical and experimental investigation on transmission loss of clamped double panels: Implication of boundary effects. *The Journal of the Acoustical Society of America*, 125(3), 1506–1517.

- Xin & Lu. (2010). Analytical modeling of fluid loaded orthogonally rib-stiffened sandwich structures: sound transmission. *Journal of the Mechanics and Physics of Solids*, 58(9), 1374–1396.
- Xin & Lu. (2011a). Analytical modeling of sound transmission through clamped triple-panel partition separated by enclosed air cavities. *European Journal of Mechanics-A/Solids*, 30(6), 770–782.
- Xin & Lu. (2011b). Transmission loss of orthogonally rib-stiffened double-panel structures with cavity absorption. *The Journal of the Acoustical Society of America*, 129(4), 1919–1934.
- Xin, Lu & Chen. (2008). Vibroacoustic behavior of clamp mounted double-panel partition with enclosure air cavity. *The Journal of the Acoustical Society of America*, 124(6), 3604–3612.
- Xing & Liu. (2009). New exact solutions for free vibrations of thin orthotropic rectangular plates. *Composite Structures*, 89(4), 567–574.
- Yang, Mace & Kingan. (2018). Wave and finite element method for predicting sound transmission through finite multi-layered structures with fluid layers. *Computers & Structures*, 204, 20–30.
- Zhou, Lainé, Ichchou & Zine. (2015). Wave finite element method based on reduced model for one-dimensional periodic structures. *International Journal of Applied Mechanics*, 7(02), 1550018.

# Appendix A

Evaluation of the Integrals and the final form of the governing equations for Type 1 and Type 2 boundary conditions are given here. The integrals in Equation (4.11) to Equation (4.16) corresponding to the mixed boundary conditions are calculated in this Appendix based the appropriate modal functions. Two type of mixed boundary conditions, Type 1 and Type 2, are considered in this thesis. The values of the integrals are given separately for both these types.

## A.1 Type 1 boundary condition

The modal functions corresponding to the Type 1 boundary conditions are

$$\mathcal{A}_m(x) = \sqrt{\frac{2}{A}} \sin k_m x, \mathcal{B}_n(y) = \sqrt{\frac{2}{3A}} (1 - \cos 2k_n y),$$

and with these modal functions, the plate displacements take the form

$$w_i(x, y) = \frac{2}{\sqrt{3A}} \sum_{m,n=1}^M C_{mn}^{i,i} \sin k_m x (1 - \cos 2k_n y). \quad (\text{A.1})$$

The terms  $\mathcal{G}\mathcal{A}_m(x)$  and  $\mathcal{D}_i\mathcal{A}_m(x)\mathcal{B}_n(y)$  corresponding to the selected  $\mathcal{A}_m(x)$  and  $\mathcal{B}_n(y)$  (type 1 boundary condition) are expressed as

$$\begin{aligned}\mathcal{G}\mathcal{A}_m(x) &= \left(E_b I_b k_m^4 - A_b \rho_b \omega^2\right) \mathcal{A}_m(x) \\ \mathcal{D}_i\mathcal{A}_m(x)\mathcal{B}_n(y) &= D_i \left( k_m^4 \mathcal{B}_n(y) - \sqrt{\frac{2}{3A}} (2k_n)^4 \cos 2k_n y \right. \\ &\quad \left. - 2\sqrt{\frac{2}{3A}} k_m^2 (2k_n)^2 \cos 2k_n y \right) \mathcal{A}_m(x) - \sigma_i \omega^2 \mathcal{A}_m(x) \mathcal{B}_n(y).\end{aligned}$$

Inserting  $\mathcal{A}_m(x)$ ,  $\mathcal{B}_n(y)$ ,  $\alpha_m(x)$  and  $\beta_n(y)$  in Equation (4.11) to Equation (4.16) the integrals corresponding to the Type 1 boundary conditions are evaluated as

$$\begin{aligned}I_{mm'}^{s,x} &= \begin{cases} 1 & m = m', \\ 0 & m \neq m', \end{cases}, & I_{nn'}^{c,y} &= \begin{cases} 1 & n = n', \\ \frac{2}{3} & n \neq n', \end{cases}, \\ II_{mm'}^{sx} &= \begin{cases} \frac{4m}{\pi(m^2 - m'^2)} & m = m' \\ 0 & m \neq m' \end{cases}, & II_{nn'}^{c,j} &= \begin{cases} \sqrt{\frac{l}{3A}} & n' = 0, \\ -(-1)^{n'j} \sqrt{\frac{l}{3A}} & 2n = n', \\ \Pi_{\text{cav}} & \text{Otherwise,} \end{cases}.\end{aligned}$$

where

$$\begin{aligned}\Pi_{\text{cav}} &= \frac{2\sqrt{Al}}{\pi} \left[ \frac{1}{nl + n'A} \sin \left( \frac{(nl + n'A)n\pi}{2A} (2j + 1) - n'j\pi \right) \sin \left( \frac{(nl + n'A)n\pi}{2A} \right) \right. \\ &\quad \left. + \frac{1}{nl - n'A} \sin \left( \frac{(nl - n'A)n\pi}{2A} (2j + 1) + n'j\pi \right) \sin \left( \frac{(nl - n'A)n\pi}{2A} \right) \right].\end{aligned}$$

Having these integrals evaluated, Equation (4.7) to Equation (4.10) can be simplified as the followings

$$\begin{aligned} & \sum_{m,n=1}^M \left[ \left( \frac{D_1}{3} (3k_{m'}^4 + 2k_{m'}^2 \zeta_{nn'}^2 + \zeta_{nn'}^4) - \sigma_1 \omega^2 I_{mm'}^{s,x} I_{nn'}^{c,y} \right) + \frac{2}{3} \left( \frac{E_b I_b \zeta_{mm'}^4}{3} \right. \right. \\ & \quad \left. \left. - \rho_b A_b \omega^2 I_{mm'}^{s,x} + K I_{mm'}^{s,x} \right) \mathcal{J}_n^c \right] \mathcal{C}_{mn}^{t,1} - \sum_{m,n=1}^M \frac{2}{3} K I_{mm'}^{s,x} \mathcal{J}_n^c \mathcal{C}_{mn}^{t,2} \\ & + \sum_{j=0}^J \sum_{m=0}^M \sum_{n=0}^{N_c} (S_{mn}^{t,j} + T_{mn}^{t,j}) I I_{mm}^{s,x} I I_{nn}^{c,j} = 2p_e \mathcal{I}_{m'}^{s,x} \mathcal{I}_{n'}^{c,y}, \end{aligned} \quad (\text{A.2})$$

$$\begin{aligned} & - \sum_{m,n=1}^M \frac{2}{3} K I_{mm'}^{s,x} \mathcal{J}_n^c \mathcal{C}_{mn}^{t,1} + \sum_{m,n=1}^M \left[ \left( \frac{D_2}{3} (3k_{m'}^4 + 2k_{m'}^2 \zeta_{nn'}^2 + \zeta_{nn'}^4) - \sigma_2 \omega^2 \right) I_{mm'}^{s,x} I_{nn'}^{c,y} \right. \\ & \quad \left. + \frac{2}{3} K I_{mm'}^{s,x} \mathcal{J}_n^c \right] \mathcal{C}_{mn}^{t,2} + \sum_{j=0}^J \sum_{m=0}^M \sum_{n=0}^{N_c} (S_{mn}^{t,j} e^{\gamma_{mn} d} + T_{mn}^{t,j} e^{-\gamma_{mn} d}) I I_{mm'}^{s,x} I I_{nn'}^{c,y,j} = 0, \end{aligned} \quad (\text{A.3})$$

$$\frac{1}{\gamma_{m''n''}} \sum_{m,n=1}^M \mathcal{C}_{mn}^{t,1} I I_{mm''}^{s,x} I I_{nn''}^{c,y,j} - \sum_{j=0}^J \sum_{m=0}^M \sum_{n=0}^{N_c} (S_{mn}^{t,j} - T_{mn}^{t,j}) I_{mm''}^{s,x} I_{nn''}^{c,y,j} = 0, \quad (\text{A.4})$$

$$\begin{aligned} & \frac{1}{\gamma_{m''n''}} \sum_{m,n=1}^M \mathcal{C}_{mn}^{t,2} I I_{mm''}^{s,x} I I_{nn''}^{c,y,j} \\ & - \sum_{j=0}^J \sum_{m=0}^M \sum_{n=0}^{N_c} (S_{mn}^{t,j} e^{\gamma_{mn} d} - T_{mn}^{t,j} e^{-\gamma_{mn} d}) I_{mm''}^{s,x} I_{nn''}^{c,y,j} = 0, \end{aligned} \quad (\text{A.5})$$

where

$$\mathcal{J}_n^c = J - \sum_{j=1}^J \cos(2k_n j l), \quad \zeta_{nn'} = \begin{cases} 2k_n & n = n', \\ 0 & n \neq n', \end{cases},$$

$$\mathcal{I}_m^{s,x} = \left\{ \begin{array}{ll} i\sqrt{\frac{A}{2}}, & k_m = -ik \sin \theta_i \cos \phi_i x, \\ \sqrt{\frac{2}{A}} \frac{k_m (1 - (-1)^m e^{-ik \sin \theta_i \cos \phi_i A})}{k_m^2 - (k \sin \theta_i \cos \phi_i)^2}, & \text{otherwise} \end{array} \right\},$$

$$\mathcal{I}_n^{c,y} = \left\{ \begin{array}{ll} \sqrt{\frac{2}{3A}} \left( \frac{1 - e^{-ik_n A}}{ik_n} - \frac{A}{2} \right), & k_n = -ik \sin \theta_i \cos \phi_i, \\ \sqrt{\frac{2}{3A}} \frac{ik_n (1 - e^{-ik \sin \theta_i \sin \phi_i A})}{(k \sin \theta_i \sin \phi_i)^2 - k_n^2}, & \text{otherwise} \end{array} \right\}.$$

$m', n' = 1, 2, 3, \dots, M$ ,  $m'' = 0, 1, 2, \dots, M$ ,  $n'' = 0, 1, 2, \dots, N_c$  and  $j = 0, 1, 2, \dots, J$ .

### A.1.1 $\mathcal{T}_L$ calculation

$\mathcal{T}_L$  is calculated following the same procedure in Section 3.3.2. Equation (A) need to be updated corresponding to the Type 1 boundary condition, which is

$$I_t = \frac{\rho_0 \omega^4}{8C_0 \pi^2 r^2} (|C_{mn}^{t,2}|^2 \mathcal{R}_m^{\text{sx}} \mathcal{R}_m^{*\text{sx}} \mathcal{R}_n^{\text{cy}} \mathcal{R}_n^{*\text{cy}}), \quad (\text{A.6})$$

where

$$\mathcal{R}_m^{\text{sx}} = \left\{ \begin{array}{ll} i\sqrt{\frac{A}{2}}, & k_m = -ik \sin \theta_t \cos \phi_t x, \\ \sqrt{\frac{2}{A}} \frac{k_m (1 - (-1)^m e^{-ik \sin \theta_t \cos \phi_t A})}{k_m^2 - (k \sin \theta_t \cos \phi_t)^2}, & \text{otherwise} \end{array} \right\},$$

$$\mathcal{R}_n^{\text{cy}} = \left\{ \begin{array}{ll} \sqrt{\frac{2}{3A}} \left( \frac{1 - e^{-ik_n A}}{ik_n} - \frac{A}{2} \right), & k_n = -ik \sin \theta_t \cos \phi_t, \\ \sqrt{\frac{2}{3A}} \frac{ik_n (1 - e^{-ik \sin \theta_t \sin \phi_t A})}{(k \sin \theta_t \sin \phi_t)^2 - k_n^2}, & \text{otherwise} \end{array} \right\}.$$

## A.2 Type 2 boundary condition

The modal functions corresponding to the Type 2 boundary conditions are

$$\mathcal{A}_m(x) = \sqrt{\frac{2}{3A}} (1 - \cos 2k_m x), \mathcal{B}_n(y) = \sqrt{\frac{2}{A}} \sin k_n y,$$

and with these modal functions, the plate displacements take the form

$$w_i(x, y) = \frac{2}{\sqrt{3A}} \sum_{m,n=1}^M C_{mn}^{\text{q},i} (1 - \cos 2k_m x) \sin k_n y. \quad (\text{A.7})$$

The terms  $\mathcal{G}\mathcal{A}_m(x)$  and  $\mathcal{D}_i\mathcal{A}_m(x)\mathcal{B}_n(y)$  corresponding to the selected  $\mathcal{A}_m(x)$  and  $\mathcal{B}_n(y)$  (type 2 boundary condition) are expressed as

$$\begin{aligned}\mathcal{G}\mathcal{A}_m(x) &= -\sqrt{\frac{2}{3A}}E_b I_b (2k_m)^4 \cos 2k_m x - A_b \rho_b \omega^2 \mathcal{A}_m(x) \\ \mathcal{D}_i\mathcal{A}_m(x)\mathcal{B}_n(y) &= -D_i \left( \sqrt{\frac{2}{3A}}(2k_m)^4 \cos 2k_m x - k_n^4 \mathcal{A}_m(x) \right. \\ &\quad \left. + 2\sqrt{\frac{2}{3A}}(2k_m)^2 k_n^2 \cos 2k_m x \right) \mathcal{B}_n(y) - \sigma_i \omega^2 \mathcal{A}_m(x)\mathcal{B}_n(y).\end{aligned}$$

Inserting  $\mathcal{A}_m(x)$ ,  $\mathcal{B}_n(y)$ ,  $\alpha_m(x)$  and  $\beta_n(y)$  in Equation (4.11) to Equation (4.16) the integrals corresponding to the Type 1 boundary conditions are evaluated as

$$\begin{aligned}I_{mm'}^{c,x} &= \begin{cases} 1 & m = m', \\ \frac{2}{3} & m \neq m', \end{cases}, & I_{nn'}^{s,y} &= \begin{cases} 1 & n = n', \\ 0 & n \neq n', \end{cases}, \\ II_{mm'}^{cx} &= \begin{cases} -\frac{1}{\sqrt{3}} & 2m = m', \\ \frac{1}{\sqrt{3}} & m' = 0, \\ 0 & \text{Otherwise,} \end{cases}, & II_{nn'}^{sy,j} &= \begin{cases} 0, & \frac{n}{A} = \frac{n'}{l}, \\ \Pi_{\text{cav}}^1, & n' = 0, \\ \Pi_{\text{cav}}^2 & \text{Otherwise,} \end{cases}.\end{aligned}$$

where

$$\begin{aligned}\Pi_{\text{cav}}^1 &= \frac{2}{n\pi} \sqrt{\frac{A}{l}} \sin \left[ (2j+1) \frac{n\pi}{2} \frac{A}{l} \right] \sin \frac{n\pi}{2} \frac{l}{A} \\ \Pi_{\text{cav}}^2 &= \frac{2\sqrt{Al}}{\pi} \left[ \frac{1}{nl+n'A} \sin \left( \frac{(nl+n'A)n\pi}{2A} (2j+1) - n'j\pi \right) \sin \left( \frac{(nl+n'A)n\pi}{2A} \right) \right. \\ &\quad \left. + \frac{1}{nl-n'A} \sin \left( \frac{(nl-n'A)n\pi}{2A} (2j+1) + n'j\pi \right) \sin \left( \frac{(nl-n'A)n\pi}{2A} \right) \right].\end{aligned}$$

Having these integrals evaluated, Equation (4.7) to Equation (4.10) can be simplified as the followings

$$\begin{aligned} & \sum_{m,n=1}^M \left[ \left( \frac{D_1}{3} (\zeta_{mm'}^4 + 2\zeta_{mm'}^2 k_{n'}^2 + 3k_{n'}^4) - \sigma_1 \omega^2 \right) I_{mm'}^{c,x} I_{nn'}^{s,y} + \mathcal{P} \left( \frac{E_b I_b \zeta_{mm'}^4}{3} \right. \right. \\ & \quad \left. \left. - \rho_b A_b \omega^2 I_{mm'}^{c,x} + K I_{mm'}^{c,x} \right) \mathcal{J}_n^s \right] \mathcal{C}_{mn}^{q,1} - \sum_{m,n=1}^M \mathcal{P} K I_{mm'}^{c,x} \mathcal{J}_n^s \mathcal{C}_{mn}^{q,2} \\ & + \sum_{j=0}^J \sum_{m=0}^M \sum_{n=0}^{N_c} (S_{mn}^{q,j} + T_{mn}^{q,j}) I I_{mm'}^{c,x} I I_{nn'}^{s,j} = 2p_e \mathcal{I}_m^{c,x} \mathcal{I}_m^{s,y}, \end{aligned} \quad (\text{A.8})$$

$$\begin{aligned} & - \sum_{m,n=1}^M \mathcal{P} K I_{mm'}^{c,x} \mathcal{J}_n^s \mathcal{C}_{mn}^{q,1} + \sum_{m,n=1}^M \left[ \left( \frac{D_2}{3} (3k_{m'}^4 + 2k_{m'}^2 \zeta_{nn'}^2 + \zeta_{nn'}^4) - \sigma_2 \omega^2 \right) I_{mm'}^{c,x} I_{nn'}^{s,y} \right. \\ & \quad \left. + \mathcal{P} K I_{mm'}^{c,x} \mathcal{J}_n^s \right] \mathcal{C}_{mn}^{q,2} + \sum_{j=0}^J \sum_{m=0}^M \sum_{n=0}^{N_c} (S_{mn}^{q,j} e^{\gamma_{mn} d} + T_{mn}^{q,j} e^{-\gamma_{mn} d}) I I_{mm'}^{c,x} I I_{nn'}^{s,y,j} = 0, \end{aligned} \quad (\text{A.9})$$

$$\frac{1}{\gamma_{m''n''}} \sum_{m,n=1}^M \mathcal{C}_{mn}^{q,1} I I_{mm''}^{c,x} I I_{nn''}^{s,j} - \sum_{j=0}^J \sum_{m=0}^M \sum_{n=0}^{N_c} (S_{mn}^{q,j} - T_{mn}^{q,j}) I_{mm''}^x I_{nn''}^{y,j} = 0, \quad (\text{A.10})$$

$$\begin{aligned} & \frac{1}{\gamma_{m''n''}} \sum_{m,n=1}^M \mathcal{C}_{mn}^{q,2} I I_{mm''}^{c,x} I I_{nn''}^{s,j} \\ & - \sum_{j=0}^J \sum_{m=0}^M \sum_{n=0}^{N_c} (S_{mn}^{q,j} e^{\gamma_{mn} d} - T_{mn}^{q,j} e^{-\gamma_{mn} d}) I_{mm''}^x I_{nn''}^{y,j} = 0, \end{aligned} \quad (\text{A.11})$$

where

$$\mathcal{J}_n^s = \sum_{j=1}^J \sin(k_n j l), \quad \mathcal{P} = \begin{cases} \frac{4}{n\pi}, & n \text{ is odd,} \\ 0, & n \text{ is even,} \end{cases}, \quad \zeta_{mm'} = \begin{cases} 2k_m, & m = m', \\ 0, & m \neq m', \end{cases},$$

$$\mathcal{I}_m^{\text{cx}} = \left\{ \begin{array}{ll} \sqrt{\frac{2}{3A}} \left( \frac{1 - e^{-ik_m A}}{ik_m} - \frac{A}{2} \right), & k_m = -ik \sin \theta_i \cos \phi_i, \\ \sqrt{\frac{2}{3A}} \frac{ik_m (1 - e^{-ik \sin \theta_i \cos \phi_i A})}{(k \sin \theta_i \cos \phi_i)^2 - k_m^2}, & \text{otherwise} \end{array} \right\},$$

$$\mathcal{I}_n^{\text{sy}} = \left\{ \begin{array}{ll} i\sqrt{\frac{A}{2}}, & k_n = -ik \sin \theta_i \cos \phi_i, \\ \sqrt{\frac{2}{A}} \frac{k_n (1 - (-1)^n e^{-ik \sin \theta_i \cos \phi_i A})}{k_n^2 - (k \sin \theta_i \cos \phi_i)^2}, & \text{otherwise} \end{array} \right\}.$$

$m', n' = 1, 2, 3, \dots, M$ ,  $m'' = 0, 1, 2, \dots, M$ ,  $n'' = 0, 1, 2, \dots, N_c$  and  $j = 0, 1, 2, \dots, J$ .

### A.2.1 $\mathcal{T}_L$ calculation

$\mathcal{T}_L$  is calculated following the same procedure in Section 3.3.2. Equation (A) need to be updated corresponding to the Type 2 boundary condition, which is

$$I_t = \frac{\rho_0 \omega^4}{8c_0 \pi^2 r^2} (|\mathcal{C}_{mn}^{q,2}|^2 \mathcal{R}_m^{\text{cx}} \mathcal{R}_m^{*\text{cx}} \mathcal{R}_n^{\text{sy}} \mathcal{R}_n^{*\text{sy}}), \quad (\text{A.12})$$

where

$$\mathcal{R}_m^{\text{cx}} = \left\{ \begin{array}{ll} \sqrt{\frac{2}{3A}} \left( \frac{1 - e^{-ik_m A}}{ik_m} - \frac{A}{2} \right), & k_m = -ik \sin \theta_t \cos \phi_t, \\ \sqrt{\frac{2}{3A}} \frac{ik_m (1 - e^{-ik \sin \theta_t \cos \phi_t A})}{(k \sin \theta_t \cos \phi_t)^2 - k_m^2}, & \text{otherwise} \end{array} \right\},$$

$$\mathcal{R}_n^{\text{sy}} = \left\{ \begin{array}{ll} i\sqrt{\frac{A}{2}}, & k_n = -ik \sin \theta_t \cos \phi_t, \\ \sqrt{\frac{2}{A}} \frac{k_n (1 - (-1)^n e^{-ik \sin \theta_t \cos \phi_t A})}{k_n^2 - (k \sin \theta_t \cos \phi_t)^2}, & \text{otherwise} \end{array} \right\}.$$